THESIS FOR THE DEGREE OF DOCTOR OF PHARMACY

Diastereomeric Effects in DNA Binding

Biological and Biophysical Studies on Ruthenium Complexes

ANNA K. F. MÅRTENSSON

Department of Chemistry and Chemical Engineering
CHALMERS UNIVERSITY OF TECHNOLOGY
Göteborg, Sweden 2018

Diastereomeric Effects in DNA Binding – Biological and Biophysical Studies on Ruthenium Complexes
ANNA K. F. MÅRTENSSON
ISBN 978-91-7597-693-8

Doktorsavhandlingar vid Chalmers tekniska högskola
Ny serie nr. 4374
ISSN 0346-718X

Department of Chemistry and Chemical Engineering
Division of Chemistry and Biochemistry – Physical Chemistry
Chalmers University of Technology
SE - 412 96 Göteborg
Sweden
Telephone: +46 (0)31 - 772 1000

Front cover: The one-dimensional lattice model imagined as a string of beads where the string is a polymer of identical binding sites and the beads are ligands. The different colors on the beads depict the diastereomeric nature of the binding.

Chalmers Reproservice
Göteborg, Sweden 2018

Diastereomeric Effects in DNA Binding – Biological and Biophysical Studies on Ruthenium Complexes

ANNA K. F. MÅRTENSSON
Department of Chemistry and Chemical Engineering
Chalmers University of Technology

ABSTRACT

Organic molecules, such as glucose and amino acids, are most often chiral. This means that their mirror-images are different, in the same way a left and a right hand are different from each other. For example, the DNA double helix in its standard form twists like a right-handed screw. Therefore, when chiral DNA-binding ligands interacts with DNA the effect will depend on their handedness – that is, the interactions will be diastereomeric. Hence, it is essential to always consider the effects chirality may have on ligand-DNA interactions when developing new DNA-targeting drugs. By improving properties such as binding affinity and sequence selectivity, many adverse effects present in currently available treatments could be avoided. Therefore, to have efficient methods for evaluating ligand-DNA binding properties would greatly simplify the search for potential therapeutic candidates.

The key focus in this thesis is the binding interactions between DNA and a group of DNA intercalating ruthenium complexes. It is demonstrated using spectroscopic and calorimetric methods that both chirality and small changes in the molecular structure of the complex can have significant impact on the binding properties of the complex. Furthermore, a general algorithm used for thermodynamically characterize the ligand-DNA binding interactions is presented as a simplified method for fitting binding models to complex systems. From both photophysical and calorimetric results it is evident that cooperativity between neighboring bound ligands has a huge impact on the overall binding interactions between ruthenium complexes and DNA and must be taken into account in order to find a satisfactory fit of a theoretical binding model. Finally, ruthenium complexes are shown *in vitro* to have a high antimicrobial activity comparable to clinically available antibiotics and it is again evident that chirality have a strong influence on the binding properties of the complex. As a continuance to the promising antimicrobial results, an alternative type of antibiotic is presented in the concluding remarks as a possible counteract to the ongoing and growing problem of multi-resistant bacteria.

KEYWORDS: DNA, ruthenium, intercalation, enantiomer, diastereomeric, kinetics, spectroscopy, calorimetry, neighbor interaction, antimicrobial activity

To my husband and two children, without whom this thesis would have been completed one year earlier

LIST OF PUBLICATIONS

This thesis is based on the work presented in the following papers:

I. **Binding of Ru(terpyridine)(pyridine)dipyridophenazine to DNA studied with polarized spectroscopy and calorimetry**
Anna K. F. Mårtensson and Per Lincoln*
Dalton Trans. **2015,** 44, 3604-3613

II. **Competitive DNA binding of $Ru(bpy)_2dppz^{2+}$ enantiomers studied with isothermal titration calorimetry (ITC) using a direct and general binding isotherm model**
Anna K. F. Mårtensson and Per Lincoln*
Phys. Chem. Chem. Phys. **2018,** 20, 7920-7930

III. **Effects of methyl substitution on DNA binding enthalpies of enantiopure $Ru(phenanthroline)_2dipyridophenazine^{2+}$ complexes**
Anna K. F. Mårtensson and Per Lincoln*
Phys. Chem. Chem. Phys. **2018,** Advance Article
DOI: 10.1039/C8CP01151F

IV. **Diastereomeric crowding effects in the competitive DNA intercalation of $Ru(phenanthroline)_2dipyridophenazine^{2+}$ enantiomers**
Anna K. F. Mårtensson and Per Lincoln*
Manuscript in preparation

V. **Diastereomeric bactericidal effect of $Ru(phenanthroline)_2$-dipyridophenazine**
Anna K. F. Mårtensson*, Mattias Bergentall, Valentina Tremaroli and Per Lincoln
Chirality **2016,** 28, 713-720

CONTRIBUTION REPORT

Paper I I suggested the project and performed all of the experimental work. I analyzed the data together with PL using an algorithm developed by PL. I wrote the majority of the paper.

Paper II I performed all of the experimental work for this paper. The data analysis was performed together with PL using an algorithm developed by PL. I wrote the majority of the paper.

Paper III I performed all of the experimental work for this paper. The data analysis was done together with PL using an algorithm developed by PL. I wrote the majority of the paper.

Paper IV I did all of the experimental work for this paper. I analyzed the data together with PL using an algorithm developed PL. I wrote the majority of the paper.

Paper V I suggested the project and did all the experimental work except for the confocal microscopy imaging (done by MB). I did all of the data analysis with input from VT. I wrote the paper.

LIGAND ABBREVIATIONS

10-Me-dppz	10-methyldipyrido[3,2-*a*:2’3’-*c*]phenazine
11,12-diMe-dppz	11,12-dimethyldipyrido[3,2-*a*:2’3’-*c*]phenazine
bidppz	11,11’-bis(dipyrido[3,2-*a*:2’,3’-*c*]phenazinyl)
bpy	2,2’-bipyridine
dab	1,2-diaminobenzene
dabd	3,3’-diaminobenzidine
dppz	dipyrido[3,2-*a*:2’3’-*c*]phenazine
phen	1,10-phenanthroline
pq	1,10-phenanthroline-5,6-dione
py	pyridine
tpy	2,2’:6’,2’’-terpyridyl

LIGAND STRUCTURES

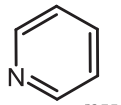

py

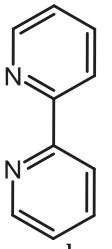

bpy

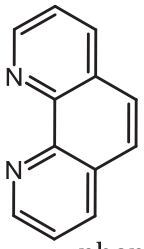

phen

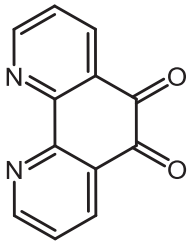

pq

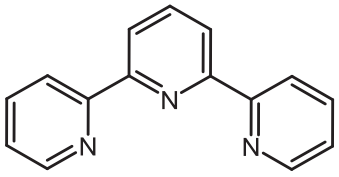

tpy

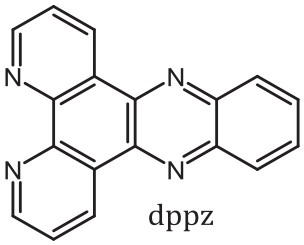

dppz

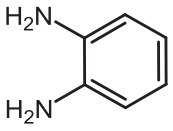

dab

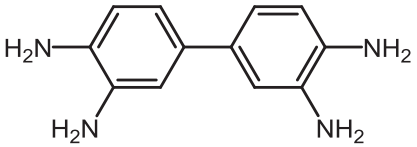

dabd

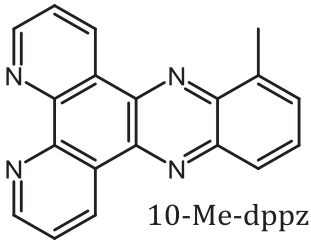

10-Me-dppz

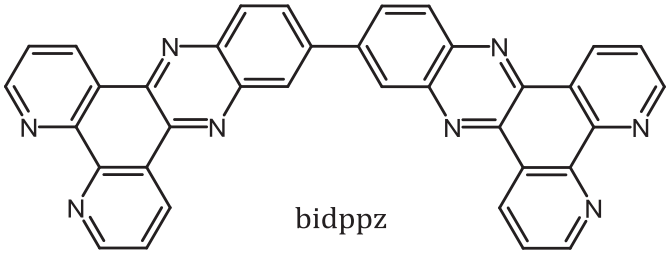

bidppz

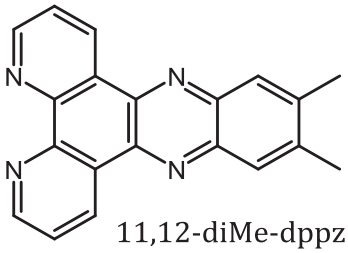

11,12-diMe-dppz

TERM ABBREVIATIONS

CD	circular dichroism
CFU	colony-forming units
ct	calf thymus
DNA	deoxyribonucleic acid
DAPI	4’,6-diamidino-2-phenylindole
ICD	induced circular dichroism
ITC	isothermal titration calorimetry
LB	Luria-Bertani
LD	linear dichroism
MBC	minimum bactericidal concentration
MBEC	minimum biofilm eradication concentration
MIC	minimum inhibitory concentration
MLCT	metal-to-ligand charge transfer
OD	optical density
nRMSD	normalized root-mean-square deviation
RMSD	root-mean-square deviation
RNA	ribonucleic acid
TEM	trial-and-error method

TABLE OF CONTENTS

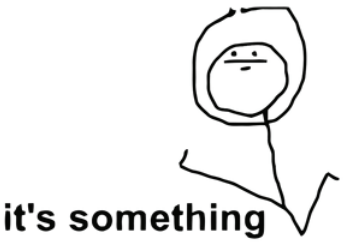
it's something

1 INTRODUCTION

The cell is the basic unit of life. We all have them. They are the building blocks of every living organism, but each cell is on its own an isolated system capable of replication, growth and metabolism. From the smallest bacterium to higher order multicellular organisms, all cells share certain features: ribosomes; where proteins are produced, the plasma membrane; a selective barrier separating the cell from the surrounding environment, and the cytoplasm; the material within the plasma membrane. These are all essential components of the cell, but the most central of all is the carrier of all genetic information of that cell, deoxyribonucleic acid, more commonly known as DNA. DNA is often referred to as the blueprint of life. Although only a metaphor, this would imply that DNA is something prescriptive and static. Nothing could be farther from the truth. Although composed of merely four simple building units, DNA is a multi-dimensional, complex, and dynamic molecule that is ever-changing and ever-adapting. It is responsible for the growth, functioning and reproduction of a living organism. Quite simply, DNA is what make us who we are.

Every day something bad happens to your DNA. At a rate of several thousand errors per day, DNA is damaged by a vast number of causes. It could be environmental, such as exposure to ultra-violet light, or endogenous, such as an oxidative attack from normal metabolic byproducts. Should the integrity and availability of essential information of the genome be lost, the cell can no longer function normally. Fortunately, the cell has developed several DNA repair mechanisms that is implemented depending on the nature of the damage, so most of the time the damage is harmless. Sometimes, however, the DNA repair mechanism fails, and the cell may enter a state of unregulated cell division, resulting in cancer. Ironically, cancer is often effectively treated with DNA-damaging drugs. However, an ongoing problem with cancer-treating drugs are their non-specificity towards cancerous cells. Healthy tissues sharing the high proliferation rate characteristic of many types of cancers will often suffer the same damaging effects of the treatment resulting in nasty side effects.

Other diseases dependent on cellular division such as bacterial infections could also be treated by DNA-targeting drugs. Many attempts have already been made to develop effective treatments targeting bacterial DNA, but the reoccurring problem of non-specificity results in the drug being deemed to cytotoxic for the host. Interestingly, many of them were instead developed (quite successfully) as anti-cancer drugs. However, pathogenic bacterial strains are becoming more and more resistant to available antibiotics so it is much needed (now more than ever) that new antibiotics with alternative targets, such as bacterial DNA, are found.

Large biological molecules, such as DNA and proteins, are really just long chains of simpler building blocks molecules (nucleotides for DNA and amino acids for proteins). These building block molecules are chiral, meaning that they could in theory exist naturally as 50:50 racemic mixtures. However, both nucleotides and amino acids occur in nature as single enantiomers. Consequently, the DNA structure itself is chiral and exists as a single enantiomer, a right-handed helix. Any interactions between the DNA molecule and another chiral molecule will therefore be diastereomeric. Hence, in medicine, any drug with a chiral center and with a chiral target should be given as a single enantiomer, as the different enantiomers will interact differently with the chiral molecule in the body.

Fifty years after their discovery, in the 80s, ruthenium(II) polypyridyl complexes were proposed to bind to DNA by inserting one of its ligands between the DNA base pairs in a binding mode called intercalation. The search for stronger binding affinity and enantioselectivity, combined with the interesting photophysical properties of ruthenium(II) polypyridyl complexes, prompted a synthesis cascade of intercalating complexes with the hopes of developing a new DNA targeting drug or probe. Even so, there is still much that is unknown of the underlying mechanisms behind the ligand-DNA interactions. Factors such as the chirality of the complex or substitution groups on the ancillary and intercalating ligands not only affect the binding between the DNA strand and the ruthenium complex, but also the interactions between bound complexes in close proximity of each other. Only when the kinetics behind the ligand-DNA binding is fully understood and hence (more importantly), predictable, effective DNA-binding pharmacotherapeutics can be developed.

In this thesis, I will explore how ruthenium complexes may influence each other's binding interactions to DNA and how seemingly small molecular differences such as chirality and the addition of substitution groups can have significantly affect the binding properties of the complex. I will furthermore demonstrate how satisfactory model fitting can be achieved using quite simple methods, regardless the complexity of the binding system investigated.

2 BACKGROUND

This thesis has a main theme of the binding interactions between small molecules and DNA using ruthenium complexes as model compounds. This chapter focuses on providing a basic understanding to why DNA is an attractive drug target, the properties of ruthenium complexes and how they interact with DNA, emphasizing the influences of molecular structure and chirality to binding affinity. Lastly, the fundamental concepts of cellular uptake mechanisms and the potential of developing ruthenium complexes as a new family of antibiotics will be addressed.

2.1 Structure and Functional Role of DNA

Deoxynucleic acid, or DNA, is a molecule that carries all genetic information of all known living organisms (with the exception of viruses that, rather than being "alive", are free forms of DNA or RNA that cannot replicate on their own). The reading out of this information tells every cell which proteins to build, and where and when to build them. The proteins, in turn, are the building blocks of the living organism. In order to develop DNA-binding molecules with improved properties, such as binding affinity and sequence selectivity, the basic structure of DNA must first be understood.

DNA is a long polymer consisting of two helical strands coiled around the same axis, where the 5' end of one strand is paired with the 3' end of its complementary strand, forming an anti-parallel double helix. Each strand is composed of the same repetitive unit called a nucleotide, consisting of a deoxyribose sugar with a nitrogenous nucleobase bound to one side and a phosphate group bound to the other side (Fig. 2.1 (left)). The nucleotides are covalently linked to each other with alternating sugar-phosphate residues, forming the DNA backbone. The nucleobase can either be a double-ringed structure (purine) or a single-ringed structure (pyrimidine). There are in total four available nucleobases: adenine (A) (a purine), cytosine (C) (a pyrimidine), guanine (G) (a purine) and thymine (T) (a pyrimidine). The nucleobases are hydrophobic, hence they point inwards protecting themselves from the aqueous environment. Together with the nucleobases on the opposite strand, they form pairs bound together by hydrogen bonds. Each base pair is formed from two complementary nucleotides (purine with pyrimidine). In accordance to Chargaff's rules, A always pairs with T and C always with G (Fig. 2.1(right)).[1-3]

There are three different conformations of the DNA double helix: A-, B- and Z-form (Fig. 2.2). The most common form, present in most DNA at neutral pH and physiological conditions, is the B-form. This is the classic right-handed double helical structure, first proposed by James D. Watson and Francis Crick in 1953,[4] where the grooves formed by

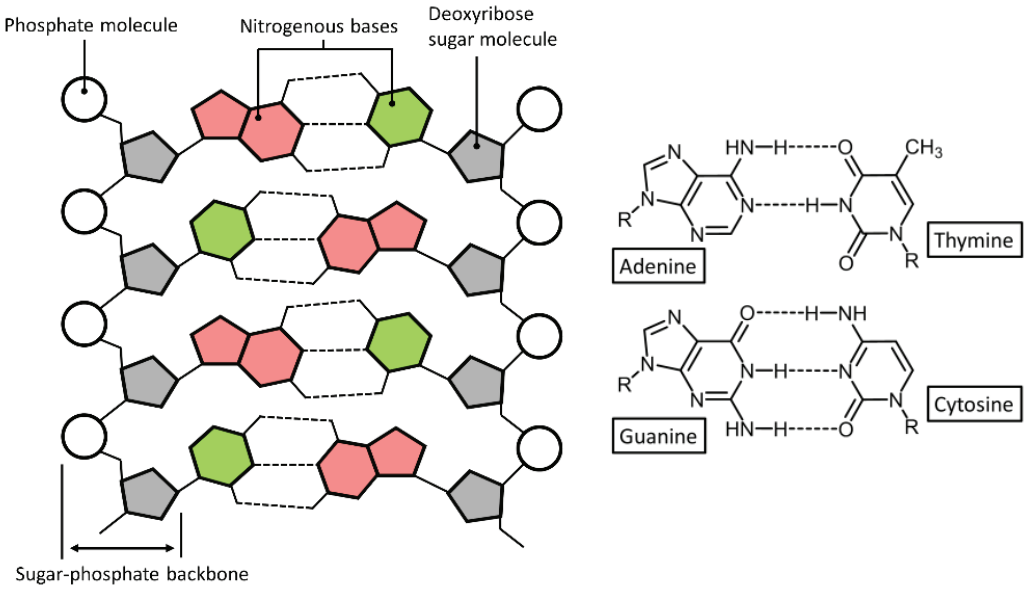

Figure 2.1 *A simplified illustration showing the anti-parallel structure of a small part of DNA (left) and molecular structure of the four nucleobases connected via hydrogen bonding (right).*

between the backbones of the helix have equal depths, but two different widths. Their names, the major and minor groove, reflect their difference in size. The A-form is also a right-handed double helix, but is thicker with a shorter distance between the base pairs, due to a different conformation of the deoxyribose sugar ring. In contrast to the B-form, the base pairs are not perpendicular to the helix axis, but more displaced from the central axis and closer to the major groove. The result is a ribbon-like helix with a more open cylindrical core. This conformation is found in nature mainly in RNA-RNA duplexes, but also in DNA-RNA hybrids. It can also appear in dehydrated DNA samples used in crystallographic experiments. The third conformation, the Z-form, has a strikingly different left-handed helical structure. Z-DNA is formed by stretches of alternating purines and pyrimidines, e.g. GCGCGC, especially in negatively supercoiled DNA (underwound DNA).

DNA has two major functions, both crucial for the survival of an organism. The first function is coding for proteins, where the genetic code is translated to a language of amino acids – the building blocks of proteins. Proteins play many critical roles in the body, including repair and maintenance, chemical reactions, and transportation of molecules. Indeed, with the exception of water, proteins are the most abundant substance found in an organism. The second function of DNA is replication; the ability to copy itself is vital for the reproduction and growth of an organism. As DNA plays such a critical role for cellular growth and reproductivity of an organism, malignant conditions dependent on uncontrolled cell division, such as cancer and infectious diseases, are often treated (quite successfully) with DNA-targeting drugs. However, while there are already effective treatments available that eradicate cancerous and bacterial cells though various

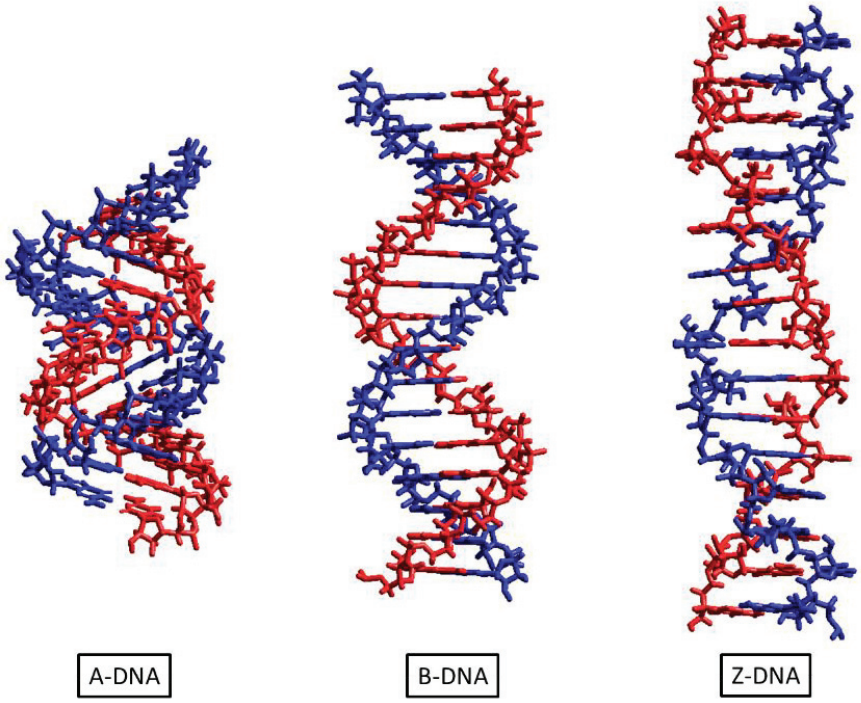

Figure 2.2 *A-, B- and Z-form of a 16 base pair DNA double helix.*

DNA-damaging mechanisms, the specificity is still so poor that healthy cells are also affected. The challenge lies in finding new therapeutics with a more sequence-specific DNA binding affinity.

2.2 Non-Covalent Binding Interactions with DNA

In principle, there are six modes for reversible (noncovalent) binding of molecules with the DNA double helix: electrostatic attractions with the anionic sugar-phosphate backbone of DNA, interactions with the DNA major groove, interactions with the DNA minor groove, intercalation between base pairs via the DNA major groove, intercalation between base pairs via the DNA minor groove, and a threading intercalation mode (Fig. 2.3).

For groove binders, the major groove is generally reserved for proteins composed of DNA-binding domains as it exposes more functional groups that identify a base pair. Minor groove binding ligands are typically composed of several aromatic rings connected by bonds that possess torsional freedom. As a result, minor groove binders generally adopt a characteristic curved shape that is isohelical with the target groove. Minor groove binders generally exhibit a binding preference for A-T base pairs due to favorable hydrophobic contacts, the more well-known examples of this being the synthetic dyes DAPI[5] and Hoechst[6-7]. In addition, sequence selectivity is easier to achieve compared to intercalators, as groove binders can recognize a longer base sequence. Minor groove

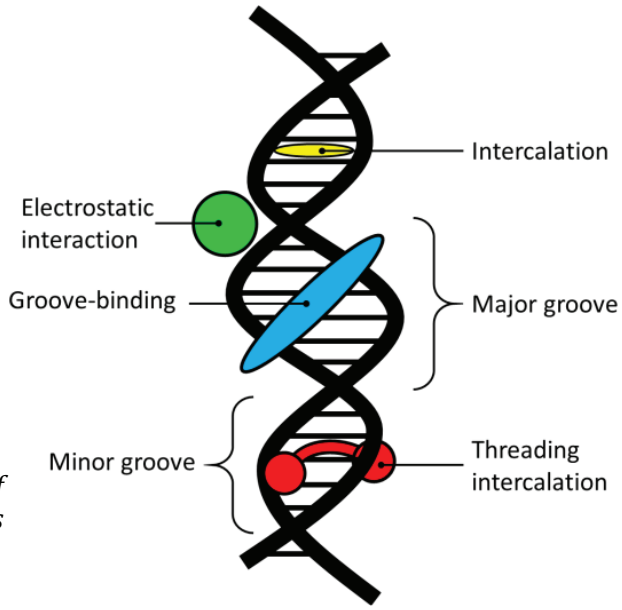

Figure 2.3 *Schematic illustration of possible non-covalent binding modes between small molecules and DNA.*

binders are usually preferred for fluorescent staining of the DNA in, for example, microscopy as they do not cause structural distortions of the DNA, in contrast to intercalating ligands.

Intercalating ligands typically possess flat, heteroaromatic ring systems capable of inserting between two adjacent base pairs in a double helix. The ligand-DNA complex is stabilized by π-π stacking interactions between the ligand and the DNA bases surrounding it. Also, cationic compounds stabilize the ligand-DNA interactions as there is an additional electrostatic attraction between the positive charge of the ligand and the negative charge of the phosphate backbone groups. Intercalation causes several distortions of the DNA backbone, e.g. lengthening of the DNA polymer and some unwinding. Conformational changes in the DNA polymer initiated by the first binding event will mediate the binding of additional ligands, i.e. cooperative binding. In addition, these structural changes can readily be used as a reliable diagnostic tool for this binding mode. Intercalating ligands can interfere with the recognition and function of DNA associated proteins and hence slow down or even inhibit replication and transcription processes.

A more unusual DNA-binding mode is threading intercalation, associated with molecules containing an aromatic ring system with bulky substituents on opposite ends, much like a dumbbell shape. A well-known example is the naturally occurring antibiotic nogalamycin.[8] For both binding and dissociation to occur, one of the bulky substituents must pass through the base pair stack. The resulting bound state leaves the flat middle part intercalated between the base pairs and the bulky substituents located one in each groove. Obviously, the large molecular thickness of the bulky substituents requires some

base pair dissociation (i.e. partial breakage of the DNA double helix) for penetration to occur. Such a process will effectively result in kinetic inertness and a higher stabilization of the ligand-DNA complex not seen in those formed from conventional intercalators. The reduced dissociation rate associated with a threading intercalation binding mode have been shown to be important for cytotoxic activity[9], making these types of molecules very attractive as potential new DNA-binding drugs.

2.3 General Properties of Metallointercalators

Metallointercalators refer to positively charged transition metal complexes that contain planar, heterocyclic, aromatic ligands with at least one of the ligands capable of DNA intercalation. Most metallointercalators, with very few exceptions, share a few characteristics important for their functionality. They are coordinately saturated making them kinetically inert which, in turn, give the metal complexes a much desired stability. They are either d^6 octahedral or d^8 square-planar, thus exhibiting a rigid or mostly rigid three-dimensional structure, also an important property since excessive fluxionality could negatively affect DNA-sequence recognition. It is also possible for the stereochemistry of the metal complex to provide specificity. The metal center serves as an anchor, and its stability enables interchangeability of the ligands, thus the DNA-binding and recognition properties of the complex can be varied quite easily. Finally, most of the complexes are photochemically or photophysically active thanks to the transition metal center, thus extending the potential use of metallointercalators to more than just a passive molecular recognition agents. As a result, metallointercalators can be used in various capabilities, such as fluorescent markers[10], DNA foot-printing agents[11-12] and electrochemical probes[13].

2.4 Ruthenium(II) Polypyridyl Complexes as DNA Intercalators

The first clues suggesting interactions between inert metal complexes and DNA can be traced back as far as the 1950s, in the work of F.P. Dwyer and coworkers where simple tris(chelate) complexes of Ru(II) and Ni(II) were found to have antimicrobial and antiviral activities.[14-17] Even this early, an enantioselective biological activity could be observed in some cases. It was, however, not until the 1980s that the binding interactions between ruthenium complexes and DNA were described. These earliest studies focused on tris(phenanthroline) complexes of several transition metals[18-19], among which ruthenium[20-22], indicating the DNA-binding mode for $Ru(phen)_3^{2+}$ to be partial intercalation of a phenanthroline (phen) ligand into the helix in the major groove[23-24]. These early studies suggested that ruthenium(II) polypyridyl complexes of the general form $Ru(L)_2(IL)^{2+}$ (L = ancillary ligand and IL = intercalating ligand) interact with DNA via intercalation of one of the ligands between the base pairs. Furthermore, depending on the type of ligand coordinated, the mode and strength of the DNA interaction could be modified. This initiated a search for ruthenium complexes with improved DNA-binding

as well as photophysical properties, the most famous examples probably being the light-switch complexes, $Ru(bpy)_2dppz^{2+}$ and $Ru(phen)_2dppz^{2+}$, so named for becoming completely quenched in aqueous solution but become brightly luminescent upon intercalation into DNA.[25-28] This effect is considered to be caused by hydrogen bonding of the aqueous environment to the phenazine nitrogens of the dppz ligand, leading the emissive ^{3}MLCT state (located on the dppz ligand) to be effectively quenched.[29-30] That it is the dppz ligand in tri-bidentate complexes that intercalates between the base pairs has been established by both spectroscopic and biophysical methods, with the most recent examples being a series of X-ray crystallography studies by Hall and coworkers.[31-33] Once intercalated, the dppz ligand is shielded from the surrounding solvent and hydrogen bonding is made more difficult. The "light-switch effect" aside, the increased overlap between the extended phenazine rings of the dppz ligand and the aromatic nucleobases significantly improved DNA-binding affinity.[25] As even seemingly small changes in the structures of both the ancillary as well as the intercalating ligands may tune the photophysical properties of the complex, numerous variations of dppz-ruthenium-centered complexes have been reported, with the aim of improving both DNA-binding strength and DNA sequence selectivity.

The octahedral coordination geometry that comes from coordinating three bidentate ligands to the ruthenium ion leads to a structure much like a three-winged propeller structure (Fig. 2.4). A propeller can either have a right-handed (Δ) or a left-handed (Λ) configuration, resulting in a chiral ruthenium complex able to exist in two enantiomeric forms, which are non-superimposable mirror images of each other. DNA, being a right-handed double helix in its most naturally occurring B-form, is consequently also a chiral molecule and will interact differently with the Δ- respectively Λ-enantiomer, as numerous studies have already demonstrated.[21, 34-41]

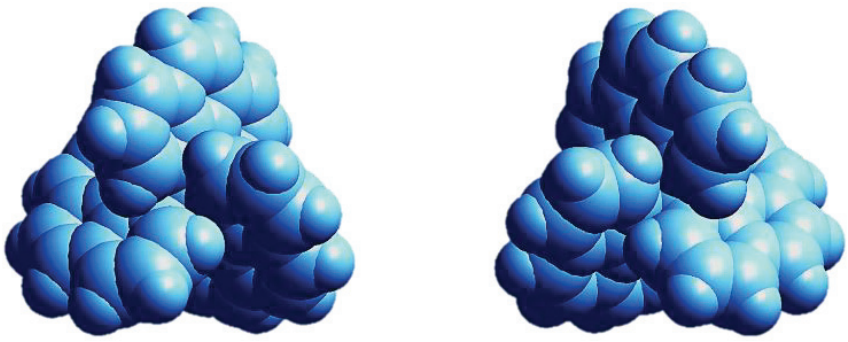

Figure 2.4 *The Λ- (left) and Δ-enantiomer (right) of* $Ru(phen)_3^{2+}$.

If instead a tridentate moiety is coordinated to the ruthenium ion, a plane of symmetry is introduced and there will no longer be a stereocentre at the ruthenium ion and the complex will thus not be chiral. This eliminates the need for resolving racemic mixtures into pure enantiomeric forms. However, in contrast to the well-studied light-switch complexes and their derivatives, complexes with a tridentate moiety such as tpy have generally very small quantum yields at room temperature.[42-43] As a result the interest for intercalating ruthenium complexes with a tridentate moiety has been much lower. However, this type of intercalating ruthenium complex has a single free coordination site left available, enabling a fine-tuning of its DNA-binding properties.

As mentioned above, threading intercalation is an unusual binding form with a significantly slower association and dissociation rates when binding to DNA. Binuclear ruthenium(II) polypyridyl complexes of the form μ-bidppz$(L)_4Ru_2^{4+}$ (L = phen or bpy) were found to bind with extremely high affinities to DNA through a binding mode later identified as threading intercalation.[37, 44-45] Not only do these ruthenium complexes have extremely slow kinetics, even in comparison with other synthetic threading intercalators, but they also possess light-switch properties. In combination, the threading process can be easily studied using only conventional spectroscopic techniques. Our group has previously shown both μ-bidppz$(phen)_4Ru_2^{4+}$ and μ-bidppz$(bpy)_4Ru_2^{4+}$ to be kinetically selective towards long AT-rich sequences of DNA.[46-47] Later studies on binuclear ruthenium complexes with structural modifications on the bridging ligand showed the same selectivity.[48-49] This property could potentially be exploited for targeting genomes with AT-rich DNA, for example the *Mycoplasma* species[50], which are endosymbiotic bacteria, and the malaria parasite *Plasmodium falciparium*[51].

2.5 Cellular Uptake of Ruthenium Complexes

In order to reach the DNA in a living cell, a compound must be able to penetrate a series of barriers, one of the first being the cell membrane. Composed primarily by a lipid bilayer of phospholipids containing a variety of proteins and lipids, the cell membrane regulates the uptake (and expulsion) of compounds. The organization of the lipid bilayer, which is composed of a hydrophilic head group attached to hydrophobic chains, provides a hydrophobic interior of the membrane. As a result, a large and/or hydrophilic compound will have more difficulty permeating the membrane via passive diffusion. Such compound would instead require a transport mechanism or endocytosis, both tightly regulated by different membrane proteins and receptors. Often the cell membrane is permeabilized during the initial assessment of a compound. While the barrier is removed to allow free passage into the cytosol, the internal structure of the cell remains intact (although non-viable). This provides information of the compound's intracellular targets as well as what photophysical properties that might be present.

The ^{3}MLCT light-switch properties of $Ru(L)_2dppz^{2+}$systems greatly simplifies the assessment of cellular uptake and localization within the cell. Initial studies by the Barton group indicated passive diffusion as the uptake mechanism and hence a strong dependence on the hydrophobicity of the ancillary ligands.[52-53] This comes as no greater surprise, considering the largeness and positive charge of these types of Ru complexes, making them relatively hydrophilic. While mononuclear ruthenium(II) polypyridyl complexes appear to rely on passive diffusion as the transport mechanism, binuclear complexes enter the cell via active transport, using both endocytic and non-endocytic pathways, depending on the structure of the complex. Again not surprisingly, as the sheer size of such a complex would greatly diminish its ability to enter the cell through passive diffusion. Complexes entering the cell through an endocytic drug delivery mechanism appear to have limited nuclear staining when compared to those transported through the cell membrane in a non-endocytic way.[54] Complexes that enter the cell through endocytosis appear instead to be trapped in the endosomes[55] or transported to the mitochondria[56]. Evidently, the initial transport mechanism chosen to surpass the first obstacle for the complex heavily influences what the final destination will be, making it even more important for the uptake properties of the complex to be fully understood. While it is already well-established that the chirality of a complex have great impact on its DNA-binding properties, should a complex need to enter a cell through non-endocytic active transport, it is likely that the chirality would also influence the ability to permeate the cell membrane in the first place, emphasizing the importance of using enantiopure complexes when assessing cellular uptake.

2.6 Morphology of Prokaryotic Cells

Cells are regarded as the basic building blocks of life and all living organisms can be broadly classified either as prokaryotes or as eukaryotes, depending on the fundamental structure of their cells (Fig. 2.5). Prokaryotes are subsequently divided into two groups: bacteria and archaea, while all other groups of living organisms are eukaryotes. In contrast to eukaryotic cells, the more primitive prokaryotic cell lack a cell nucleus (which holds genetic material) as well as any other membrane-encased organelles. Although prokaryotic cells do not contain a cell nucleus, its genetic material is still located in a discrete region in the cytoplasm called the nucleoid. Unlike the linear DNA of eukaryotes, bacterial DNA consists typically of a single circular chromosome. Many bacteria also contain one or more plasmids, which are small circular DNA molecules. These can readily be picked up from the surrounding environment (transformation) or by direct contact from other bacteria (conjugation).

All plasmids have their own “Origin of replication” – a stretch of DNA making the plasmid capable of copy themselves independently of the bacterial chromosome, resulting sometimes in hundreds of copies within one bacterial cell. The plasmids contain only a

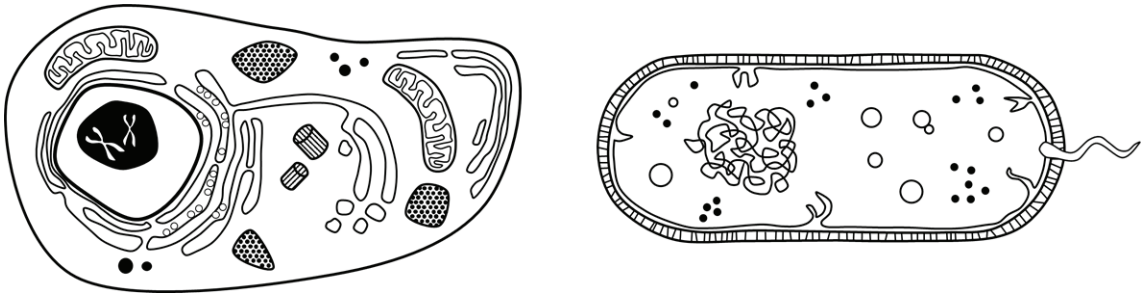

Figure 2.5 *Simplified illustration showing the fundamental differences in basic structure between a eukaryotic cell (left) and a prokaryotic cell (right). Note that their relative size is not accurate as prokaryotic cells are much smaller (0.1-5.0 μm in diameter) compared to eukaryotic cells (10-100 μm in diameter).*

few genes that are helpful for the cell in particular stressful situations, such as exposure to an antibiotic.

All cells have a plasma membrane, acting as a protective barrier separating the internal content of the cell from the surrounding environment. In addition, almost all prokaryotes have a chemically complex cell wall outside of the plasma membrane, separated from it by a periplasmic space. Bacteria can, in broad terms, have two types of cell walls and can hence be classified into two groups of bacterial species: Gram-positive or Gram-negative. The names refer to the bacteria's ability to retain the color of the Gram stain: originally devised by Danish bacteriologist Hans Christian Gram in 1882 (published 1884)[57] and is considered one of the most important staining techniques in microbiology. While Gram-positive bacteria have a thick homogeneous cell wall with several layers made of peptidoglycan and teichoic acids, Gram-negative cell walls are much thinner with only a few layers of peptidoglycan. An additional outer membrane consisting of lipopolysaccharides and lipoproteins surrounds the cell wall. Because of the multiple layers, the outer covering of a Gram-negative bacteria is near-impossible to penetrate and the reason to why Gram-negative pathogens are much harder in general to successfully treat with antibiotics compared to Gram-positive.[58-59] Its protective qualities can be compared to those of a bullet-proof west. Depending on the charge and shape of the antibiotic some are able to traverse the outer lipid layer via porin proteins.[60-61] However, these transport proteins can change their properties through mutations,[62-64] thus increasing the risk of the bacterial strain developing antibiotic resistance.

Gram-negative *Escherichia coli* and Gram-positive *Bacillus subtilis* are both frequently used as model organisms in microbiology and both have had their entire genome sequenced.[65-66] *E. coli* is rod-shaped and most commonly found in the lower intestines of warm-blooded organisms. Most strains are harmless and part of the normal gut flora. *B. subtilis* is also rod-shaped and most commonly found in the upper layers of soil, but is also considered to be a part of the normal human gut flora. *B. subtilis* is one of the best

studied Gram-positive bacterium and is often considered as the Gram-positive equivalent of *E. coli* (in terms of popularity).

2.7 Antibiotics and Multidrug Resistant Pathogens

Antibiotics such as we know them were first introduced into clinical practice in the 1940s, after the initial observation made by Alexander Fleming 12 years prior of the antimicrobial activity of the mold *Penicillium*[67]. This marked the beginning of the "golden era" of antibiotics and the discovery of several other antibiotic classes followed. Initially, these first types of antibiotics were so efficient in treating pathogenic bacteria so that infectious diseases were believed to eventually be wiped out completely, but it soon became clear that bacteria could become resistant to them. For a while, a continuous flow of new antibiotics alleviated this problem, but in recent years this flow has significantly slowed down. As a consequence, the prevalence of antibiotic-resistant bacteria, in particular multidrug resistant pathogens, have rapidly risen.[68-69] Apart from preventing the antibiotic from entering the cell, the bacteria may also alter its antibiotic target, or directly destroy or modify antibiotics, thus resisting their effect (Fig. 2.6).[70-71] Most types of antibiotics clinically available today target the same limited set of bacterial components, usually by either disrupting the bacterial cellular wall or inhibiting protein synthesis of the bacterial cell.[72-73] While bacterial-exclusive targets decreases the risk of adverse side effects from the treatment, it also increases the risk of antibiotic resistance. In addition, most "new" antibiotics that are coming onto the market are merely variants of existing drugs, with the risk that resistance mechanisms have already (at least in part) developed.[74] Only quinolones, another family of antibiotics, target bacterial DNA by preventing it from unwinding and duplicating.[75] This is however not done by direct interaction with bacterial DNA, but by targeting either the bacterial DNA gyrase or the topoisomerase enzyme.

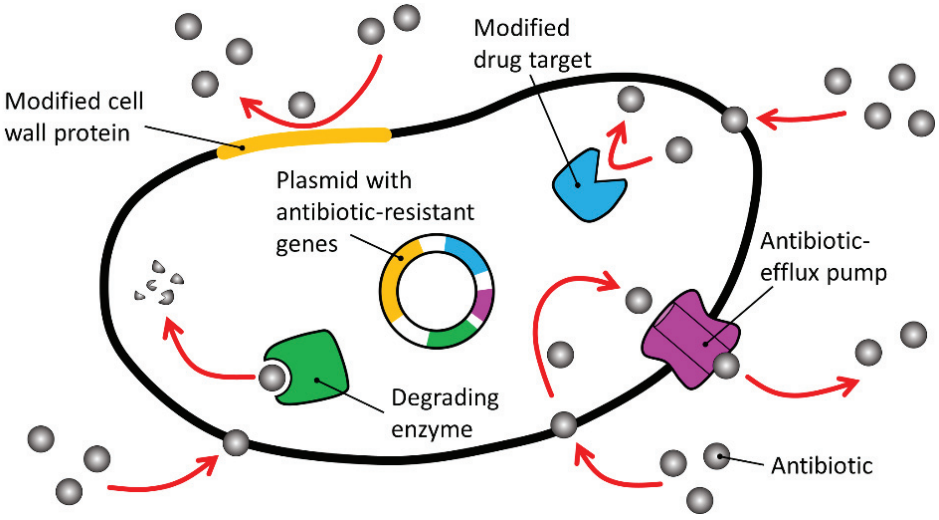

Figure 2.6 *Summary of common antibiotic-resistance mechanisms.*

While many DNA-binding compounds have proven to have a strong antibiotic activity, the lack of specificity towards bacterial DNA have deemed all too cytotoxic against the host. Indeed, many potential antibiotics where instead developed as anticancer treatments, with the most famous example probably being actinomycin D.[76] Bacterial DNA is still an attractive target, provided that specificity to bacterial cells can be established, either by cellular uptake or by specific affinity towards bacterial DNA.[77]

Ruthenium(II) polypyridyl complexes possess many of the sought-after qualities in an antibiotic, being water soluble, coordinately saturated and inert to substitution. In addition, their properties can be easily modulated in order to increase specificity towards bacterial targets. Despite this, as well as the pioneering work of Dwyer and coworkers, there has not been any major interest in testing ruthenium(II) polypyridyl complexes for their antimicrobial activity until recently. While these studies show promising results[78-79], with the exception of Li and Keene et al.[80-86], they only test racemic complexes thus not taking into consideration any potential enantiomeric difference in antimicrobial activity.

3 METHODS

The focus in this thesis has been on how the molecular structure of ruthenium(II) polypyridyl complexes affects DNA-binding properties such as binding affinity and interactions between neighboring bound ligands. This has been done by using various spectroscopic techniques, evaluating the binding orientation and binding constants to both ctDNA and AT-DNA. With the development of a general algorithm for the global fitting of ligand-DNA interactions, it has also been possible to find appropriate binding models for intercalative dppz complexes based on experimental isothermal titration calorimetry (ITC) data. Finally, the antimicrobial activity and mode of action of both mono- and binuclear complexes are thoroughly investigated using metal susceptibility assays as well as fluorescence confocal microscopy. Below follows a brief description of the techniques used in this project as well as some fundamental concepts explained.

3.1 Synthesis of a Terpyridine-Based Ruthenium Complex

The octahedral structure of tris-bidentate ruthenium-centered complexes results in the existence of two enantiomeric forms, the right-handed Δ-form and the left-handed Λ-form. By instead coordinating a tridentate ligand to the ruthenium ion the metal loses its stereocentre, thus making the molecule achiral. This eliminates the need for separating the Δ and Λ racemic mixtures characteristic of tris-bidentate systems. In addition, a

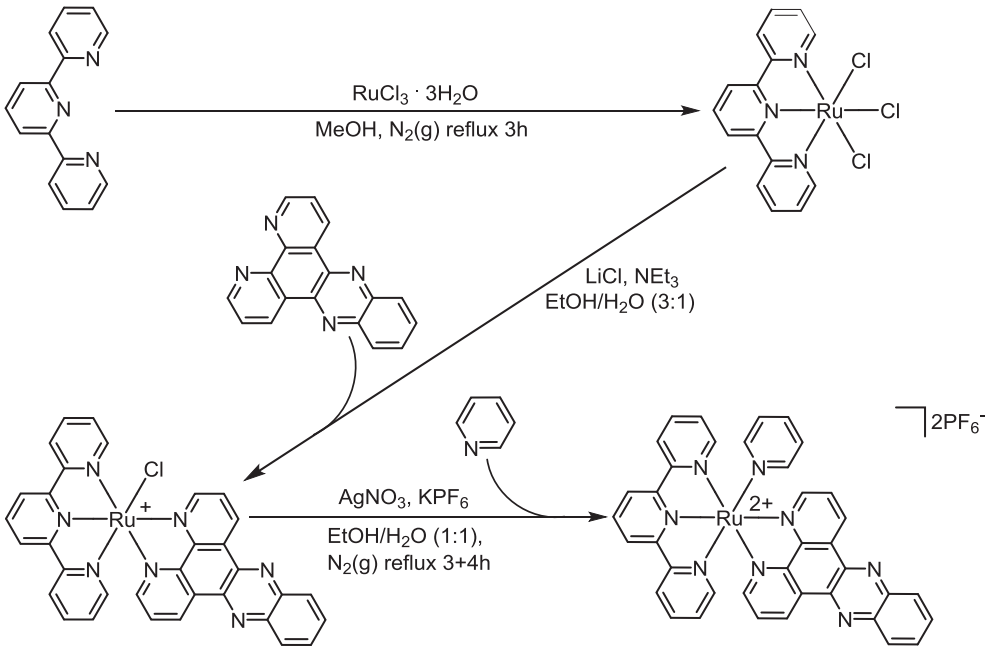

Figure 3.1 *Synthetic route for Ru(tpy)(py)dppz²⁺*

ruthenium complex with dppz as the intercalating ligand together with a tridentate ligand will have a single free coordination site left free on the ruthenium ion, enabling a fine-tuning of the ligand-DNA interactions not possible in the tris-bidentate systems. In **Paper I**, the tridentate ligand terpyridine (tpy) was coordinated to a dppz-ruthenium-centered complex. For the purpose of comparison, a single pyridine ring was attached to the remaining single coordination site, making the resulting complex an achiral structural isomer of the chiral $Ru(bpy)_2dppz^{2+}$ (the original "light-switch" complex). The synthetic route is summarized in Fig. 3.1 and is a modified version of the method previously described by Zhou et al. and Leising et al.[87-88]

3.2 Exploring the Photophysical Properties of Ru Complexes

Light is a kind of electromagnetic radiation, which is a type of energy consisting of both an electric (E) and magnetic (B) component. Both components oscillate a sinusoidal wave pattern in perpendicular directions relative to each other and to the direction of propagation (k). When molecules interact with light (carried by photons) so that they are excited from their ground state to higher electronic states, the light is said to be absorbed. For absorption to occur, the incident light has to have the same energy as the difference in energy between the ground state and the excited state of the absorbing molecule. A molecule, or part of a molecule, that can be excited and absorb light is called a chromophore. This energy difference depends not only on the structure of the absorbing chromophore but also on its surrounding environment. This means the absorption of a molecule will change when bound to DNA as the environment will be different compared to when the molecule is free in solution. It is therefore possible to utilize a variety of spectroscopic techniques where the extent of absorption is measured as a function of wavelength (inversely related to the energy of the light).

Ultraviolet-visible (UV-vis) absorption spectroscopy (also known as spectro-photometry) is one of the simplest but also one of the most versatile spectroscopic techniques used for study molecules and the interactions between molecules. Organic compounds with multiple bonds such as C=C, C=O or C=N often have a strong in the UV-vis portions of the light spectrum so measurements are normally done in the 200-800 nm interval. In a typical experiment, the spectrophotometer will direct light of a specific wavelength on the sample, and the absorbance is measured as the log of the ratio of the incident light and the transmitted light. The intensity of the transmitted light will depend on the number of absorbing molecules in the light beam. As a result, the absorption of a sample will be linearly proportional to the molar concentration of the sample tube:

$$A(\lambda) = \log\left(\frac{I_0}{I_T}\right) = \varepsilon(\lambda)cl \qquad (1)$$

where $A(\lambda)$ is the absorbance at wavelength λ, I_0 is the intensity of the incident light, I_T is the intensity of the transmitted light, ε is the molar extinction coefficient, c is the molar

concentration of the sample and l is the path length of the light beam (length of the sample tube).

Once excited, the molecule may return to the ground state (S_0) by both radiative and non-radiative pathways. Some energy is rapidly lost to vibrational relaxation (heat) in a process called internal conversion, leaving the excited molecule in the lowest level of the first excited state (S_1). From there, the molecule may fall to one of the sub-levels of the ground state, whilst emitting a photon with energy equivalent to the energy difference of the transition. This process is termed fluorescence. The energy of fluorescent photons is always less than that of the exciting photons, meaning that the emission wavelength will be longer compared to the absorbing wavelength. Another path that a molecule may take in the dissipation of energy is called intersystem crossing. This is also a non-radiative path but in contrast to internal conversion, which does not involve a change of spin multiplicity, intersystem crossing is the conversion of an excited singlet state to an excited triplet state (T_1). This is a forbidden transition, hence it should not happen if only electronic selection rules applied. However, by coupling vibrational factors into the selections rules, the transition becomes more allowed, yet it is still a much slower process compared to fluorescence. From the excited triplet state, the molecule can fall back to the singlet ground state via a radiative transition called phosphorescence. Like intersystem crossing, this process is spin-forbidden and hence also very slow. There are other, non-radiative transitions from excited state to ground state that compete with

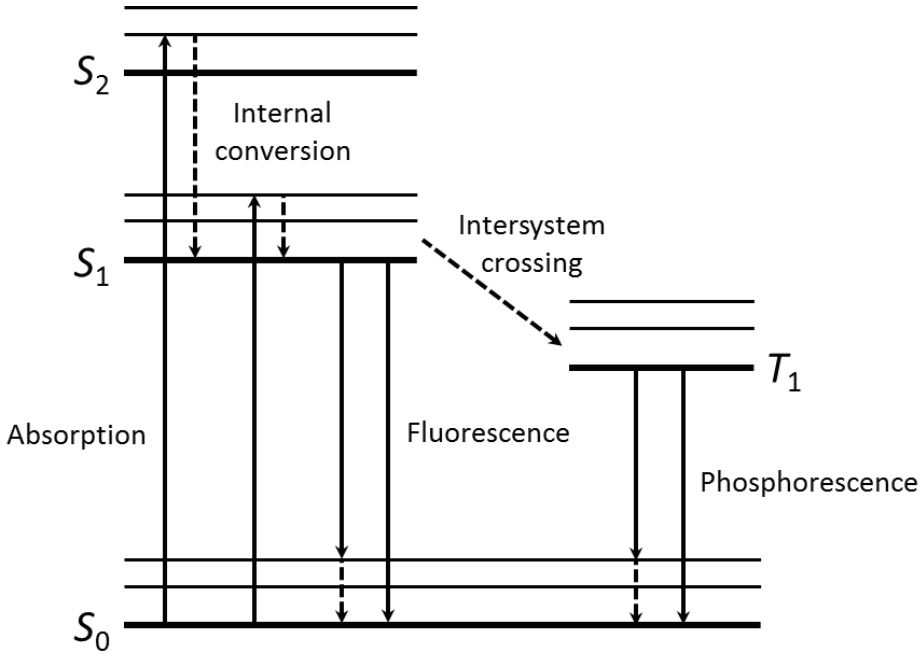

Figure 3.2 *Jabłoński diagram illustrating energy levels and the transitions between different electronic states. Non-radiative transitions are represented by dashed arrows, radiative transitions by solid arrows.*

fluorescence as the molecule relaxes back to the ground state. Such transitions are energy transfer between molecules through molecular collisions, and quenching where energy is transferred between molecules trough overlap in absorption and fluorescence spectrums. This explains why many molecules are not fluorescent or phosphorescent. All these possible electronic transitions are often summarized in a Jabłoński diagram (Fig. 3.2).

3.3 DNA-Binding Orientation Determined by Linear Dichroism

When light is absorbed by a chromophore there is an interaction between the electric field of the light and the local charges on the chromophore, yielding an oscillating charge displacement. This displacement is represented by the transition dipole moment. The more parallel the orientation of the electric field of the light is to that of the transition dipole moment, the more effective is the charge displacement resulting in stronger absorption.[89-90] By keeping the transition dipole moment of a chromophore constant, its absorption of linearly polarized light will depend solely on the direction of the polarization. The difference in absorption between two perpendicularly polarized light beams is called the linear dichroism (LD):

$$\mathrm{LD} = A_{||} - A_{\perp} \tag{2}$$

where $A_{||}$ and $A_{\perp}$ are the absorption of the polarized light parallel and perpendicular to a macroscopic orientation axis, respectively. For a randomly oriented sample, such as DNA polymers in solution, introducing an orientation during the experiment requires some kind of external force. There are several means available, but the most convenient

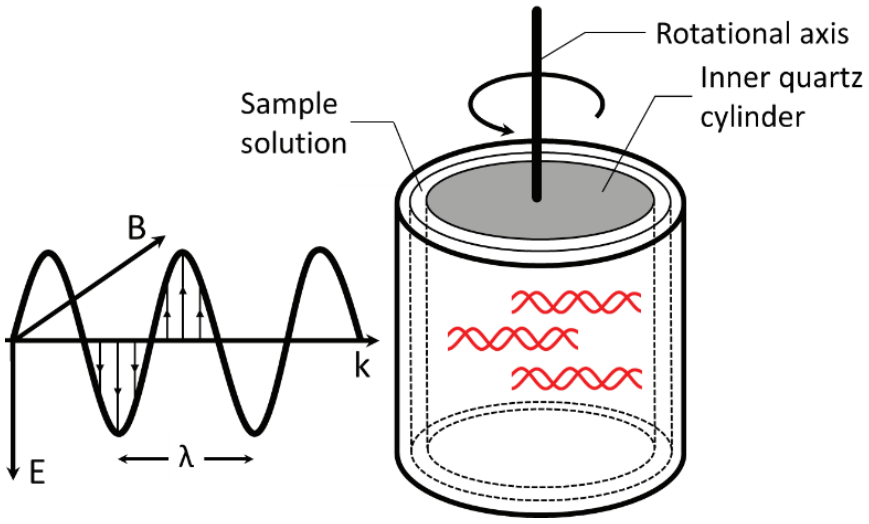

Figure 3.3 *Schematic illustration of the Couette flow cell with radial incident light linearly polarized in XY (as shown) or XZ plane. Also showing are the direction of the electric field E, the magnetic field B and the propagation direction k.*

method for orientation of long polymers such as DNA is the Couette flow cell orientation system.[91] Only small amounts of sample is required and the constant recirculation of the sample enable many repeat measurements thus decreasing the effect of background noise. A schematic illustration of the Couette cell is shown in Fig. 3.3. The sample is inserted into the narrow gap between two quartz cylinders. By rotating one of the cylinders, a shear flow gradient is created in-between the cylinders that causes the long DNA polymer to align in the flow direction. Only molecules long enough to align in the sample will exhibit a LD signal. Unbound ruthenium complexes are too small to be properly oriented, hence only ruthenium complexes bound to an oriented DNA polymer will give rise to a LD signal.

Assuming the helix axis of the flow-oriented DNA as the orientation axis, LD signals >0 would indicate the transition dipole moment responsible for that signal to be oriented closer to parallel to the DNA polymer helix axis.[89-90] A LD signal <0 would thus indicate a more perpendicular orientation. In DNA, only the nucleic bases contribute to absorption at wavelengths >200 nm. Since the bases are almost perpendicular to the DNA helix axis, their transition moments will be oriented perpendicular to the orientation axis in flow-oriented DNA. Using the same principle, LD spectroscopy can be used to obtain the orientation of ligand-DNA interactions, provided that the polarization direction of a transition dipole moment within the ligand is known.[92]
Using the reduced linear dichroism, LD^r, which is the LD divided by the isotropic absorption (A_{iso}), it is possible to determine the angle between a specific transition dipole moment (transition i) and the orientation axis provided that the transitions are non-overlapping:

$$\mathrm{LD^r} = \frac{\mathrm{LD}}{A_{\mathrm{iso}}} = \gamma \frac{3}{2} S(3\cos^2\theta_i - 1) \qquad 0 \leq S \leq 1 \tag{3}$$

where θ_i is the angle between the transition dipole moment and the orientation axis of the molecular system, γ is the ratio of the optical path-length of the absorption measurement to that of the LD measurement, and S is the orientation factor which describes the degree of orientation of a sample (S=1 means perfect orientation of the sample, whereas S=0 means random orientation). Should the magnitude of S increase due to some change in the system (such as the introduction of a DNA-binding molecule) the DNA has become more oriented and consequently the LD signal becomes stronger. This increase is usually caused by the DNA polymer becoming elongated or stiffened or both.

However, in most cases, and also for ruthenium(II) polypyridyl complexes, electronic transitions overlap over the whole range of the spectrum. In such cases, A_{iso} of each sample can be regarded as a sum of component spectral envelopes e_i of the absorption bands of all transition dipole moments:

$$A_{\mathrm{iso}} = \sum_i e_i \tag{4}$$

The LD spectrum will then be the weighted sum of the weights w_i of the same component spectral envelopes:

$$\mathrm{LD} = \sum_i w_i e_i \tag{5}$$

In cases where a single component spectral envelope e_i dominates the absorption spectrum, e.g. as seen for the absorption band of B-DNA at around 260 nm, the $\mathrm{LD^r}$ curve will be more or less constant and take the value w_i. The angle θ_i for the in-plane polarized nucleobase transitions at this absorption band is close to 90°, hence the orientation factor S_0 for ligand-free DNA can be calculated from the $\mathrm{LD^r}$ values as follows:

$$\mathrm{LD}^{\mathrm{r}}_{260} = w = -\gamma \frac{3}{2} S_0 \tag{6}$$

However, the absorption spectra of ruthenium(II) polypyridyl complexes are composed of several different electronic transitions which substantially overlap each other. As a consequent, the $\mathrm{LD^r}$ curve will vary strongly with wavelength, making it not possible to directly determine the $\mathrm{LD^r}$ of each individual transition dipole moment. Instead, the experimental A_{iso} and LD spectrum for a ruthenium complex may be divided into separate absorption bands, one for each polarization direction. This was done in **Paper I**, where we analyzed the LD data of $\mathrm{Ru(tpy)(py)dppz^{2+}}$ in the presence of calf thymus DNA (ctDNA) using the TEM method.[38, 93] where a system of a two component envelope spectra, with distinct characteristic absorption band features and distinct weights, make it possible to combine Eqs. (4) and (5) into a matrix system:

$$[\mathbf{a}\ \ \mathbf{b}] \begin{bmatrix} 1 & w_1 \\ 1 & w_2 \end{bmatrix}^{-1} = [\mathbf{e_1}\ \ \mathbf{e_2}] \tag{7}$$

where $\mathbf{a}$, $\mathbf{b}$, $\mathbf{e_1}$ and $\mathbf{e_2}$ are column vectors corresponding to the A_{iso}, LD and the two components envelope spectra, respectively. When varying the weights w_1 and w_2 in Eq. (7) the characteristic features of component $\mathbf{e_1}$ will visibly vanish in component $\mathbf{e_2}$, and *vice versa*.

The angular orientation can be determined only if the orientation factor S is known. If a ligand strongly binds to DNA, has significant absorbance at wavelengths above the DNA absorption range (>300 nm) and invariant binding geometry and absorption spectrum (within a known range of [ligand]/[DNA] ratios), S can readily be obtained as follows:

Let column vectors $\mathbf{L_1}$ and $\mathbf{L_2}$ be two LD spectra with different [ligand]/[DNA] ratios and $\mathbf{L_0}$ be the LD spectrum of a sample with DNA only. The three columns are linearly dependent if the DNA and bound ligand spectral profiles are invariant with the

[ligand]/[DNA] ratios, thus scalars α and β can be found so that $\alpha\mathbf{L_1} + \beta\mathbf{L_2} = \mathbf{L_0}$. Let $\mathbf{M} = [\mathbf{L_1}\ \mathbf{L_2}]$ and $\mathbf{x} = [\alpha; \beta]$ in matrix notation:

$$\mathbf{Mx} = \mathbf{L_0} \tag{8}$$

Solving Eq. (8) by a least square projection gives α and β:

$$(\mathbf{M^T M})^{-1}\mathbf{M^T L_0} = \mathbf{x} \tag{9}$$

If a ligand binds strongly to DNA it is assumed that no added complex will remain unbound in a DNA solution (within reasonable concentrations). Therefore, the DNA concentration can be considered equal in the three samples and the vectors can be written as:

$$\mathbf{L_0} = \gamma S_0 \mathbf{d} \qquad \mathbf{L_1} = \gamma S_1(\mathbf{d} + c_1\mathbf{b}) \qquad \mathbf{L_2} = \gamma S_2(\mathbf{d} + c_2\mathbf{b}) \tag{10}$$

where (with γ = 1), **d** is the LD spectrum at perfect orientation of DNA only, **b** is the LD spectrum at perfect orientation of bound complex at unit concentration, and c_1 and c_2 are the two known complex concentrations. At wavelengths >300 nm **d** will be zero and if **b** is non-zero, so by inserting Eq. (10) in (8) the following two equations are obtained:

$$\alpha S_1 + \beta S_2 = S_0 \qquad c_1\alpha S_1 + c_2\beta S_2 = 0 \tag{11}$$

Since γS_0 can be evaluated from Eq. (11) it is possible to obtain S_1 and S_2 from known quantities:

$$S_1 = \frac{S_0 c_2}{\alpha(c_2 - c_1)} \qquad S_2 = \frac{S_0 c_1}{\beta(c_2 - c_1)} \tag{12}$$

3.4 Ligand-DNA Interactions Studied Using Circular Dichroism

Circular dichroism (CD) spectroscopy is, like linear dichroism, based on the differences in absorbance of polarized light. In contrast to linear polarized light where the electric field vector oscillated only in one plane, circularly polarized light occur when the electric field vector rotates around the propagation axis while maintaining constant magnitude. As the radiation propagates the electric field vector traces out a helix in space, which can be either left-handed or right-handed. CD is defined as the difference in absorbance between left- and right-handed polarized light:

$$\mathrm{CD}(\Delta A) = A_\mathrm{L} - A_\mathrm{R} \tag{13}$$

where A_L and A_R are the observed absorbance of left- and right-handed polarized light, respectively. As Eq. 13 indicates, a circular dichroism signal can be positive or negative,

depending on left-handed circularly polarized light is absorbed to a greater (positive) or lesser (negative) extent than right-handed circularly polarized light. Achiral chromophores absorb left- and right-handed circularly polarized light in the same extent, hence the CD signal would be zero. If, on the other hand, the chromophore is chiral or perturbed by a chiral environment, the differential absorption would result in different amplitudes of left- and right-handed circularly polarized light. As previously mentioned, many ruthenium complexes are chiral and would exhibit CD signals on their own. The same goes for the DNA polymer, being a right-handed helix. Binding to DNA, both chiral and achiral molecules can result in a new CD signal not otherwise present, the induced CD, due to interactions between the transition dipole moments of the bound molecule and the nucleobases.[90] The distances and angles between the interacting transition dipole moments will dictate the magnitude and sign of the induced CD signal. Therefore, similar binding geometries are expected to result in similar patterns in the induced CD signal.

3.5 Metal Susceptibility Assay for Testing Antimicrobial Activity

When evaluating a substance's potential usage as an antibiotic, the minimum inhibitory concentration (MIC) and the minimum bactericidal concentration (MBC) are normally determined at an early stage, as it provides quantitative data useful when predicting necessary tissue and blood levels for an antibiotic to be effective. MIC is defined as the lowest concentration of a compound that inhibits visual growth of an organism; the MBC is defined as the lowest concentration of a compound required to kill a particular bacterial strain.

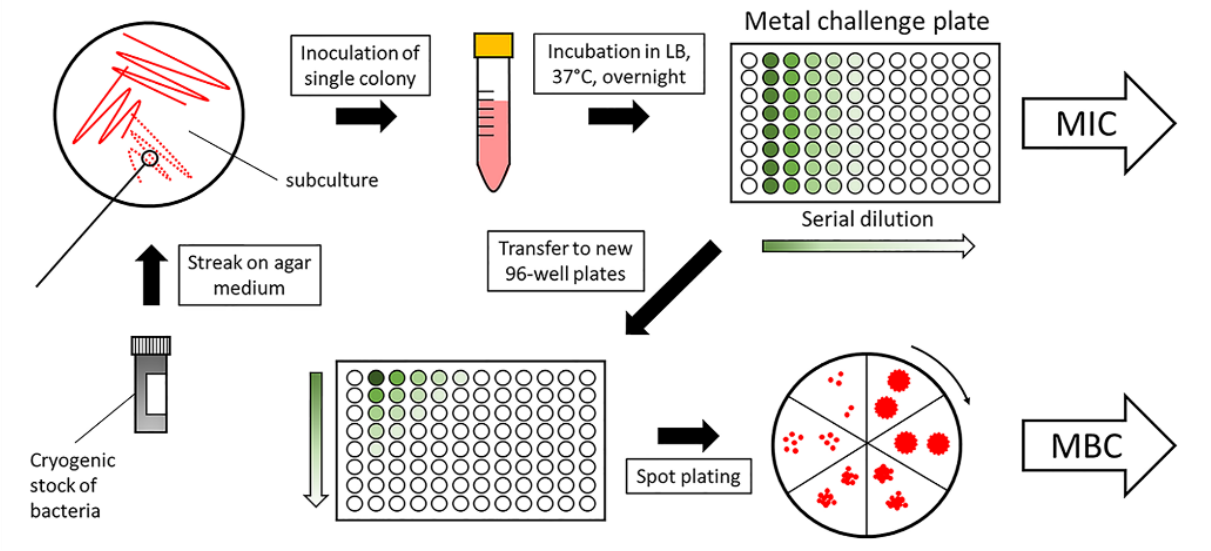

Figure 3.4 *Experimental setup of the metal susceptibility assay for the determination of MIC and MBC of an antibiotic.*

In **Paper V**, we used a modified version of the MBEC high-throughput assay[94] in order to determine the antibiotic activity of enantiopure $Ru(phen)_2dppz^{2+}$and μ-(11,11'-bidppz)$(phen)_4Ru_2^{4+}$ to a Gram-positive and a Gram-negative bacterial strain. The method (summarized in Fig. 3.4) allows for both MIC and MBC to be determined in a single experiment. In a typical experimental setup, frozen stocks of bacterial strains are streaked out on Luria-Bertani (LB) agar to obtain a subculture. After overnight incubation, a single colony is picked and suspended in LB medium to grow for 3-4 hours, after which the suspension is diluted 100-fold. Serial dilutions of the ruthenium complexes are set up on a 96-well microtiter plate followed by the diluted bacteria suspension. After overnight growth, the MIC values are determined by reading the optical density (OD) at 650 nm of the plate. In order to obtain the MBC values, the Ru-bacteria suspensions are diluted 10^1-10^8 fold and spot plated on LB agar plates. After an appropriate growing period (depending on the growth rate of the bacterial strain) the colonies are counted and CFU/mL (colony-forming units) is determined:

$$\frac{CFU}{mL} = \frac{Average\ colony\ count}{Volume} \times dilution \tag{14}$$

If no colonies are formed at a certain concentration, that concentration is determined as the MBC value for that bacterial strain.

3.6 Bacterial DNA Intercalation Visualized by Confocal Microscopy

For a ruthenium complex to function as a DNA interacting antibiotic it must first and foremost be able to reach the DNA in live bacterial cells. Emissive molecules such as (many) ruthenium complexes can easily be located inside cells using fluorescence confocal microscopy, which is done in **Paper V**. Here, bacterial cells were incubated with enantiopure $Ru(phen)_2dppz^{2+}$ and then washed and fixated using formaldehyde. Thanks to the well-established light-switch effect of $Ru(phen)_2dppz^{2+}$, the uptake and DNA intercalation of the complex could be visualized.

In regular fluorescence microscopy the sample is completely illuminated by the excitation light, so all of the sample is fluorescing at the same time. Because of this, there will be a background haze in the resulting image. By adding a pinhole in front of the detector, only the light originating from an in-focus plane will freely pass the pinhole, while light coming from the out-of-focus planes will effectively be blocked out.[95] Usually a laser provides the excitation light (in order to get high enough intensities). The laser light passes through a second pinhole, is reflected by a dichroic mirror, and focused by a microscope objective to a small spot in the sample. The dichroic mirror reflects light of a shorter wavelength while transmitting that of a longer wavelength. The image is then built up by a computer connected to the detector, one pixel at a time. By scanning several thin sections of the sample while rejecting out-of-focus light, a very clean three-dimensional image can be obtained.

3.7 Ligand-DNA Thermodynamics and Isothermal Titration Calorimetry

Often referred to as the "gold standard" for quantitative measurements of bio-molecular interactions, isothermal titration calorimetry (ITC) is a high-precision tool for studying the binding interactions between a ligand and a macromolecule. It is also the only direct thermodynamic method that enables a full thermodynamic characterization of the interaction (stoichiometry, enthalpy, entropy of binding, and association constant) after a single titration experiment.[96-98] In a typical experiment (Fig. 3.5), a solution of the macromolecule is placed in the sample cell of the calorimeter. The ligand is then titrated in aliquots using an automated precision syringe lowered into the sample cell. A paddle at the end of the syringe stirs the content of the sample in order to ensure rapid mixing of the reactants. After each addition, the heat released or absorbed in the sample cell is measured with respect to a reference cell of the same volume. The heat change (ΔT) is expressed as the electrical power (µcal s^{-1}) required to maintain a constant temperature in the sample cell and the reference cell. The integrated heat flow from each injection Q_i corresponds to the enthalpy change ΔH from the interaction between ligand and macromolecule:

$$Q_i = \Delta[L_i]_{\text{bound}} \times V_{\text{cell}} \tag{15}$$

where $\Delta[L_i]_{\text{bound}}$ x V_{cell} corresponds to the molar increase of bound ligand with each injection.

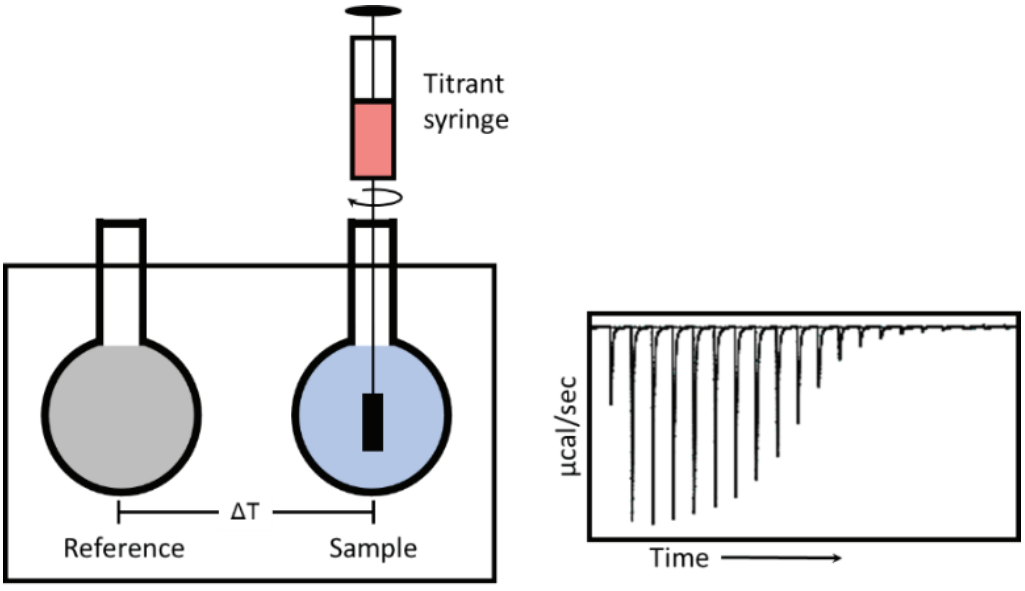

Figure 3.5 *Left: Schematic of the ITC cells and injection syringe. Right: Representative raw data from an ITC experiment showing the standard sigmoidal shape typical of independent non-cooperative binding.*

In the simplest of scenarios, where the binding sites of the macromolecule are independent of each other and the binding of the ligand is non-cooperative, nearly all injected ligand will bind to the macromolecule in the beginning of the titration, as nearly all binding sites are available. As the titration progresses, more and more binding sites will become occupied resulting in only a fraction of injected ligand able to bind to the now saturated macromolecule. Since the integrated heat is proportional to the total binding enthalpy of each injection, the ITC curve will have a sigmoidal shape. The small heat changes registered at the end of the titration are caused by the heat of ligand dilution and other nonspecific effects. Usually these are corrected for by performing a blank titration of ligand into buffer. In some cases, however, the heat of dilution is too large to simply be corrected by a blank titration. A large dilution heat could simply be caused by buffer mismatch, where the buffer composition (including pH) of the cell and syringe samples are different. This can be easily adverted by matching the buffers using co-dialysis prior to the measurements. A second possible cause for large dilution heats is dissociation, where the high concentration in the syringe causes the ligands to form oligomers (for example dimers), which dissociate upon injection (i.e. dilution). This is an equilibrium process by itself and cannot simply be subtracted from the ITC curve by a blank titration. In **Paper III** a model is described that explicitly takes into account the ligand oligomerization equilibrium, as well as the external aggregation of further ligands on already saturated DNA at the end of the titration.

3.8 Binding Isotherms and Model Fitting

As stated above, in the simplest systems the binding sites on the macromolecule are independent of each other and the ligand binding is non-cooperative, resulting in a sigmoidal shaped curve. In such cases the curvature of the ITC profile depends on the binding constant K and the total number of binding sites. While proteins and short oligonucleotides often have independent and isolated binding sites, the DNA used in the experiments presented here consist of long polymers of binding sites, which overlap each other when occupied by bulky ligands (such as DNA-binding ruthenium complexes). In addition, neighboring bound ligands may affect each other by either cooperative or anti-cooperative interactions, which gives rise to an interaction enthalpy Δh in addition to the intrinsic binding enthalpy ΔH. The classical McGhee and von Hippel model, which was presented in 1974, treats DNA as a one-dimensional infinite lattice of which the subunits are the identical binding sites.[99] The model accounts for both nearest-neighbor interactions as well as bound ligands covering more than one binding site. In **Paper I** a non-unity cooperativity parameter y was introduced together with two other adjustable parameters: the thermodynamic binding constant K and the binding site coverage parameter n. Knowing the total concentration of binding sites $[B]_{tot}$ (i.e. base pairs) and DNA-ligand $[L]_{tot}$ (i.e. ruthenium complex) for each step of the titration, the mass-balance equations can be solved by guessing values for K, n and y, which are then optimized by

iteration using a Newton-Raphson procedure as previously described by Lincoln (1998)[100] and Andersson et al. (2013)[39] and briefly summarized below.

By using a variant of the formulation by Chen[101], where the lattice of bound ligand is seen as a heteropolymer of N+1 types of elementary units i (i = 0, 1…N). While unit 0 is the bare binding site unit, the other N elementary units i are composed of n_i consecutive binding sites of varying lengths. The binding potential x_i for elementary unit i is a function of the intrinsic binding constant K_i (the binding equilibrium constant in the absence of neighbor interactions) and the free ligand concentrations; for a simple 1:1 case $x_i = K_i[L_i]_{\text{free}}$. The binding density θ_i is defined as the ratio between the concentrations of bound ligand of type i and the total concentration of binding sites. Thus, for the 1:1 case, x_i and θ_i should satisfy the mass balance:

$$[L_i]_{\text{tot}} = [L_i]_{\text{free}} + [L_i]_{\text{bound}} = K_i^{-1}x_i + [B]_{\text{tot}}\theta_i \qquad (16)$$

θ_i gives the probability of finding a ligand of type i bound to a randomly chosen binding site. When moving in one direction along the DNA strand there is a conditional probability, denoted p_{ij}, that given a binding site occupied by a bound ligand of type i, it is followed by a bound ligand of type j.

As a result, the change in the concentration for each titration step can be obtained and ΔH and Δh calculated from a least-square fit to the experimental data. Finally the error between the simulated and the experimental ITC data is minimized by varying K, y and n.

The algorithm employed in **Paper I**, although efficient, is limited by its complexity and has never had any wide-spread use. In addition, it is limited to describe interactions between 1:1 binding site:ligand equilibria. Therefore, a much simplified and "user-friendly" algorithm was developed in **Paper II** and implemented further in **Paper III** and **Paper IV**. This algorithm can be implemented to any type of biopolymer with a long chain of repeating binding sites, regardless of the complexity of the binding system. The new algorithm avoids the tedious nested iteration procedures of the previous algorithm, since it takes advantage of the fact that both the free and bound ligand concentrations can be simply and uniquely determined by any positive vector **r**.

The matrix algebra involved in the fitting of a generalized binding model to ITC-data might appear daunting to the reader at first glance. Therefore, the remaining part of this chapter will take a closer look on the classical McGhee and von Hippel model by giving an example of the model fitting of the binding of a single ligand, hence characterized by a single variable r. The interactions between neighboring elementary units are written as a set of non-negative cooperativity constants y_{ij} and are elements of the cooperativity matrix $\mathbf{Y} = [y_{ij}]$, i, j = 0, 1, …N. Here, the binding is set to be non-cooperative (y = 1), hence the matrix is written as:

$$\mathbf{Y} = \begin{bmatrix} 1 & 1 \\ 1 & y \end{bmatrix} \tag{17}$$

From Eq. (8) in **Paper II** we have:

$$s_0 = (1 + r)^{-1} \qquad s_1 = (1 + yr)^{-1} \tag{18}$$

where s_i are the elements of the $N + 1$ vector **s**.

From Eq. (9) in **Paper II** we can write the stochastic matrix **P** as such:

$$\mathbf{P} = \begin{bmatrix} \dfrac{1}{1+r} & \dfrac{r}{1+r} \\ \dfrac{1}{1+yr} & \dfrac{yr}{1+yr} \end{bmatrix} \tag{19}$$

From Eqs. (12) and (18) in **Paper II** we get:

$$x = \frac{r(1+r)^n}{1+yr} \tag{20}$$

$$\theta = p_{01}V^{-1} = \frac{r}{1+r} \cdot \left(1 + \frac{nr}{1+r} - \frac{yr}{1+yr}\right)^{-1} = \frac{r(1+yr)}{1+(n+1)r+ynr^2} \tag{21}$$

In order to keep it simple, for the purpose of illustration, the binding system will be assumed to not have any binding site overlap (n = 1) and the binding will be non-cooperative (y = 1). Hence, Eqs. (20) and (21) can be simplified to:

$$x = r \tag{22}$$

$$\theta = \frac{r}{1+r} \tag{23}$$

$$L_0 = xK^{-1} + B_0\theta = \frac{r}{K} + \frac{rB_0}{1+r} \tag{24}$$

Derivation with respect to r gives:

$$\frac{\mathrm{d}L_0}{\mathrm{d}r} = \frac{1}{K} + \frac{B_0}{(1+r)^2} = \frac{(1+r)^2 + KB_0}{K(1+r)^2} \tag{25}$$

For this simple case (n = 1 and y = 1), the mass balance equation (24) can be rearranged into an equation quadratic in r:

$$r^2 + [1 + K(B_0 - L_0)]r - KL_0 = 0 \tag{26}$$

Hence:

$$r = -\frac{1 + K(B_0 - L_0)}{2} + \sqrt{\left(\frac{1 + K(B_0 - L_0)}{2}\right)^2 + KL_0} \qquad (27)$$

The enthalpy changes monitored during an ITC experiment comes from the concentration differences occurring when small additions of ligand is titrated into the macromolecule solution. If the additions are very small and the dilution heat is small enough to be neglected, it is possible to make an approximation of the concentration differences per mole added ligand by the derivative of the concentration with respect to total ligand concentration. In order to model the ITC curve with the changes in concentration of both total bound ligand and neighboring bound ligand, we need the derivatives with respect to r of θ and of θP_{11}, respectively.

Using this model to calculate an ITC-curve will give a linear combination of these two functions, which are weighted by the enthalpy of binding and the enthalpy of nearest-neighbor interaction, respectively. The following three figures (Fig. 3.6, 3.7 and 3.8) will demonstrate example titrations on how the shape of these functions are affected by the different binding model parameters: the first figure show the effect on the curve with the intrinsic binding constant K; the second figure shows the effect on the shape of the curve with a non-unity cooperativity parameter y; lastly the third shows the effect of changing the binding site size n. Note that in all examples, the ligand is assumed to cover two base pairs (nearest neighbor exclusion, as commonly observed for most small intercalating ligands). That means that should the binding be infinitely strong, all binding sites would be occupied (saturation) at ratio L_0/[base pairs] = 0.5.

As demonstrated by the examples below, this correlation of K, y and n is important to have in mind when comparing fits of different binding models to ITC data.

Example 1 (Fig. 3.6)

Here the ligand is assumed to bind only to one type of base pair of an alternating DNA lattice, hence the binding sites does not overlap and n = 1. Note that the ligand binding curve has the shape of the classical sigmoidal ITC isotherm, with sharper edges closer to the saturation ratio as K increases. A lower K leads to the interaction curve peaking before the saturation ratio. However, if the binding constant K increases, the peak moves closer towards the saturation ratio 0.5. In addition, the initial part of the interaction curve becomes more linear with a higher K value.

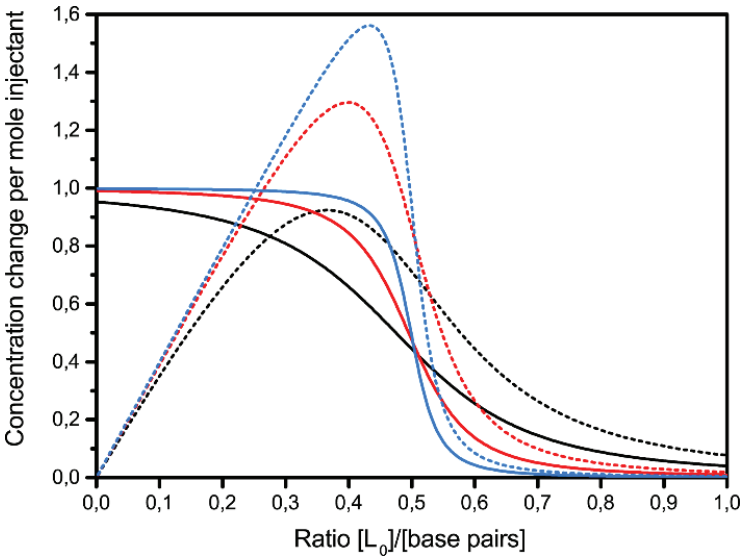

	K	*n*	*y*
Black	0.2	1	1
Red	1	1	1
Blue	5	1	1

Figure 3.6 *Left: Example titration showing the effects of an increasing intrinsic binding constant K on the binding curve (solid line) and interaction curve (dashed line) of the ligand-DNA interactions; Right: Table summarizing the different binding model parameters for each curve.*

Example 2 (Fig. 3.7)

Here we see the effect of introducing cooperativity. For anti-cooperative binding ($y < 1$), the initial part of the interaction curve is concave, while for cooperative binding ($y > 1$) it is convex due to the facilitated binding of additional ligands. By setting $Ky^2 = 1$ the plots will be more similar at high loading (from ratio 0.5 and over), which facilitates comparison of the plots. At ratios > 0.5 the DNA lattice is so saturated that further binding will in most probability result in nearest-neighbor interactions.

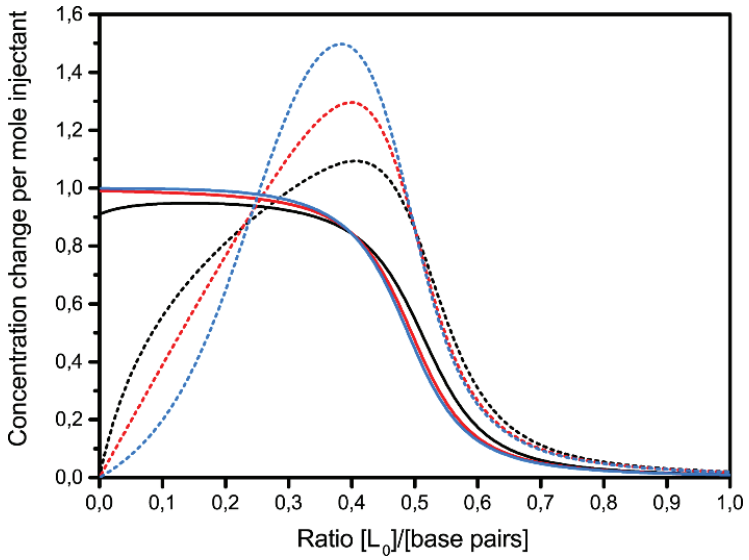

	K	*n*	*y*
Black	0.1	1	3.16
Red	1	1	1
Blue	10	1	0.316

Figure 3.7 *Left: Example titration showing the effects on the binding curve (solid line) and interaction curve (dashed line) by introducing a cooperativity binding parameter y to the ligand-DNA system; Right: Table summarizing the different binding model parameters for each curve.*

Example 3 (Fig. 3.8)

Here we assume one binding site on every base pair and n = 2. This means that gaps between bound ligands on the binding lite lattice could be as small as 1 base pair wide. As ligands still cover more than 1 base pair when bound, the nearest-neighbor exclusion rule still apply. Consequently, some gaps between bound ligands will be too small fit an additional ligand and the number of available binding sites decreases more rapidly as the titration progresses (see Fig. 3.9 for comparison of the two models). Hence the concave shape of the initial interaction curve. A second consequence of the faster decrease of available binding sites is that the saturation of the lattice is slowed down, which can be observed at the end of the interaction curve. This can partly be compensated for by increasing y and decreasing K as shown by the least-square fit (blue) in Fig. 3.8.

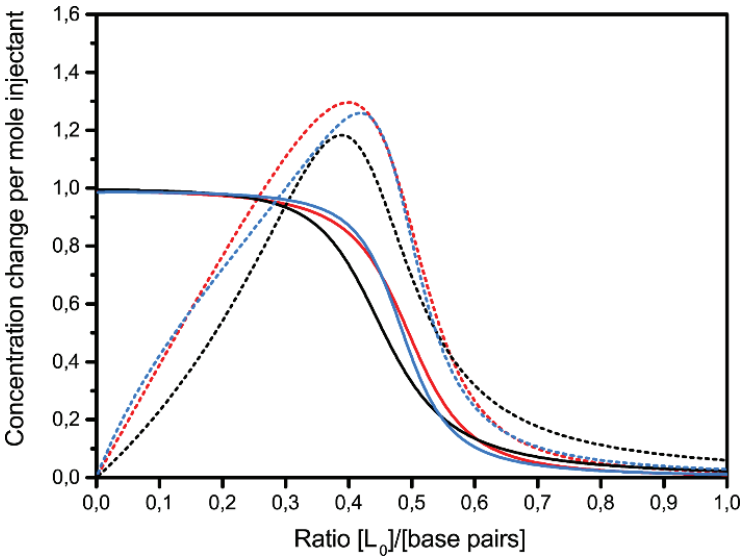

	K	*n*	*y*
Black	1	2	1
Red	1	1	1
Blue	0.338	2	2.91

Figure 3.8 *Left: Example titration showing the effect of assuming the binding site size n = 2 instead of 1 on the binding curve (solid line) and interaction curve (dashed line) and how this effect can be compensated for by increasing the cooperativity and decreasing the binding constant; Right: Table summarizing the different binding model parameters for each curve.*

Figure 3.9 *Schematic illustration comparing the two lattice models of the DNA-ligand system with n = 2 (top) or n = 1 (bottom). When n = 2 some gaps will be too narrow for any additional ligands to be able to bind (as each ligand cover more than one base pair), therefore there will be a steeper decrease of available binding sites as the titration progresses compared to when n = 1.*

4 RESULTS AND DISCUSSION

The aim of this thesis is to investigate how the binding affinity of ruthenium(II) polypyridyl complexes to DNA is correlated to the molecular structure and how this affinity can be affected by slight changes of said structure. Factors such as chirality and the addition of substituent groups to the intercalating ligand will be addressed. In addition, the influence that complexes have on their neighbors when bound to DNA will also be shown to have a significant impact on the overall ligand-DNA interactions. Ruthenium(II) polypyridyl complexes have previously shown a strong antimicrobial activity, which will be further explored in this thesis. By predicting the outcome of modulating these factors, using binding models to fit experimental data, the development of ruthenium complexes as DNA-binding antibiotic can be further explored. In this chapter the results of **Paper I-V**, which are included in this thesis, will be presented and discussed.

Paper I initiates the exploration of heterochiral cooperativity and introduces new techniques in LD resolution and ITC model fitting. **Paper II** follows with an improvement of the binding model algorithm. This is applied to competitive ITC experiments, where enantiomers of intercalating ruthenium complexes compete for DNA binding sites, and allows the systematic study of the diastereomeric interactions between bound complexes. **Paper III** then investigates the possible effects of altering the intercalating ligand by methyl substitution and shows how non-constant heat of dilution can be accounted for. **Paper IV** further demonstrates the improved model fitting algorithm when combining competitive titration experiments with luminescence titration data. Finally, **Paper V**, moves the project to a more biological setting where the antimicrobial activity of DNA-binding ruthenium complexes is evaluated with DNA-binding confirmed as the antimicrobial mode of action.

4.1 The Binding Geometry of Ru(terpyridine)(pyridine)dppz^{2+}

The discovery of the original “light-switch” complexes lead to a huge interest in dppz-ruthenium complexes with an octahedral tris-bidentate structure and numerous structural variations have been reported ever since. It has already been well-established that these types of complexes bind to DNA by intercalation of the dppz ligand between the base pairs, and that the binding affinity can be tuned by modulation of the ancillary ligands.[28, 31-32, 38-39] Should the tri-bidentate system be replaced by a dppz-ruthenium complex carrying a tridentate ligand, such as terpyridine (tpy), a single free coordination site on the metal is left free, allowing for additional fine-tuning of the complex in a manner not possible for the tris-bidentate systems. Furthermore, the lack of a

stereocentre at the metal results in an achiral complex, thus eliminating the need of separating the Δ and Λ racemic mixtures characteristic of tris-bidentate systems. Complexes carrying the tridentate tpy ligand have in general a very low quantum yield in room temperature and as a result the interest in these types of structures have not been as intense compared to the brightly luminescent bpy and phen complexes. Consequently, the binding geometry of tpy-based complexes has not yet been fully determined. Our group have previously shown the influence tris-bidentate complexes have on each other when intercalated in close proximity of each other on the DNA polymer; they can either inhibit (anti-cooperative) or facilitate (cooperative) additional complexes binding.[39] Here, the same approach was used for finding the most likely binding model for $Ru(tpy)(py)dppz^{2+}$ (Ru-tpy). A series of spectrophotometric and calorimetric measurements were carried out and analyzed using the classical McGhee-von Hippel cooperative binding model[99] in order to find the best global fit. As a comparison we used the original "light-switch" complex $Ru(bpy)_2dppz^{2+}$ (Ru-bpy) which, in addition to having its binding interactions with DNA much more evaluated, is the chiral structural isomer of Ru-tpy.

Ru-tpy, being achiral, will not show a proper induced CD (ICD) signal unless bound to a chiral molecule, such as DNA. We could observe a negative ICD band in the long-axis polarized tpy band at 300 nm for Ru-tpy, much similar to the negative ICD band seen at 290 nm for their long-axis bpy band of both Δ- and Λ-Ru-bpy, as could be expected for electronic transitions positioned in the minor groove close to parallel to the helix axis.

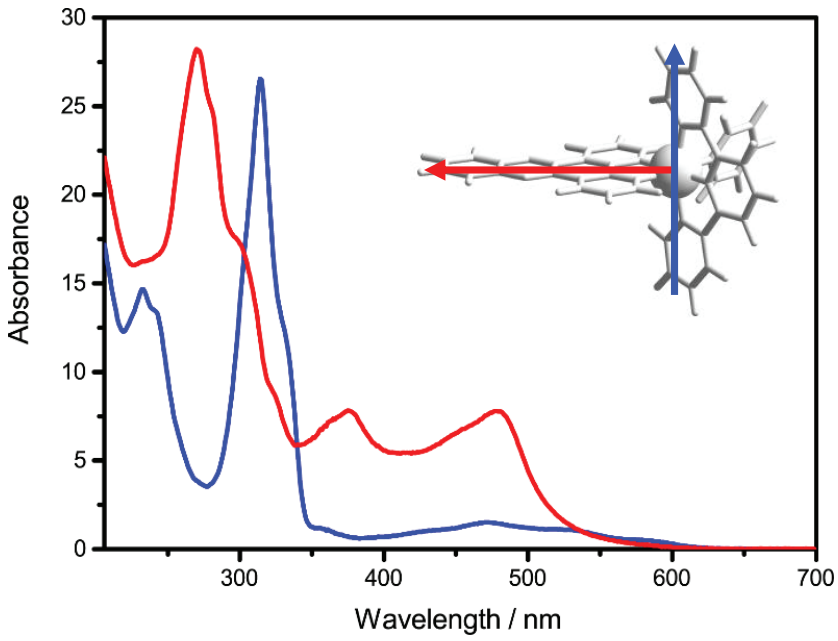

Figure 4.1 *Resolved spectra of the x and y (red) and the z (blue) polarized absorption bands of Ru-tpy bound to ct-DNA. The Y-axis units are ε/(1000 $M^{-1}cm^{-1}$). The arrows on the molecular structure of the complex show the direction of the x and z transition moments.*

In correlation to the observations made with absorption and CD, the linear dichroism (LD) spectra for Ru-tpy were found to be almost invariant with the binding ratio, which allowed us to determine the orientation factor *S* and to quantitatively analyze the angular binding geometry. By varying weight values w_1 and w_2 in Eq. (7) until the dppz band at 375 nm vanished in component $\mathbf{e_1}$ and the sharp tpy band at 310 nm vanished in component $\mathbf{e_2}$, it was possible to resolve the LD spectrum of Ru-tpy into its x, y and z components (Fig. 4.1). The results showed the tpy long-axis (z) to be aligned parallel and the dppz long-axis (x) perpendicular to the DNA helix axis, consistent with the dppz ligand being inserted between the base pairs.

The calorimetric titration of Ru-tpy resulted in non-classical isothermal titration calorimetry (ITC) curves similar to those of $Ru(L)_2dppz^{2+}$ (L = bpy or phen) as previously reported by Andersson et al. (2013).[39] In comparison to Δ- and Λ-Ru-bpy, Ru-tpy showed an ITC-profile most similar to the latter (Fig. 4.2). The ITC data for Ru-tpy was excellently globally fitted with the classical McGhee-von Hippel cooperative binding model. The parameters and derived thermodynamic data are summarized in Table 4.1. Contrary to previous results, where a satisfactory global fit to both luminescence and ITC data for $Ru(L)_2dppz^{2+}$ complexes required two binding geometries (perpendicular and polar), the experimental data (ITC and absorption titration) of Ru-bpy and Ru-tpy could both be

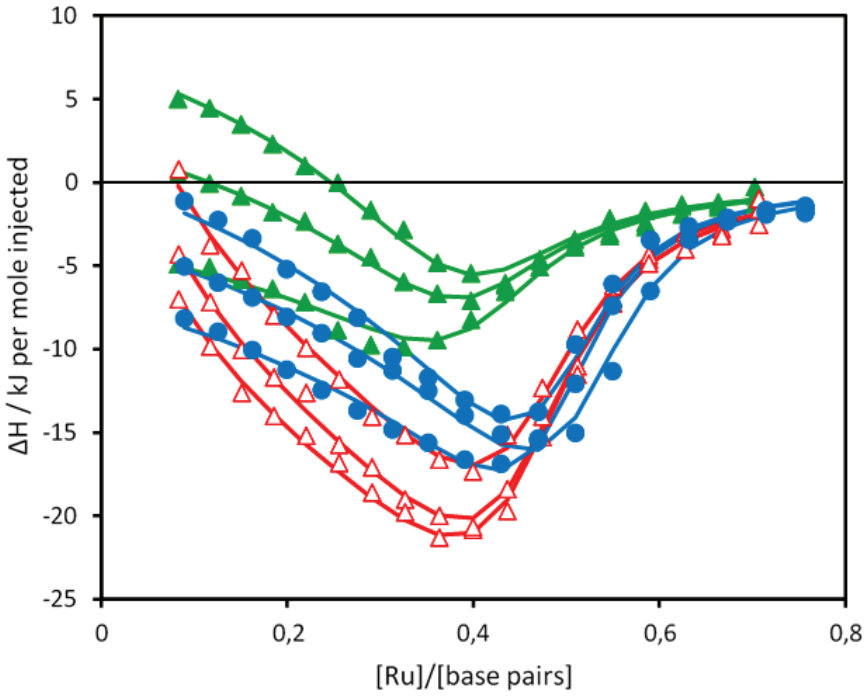

Figure 4.2 *ITC profiles with fitted traces for the binding of Ru-tpy (blue circles), Δ-Ru-bpy (green triangles), and Λ-Ru-bpy (red triangles) to AT-DNA in 150 mM aqueous solution at 20, 25, and 30°C. Symbols indicate the normalized heat absorbed or evolved upon sequential injections (2 μL) of complex into the 206 μL cell containing the DNA. The data has been corrected for heat of complex dilution.*

fitted using a much simpler model, where only one distinct binding geometry is assumed with a single cooperativity parameter *y*.

Table 4.1 *Binding constant K, cooperativity parameter y, and binding sites n that gave the best fit to experimental data, and the derived thermodynamic parameters for the intrinsic binding at 20°C.*

Sample	K^1	*y*	*n*	$\Delta H_b{}^2$	$\Delta H_{nn}{}^2$	$\Delta Cp_b{}^3$
Ru-tpy	1	2.8	2.0	3.0	-10.2	-680
Δ-Ru-bpy	0.9	1	2.2	4.3	-6.9	-800
Λ-Ru-bpy	0.06	5.5	2.3	7.2	-17.6	-560

1) $K/10^6 M^{-1}$ 2) $\Delta H°/kJ\ mol^{-1}$ 3) $\Delta Cp/J\ mol^{-1}K^{-1}$

Even though a simple single binding geometry model is sufficient to fit the experimental data for Ru-tpy, due to the lack of two-fold symmetry, two types of neighbor interactions are possible: either the neighboring tpy ligands of two consecutive complexes are oriented toward the same strand (T_{SS}) or toward alternating strands (T_{AS}). We found that the T_{SS} model was the most consistent with the single binding geometry model since it only had one type of intermolecular contact (similar to that of alternating bound Δ and Λ-Ru-bpy). However, the *y*-values of the corresponding Δ-Δ and Λ-Λ interactions were similar enough in magnitude to suggest that the T_{AS} model also is relevant.

4.2 Competitive ITC Demonstrating a General Binding Isotherm Algorithm

While ITC is a powerful tool for direct thermodynamic profiling of binding interactions, currently available analysis software is in general limited to binding systems with non-interactive binding sites, unable to adequately include cooperative or anti-cooperative behavior between bound ligands. The algorithm utilized in **Paper I**, while taking binding site interactions into account, is too complex for any wide-spread usage. In order to facilitate the search for new and improved pharmaceutical treatments, it is vital to be able to evaluate the binding properties of new molecules in a quick and effective manner. The general algorithm developed in **Paper II** allows for the fitting of lattice binding models of a wide variety of complexity levels. While this algorithm is general enough to be utilized for modelling ligand binding to any type of linear biopolymers, the most frequent usage would probably be for studying the binding interactions between ligands to the closely spaced binding sites of DNA. Therefore, as a practical example, the competitive binding interactions between the two enantiomers of $Ru(bpy)_2dppz^{2+}$ and $poly(dAdT)_2$ is analyzed using this new algorithm in **Paper II**.

Here 5 models are evaluated, schematically summarized as lattice models in Fig. 4.3. Model 1 is the classical model, where each lattice subunit is one base pair (and the binding site coverage parameter *n* is expected to be close to 2) and assumes all intercalation pockets to be equal. In Model 2 and 3 the lattice subunit is instead taken to be 2 base pairs (and *n* = 1). While Model 2 assumes a strict TA (or AT) selectivity, this

selectivity is relaxed in Model 3 for Δ which is then able to bind in either of the intercalation pockets 1 or 2 of the lattice subunit. Model 1-3 take both intrinsic ($\Delta H°_b$) and neighbor interaction ($\Delta H°_{ab}$) reaction enthalpies into consideration. In contrast, Model 4 and 5 assumes two binding modes for each enantiomer, and considers only intrinsic reaction enthalpies. In Model 4, the two binding modes are modelled as two independent binding sites with the fraction of base pairs for each binding site as a freely adjustable parameter. However, it is possible to construct a mathematically equivalent lattice model if the fractions of the two binding sites have the same value, as depicted in Model 4*. In Model 5, the two binding modes are set to alternating in consecutive sequences, thus only interacting with neighbors of different binding mode.

Upon evaluation of the different binding models, it was not possible to produce any reasonable global fit without including a cooperativity parameter. In addition, Model 4 and 5, which do not consider any neighbor enthalpy, require significantly more fitting parameters in order to produce acceptable fits.

As a large number of fitting parameters could easily reduce the physical relevance of any best-fit values, a binding model with a satisfactory global fit with the smallest number of adjustable parameters is the most desirable outcome. Therefore, to understand the binding interactions of the system presented here, it is absolutely necessary to include the interactions between bound ligands in close proximity of each other. Furthermore, previous X-ray structure results showing 5´-TA-3´selectivity for Λ-Ru-bpy suggest that it is incorrect to treat all intercalation pockets identically, as is assumed in Model 1. The best fit was produced in Model 3, with a strict TA selectivity for Λ-Ru-bpy but with that selectivity relaxed for Δ-Ru-bpy. Model 3 gives the lowest RMSD of all models investigated and even with the binding and enthalpy parameters constrained to be the

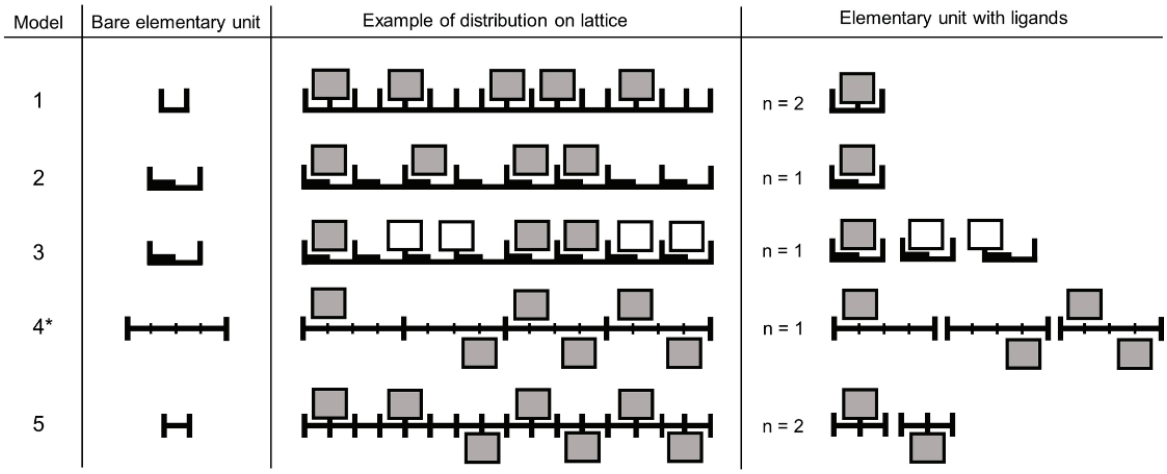

Figure 4.3 *Schematic illustration summarizing the 5 proposed lattice models of the ligand-DNA binding interactions.*

same for the two base pair steps (total number of fitting parameters 7 + 5 = 12) the RMSD is only slightly increased. The best fit value of the yΔΔ cooperativity parameter was found to be close to one, and defining yΔΔ = 1 (thus fitting only 6+5 parameters) increased the RMSD by less than 0.5%. The excellent fit of the (6+5) parameter Model 3 to the integrated peaks of the experimental ITC data is shown in Fig. 4.4.

Model 3 gave a lower intrinsic binding constant *K* and higher cooperativity for Λ-Ru-bpy than for Δ-Ru-bpy. A simple allosteric explanation for this would be the seemingly less good steric fit in the groove compared to the Δ-enantiomer, resulting in an extra free energy penalty when Λ is forced to widen the groove. This is in turn payed back when the second Λ-enantiomer intercalates to an already widened groove. This does not, however, fully explain the hetero-chiral cooperativity observed since the better fitting, non-cooperative Δ-enantiomer should not need to widen the groove. It is likely that ligand-ligand interactions also make a significant contribution. Three types of arrangements of the close-by bipyridine moieties of neighboring Ru-bpy are possible: ΔΔ: face to face; ΛΛ:

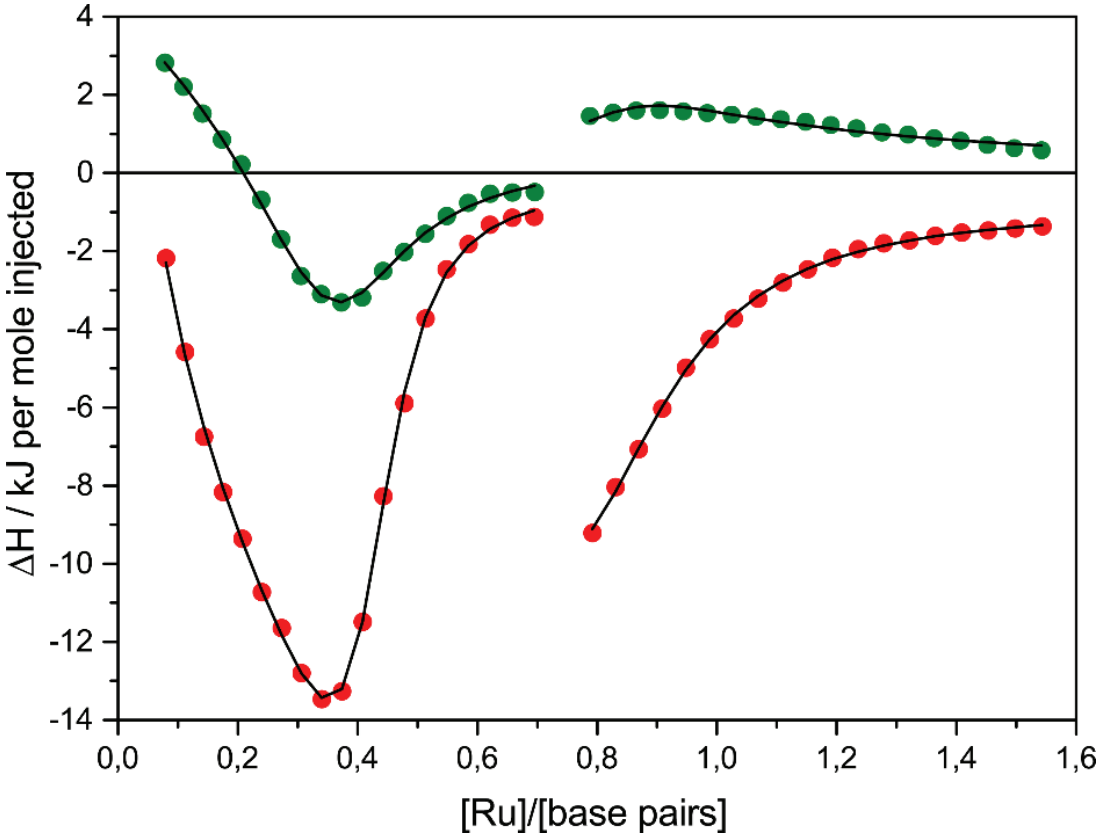

Figure 4.4 *ITC profiles with fitted traces of (6+5) parameter Model 3 for the binding of the Δ- and Λ-Ru-bpy to AT-DNA alone (left) followed by a second titration of opposite enantiomer to already complex-saturated AT-DNA (right) in 150 mM NaCl aqueous solution at 25°C. Symbols (Δ: green; Λ: red) indicate the normalized integrated heat absorbed or evolved upon sequential 2 μL injections of complex (~470 μM) into the 206 μL cell containing the DNA (~300 μM nucleotides).*

edge to edge; ΔΛ: face to edge. These arrangements are expected to be essentially different with regard to interactions such as pi-stacking and electrostatic repulsion (enthalpic effects) but also water solvation and counter ion distribution (enthropic effects).

4.3 Methyl Substitution Groups and the Effects on Ligand-DNA Enthalpy

The introduction of small changes into the molecular structure of the ruthenium complex, it might be possible to modify the DNA binding affinity and specificity. Added methyl substituents on the intercalating dppz ligand of the enantiomers of the parent complex $Ru(phen)_2dppz^{2+}$ will have steric consequences on the complex, possibly with altered ligand-DNA binding motifs. While previous studies suggest that methyl substituents do indeed alter the binding properties of intercalative ruthenium complexes,[28, 102-103] the underlying binding kinetics are still much left unexplored. By utilizing the general algorithm developed and demonstrated in **Paper II**, we seek to thermodynamically characterize the DNA-binding of $Ru(phen)_2dppz^{2+}$ with methyl groups substituted in the 10-position or in the 11,12-position of the dppz moiety using ITC experimental data. The complexes are denoted **1**, **2** and **3**, respectively (Fig 4.5).

The raw ITC data show that while all complexes have a non-constant heat of dilution, it is small for complex **1** but very prominent for the methylated complexes **2** and **3**. The added methyl substituents results in an increased hydrophobicity of complex **2** and **3** that, in turn, causes a more prominent self-aggregation of dimer/trimer structures in free ligand solution. In addition, at the end of the titration when most binding sites on the DNA strand are occupied, complex **2** and **3** both show intense endothermal heat peaks in comparison to the parent complex **1**. To account for this additional equilibrium process aside from the ligand-DNA interactions, we have here considered both the heat of aggregation from the highly-concentrated free ligand solution, as well as an external ligand binding to saturated DNA. Therefore, a ligand solution oligomerization equilibrium $m\ L \rightarrow L_m$ has been incorporated into the mass balance. In addition, to account for the prominent endothermal heat change upon DNA saturation each intercalating ligand is assumed to be able to become an external binding site for an additional ligand. This is characterized by an external binding constant K_{ext}.

Fig. 4.6 summarizes the best global fit to the integrated peaks of the raw data of all complexes. As previous linear dichroism studies do not indicate any major differences in binding geometry between complex **1**, **2** and **3**,[103] the intercalation equilibrium constants K and neighbor interaction parameters y were assumed identical for each set of enantiomers, leaving only the binding site coverage parameter n to vary freely. Allowing K and y to vary freely gave only a slightly lower nRMSD (6.4% compared to 7.3%) indicating that the assumption of similar binding affinity parameters for each set of enantiomers to have been correct. Interestingly, the Λ-enantiomers consistently all

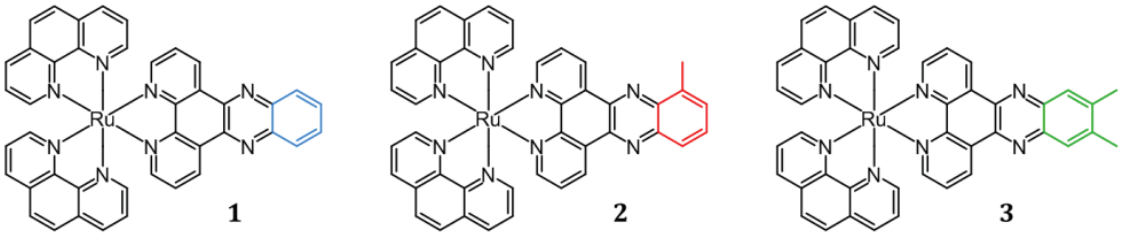

Figure 4.5 *Structures of ruthenium complexes $Ru(phen)_2dppz^{2+}$ (**1**), $Ru(phen)_2dppzCH_3^{2+}$ (**2**) and $Ru(phen)_2dppz(CH_3)_2^{2+}$ (**3**).*

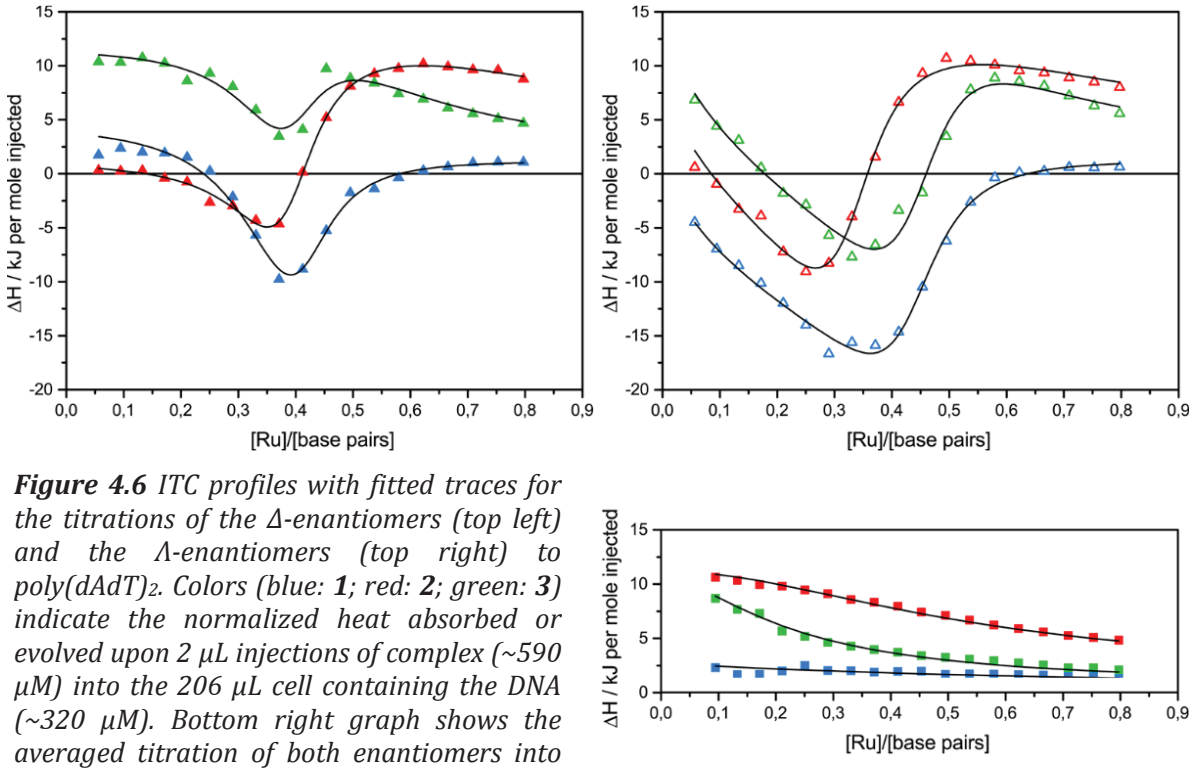

Figure 4.6 *ITC profiles with fitted traces for the titrations of the Δ-enantiomers (top left) and the Λ-enantiomers (top right) to poly(dAdT)₂. Colors (blue: **1**; red: **2**; green: **3**) indicate the normalized heat absorbed or evolved upon 2 µL injections of complex (~590 µM) into the 206 µL cell containing the DNA (~320 µM). Bottom right graph shows the averaged titration of both enantiomers into pure buffer. All titrations were performed in 150 mM NaCl aqueous solution at 25°C.*

have larger binding site coverage parameter *n* compared to Δ, with the difference being most prominent for complex **2**.

In general, the differences in enthalpy values due to methyl substitution were small (less than 4 kJ mol^{-1}), with the much more exothermic intercalation for the Δ-enantiomer of **2** compared to **1** being the most significant exception. The most prominent differences between the complexes are shown in Table 4.2.

Table 4.2 *Changes in enthalpy values due to methyl substitution (in kJ mol^{-1})*

Complex	$\Delta(\Delta H°_{K\Delta})$	$\Delta(\Delta H°_{y\Delta})$	$\Delta(\Delta H°_{K\Lambda})$	$\Delta(\Delta H°_{y\Lambda})$
2	-11.6	+3.4	-1.6	-1.1
3	-0.8	+3.3	+4.3	-2.6

In order for a binding model to be of practical use, the number of fitting parameters must be limited. Even with the additional heat of dilution added in the analysis, we have shown here that the model does not have to become overly-complicated.

4.4 Model Fitting of Ru(phen)$_2$dppz^{2+} Demonstrating Diastereomeric Crowding

Tris-bidentate ruthenium complexes of the general form Ru(L)$_2$dppz^{2+} exhibit almost invariably biexponential excited-state emission decays when bound to DNA. This has previously been assigned to two distinct binding geometries, with the shorter lifetime attributed to a centered intercalation geometry and the longer lifetime to a more canted geometry. However, photophysical results have shown that upon DNA-binding of the enantiomers of Ru(phen)$_2$dppz^{2+} the fractions of short and long lifetimes are strongly dependent on salt concentration and, in particular, temperature, which cannot be satisfactory explained using this old model.[104] By using the simplified algorithm (introduced in **Paper II**) to analyze ITC data in a competitive setting, the aim of **Paper IV** is to find an improved binding model for Ru-phen that also accounts for the excited-state populations of the complex.

Here, two models are compared: in Model A the ligand-ligand interaction energy is assumed to be additive and independent of the environment while in Model B (Fig. 4.7) it is possible for the ligand-ligand interaction energies to be different for ligands at the ends and in the middle of a sequence of consecutively bound ligands. In the more complicated Model B the ligands are modelled as 4 different elementary units (two canted, unsymmetrical units *a* and *b*, which only occur to the left and right, respectively, of a ligand neighbor while having one empty binding site on the other side (end binding); two symmetrical units: *c*, which only occur "sandwiched" in between a ligand sequence (interior binding), and *d,* only occurring without any neighboring ligands (isolated binding)).

The best fit for model B was obtained when assuming ligand binding exclusively at either the AT/AT or TA/TA steps. In addition, setting the binding site coverage parameter *n* to be exactly 1 did not significantly affect the residual norm. The best global fit to the integrated peaks of the raw data (see **Paper IV**) using Model B is shown in Fig 4.8.

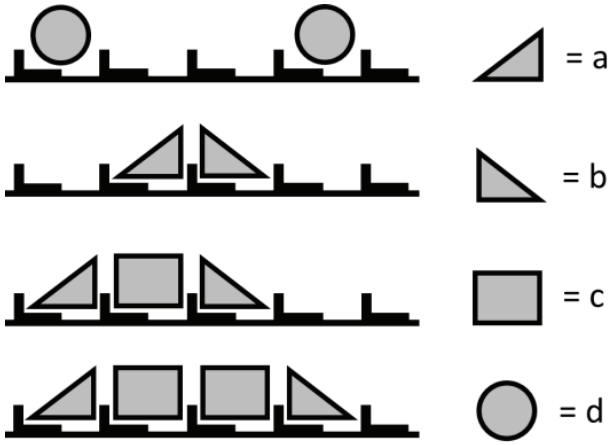

Figure 4.7 *Schematic illustration of the proposed lattice Model B with the 4 different element units and their possible ligand-DNA interactions.*

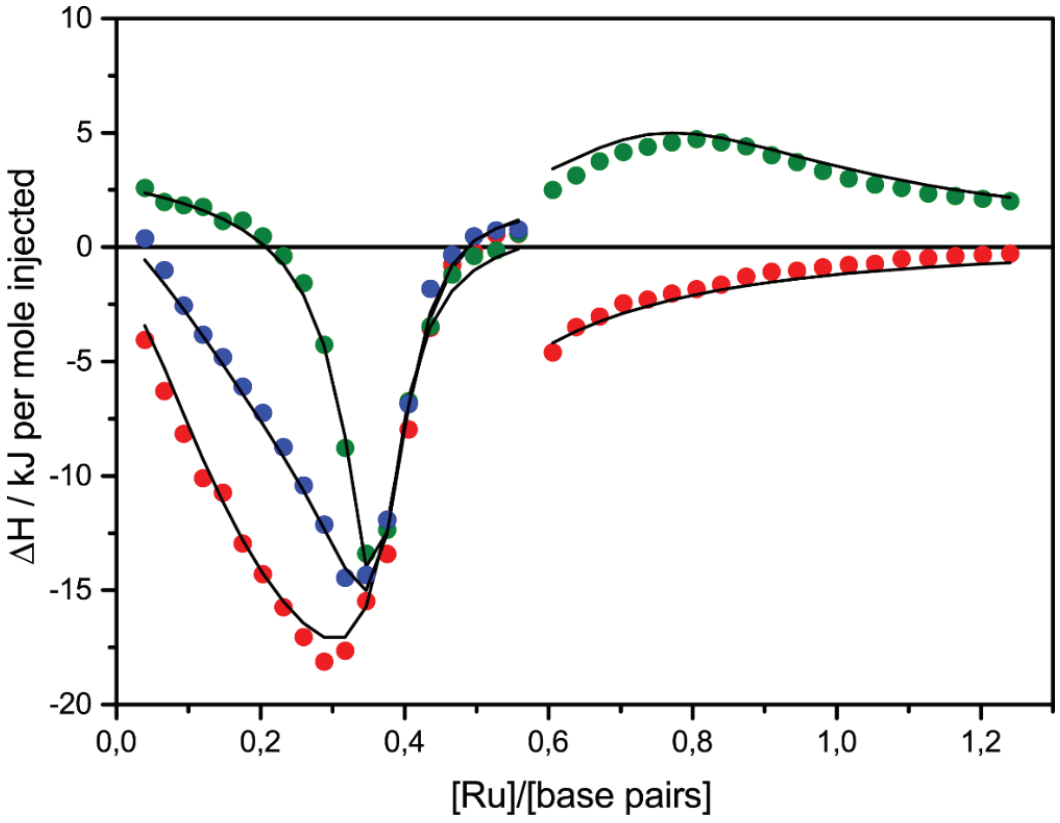

Figure 4.8 *ITC profiles with fitted traces of Model B for the titrations of Δ- and Λ-Ru-phen to AT-DNA alone (left) followed by a second titration of opposite enantiomer to already ligand-saturated AT-DNA (right). Also shown is the ITC profile for rac-Ru-phen titrated to AT-DNA alone. Symbols (Δ: green; Λ: red; rac: blue) indicate the normalized integrated heat absorbed or evolved upon 19 sequential 2 µL injections of the complex (~550 µM) into the 206 µL cell containing the DNA (~408 µM nucleotides). All titrations were performed in 150 mM NaCl aqueous solution at 25°C.*

A summary of the best global fit for the binding of the different categories of Model B is presented in Table 4.3. The enthalpy ΔH° parameter values for the outer binding mode to saturated DNA and the formation of dimer in solution are also presented. Pronounced diastereomeric differences for the bound Ru-phen enantiomers can be seen in all categories, reflecting the differences in the factors discussed below. For Δ-Ru-phen, fitting the α_{short} data[105] assigns the short lifetime almost exclusively to interior and isolated elementary units, while the long lifetime is assigned to the end ligands. In contrast, the long lifetime of Λ-Ru-phen is mostly contributed from the interior ligands.

Rather than directly associating each lifetime with a distinct binding geometry, each intercalated complex should instead be regarded as being in equilibrium with a short and long lifetime state. This equilibrium of lifetimes may then be affected by nearest-neighbor ligands and consequently also much more affected by the surrounding environment.

Table 4.3 *The best global fit of Model B to experimental ITC data (enthalpy parameter values ΔH°/kJ mol^{-1}) and α_{short} data[105] (coefficients c).*

	outer[a]	isolated	end	interior	end, mix	interior, mix	dimer
ITC[b]							
Δ	+0.4	-0.7	-0.6	-24.5	-7.4	-21.3	-24.1
Λ	+0.8	-4.4	-17.3	-14.3			
α_{short}[c]							
Δ		0.89	0.07	1.00			
Λ		0.91	0.65	0.11			

[a]*Assuming K_{outer} = 100* [b]*Enthalpy parameter values (ΔH°/kJ mol^{-1})* [c]*coefficients c*

In contrast to the global fitting of the competitive ITC data of $Ru(bpy)_2dppz^{2+}$ binding to $poly(dAdT)_2$ (**Paper II**), the addition of the phenanthroline B-ring of the ancillary ligands of Ru-phen results in increased steric crowding of the intercalated complexes. Consequently, Ru-phen is much more affected by diastereomeric differences in the attractive and repulsive intermolecular contacts, in particular upon full lattice saturation.

Table 4.4 summarizes the best global fit parameters of Model B. When bound to the DNA lattice, Δ showed a modest cooperativity in the *a-b* dimer configuration but was essentially non-cooperative when bound as an isolated trimer *a-c-b*. In addition, Δ showed strong anti-cooperativity for the *c-c* arrangement, indicating an inert reluctance for expanding to larger *a-c-c-b* arrangements. For Λ, the isolated dimer *a-b* interaction was also anti-cooperative.

Table 4.4 *Binding parameter values from global fitting of Model B to ITC data.*

	$K/10^6$	n	y_{ab}	y_{ac}	y_{cc}
Δ	13.7	1.00	2.70	1.12	0.07
Λ	3.71	1.00	0.45	0.93	0.25
Δ-Λ			0.70	1.26	0.19
dimer	2.9E-4				

The prominent diastereomeric influence from neighboring bound ligands is reflected in the values of the cooperativity *y* parameters, which can be seen as combinations of both attractive and repulsive factors, the most important being:

1. Electrostatic repulsion of neighboring positive cations.
2. Repulsion caused by inter-complex steric clashes.
3. Attraction due to hydrophobic/stacking interactions, primarily for Δ.
4. Attraction from binding to an already widened groove (by the first bound complex), primarily for Λ.

The molecular models shown in Fig. 4.9 summarizes the possible nearest-neighbor arrangements of the Ru-phen-enantiomers. Only for the homochiral ΔΔ-pairs can the phenanthroline B-ring make close contact with a neighboring complex, which is consistent with the heterochiral *y*-values being more similar to ΛΛ than to ΔΔ. In addition, this offers an explanation for the apparent similarity in the ITC and luminescence data

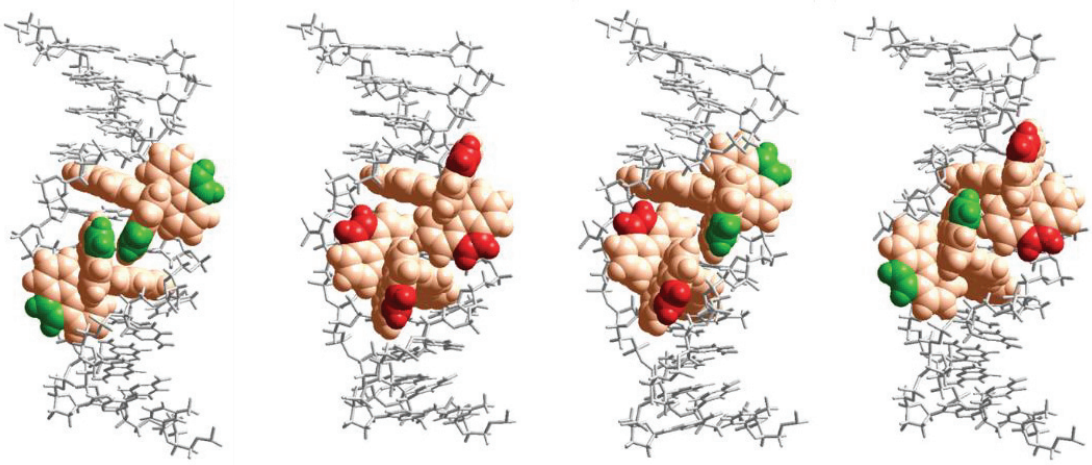

Figure 4.9 *Schematic illustration of the proposed nearest-neighbor interaction geometries for the Δ- and Λ-enantiomers of* $Ru(phen)_2dppz^{2+}$ *when intercalated to DNA via the minor groove. The 5,6-carbons on the phen moieties are highlighted (green: Δ; red: Λ). The models were constructed by manual docking and subsequent energy minimization in a vacuum, using the Amber 2 force field in the HyperChem 8.0 software package (HyperCube, Inc.).*

for the Λ-enantiomers of Ru-phen and Ru-bpy, as the bipyridine moiety is missing the CH=CH part of the phenanthroline B-ring.[39]

Altogether, Model B provides an excellent global fit of both ITC and photophysical data while still being in accordance to previous ligand-DNA interactions studies. In particular, Model B have two advantages compared to the simpler Model A that give a physical interpretation of the ligand-DNA interactions closer to reality:

1. Model B assumes exclusive binding at either the AT/AT step or TA/TA step which is supported by X-ray crystallography structures.[31]
2. The binding site coverage parameter *n* is no longer a freely adjustable non-integer parameter with different values for Δ and Λ, is set to unity for all bound ligands. Thus in Model B, all diastereomeric variation in binding affinity is limited to the only freely adjustable binding parameters left, *K* and y_{ij}.

4.5 Enantioselective Antimicrobial Activity of $Ru(phen)_2dppz^{2+}$

The problem of bacterial pathogens developing multidrug-resistance toward clinically available antibiotic is growing larger, making is necessary to develop new types of antibiotics targeting alternative bacterial components. Bacterial DNA is such a potential target, but so far the specificity for bacterial cells has not been good enough in previous antibiotic candidates and they were deemed too cytotoxic to the human host. While ruthenium(II) polypyridyl complexes have previously been demonstrated to have a strong antimicrobial activity, we felt that the potential of developing Ru complexes as DNA-targeting antibiotics has been left mostly unexplored. To the best of our knowledge, no reported antibiotic studies of intercalating $Ru(L)_2dppz^{2+}$ complexes had tested the complexes in their resolved enantiopure forms. This surprised us, as it has been repeatedly demonstrated that chirality have a significant effect on binding affinity.

Here, we analyzed the antimicrobial activity of enantiomeric pure $Ru(phen)_2dppz^{2+}$ (Ru-phen) and μ-$bidppz(phen)_4Ru_2^{4+}$ (biRu-phen), both well-established DNA-intercalators, with Gram-negative *Escherichia coli* and Gram-positive *Bacillus subtilis* as the bacterial models.

It is expected for DNA, being a chiral molecule itself, to interact differently with the dissymmetric non-intercalating peripheral pair of phen ligands on the ruthenium complex depending on the chirality of the complex. This is also what we observed for the mononuclear Ru-phen, with the Δ-form having a significantly higher inhibitory and bactericidal effect in comparison to the Λ-form (Fig 4.10). In contrast, the binuclear biRu-phen complex showed very little antimicrobial activity against either bacterial strain with no enantiomeric difference. Only at the highest concentration level tested did the complex have an effect against the bacteria, with a sudden decrease in bacterial growth. This was more likely caused by lysis of the cellular membrane rather than DNA

intercalation. By quantifying the release of nucleic acids through absorption spectroscopy from bacterial cells after 60 min exposure of ruthenium complex, we found the binuclear complexes to have a similar effect as a 3% SDS solution.

The same chiral discrimination for DNA has been previously reported with Δ-Ru-phen showing as much as 2-5 times stronger binding affinity than Λ-Ru-phen, indicating that the bactericidal mechanism of action is indeed DNA interaction. To further test this hypothesis, the emission of the bacterial cells was measured after exposure to an excess of ruthenium complex.

Any fluorescence observed would indicate DNA-binding as Ru-phen is completely quenched when unbound in aqueous solution. In both bacterial strains, the intensity of emission from the bacterial cells were significantly higher after exposure to Δ-Ru-phen compared to Λ-Ru-phen. A small redshift could be seen for Λ-Ru-phen in both strains, a phenomena associated with DNA-complex interactions. In addition, no emission from the binuclear complexes was observed, further supporting that there was no DNA interaction.

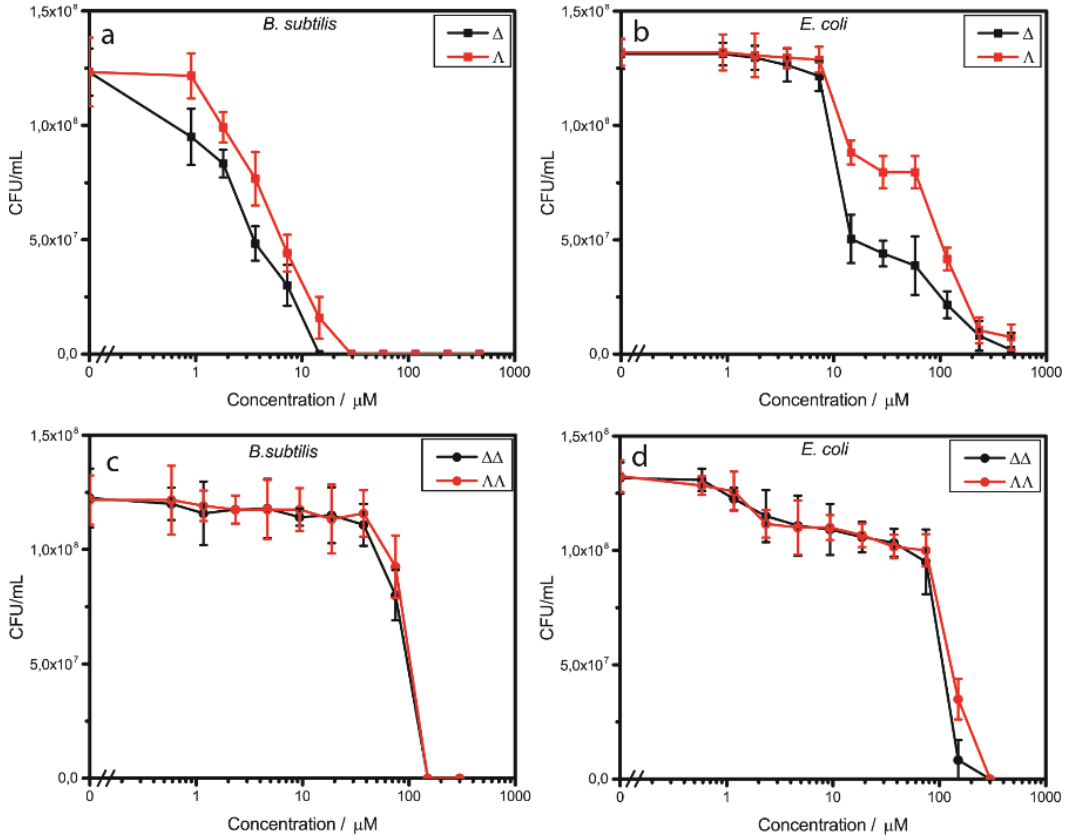

Figure 4.10 *Surviving bacterial counts (CFU/mL) of B. subtilis (left) and E. coli (right) after 24 hours exposure to Ru-phen (top, a and b) and biRu-phen (bottom, c and d) at 37°C. Each point is the mean of 6 replicate cultures. Error bars show standard deviations (SD: 3σ); when not visible, these bars are as small or smaller than the symbols plotted.*

Fig. 4.11 shows a confocal microscopic picture of Hoechst-stained *E. coli* that had been previously treated with either enantiomer of Ru-phen. Both enantiomers are clearly fluorescent, but with a much higher intensity coming from Δ-form, further indicating enantiomeric dependence of binding affinity and consequently, also antimicrobial activity. Interestingly, the relation between the intensity of the Hoechst-stain and the intensity of the complex appears to be inverse; the cells with the highest intensity of ruthenium complex appears to have very weak, if any, fluorescence from the Hoechst-staining, and vice versa. This relation is apparent for both enantiomers. A possible explanation could be that the ruthenium complexes and the DNA-stain compete for binding in the minor groove of DNA, and bacterial cells with a poor emission from the DNA-stain have their DNA binding sites already occupied by ruthenium complexes. Furthermore, unexposed bacterial cells used as controls showed significantly stronger emission from the Hoechst dye compared to bacteria exposed to ruthenium complex, again indicating that ruthenium complexes and the DNA-binding dye competes for the same binding sites.

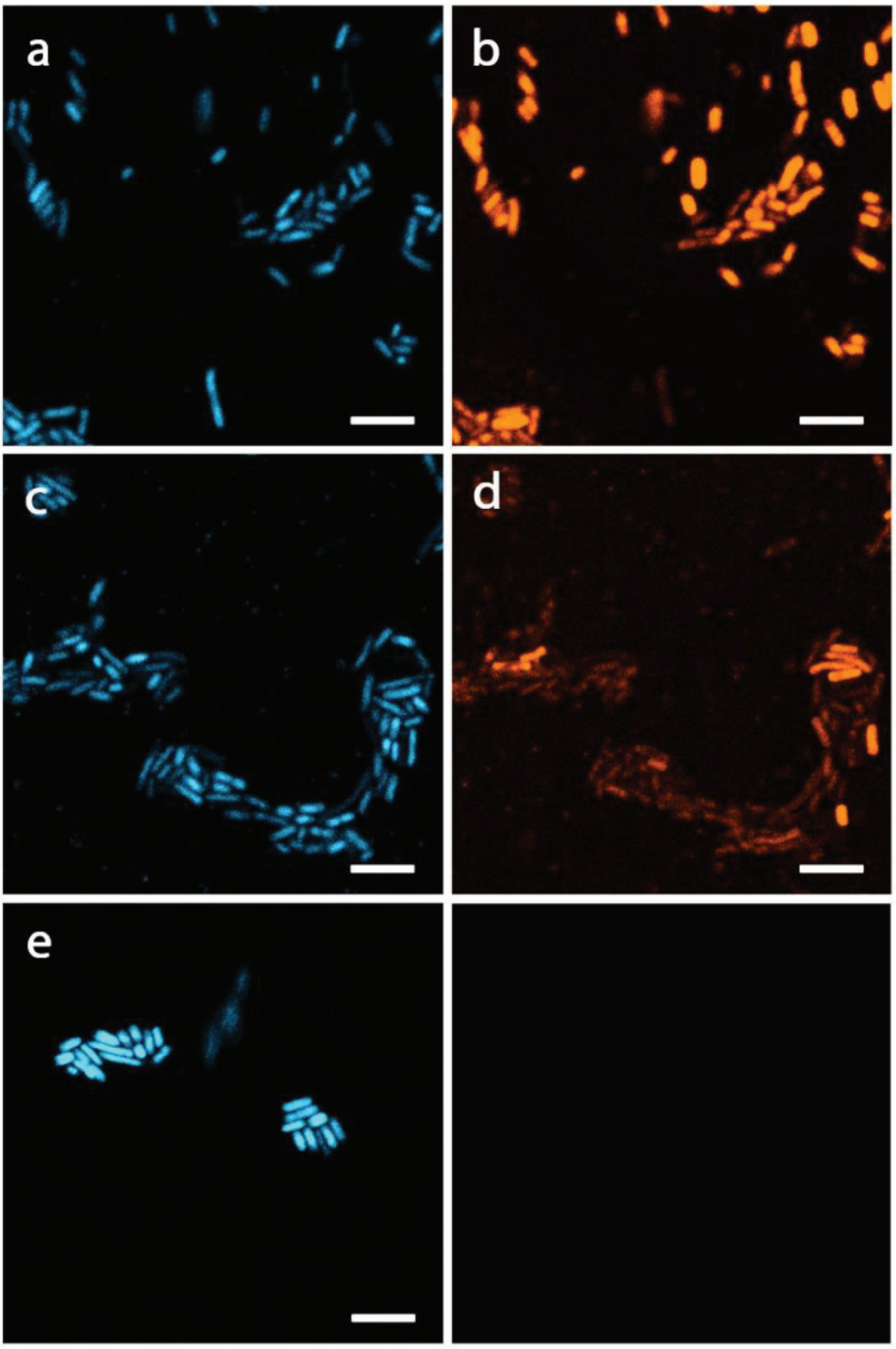

Figure 4.11 *Confocal microscopy images of formaldehyde fixed E. coli samples incubated with Δ- (top row) and Λ-Ru-phen (middle row) overnight and then stained with Hoechst 33342. (a) fluorescence - Hoechst 33342 (Δ-sample); (b) fluorescence – Δ-Ru-phen; (c) fluorescence - Hoechst 33342 (Λ-sample); (d) fluorescence – Λ-Ru-phen; (e) fluorescence - control sample E. coli stained with Hoechst 33342 (Bottom right: a black square for visual aid). Scale bar = 5 μm*

5 CONCLUSIONS AND OUTLOOK

As a continuance to the potential use of ruthenium complexes as antibiotics, our group aim to realize a binary antibiotic, with the active drug synthesized inside the bacterial from two prodrug reactants. These prodrugs will be bulky and substituted with moderately reactive groups. Once the two prodrugs have reach the bacterial DNA, they are able to reversibly insert themselves into the double helix. Unconnected, the prodrugs are harmless to the bacterial cell, but when a pair of complimentary prodrugs happens to be inserted next to each other, they react by forming a connecting covalent bond and the now active antibiotic becomes entangled to the DNA (Fig. 5.1), blocking its function and ultimately killing the cell.

By controlling the rate of the biomolecular reaction, the active drug will be under kinetic control. The rate constant of the synthesis of the active drug is determined by the structure of the two prodrug and of the concentration of the prodrugs in close proximity of the target DNA. Effectively, the dose-response curve will be much steeper compared to a more conventional antibiotic (Fig. 5.2) and the significantly lower concentration of the binary antibiotic needed for an bactericidal effect will most likely slow down any resistance development.

For the initial prodrug design and synthesis, binuclear ruthenium(II) polypyridyl complexes will be used as template. As demonstrated previously by our group, these types of bulky "dumbbell-like" complexes have a very slow dissociation rate and could provide a potent blockage for DNA transcription. In addition, by variating the distance between the ruthenium centers and the flexibility of the tether connecting the ruthenium groups it is possible to alter the sequence and stereo-selectivity of the complex.[49, 106-107] In addition, ruthenium complexes allow for fairly simple modular construction where the intercalating ligands, ancillary ligands and connecting moieties may be (almost)

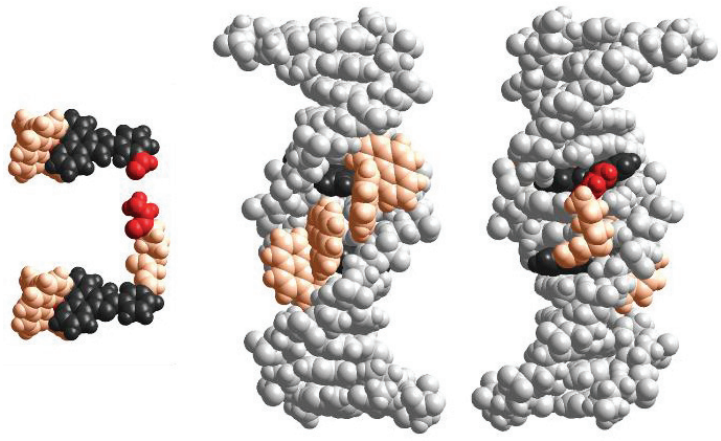

Figure 5.1 *A pair of ruthenium complex precursor drugs: the intercalating ligand is colored black, the ruthenium(II) ion and the reactive groups red, the ancillary ligands and the chain connecting the reactive group orange (left); a DNA model showing the adjacent intercalation of the two precursor drugs after reaction, viewed from the minor groove (middle) and the major groove (right). The reacting groups are here aldehyde (-CHO) and acylhydrazine (-CONHNH$_2$).*

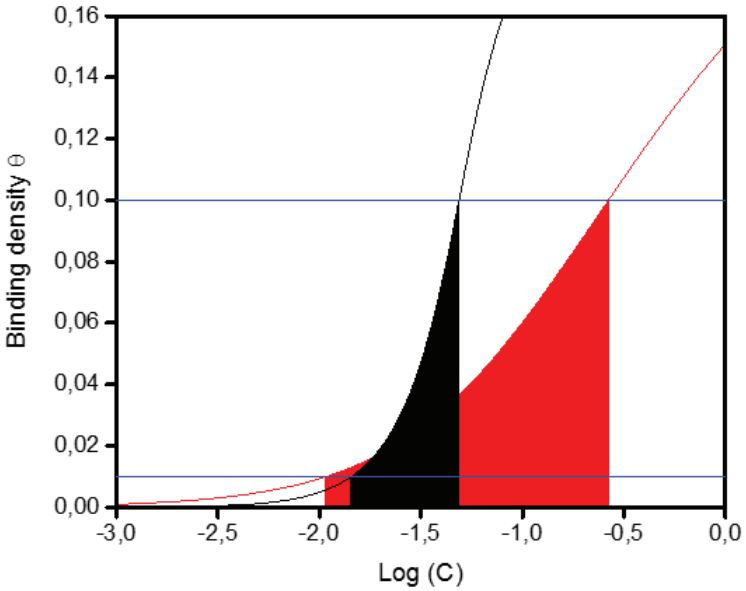

Figure 5.2 *Antibiotic binding density θ vs the concentration C of a conventional drug (red curve) and of a 1:1 mixture of prodrugs (black curve). Assuming that bacteria are killed when θ > 0.1and that θ < 0.01 is harmless, the critical drug concentration intervals are indicated by the colored areas.*

freely varied in order to fine-tune the reactivity of the prodrug molecules. As an added bonus, the long-lived excited state of many ruthenium complexes make them excellent environment-sensitive luminescent reporters, which will aid the imaging of the binary antibiotic in cell uptake and intracellular distribution studies. The reactive groups will, of necessity, have well-tuned bimolecular rate constants; they must be small enough to be virtually non-reactive in a dilute solution, while still high enough for fast ligation when brought together in an intercalative state. We are currently developing a system that uses a strained cyclooctyne-azide coupling reaction (Fig 5.3), aiming for this system to be bio-orthogonal (i.e. not reacting with anything else in the cell).

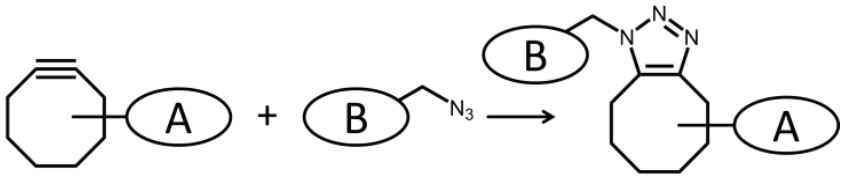

Figure 5.3 *Schematic illustration of a cyclooctyne-azide coupling reaction*

6 ACKNOWLEDGEMENTS

First of all I would like to express my gratitude to my supervisor **Per Lincoln** for his guidance, helpful advice, encouragement and perhaps most importantly, endless patience. This thesis had not been possible without your help and I sincerely appreciate you always having time for me, despite your overcrowded schedule. My many thanks also goes out to my co-supervisor **Maria Abrahamsson** who always had time to help when I needed it. Thanks to my co-author **Valentina Tremaroli** for her valuable advice and assistance with the bacteria and **Mattias Bergentall** for helping me getting some really cool confocal microscopy images. Thanks to **Fredrik Bäckhed** for letting me use his facilities and resources at the Wallenberg laboratory. Also, thank you **Johanna Andersson** and **Maria Matson Dzebo** for showing me how to operate the instruments at Physical chemistry and helping me to get a great start to my project. And thanks to **Kübra Ucar** for all the fun times together, I really value our friendship and hope all goes well for you. My many thanks to **caffeine**, which is responsible for all that is good with this thesis. Finally, my special thanks goes out to all my **colleagues** at Physical chemistry, it has been truly a joy both working and having fika with you.

7 REFERENCES

1. Chargaff, E. and Vischer, E., The composition of the deoxypentose nucleic acid of thymus and spleen. *J. Biol. Chem.* **1949,** *177* (1), 405-416.
2. Vischer, E., Zamenhof, S. and Chargaff, E., Microbial nucleic acids; the desoxypentose nucleic acids of avian tubercle bacilli and yeast. *J. Biol. Chem.* **1949,** *177* (1), 429-438.
3. Chargaff, E., Chemical specificity of nucleic acids and mechanism of their enzymatic degradation. *Experientia* **1950,** *6* (6), 201-209.
4. Watson, J. D. and Crick, F. H. C., Molecular structure of nucleic acids: A structure for deoxyribose nucleic acid. *Nature* **1953,** *171* (4356), 737-738.
5. Kapuscinski, J., DAPI: a DNA-specific fluorescent probe. *Biotech. Histochem.* **1995,** *70* (5), 220-233.
6. Loontiens, F. G., Dumortier, L., Regenfuss, P., Zechel, A. and Clegg, R. M., Binding characteristics of Hoechst 33258 with calf thymus DNA, poly[d(A-T)], and d(CCGGAATTCCGG): multiple stoichiometries and determination of tight binding with a wide spectrum of site affinities. *Biochem.* **1990,** *29* (38), 9029-9039.
7. Breusegem, S. Y., Clegg, R. M. and Loontiens, F. G., Base-sequence specificity of Hoechst 33258 and DAPI binding to five $(A/T)_4$ DNA sites with kinetic evidence for more than one high-affinity Hoechst 33258-AATT complex. *J. Mol. Biol.* **2002,** *315* (5), 1049-1061.
8. Smith, C. K., Davies, G. J., Dodson, E. J. and Moore, M. H., DNA-nogalamycin interactions – the crystal structure of d(TGATCA) complexes with nogalamycin. *Biochem.* **1995,** *34* (2), 415-425.
9. Li, L. H., Kuentzel, S. L., Murch, L. L., Pschigoda, L. M. and Krueger, W. C., Comparative biological and biochemical effects of nogalamycin and its analogs on L1210 leukemia. *Cancer Research* **1979**, *39* (12), 4816-4822.
10. Jennette, K. W., Lippard, S. J., Vassiliades, G. A. and Bauer, W. R., Metallointercalation reagents. 2-hydroxyethanethiolato(2,2′,2′-ter-pyridine)-platinum(II) monocation binds strongly to DNA by intercalation. *Proc. Natl. Acad. Sci. U S A.* **1974,** *71* (10), 3839-3843.

11. Vandyke, M. W., Hertzberg, R. P. and Dervan, P. B., Map of distamycin, netropsin, and actinomycin binding sites on heterogenous DNA: DNA cleavage-inhibition patterns with methidiumpropyl-EDTA.Fe(II). *Proc. Natl. Acad. Sci. U S A.* **1982,** *79* (18), 5470-5474.

12. Uchida, K., Pyle, A. M., Morii, T. and Barton J. K., High resolution footprinting of EcoRI and distamycin with $Rh(phi)_2(bpy)^{3+}$, a new photofootprinting reagent. *Nucleic Acids Res.* **1989,** *17* (24), 10259-10279.

13. Maruyama, K., Mishima, Y., Minagawa, K. and Motonaka, J., DNA sensor with a dipyridophenazine complex of osmium(II) as an electrochemical probe. *Anal. Chem.* **2002,** *74* (15), 3698-3703.

14. Dwyer, F. P., Gyarfas, E. C., Rogers, W. P. and Koch, J. H., Biological activity of complex ions. *Nature* **1952,** *170* (4318), 190-191.

15. Dwyer, F. P., Reid, I. K., Shulman, A., Laycock, G. M. and Dixson, S., The biological actions of 1,10-phenanthroline and 2,2´-bipyridine hydrochlorides, quaternary salts and metal chelates and related compounds. 1. Bacteriostatic action on selected gram-positive, gram-negative and acid-fast bacteria. *Aust. J. Exp. Biol. Med. Sci.* **1969,** *47* (2), 203-218.

16. White, D. O., Dwyer, F. P., Shulman, A. and Harris A. W., Actions of metal chelates of substituted 1,10-phenanthrolines on viruses and cells. 1. Inactivation on viruses. *Aust. J. Exp. Biol. Med. Sci.* **1963,** *41* (5), 517-526.

17. Shulman, A. and Dwyer, F. P., Metal chelates in biological systems. In *Chelating Agents and Metal Chelates,* Dwyer, F. P. and Mellor, D. P., Eds. Academic Press: New York, **1964,** 383-435.

18. Barton, J. K., Dannenberg, J. J. and Raphael, A. L., Enantiomeric selectivity in binding tris(phenanthroline)zinc(II) to DNA. *J. Am. Chem. Soc.* **1982,** *104* (18), 4967-4969.

19. Barton, J. K. and Raphael, A. L., Site-specific cleavage of left-handed DNA in pBR322 by lambda-tris(diphenanthroline)cobalt(III). *Proc. Natl. Acad. Sci. U S A.* **1985,** *82* (19), 6460-6464.

20. Yamagishi, A., Evidence for stereospecific binding of tris(1,10-phenanthroline)-ruthenium(II) to DNA is provided by electronic dichroism. *J. Chem. Soc., Chem. Commun.* **1983,** (10), 572-573.

21. Barton, J. K., Danishevsky, A. T. and Goldberg, J. M., Tris(phenanthroline)ruthenium(II): Stereoselectivity in binding to DNA. *J. Am. Chem. Soc.* **1985,** *13* (17), 6017-6034.

22. Kelly, J. M., Tossi, A. B., McConnell, D. J. and Ohuigin, C., A study of the interactions of some polypyridylruthenium(II) complexes with DNA using fluorescence

spectroscopy, topoisomerisation and thermal denaturation. *Nucleic Acids Res.* **1985,** *13* (17), 6017-6034.

23. Barton, J. K., Goldberg, J. M., Kumar, C. V. and Turro, N. J., Binding modes and base specificity of tris(phenanthroline)ruthenium(II) enantiomers with nucleic acids: Tuning the stereoselectivity. *J. Am. Chem. Soc.* **1986,** *108* (8), 2081-2088.

24. Kumar, C. V., Barton, J. K. and Turro, N. J., Photophysics of ruthenium complexes bound to double helical DNA. *J. Am. Chem. Soc.* **1985,** *107* (19), 5518-5523.

25. Friedman, A. E., Chambron, J. C., Sauvage, J. P., Turro, N. J. and Barton, J. K. Molecular light switch for DNA: $Ru(bpy)_2(dppz)^{2+}$. *J. Am. Chem. Soc.* **1990,** *112* (12), 4960-4962.

26. Friedman, A. E., Kumar, C. V., Turro, N. J. and Barton, J. K. Luminescence of ruthenium(II) polypyridyls: Evidence for intercalative binding to Z-DNA. *Nucleic Acids Res.* **1991,** *19* (10), 2595-2602.

27. Jenkins, Y, Friedman, A. E., Turro, N. J. and Barton, J. K., Characterization of dipyridophenazine complexes of ruthenium(II): The light switch effect as a function of nucleic acid sequence and conformation. *Biochem.* **1992,** *31* (44), 10809-10816.

28. Hartshorn, R. M. and Barton, J. K., Novel dipyridophenazine complexes of ruthenium(II): Exploring luminescent reporters of DNA. *J. Am. Chem. Soc.* **1992,** *114* (15), 5919-5925.

29. Önfelt, B., Lincoln, P., Nordén, B., Baskin, J. S. and Zewail, A. H., Femtosecond linear dichroism of DNA-intercalating chromophores: Solvation and charge separation dynamics of $Ru(phen)_2dppz^{2+}$ systems. *Proc. Natl. Acad. Sci. USA.* **2000,** *97* (11), 5708-5713.

30. Coates, C. G., Olofsson, J., Coletti, M., McGarvey, J. J., Önfelt, B., Lincoln, P., Nordén, B., Tuite, E., Matousek, P. and Parker, A. W., Picosecond time-resolved resonance Raman probing of the light-switch states of $Ru(phen)_2dppz^{2+}$. *J. Phys. Chem. B* **2001,** *105* (50), 12653-12664.

31. Niyazi, H., Hall, J. P., O'Sullivan, K., Winter, G., Sorensen, T., Kelly, J. M. and Cardin, C. J., Crystal structures of Λ-$[Ru(phen)_2dppz]^{2+}$ with oligonucleotides containing TA/TA and AT/AT steps show two intercalating modes. *Nat. Chem.* **2012,** *4* (8), 621-628.

32. Hall, J. P., Cook, D., Morte, S. R., McIntyre, P., Buchner, K., Beer, H., Cardin, D. J., Brazier, J. A., Winter, G., Kelly, J. M. and Cardin, C. J., X-ray crystal structure of rac-$[Ru(phen)_2dppz]^{2+}$ with $d(ATGCAT)_2$ shows enantiomer orientations and water ordering. *J. Am. Chem. Soc.* **2013,** *135* (34), 12652-12659.

33. Hall, J. P., Keane, P. M., Beer, H., Buchner, K., Winter, G., Sorensen, T. L., Cardin, D. J., Brazier, J. A. and Cardin, C. J., Delta chirality ruthenium 'light-switch' complexes can bind in the minor groove of DNA with five different binding modes. *Nucleic Acids Res.* **2016,** *44* (19), 9472-9482.

34. Satyanarayana, S., Dabrowiak, J. C. and Chaires, J. B., Tris(phenanthroline)ruthenium(II) enantiomer interactions with DNA: Mode and specificity of binding. *Biochem.* **1993,** *32* (10), 2573-2584.

35. Haq, I., Lincoln, P., Suh, D., Nordén, B., Chowdhry, B. Z. and Chaires, J. B., Interaction of Δ- and Λ-$[Ru(phen)_2DPPZ]^{2+}$ with DNA: A calorimetric and equilibrium binding study. *J. Am. Chem. Soc.* **1995,** *117* (17), 4788-4796.

36. Hiort, C., Lincoln, P. and Nordén, B., DNA binding of Δ- and Λ-$[Ru(phen)_2DPPZ]^{2+}$. *J. Am. Chem. Soc.* **1993,** *115* (9), 3448-3454.

37. Lincoln, P. and Nordén, B., Binuclear ruthenium(II) phenanthroline compounds with extreme binding affinity for DNA. *Chem. Commun.* **1996,** (18), 2145-2146.

38. Lincoln, P., Broo, A. and Nordén, B., Diastereomeric DNA-binding geometries of intercalated ruthenium(II) trischelates probed by linear dichroism: $Ru(phen)_2(DPPZ)^{2+}$ and $Ru(phen)_2(BDPPZ)^{2+}$. *J. Am. Chem. Soc.* **1996,** *118* (11), 2644-2653.

39. Andersson, J., Fornander, L. H., Abrahamsson, M., Tuite, E., Nordell, P. and Lincoln, P., Lifetime heterogeneity of DNA-bound dppz complexes originates from distinct intercalation geometries determined by complex-complex interactions. *Inorg. Chem.* **2013,** *52* (2), 1151-1159.

40. Lim, M. H.; Song, H.; Olmon, E. D.; Dervan, E. E.; Barton, J. K., Sensitivity of $Ru(bpy)_2(dppz)^{2+}$ luminescence to DNA defects. *Inorg. Chem.* **2009,** *48* (12), 5392-5397.

41. Pyle, A. M., Rehmann, J. P., Meshoyrer, R., Kumar, C. V., Turro, N. J. and Barton, J. K., Mixed-ligand complexes of ruthenium(II): Factors governing binding to DNA. *J. Am. Chem. Soc.* **1989,** *111* (8), 3051-3058.

42. Sauvage, J. P., Collin, J. P., Chambron, J. C., Guillerez, S., Coudret, C., Balzani, V., Barigelletti, F., Decola, L. and Flamigni, L., Ruthenium(II) and osmium(II) bis(terpyridine) complexes in covalently-linked multicomponent systems: Synthesis, electrochemical behavior, absorption spectra, and photochemical and photophysical properties. *Chem. Rev.* **1994,** *94* (4), 993-1019.

43. Maestri, M., Armaroli, N., Balzani, V., Constable, E. C. and Thompson, A., Complexes of the ruthenium(II)-2,2':6',2''-terpyridine family. Effect of electron-accepting and electron-donating substituents on the photophysical and electrochemical properties. *Inorg. Chem.* **1995,** *34* (10), 2759-2767.

44. Wilhelmsson, L. M., Westerlund, F., Lincoln, P. and Nordén, B., DNA-binding of semirigid binuclear ruthenium complex ΔΔ-[μ-(11,11'-bidppz)(phen)$_4$Ru$_2$]$^{4+}$: Extremely slow intercalation kinetics. *J. Am. Chem. Soc.* **2002,** *124* (41), 12092-12093.

45. Wilhelmsson, L. M., Esbjörner, E. K., Westerlund, F., Nordén, B. and Lincoln, P., Meso stereoisomer as a probe of enantioselective threading intercalation of semirigid ruthenium complex [μ-(11,11′-bidppz)(phen)$_4$Ru$_2$]$^{4+}$. *J. Phys. Chem. B* **2003,** *107* (42), 11784-11793.

46. Nordell, P., Westerlund, F., Wilhelmsson, L. M., Nordén, B. and Lincoln, P., Kinetic recognition of AT-rich DNA by ruthenium complexes. *Angew. Chem. Int. Ed. Engl.* **2007,** *46* (13), 2203-2206.

47. Westerlund, F. and Lincoln, P., AT-dependent luminescence of DNA-threading ruthenium complexes. *Biophys. Chem.* **2007,** *129* (1), 11-17.

48. Andersson, J., Li, M. and Lincoln, P., AT-specific DNA binding of binuclear ruthenium complexes at the border of threading intercalation. *Chem. Eur. J.* **2010,** *16* (36), 11037-11046.

49. Johansson, J. R., Wang, Y., Eng, M. P., Kann, N., Lincoln, P. and Andersson, J., Bridging ligand length controls at selectivity and enantioselectivity of binuclear ruthenium threading intercalators. *Chem. Eur. J.* **2013,** *19* (20), 6246-6256.

50. Razin, S., Barile, M. F., Harasawa, R., Amikam, D. and Glaser, G., Characterization of the mycoplasma genome. *Yale J. Biol. and Med.* **1983,** *56* (5-6), 357-366.

51. Gardner, M. J., Hall, N., Fung, E., White, O., Berriman, M., Hyman, R. W., Carlton, J. M., Pain, A., Nelson, K. E., Bowman, S., Paulsen, I. T., James, K., Eisen, J. A., Rutherford, K., Salzberg, S. L., Craig, A., Kyes, S., Chan, M. S., Nene, V., Shallom, S. J., Suh, B., Peterson, J., Angiuoli, S., Pertea, M., Allen, J., Selengut, J., Haft, D., Mather, M. W., Vaidya, A. B., Martin, D. M. A., Fairlamb, A. H., Fraunholz, M. J., Roos, D. S., Ralph, S. A., McFadden, G. I., Cummings, L. M., Subramanian, G. M., Mungall, C., Venter, J. C., Carucci, D. J., Hoffman, S. L., Newbold, C., Davis, R. W., Fraser, C. M. and Barrell, B., Genome sequence of the human malaria parasite Plasmodium falciparum. *Nature* **2002,** *419* (6906), 498-511.

52. Puckett, C. A. and Barton, J. K., Methods to explore cellular uptake of ruthenium complexes. *J. Am. Chem. Soc.* **2007,** *129* (1), 46-47.

53. Puckett, C. A. and Barton, J. K., Mechanism of Cellular Uptake of a Ruthenium Polypyridyl Complex. *Biochem.* **2008,** *47* (45), 11711-11716.

54. Gill, M. R., Garcia-Lara, J., Foster, S. J., Smythe, C., Battaglia, G. and Thomas, J. A., A ruthenium(II) polypyridyl complex for direct imaging of DNA structure in living cells. *Nat. Chem.* **2009,** *1* (8), 662-667.

55. Svensson, F. R., Andersson, J., Amand, H. L. and Lincoln, P., Effects of chirality on the intracellular localization of binuclear ruthenium(II) polypyridyl complexes. *J. Biol. Inorg. Chem.* **2012,** *17* (4), 565-571.

56. Tian, X. H., Gill, M. R., Canton, I., Thomas, J. A. and Battaglia, G., Live Cell Luminescence Imaging As a Function of Delivery Mechanism. *ChemBioChem* **2011,** *12* (4), 548-551.

57. Gram, H. C., Ueber die isolirte Färbung der Schizomyceten in Schnitt-und Trockenpräparaten. *Fortschritte der Medcin* **1884,** *2*, 185-189.

58. Randall, C. P., Mariner, K. R., Chopra, I. and O'Neill, A. J., The Target of Daptomycin Is Absent from Escherichia coli and Other Gram-Negative Pathogens. *Antimicrob. Agents Chemother.* **2013,** *57* (1), 637-639.

59. Tsuchido, T. and Takano, M., Sensitization by heat treatment of Escherichia coli K-12 cells to hydrophobic antibacterial compounds. *Antimicrob. Agents Chemother.* **1988,** *32* (11), 1680-1683.

60. Pages, J. M., James, C. E. and Winterhalter, M., The porin and the permeating antibiotic: a selective diffusion barrier in Gram-negative bacteria. *Nature Rev. Microbiol.* **2008,** *6* (12), 893-903.

61. Galdiero, S., Falanga, A., Cantisani, M., Tarallo, R., Della Pepa, M. E., D'Oriano, V. and Galdiero, M., Microbe-host interactions: structure and role of Gram-negative bacterial porins. *Curr. Protein Pept. Sci.* **2012,** *13* (8), 843-854.

62. Baroud, M., Dandache, I., Araj, G. F., Wakim, R., Kanj, S., Kanafani, Z., Khairallah, M., Sabra, A., Shehab, M., Dbaibo, G. and Matar, G. M., Underlying mechanisms of carbapenem resistance in extended-spectrum beta-lactamase-producing Klebsiella pneumoniae and Escherichia coli isolates at a tertiary care centre in Lebanon: role of OXA-48 and NDM-1 carbapenemases. *Int. J. Antimicrob. Agents* **2013,** *41* (1), 75-79.

63. Lavigne, J.-P., Sotto, A., Nicolas-Chanoine, M.-H., Bouziges, N., Pages, J.-M. and Davin-Regli, A., An adaptive response of Enterobacter aerogenes to imipenem: regulation of porin balance in clinical isolates. *Int. J. Antimicrob. Agents* **2013,** *41* (2), 130-136.

64. Poulou, A., Voulgari, E., Vrioni, G., Koumaki, V., Xidopoulos, G., Chatzipantazi, V., Markou, F. and Tsakris, A., Outbreak caused by an ertapenem-resistant, CTX-M-15-producing Klebsiella pneumoniae sequence type 101 clone carrying an OmpK36 porin variant. *J. Clin. Microbiol.* **2013,** *51* (10), 3176-3182.

65. Blattner, F. R., Plunkett III, G., Bloch, C. A., Perna, N. T., Burland, V., Riley, M., Collado-Vides, J., Glasner, J. D., Rode, C. K., Mayhew, G. F., Gregor, J., Davis, N. W., Kirkpatrick, H. A., Goeden, M. A., Rose, D. J., Mau, B. and Shao, Y., The complete genome sequence of Escherichia coli K-12. *Science* **1997,** *277* (5331), 1453-1462.

66. Kunst, F., Ogasawara, N., Moszer, I., Albertini, A. M., Alloni, G., Azevedo, V., Bertero, M. G., Bessières, P., Bolotin, A., Borchert, S., Borriss, R., Boursier, L., Brans, A., Braun, M., Brignell, S. C., Bron, S., Brouillet, S., Bruschi, C. V., Caldwell, B., Capuano, V., Carter, N. M., Choi, S. K., Codani, J. J., Connerton, I. F., Cummings, N. J., Daniel, R. A., Denizot, F., Devine, K. M., Düsterhöft, A., Ehrlich, S. D., Emmerson, P. T., Entian, K. D., Errington, J., Fabret, C., Ferrari, E., Foulger, D., Fritz, C., Fujita, M., Fujita, Y., Fuma, S., Galizzi, A., Galleron, N., Ghim, S. Y., Glaser, P., Goffeau, A., Golightly, E. J., Grandi, G., Guiseppi, G., Guy, B. J., Haga, K., Haiech, J., Harwood, C. R., Hénaut, A., Hilbert, H., Holsappel, S., Hosono, S., Hullo, M. F., Itaya, M., Jones, L., Joris, B., Karamata, D., Kasahara, Y., Klaerr-Blanchard, M., Klein, C., Kobayashi, Y., Koetter, P., Koningstein, G., Krogh, S., Kumano, M., Kurita, K., Lapidus, A., Lardinois, S., Lauber, J., Lazarevic, V., Lee, S. M., Levine, A., Liu, H., Masuda, S., Mauël, C., Médigue, C., Medina, N., Mellado, R. P., Mizuno, M., Moestl, D., Nakai, S., Noback, M., Noone, D., O'Reilly, M., Ogawa, K., Ogiwara, A., Oudega, B., Park, S. H., Parro, V., Pohl, T. M., Portetelle, D., Porwollik, S., Prescott, A. M., Presecan, E., Pujic, P., Purnelle, B., Rapoport, G., Rey, M., Reynolds, S., Rieger, M., Rivolta, C., Rocha, E., Roche, B., Rose, M., Sadaie, Y., Sato, T., Scanlan, E., Schleich, S., Schroeter, R., Scoffone, F., Sekiguchi, J., Sekowska, A., Seror, S. J., Serror, P., Shin, B. S., Soldo, B., Sorokin, A., Tacconi, E., Takagi, T., Takahashi, H., Takemaru, K., Takeuchi, M., Tamakoshi, A., Tanaka, T., Terpstra, P., Tognoni, A., Tosato, V., Uchiyama, S., Vandenbol, M., Vannier, F., Vassarotti, A., Viari, A., Wambutt, R., Wedler, E., Wedler, H., Weitzenegger, T., Winters, P., Wipat, A., Yamamoto, H., Yamane, K., Yasumoto, K., Yata, K., Yoshida, K., Yoshikawa, H. F., Zumstein, E., Yoshikawa, H. and Danchin, A., The complete genome sequence of the gram-positive bacterium Bacillus subtilis. *Nature* **1997,** *390* (6657), 249-256.

67. Fleming, A., On the antibacterial action of cultures of a penicillium, with special reference to their use in the isolation of B. influenzae. *Br. J. Exp. Pathol.* **1929,** *10* (3), 226-236.

68. O'Neill, J., Tackling drug-resistant infections globally: final report and recommendations. The review on antimicrobial resistance. **2016**.

69. Antimicrobial resistance: global report on surveillance. *World Health Organisation* **2014**.

70. Blair, J. M. A., Webber, M. A., Baylay, A. J., Ogbolu, D. O. and Piddock, L. J. V., Molecular mechanisms of antibiotic resistance. *Nature. Rev. Microbiol.* **2015,** *13* (1), 42-51.

71. Nikaido, H., Multidrug Resistance in Bacteria. *Annu. Rev. Biochem.* **2009,** *78* (1), 119-146.

72. Projan, S. J., New (and not so new) antibacterial targets - from where and when will the novel drugs come? *Curr. Opin. Pharmacol.* **2002,** *2* (5), 513-522.

73. Bassetti, M., Merelli, M., Temperoni, C. and Astilean, A., New antibiotics for bad bugs: where are we? *Ann. Clin. Microbiol. Antimicrob.* **2013,** *12*, 15.

74. Projan, S. J., Why is big Pharma getting out of antibacterial drug discovery? *Curr. Opin. Microbiol.* **2003,** *6* (5), 427-430.

75. Laponogov, I., Sohi, M. K., Veselkov, D. A., Pan, X. S., Sawhney, R., Thompson, A. W., McAuley, K. E., Fisher, L. M. and Sanderson, M. R., Structural insight into the quinolone-DNA cleavage complex of type IIA topoisomerases. *Nat. Struct. Mol. Biol.* **2009,** *16* (6), 667-669.

76. Demain, A. L. and Sanchez, S., Microbial drug discovery: 80 Years of progress. *J. Antibiot.* **2009,** *62* (1), 5-16.

77. Bolhuis, A. and Aldrich-Wright, J. R., DNA as a target for antimicrobials. *Bioorg. Chem.* **2014,** *55*, 51-59.

78. Bolhuis, A., Hand, L., Marshall, J. E., Richards, A. D., Rodger, A. and Aldrich-Wright, J., Antimicrobial activity of ruthenium-based intercalators. *Eur. J. Pharm. Sci.* **2011,** *42* (4), 313-317.

79. Lei, W.; Zhou, Q.; Jiang, G.; Zhang, B.; Wang, X., Photodynamic inactivation of Escherichia coli by Ru(II) complexes. *Photochem. Photobiol. Sci.* **2011,** *10* (6), 887-890.

80. Li, F., Mulyana, Y., Feterl, M., Warner, J. M., Collins, J. G. and Keene, F. R., The antimicrobial activity of inert oligonuclear polypyridylruthenium(II) complexes against pathogenic bacteria, including MRSA. *Dalton Trans.* **2011,** *40* (18), 5032-5038.

81. Li, F., Feterl, M., Mulyana, Y., Warner, J. M., Collins, J. G. and Keene, F. R., In vitro susceptibility and cellular uptake for a new class of antimicrobial agents: Dinuclear ruthenium(II) complexes. *J. Antimicrob. Chemother.* **2012,** *67* (11), 2686-2695.

82. Li, F., Feterl, M., Warner, J. M., Day, A. I., Keene, F. R. and Collins, J. G., Protein binding by dinuclear polypyridyl ruthenium(II) complexes and the effect of cucurbit[10]uril encapsulation. *Dalton Trans.* **2013,** *42* (24), 8868-8877.

83. Li, F., Feterl, M., Warner, J. M., Keene, F. R. and Grant Collins, J., Dinuclear polypyridylruthenium(II) complexes: Flow cytometry studies of their accumulation in bacteria and the effect on the bacterial membrane. *J. Antimicrob. Chemother.* **2013,** *68* (12), 2825-2833.

84. Li, F., Harry, E. J., Bottomley, A. L., Edstein, M. D., Birrell, G. W., Woodward, C. E., Keene, F. R. and Collins, J. G., Dinuclear ruthenium(II) antimicrobial agents that selectively target polysomes in vivo. *Chem. Sci.* **2014,** *5* (2), 685-693.

85. Li, F., Collins, J. G. and Keene, F. R., Ruthenium complexes as antimicrobial agents. *Chem. Soc. Rev.* **2015,** *44* (8), 2529-2542.

86. Li, X., Heimann, K., Li, F., Warner, J. M. Keene, F. R. and Grant Collins, J., Dinuclear ruthenium(II) complexes containing one inert metal centre and one coordinatively-labile metal centre: Syntheses and biological activities. *Dalton Trans.* **2016,** *45* (9), 4017-4029.

87. Leising, R. A., Kubow, S. A., Churchill, M. R., Buttrey, L. A., Ziller, J. W. and Takeuchi, K. J., Synthesis, characterization, and X-ray crystal structure of $Ru(NO_2)PMe_3)_2(trpy)(ClO_4)$. *Inorg. Chem.* **1990,** *29* (7), 1306-1312.

88. Zhou, Q. X., Yang, F., Lei, W. H., Chen, J. R., Li, C., Hou, Y. J., Ai, X. C., Zhang, J. P., Wang, X. S. and Zhang, B. W., Ruthenium(II) Terpyridyl complexes exhibiting DNA photocleavage: The role of the substituent on monodentate ligand. *J. Phys. Chem. B* **2009,** *113* (33), 11521-11526.

89. Nordén, B., Kubista, M. and Kurucsev, T., Linear dichroism spectroscopy of nucleic acids. *Q. Rev. Biophys.* **1992,** *25* (1), 51-170.

90. Nordén, B., Rodger, A. and Dafforn, T., *Linear Dichroism and Circular Dichroism: A Textbook on Polarized-Light Spectroscopy*. Royal Society of Chemistry: Cambridge, **2010**.

91. Wada, A. and Kozawa, S., Instruments for studies of differential flow dichroism of polymer solutions. *J. Polym. Sci. A* **1964,** *2* (2), 853-864.

92. Eriksson, M. and Nordén, B., Linear and circular dichroism of drug-nucleic acid complexes. *Drug-Nucleic Acid Interactions* **2001,** *340*, 68-98.

93. Michl, J., and Thulstrup, E. W., Spectroscopy with polarized light: solute alignment by photoselection. *Liquid Crystals*, *Polymers, and Membranes* VCH Publishers, New York **1986**, 120.

94. Harrison, J. J., Tremaroli, V., Stan, M. A., Chan, C. S., Vacchi-Suzzi, C., Heyne, B. J., Parsek, M. R., Ceri, H. and Turner, R. J., Chromosomal antioxidant genes have metal ion-specific roles as determinants of bacterial metal tolerance. *Environ. Microbiol.* **2009,** *11* (10), 2491-2509.

95. Lichtman, J. W. and Conchello, J. A., Fluorescence microscopy. *Nat. Methods* **2005,** *2* (12), 910-919.

96. Jelesarov, I. and Bosshard, H. R., Isothermal titration calorimetry and differential scanning calorimetry as complementary tools to investigate the energetics of biomolecular recognition. *J. Mol. Recognit.* **1999,** *12* (1), 3-18.

97. Wiseman, T., Williston, S., Brandts, J. F. and Lin, L. N., Rapid measurement of binding constants and heats of binding using a new titration calorimeter. *Anal. Biochem.* **1989,** *179* (1), 131-137.

98. Ladbury, J. E. and Chowdhry, B. Z., Sensing the heat: The application of isothermal titration calorimetry to thermodynamic studies of biomolecular interactions. *Chem. Biol.* **1996,** *3* (10), 791-801.

99. McGhee, J. D. and Hippel, P. H. V., Theoretical aspects of DNA-protein interactions: Co-operative and non-co-operative binding of large ligands to a one-dimensional homogeneous lattice. *J. Mol. Biol.* **1974,** *86* (2), 469-489.

100. Lincoln, P., A generalized McGhee-von Hippel method for the cooperative binding of different competing ligands to an infinite one-dimensional lattice. *Chem. Phys. Lett.* **1998,** *288* (5-6), 647-656.

101. Chen, Y. D., A general secular equation for cooperative binding of n-mer ligands to a one-dimensional lattice. *Biopolymers* **1990,** *30* (11-12), 1113-1121.

102. Hall, J. P., Beer, H., Buchner, K., Cardin, D. J. and Cardin, C. J., The structural effect of methyl substitution on the binding of polypyridyl Ru-dppz complexes to DNA. *Organometallics* **2015,** *34* (11), 2481-2486.

103. Olofsson, J., Wilhelmsson, L. M. and Lincoln, P., Effects of methyl substitution on radiative and solvent quenching rate constants of $Ru(phen)_2dppz^{2+}$ in polyol solvents and bound to DNA. *J. Am. Chem. Soc.* **2004,** *126* (47), 15458-15465.

104. McKinley, A. W., Lincoln, P. and Tuite, E. M., Sensitivity of $Ru(phen)_2dppz^{2+}$ light switch emission to ionic strength, temperature, and DNA sequence and conformation. *Dalton Trans.* **2013,** *42* (11), 4081-4090.

105. McKinley, A. W, Andersson, J., Lincoln, P. and Tuite, E. M., DNA sequence and ancillary ligand modulate the biexponential emission decay of intercalated $Ru(L)_2dppz^{2+}$ enantiomers. *Chem. Eur. J.* **2012,** *18* (47), 15142-15150.

106. Andersson, J. and Lincoln, P., Stereoselectivity for DNA threading intercalation of short binuclear ruthenium complexes. *J. Phys. Chem. B* **2011,** *115* (49), 14768-14775.

107. Önfelt, B., Lincoln, P. and Nordén, B., Enantioselective DNA threading dynamics by phenazine-linked $Ru(phen)_2dppz^{2+}$ dimers. *J. Am. Chem. Soc.* **2001,** *123* (16), 3630-3637.

Build your own Ru complex model

You will need:

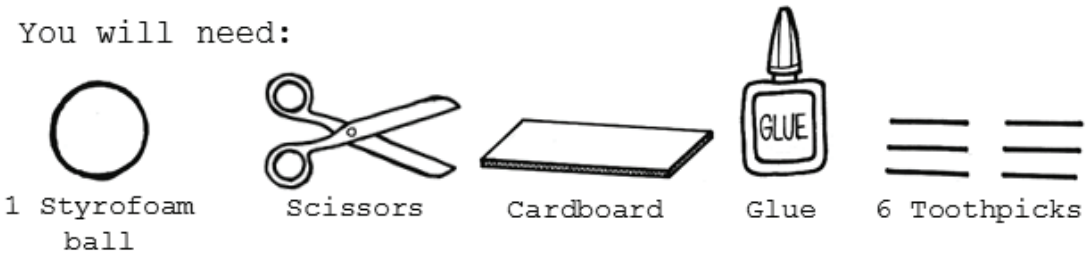

1 Styrofoam ball | Scissors | Cardboard | Glue | 6 Toothpicks

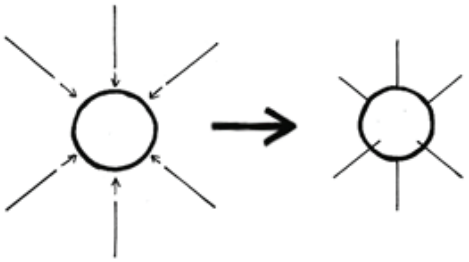

1. Stick 6 toothpicks in the Styrofoam ball to form an octahedral arrangement.

2. Cut out the shape of the ligands from the cardboard. Before cutting, glue on paper templates for guidance (optional).

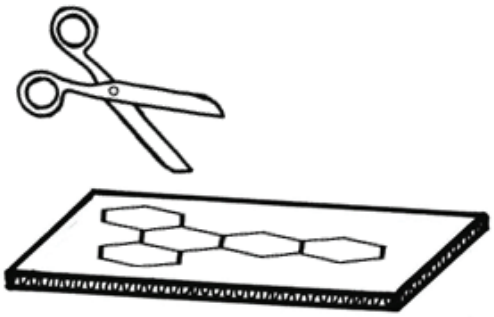

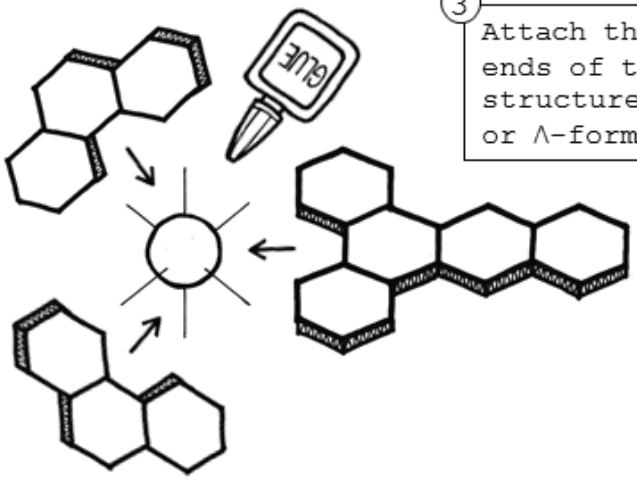

3. Attach the ligands on the free ends of the toothpicks. The final structure will either be the Δ- or Λ-form of the complex.

Paper I

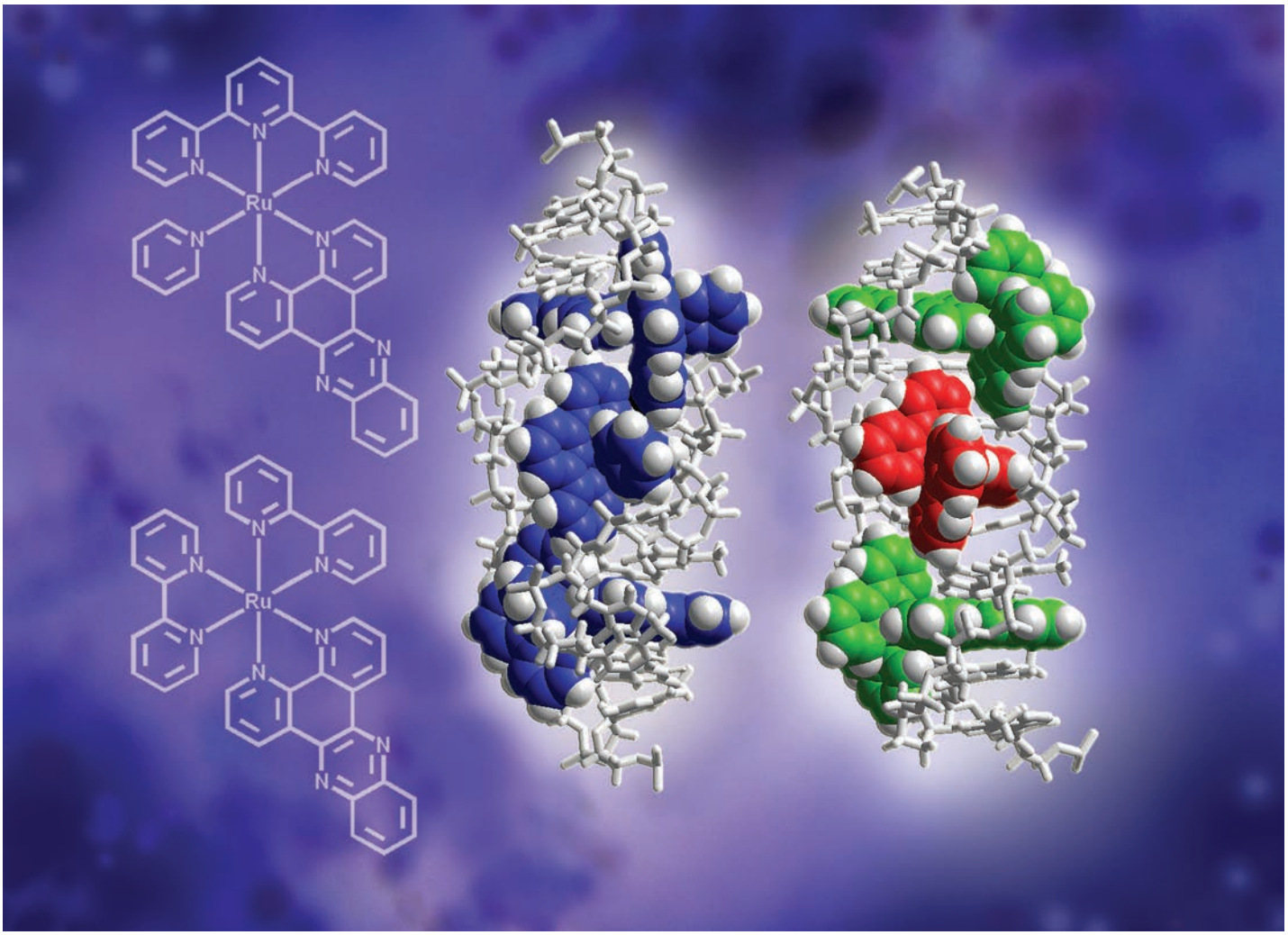

Showcasing the work on binding of ruthenium intercalators to DNA by Anna K. F. Mårtensson and Per Lincoln, Department of Chemical and Biological Engineering, Chalmers University of Technology, Sweden.

Binding of Ru(terpyridine)(pyridine)dipyridophenazine to DNA studied with polarized spectroscopy and calorimetry

Achiral Ru(tpy)(py)dppz^{2+} intercalated into the minor groove of DNA has similar intermolecular interactions as opposite enantiomers of its structural isomer, the "light-switch" complex Ru(bpy)$_2$dppz^{2+}.

As featured in:

See Anna K. F. Mårtensson and Per Lincoln, *Dalton Trans.*, 2015, **44**, 3604.

ROYAL SOCIETY OF CHEMISTRY

www.rsc.org/dalton

Registered charity number: 207890

Dalton Transactions

PAPER

View Article Online
View Journal | View Issue

Cite this: *Dalton Trans.*, 2015, **44**, 3604

Binding of Ru(terpyridine)(pyridine)-dipyridophenazine to DNA studied with polarized spectroscopy and calorimetry†

Anna K. F. Mårtensson and Per Lincoln*

Received 29th August 2014,
Accepted 29th October 2014

DOI: 10.1039/c4dt02642j

www.rsc.org/dalton

Linear and circular dichroism (LD and CD) spectroscopy as well as isothermal titration calorimetry (ITC) have been used to investigate the interaction of Ru(tpy)(py)dppz^{2+} (tpy = 2,2′:6′,2″-terpyridyl; py = pyridine; dppz = dipyrido[3,2-*a*:2′3′-*c*]phenazine) with DNA, providing detailed information about the DNA binding thermodynamics and binding geometry of the metal complex. Flow LD, CD and isotropic absorption indicate that Ru(tpy)(py)dppz^{2+} bind to DNA from the minor groove with the dppz ligand intercalated between base pairs, very similar to its chiral structural isomers Δ- and Λ-Ru(bpy)$_2$dppz^{2+} (bpy = 2,2′-bipyridine). A simple cooperative binding model with one binding geometry provide an excellent fit for calorimetric and absorption titration data. The values of the neighbor interaction thermodynamic parameters for Ru(tpy)(py)dppz^{2+} suggest that complexes bound contiguously prefer to have their tpy ligands oriented towards the same strand.

Introduction

DNA-binding drugs are small molecules that recognize and interact with specific DNA sites. Many of the chemotherapeutic anticancer agents currently in use fall under this category with cisplatin being the most prevalent example.[1] DNA intercalators that unwind DNA in order to π-stack between two base pairs have shown cytotoxicity towards cancerous cells but are often of limited therapeutic use due to their lack of specificity and frequent side effects. After the pioneering work by Barton and coworkers on the selective DNA binding of substitution-inert trisphenanthroline complexes of ruthenium, there has been an increasing interest in octahedral transition metal complexes.[2] The discovery of the "light switch" complexes Ru(phen)$_2$dppz^{2+} and Ru(bpy)$_2$dppz^{2+} (phen = 1,10-phenanthroline; bpy = 2,2′bipyridine; dppz = dipyrido[3,2-*a*:2′3′-*c*]-phenazine) lead to the synthesis of many variations of dppz-ruthenium-centered tris-bidentate structures with the potential as biosensors and therapeutic agents.[3] Interestingly, the two ruthenium complexes that have reached clinical trials have substitution-labile ligands and a proposed mode of action completely different to DNA intercalation.[4]

Spectroscopic and biophysical methods have established that it is the dppz ligand in tri-bidentate complexes that is intercalated between the base pairs of the DNA, and this has recently been confirmed by several X-ray crystal structures.[5] Compared to the intense research on the brightly luminescent bipyridine and phenanthroline complexes, the very low quantum yield at room temperature has led to less interest for ruthenium dppz complexes carrying the tridentate tpy ligand (tpy = 2,2′:6′,2″-terpyridyl), despite the fact that the absence of a stereocentre at the metal when coordinated to a tridentate ligand eliminates the need of separating Δ and Λ racemic mixtures characteristic of tris-bidentate systems. The main focus has been on tpy-based complexes with reactive oxoruthenium(IV) functionality that cleaves DNA by oxidation of guanine and the 1′-deoxyribose hydrogen.[6] However, not until recently has the single free coordination site left on the metal atom been recognized as a potential way of fine-tuning complex–DNA interactions, either by improving the DNA cleaving ability,[7] or as a novel light-activated drug delivery system.[8] Although some spectrophotometric studies have aimed at the DNA binding mode of tpy-based complexes to DNA,[9] a definite proof of the binding geometry has not yet been obtained.

Our group has previously determined that the tris-bidentate complexes affect each other, either cooperatively or anti-cooperatively, when interacting with a DNA-polymer *via* intercalation.[10] A binding model that gives a satisfactory fit to the data needs two distinct binding modes, one symmetrical (perpendicular) and one unsymmetrical (polar). This model with two modes of binding is supported by the crystallographic study by

Department of Chemical and Biological Engineering, Chalmers University of Technology, SE-41296 Gothenburg, Sweden. E-mail: marann@chalmers.se, lincoln@chalmers.se

†Electronic supplementary information (ESI) available. See DOI: 10.1039/c4dt02642j

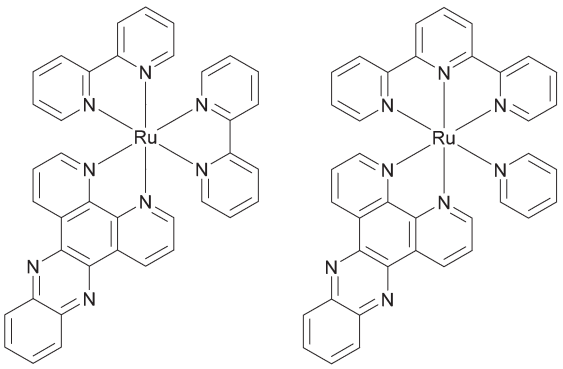

Scheme 1 Structures of ruthenium complexes $Ru(bpy)_2dppz^{2+}$ (left) and $Ru(tpy)(py)dppz^{2+}$ (right).

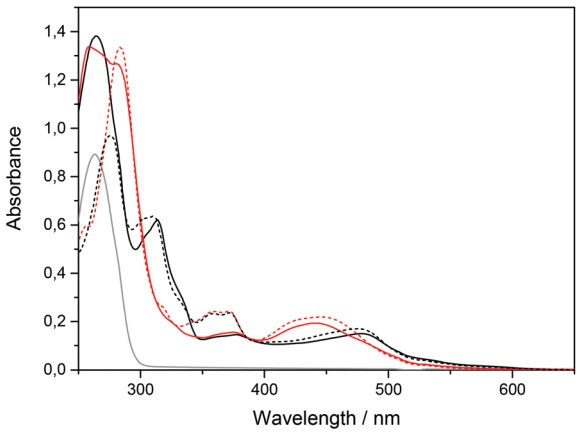

Fig. 1 Absorption spectra of Ru-tpy (black) and ΔRu-bpy (red) (14 μM) in 150 mM NaCl solution (dotted line) and in presence of AT-DNA (138 μM nucleotides) (solid line). The gray line shows AT-DNA only.

Niyazi *et al.* (2012) where a symmetric and a non-symmetric intercalation geometry was found for Λ-$Ru(phen)_2dppz^{2+}$.[5f]

In this study, we have carried out spectrophotometric and calorimetric measurements in order to determine the binding geometry and thermodynamic characteristics of $Ru(tpy)(py)dppz^{2+}$ (Ru-tpy, see Scheme 1). To simplify the system by avoiding effects from DNA sequence heterogeneity, and to compare with an earlier study,[10] we chose to primarily study the interaction of $poly(dAdT)_2$ (AT-DNA). However, since the AT-DNA was too short to orient in the flow cell for the linear dichroism study, we used calf thymus DNA (ctDNA) instead. We wanted to characterize a tpy/dppz ruthenium complex in its simplest form, and for the purpose of comparison, a pyridine (py) ligand was attached to the single coordination site, making the complex an achiral structural isomer of the original "light-switch" complex $Ru(bpy)_2dppz^{2+}$ (Ru-bpy). Once we have gained more understanding in how this mononuclear complex interacts with DNA, the substituents of this single coordination site could be varied to optimize properties that would make it and its binuclear derivatives more suitable as metallopharmaceuticals.

Results

Absorption

The absorption spectra of ΔRu-bpy and Ru-tpy in the absence and presence of AT-DNA at [base pairs]/[Ru] ratio of 5 are illustrated in Fig. 1. The broad band system centered at about 440 nm for ΔRu-bpy and 475 nm for Ru-tpy is attributed to the metal to ligand charge transfer (MLCT) transitions, which in the presence of AT-DNA show a slight hypochromicity and red shift for both complexes. The characteristic 372 nm band, assigned to the lowest π→π* transitions of the dppz chromophore is almost identical for both Ru-tpy and ΔRu-bpy, and in presence of AT-DNA there is also a very similar pronounced hypochromicity and red-shift (see Fig. 1 and Fig. S1 in ESI†).[11] For Ru-tpy, the most intense band outside the overlapping DNA absorption is the band at about 310 nm, which is assigned to the long-axis polarized lowest π→π* transition of the tpy chromophore.[12] This peak shows a red-shift of about 5 nm and in contrast to the 372 nm dppz band, only a slight hypochromicity at DNA binding, indicating that of the two large ruthenium ligands in Ru-tpy, the dppz ligand is the one that has the closest interaction with the nucleobases. As shown by titrating a constant concentration of Ru-tpy with AT-DNA (see Fig. S2 in ESI†), the hypochromicity of the dppz-band at 372 nm for Ru-tpy remains virtually constant at ratios [base pairs]/[Ru] > 2, whereas the initial hypochromicity in the 310 nm band is somewhat reduced at higher ratios.

Circular dichroism

A pure enantiomer of a chiral ruthenium complex, such as Ru-bpy, will show a strong intrinsic CD signal when free in aqueous solution, but Ru-tpy, which is an achiral complex will show zero CD signal under the same conditions. However, for both chiral and achiral molecules, binding to DNA can lead to a proper induced circular dichroism signal (proper ICD) by perturbation of the chromophores of the bound molecule by the chiral arrangement of the nucleobase chromophores. Here the magnitude and the sign of the ICD will mainly be dictated by the distances and angles between the interacting electronic transition dipole moments, and similar geometries are expected to give rise to similar ICD-patterns even for opposite enantiomers. In addition, for chiral molecules, changes merely in position and intensity of the intrinsic CD bands themselves, caused by the interaction with DNA, will add an apparent ICD contribution, but this will be characterized by a mirror-image like pattern for opposite enantiomers with similar binding geometries. Changes in CD were monitored upon addition of ΔRu-bpy, ΛRu-bpy, and Ru-tpy to a [base pairs]/[Ru] ratio of 5. In order to compare the ICD spectra of the complex–DNA interactions, the spectrum of the DNA and the spectrum of the free complex were subtracted from the spectrum in the presence of DNA. Fig. 2 shows the ICD of all three complexes as well as the CD spectrum of the AT-DNA. The general shape of the ICD below 290 nm is quite similar for all three complexes:

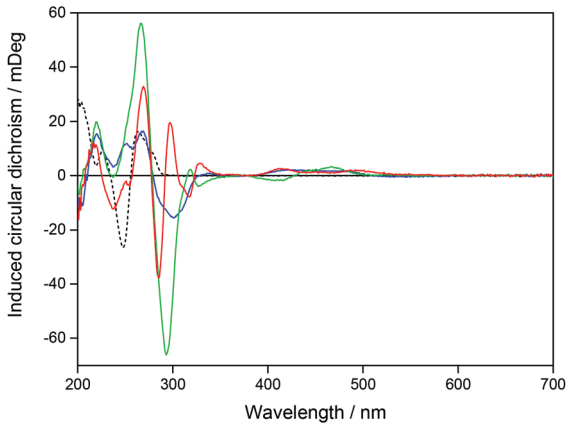

Fig. 2 Induced CD for Ru-tpy (blue), ΔRu-bpy (green), and ΛRu-bpy (red) after mixing with AT-DNA. The black dashed line shows the CD signal for AT-DNA in a 150 mM NaCl solution. The concentrations of complex and DNA were 14 and 138 μM respectively.

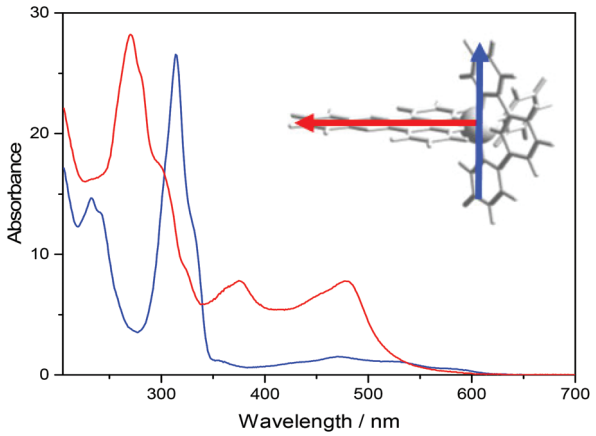

Fig. 4 Resolved spectra of the *x* and *y* (red) and the *z* (blue) polarized absorption bands of Ru-tpy bound to ctDNA. The *Y*-axis units are ε/(1000 M^{-1} cm^{-1}). The arrows on the molecular structure of the complex show the direction of the *x* and *z* transition moments.

a negative band between 275 and 290 nm and a positive band at about 260 nm, indicative of a proper ICD mechanism, while the general mirror-image relationship of the ICD curve >290 nm for Δ- and ΛRu-bpy suggests the predominance of an apparent ICD mechanism in this region. Titration of a solution with constant concentration of Ru-tpy shows an almost invariant CD spectrum >300 nm for [base pairs]/[Ru] > 2, similar to the results of the corresponding absorption titration (see Fig. S3 in ESI†).

Linear dichroism

Fig. 3 shows the LD spectra for Ru-tpy in ctDNA solution at [base pairs]/[Ru] ratios 8, 4 and 2. The ctDNA concentration remained constant at 270 μM nucleotides. The reduced LD (LD^r), which is the LD divided by the isotropic absorbance, is very similar for all [base pairs]/[Ru] ratios, indicating little or no change in the geometric orientation at higher saturation levels (see Fig. S4 in ESI†). Thus, the conditions were fulfilled

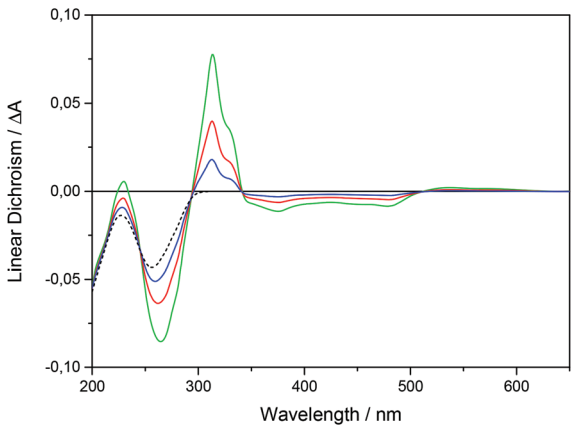

Fig. 3 Linear dichroism spectra of Ru-tpy in the presence of ctDNA at [base pairs]/[Ru] ratios 8 (blue), 4 (red) and 2 (green) in 10 mM NaCl solution, as well ctDNA alone (dotted). The concentration of ctDNA is 270 μM nucleotides.

for determining the orientation factor *S* using eqn (5), (8) and (11) (See Theory and methods section below) using the LD spectra of free DNA (L_0) and at ratios 8 (L_1) and 4 (L_2). The relative values S_1/S_0 = 1.06 and S_2/S_0 = 1.16 indicate that the DNA with bound Ru-tpy becomes better oriented, as earlier found for Δ- and ΛRu-bpy.[11a] Finally **b**, the pure (without DNA contribution) Ru-tpy LD spectrum, at perfect orientation and 10 mm optical path-length, was calculated as $\mathbf{b} = c_2^{-1}(S_2^{-1}L_1 - S_0^{-1}L_0)$. The weights w_1 and w_2 in eqn (6) were varied manually until the dppz band at 375 nm vanished in component $\mathbf{e}_1$ and the sharp tpy absorption band at 310 nm vanished in component envelope spectra $\mathbf{e}_2$, as shown in Fig. 4. The optimal weight values were $w_1 = 3 \pm 0.5$ and $w_2 = -1.5 \pm 0.3$, the theoretical limits for parallel and perpendicular orientation of a transition dipole moment relative to the orientation axis. Thus, the results show that the tpy long-axis (*z*) is aligned along and the dppz long-axis (*x*) perpendicular to the DNA helix axis, which, since the dppz ligand lies in the *x*,*y* plane, is consistent with intercalation of the dppz ligand in-between the base pairs.

Binding isotherms

ITC profiles for the binding of Ru-tpy to AT-DNA at 20, 25, and 30 °C are shown in Fig. 5 and for comparison, the corresponding ITC-profiles for Δ- and ΛRu-bpy from Andersson *et al.* (2013).[10] Ru-tpy shows a similar overall shape with a gradually increasing exothermic enthalpy until a negative maximum is reached at [Ru]/[base pairs] = 0.4–0.5, somewhat higher than for the other two complexes. The initial slope of the ITC profile is in contrast to the initial constant part of the sigmoidal curve expected for the simple binding as indicated above by absorption, circular dichroism and linear dichroism spectroscopies, where the spectra of Ru-tpy in the presence of DNA were found to be practically invariant with binding ratio. This suggests that intermolecular interactions between bound molecules must contribute to the binding enthalpy also for Ru-tpy, as earlier concluded for Δ- and ΛRu-bpy.[10] This

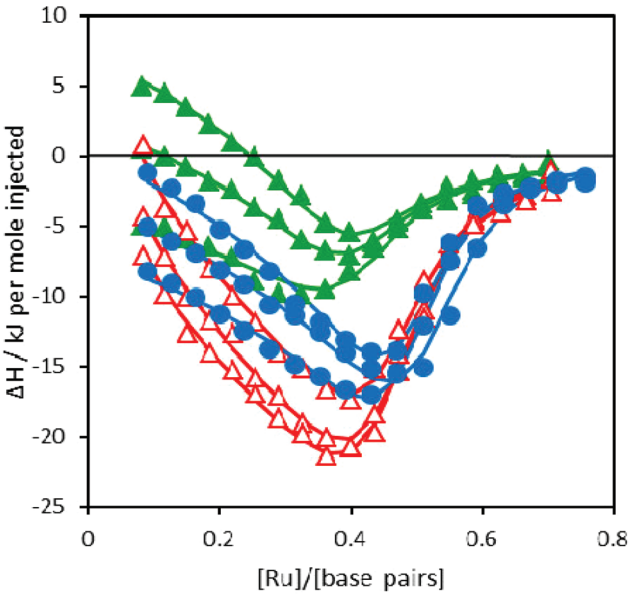

Fig. 5 ITC profiles with fitted traces for the binding of Ru-tpy (●), ΔRu-bpy (▲), and ΛRu-bpy (Δ) to AT-DNA in 150 mM NaCl solution at 20, 25, and 30 °C. Symbols indicate the normalized heat absorbed or evolved upon sequential injections (2 μL) of complex into the 206 μL cell containing the DNA. The data has been corrected for heat of complex dilution. The corresponding ITC-profiles for Δ- and ΛRu-bpy are from Andersson *et al.* (2013).[10]

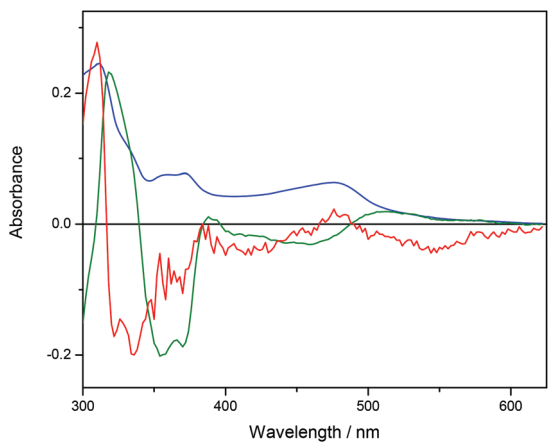

Fig. 6 The **U**-vectors corresponding to the first three singular values (s_1 blue, s_2 green, s_3 red) from the titration of Ru-tpy to a constant concentration of AT-DNA in 150 mM NaCl at 25 °C.

observation prompted us for a more thorough analysis of the spectroscopic changes, and absorption spectra were collected for addition of Ru-tpy to a constant concentration of AT-DNA at 25 °C.

The data (shown in Fig. S5 in ESI†) were analyzed with singular value decomposition (SVD) as described in Theory and methods. The first three (normalized) singular values were s_1 = 100, s_2 = 2.45 and s_3 = 0.23, and the corresponding columns of **U** and **V** are plotted in Fig. 6 and 7, respectively.

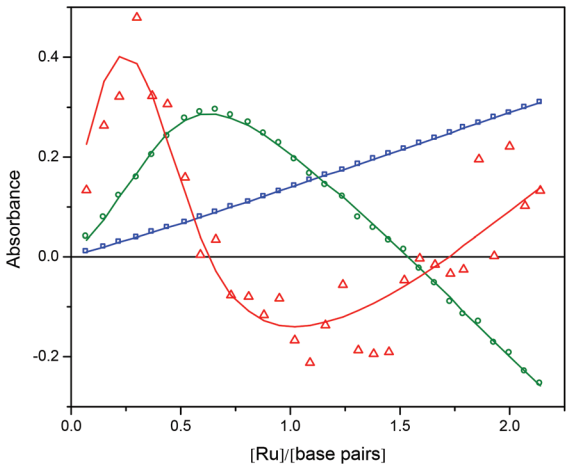

Fig. 7 The **V**-vectors corresponding to the first three singular values (s_1 blue squares, s_2 green circles, s_3 red triangles) from the titration of Ru-tpy to a constant concentration of AT-DNA in 150 mM NaCl at 25 °C. The fit of the model is shown as solid curves.

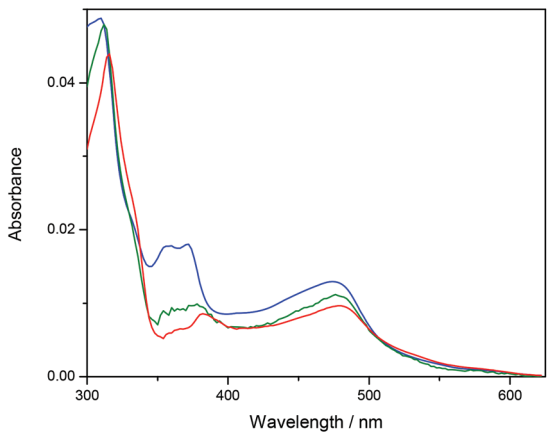

Fig. 8 Calculated absorption spectra for unbound complex (blue), bound complex with at most one neighbor (green) and bound complex with at least one neighbor (red).

Column **4** in **U** and **V** (shown in Fig. S6 and S7 in ESI†) were much less structured and were judged to be insignificant, although the fourth singular value (0.18) was close to the third.

Ru-tpy ITC and absorption data could be excellently globally fitted with the classical McGhee–von Hippel cooperative binding model (see Theory and methods), and the best fit to the data are shown with solid lines in Fig. 5 and 7. Fig. 8 shows the calculated absorption spectra for free complex, bound complex with at most one neighbor and bound complex with at least one neighbor. For comparison, the model was also used to fit the ITC data for ΔRu-bpy and ΛRu-bpy, as shown in Fig. 5. A linear fit to the calculated ΔH° values as a function of temperature is shown in Fig. 9, and Table 1 gives the parameters and derived thermodynamic data.

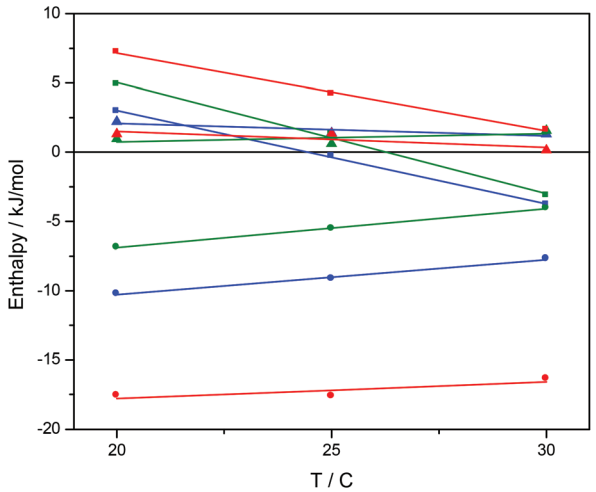

Fig. 9 The standard binding enthalpy ΔH°_{b} (■), standard nearest neighbor interaction enthalpy ΔH°_{nn} (●), and $\Delta H^{\circ}_{baseline}$ (▲) for binding of Ru-tpy (blue), ΔRu-bpy (green), and ΛRu-bpy (red) to AT-DNA in 150 mM NaCl. The slopes of the fitted lines correspond to the ΔC_p for the reactions.

Table 1 Binding constants *K*, cooperativity parameters *y*, and binding site sizes *n* that gave the best fit to experimental data, and the derived thermodynamic parameters for the intrinsic binding at 20 °C

Sample	K^a	*y*	*n*	$\Delta H^{\circ}_{b}{}^{b}$	$\Delta H^{\circ}_{nn}{}^{b}$	$\Delta C_{pb}{}^{c}$
Ru-tpy	1	2.8	2.0	3.0	−10.2	−680
ΔRu-bpy	0.9	1	2.2	4.3	−6.9	−800
ΛRu-bpy	0.06	5.5	2.3	7.2	−17.6	−560

^{a} $K/10^6$ M^{-1}. ^{b} $\Delta H°$/kJ mol^{-1}. ^{c} ΔC_p/J mol^{-1} K^{-1}.

Discussion

Recently, high-resolution structures and calorimetric studies have highlighted ligand–ligand interactions as an explanation to the complex thermodynamical and photophysical behavior of DNA-bound $Ru(L)_2dppz$ complexes.[5d–f,10] To further investigate the role of the ancillary L ligands, we chose to study the terpyridine/pyridine Ru-dppz complex Ru-tpy, an achiral isomer of $Ru(bpy)_2dppz$ formally made by breaking the pyridine–pyridine bond of one bpy unit and joining it to the second (see Scheme 1).

Absorption spectroscopy shows that the spectral changes of the dppz ligand bands are virtually identical for ΔRu-bpy and Ru-tpy upon binding to DNA, giving a first indication that the binding mode of the two isomers are similar. Circular dichroism spectroscopy shows a negative induced CD band in the long-axis polarized tpy band at 300 nm, similar to the negative induced CD shown for Δ- and ΛRu-bpy in their long-axis polarized bpy band at 290 nm, as could be expected for electronic transitions positioned in the minor groove close to parallel to the helix axis.[13] Both absorption and CD are practically invariant with binding ratio, although a small perturbation of the tpy-band at 310 nm can be observed at binding ratios close to saturation in both CD and absorption spectra. Likewise, linear dichroism spectra were found to be invariant with binding ratio too, allowing determination of the orientation factor *S* and a quantitative analysis of the angular binding geometry. In contrast to the $Ru(L)_2dppz$ complexes, where major transition moment directions have oblique angles to the plane of the dppz ligand, in Ru-tpy the long-axis polarized tpy transition is perpendicular to the dppz plane. With a weight $w_1 = +3 \pm 0.5$ we find that it is almost perfectly parallel oriented to the DNA helix axis, and the dppz long axis polarized transition, with weight $w_2 = -1.5 \pm 0.3$, perpendicularly oriented, the geometry expected for intercalation of the dppz ligand in-between the base pairs of DNA. In contrast to the very minute differences in absorption, CD and LD spectra at different binding ratios, the calorimetric titration show strong effects on the heat of binding. We have previously been reported such non-classical ITC curves for $Ru(L)_2dppz$ complexes (L = bpy or phen) and attributed them to an additional enthalpy contribution from interaction between neighboring complexes on the DNA.[10] In comparison to Δ- and ΛRu-bpy, Ru-tpy showed an ITC profile qualitatively most similar to the latter. Since a satisfactory global fit for the ITC and absorption experimental data of Ru-tpy could be obtained with the classical McGhee–von Hippel model with only one type of binding geometry, for comparison this model was also used to reanalyse our data for Δ- and ΛRu-bpy, which were originally fitted with a symmetrical and a pair of unsymmetrical intercalation geometries.[10] In this model (Model 3 in ref. 10), ligands bound with only one nearest-neighbor are assumed to have one distinct binding geometry (unsymmetrical), while ligands bound either isolated or with nearest-neighbors on both sides have a second binding geometry (symmetrical). As noted in our previous study, the fit of the simpler model to the ITC-data alone is excellent, but any attempt to rationalize the observed molar fractions of the short and the long excited state life-time fails. With the simple model, the apparent site sizes for Δ- and ΛRu-bpy were found to be 2.2 and 2.3, consistent with the neglect of the anti-cooperativity which is inherent in Model 3 for which the *n* parameters were found to be 2.0 and 1.8, respectively.[10] Interestingly, the binding site size parameter *n* was found to be 2.0 for Ru-tpy, indicating that the distinction between symmetrical and unsymmetrical intercalation geometries might be less pronounced for this complex. Although the low emission quantum yield of Ru-tpy bound to DNA precluded time-resolved luminescence measurements, the observation that spectra (absorption, CD, LD) change very little with binding density (see Fig. 3, S2 and S4†) support the conclusion that difference between intercalation geometries is small for Ru-tpy. The simple model has only one cooperativity parameter *y*, which is found to be 1 for ΔRu-bpy (*i.e.* non-cooperative binding) and 5.5 for ΛRu-bpy (cooperative binding); for Ru-tpy $y = 2.8$, in-between the values of the two Ru-bpy enantiomers. The intrinsic binding constant *K* is 10^6 M^{-1} for Ru-tpy, very similar to that of ΔRu-bpy, while *K* for ΛRu-bpy is almost 50 times smaller. The latter value is about 3 times smaller than that obtained with Model 3, however,

since simulated binding isotherms are the most sensitive to the value of the binding constant close to saturation, the best-fit value will normally be quite dependent on the binding model since the influence of the cooperativity parameters will differ.

The intrinsic binding enthalpy ΔH_b° is positive for all complexes at 20 °C, *i.e.* the binding in the absence of neighbor interactions is endothermic. The value of ΔH_b° is smaller for Ru-tpy than for either Δ- or ΛRu-bpy, but the temperature dependence is similar as evidenced by the negative ΔC_p-values of -680 ± 120 J K^{-1} M^{-1}. The nearest-neighbor interaction enthalpy ΔH_{nn}° is negative (*i.e.* exothermic) for all complexes, and exhibits a tendency similar to the cooperativity factor y, namely that the value for Ru-tpy is in-between the values for Δ- and ΛRu-bpy.

However, even if a simple, single binding geometry model is sufficient to model the binding data for Ru-tpy, the lack of a 2-fold axis of symmetry, in contrast to Δ- and ΛRu-bpy, make 2 types of neighbor interaction possible: either the tpy ligands of two consecutive complexes are oriented towards the same strand (T_{SS}, see Fig. 10) or they are oriented towards opposite (alternating) strands (T_{AS}). In comparison to Ru-bpy, neglecting the influence of the single pyridine ring of Ru-tpy, the alternating model (T_{AS}) would have intermolecular contacts resembling alternating Δ–Δ and Λ–Λ contacts, while the same-side model (T_{SS}) would everywhere have intermolecular contacts resembling Δ–Λ, comparable to that found in a recent X-ray crystal structure of Δ- and Λ-Ru(phen)$_2$dppz simultaneously intercalated to a DNA hexamer duplex.[5e]

Since the same-side model T_{SS} has only one type of intermolecular contact (Δ–Λ), it is logically consistent with the simple one-geometry binding model, and also consistent with the assumption that Ru-bpy interactions model those of Ru-tpy, since 7.8, the square of the Ru-tpy y value of 2.8, is larger than the product 5.5 of the corresponding Δ–Δ and Λ–Λ y values for Ru-bpy. However, the values 7.8 and 5.5 are similar enough in magnitude to suggest that both T_{SS} and T_{AS} arrangements will be significant for Ru-tpy, even if the former arrangement with tpy ligands oriented towards the same strand will predominate. Our results indicating a relatively modest cooperativity factor (y = 2.8) for Ru-tpy appears to be in contrast to the case of Ru(phen)$_2$dppz^{2+}, for which a rather substantial Δ–Λ cooperativity can be inferred, since Cardin and coworkers report that the hexamer duplex used in their crystal structure study preferentially binds precisely one Δ- and one Λ-Ru(phen)$_2$dppz in solution.[5e]

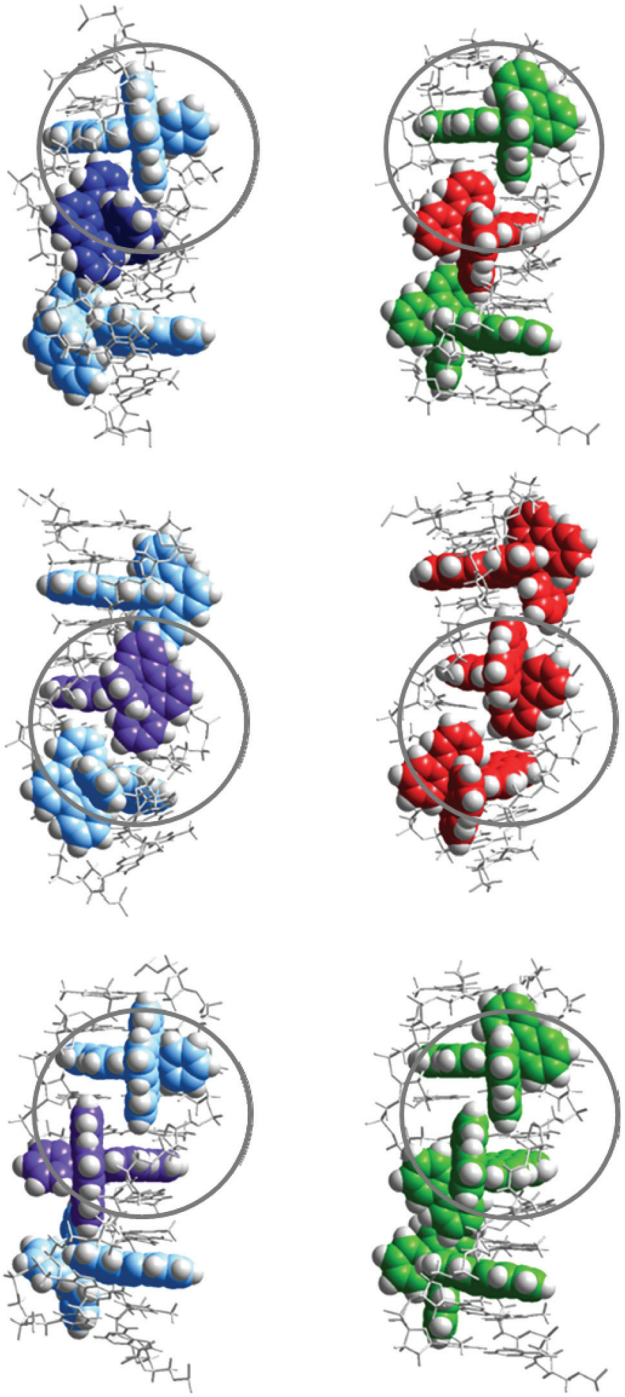

Fig. 10 Schematic illustration of the proposed interaction geometries for Ru-tpy (left) and the corresponding geometries of Δ- (green) and Λ- (red) Ru-bpy (right). Top row illustrates the "same-side" (T_{SS}) model while the middle and bottom row illustrate the "alternating side" (T_{AS}) model. Circles indicate similarities in intermolecular contacts. The models where constructed by manual docking and subsequent energy minimization in vacuum, using AMBER 2 force field in the HyperChem 8.0 software package (HyperCube, Inc.).

Experimental

Materials

All experiments were performed in aqueous solution (pH = 7.0) containing 150 mM NaCl and 1 mM cacodylate (dimethylarsinic acid sodium salt) except for the LD experiments where 10 mM NaCl was used (pH = 7.0). This was because a lower salt concentration gave a higher signal intensity without affecting the overall shape of the spectra. Stock solutions of calf thymus DNA (ctDNA) (~5 mM nucleotides) were prepared

by dissolving highly polymerized type I sodium salt calf thymus DNA (Sigma-Aldrich) in buffer. A stock solution of poly-(dAdT)$_2$ (AT-DNA) (~5 mM nucleotides) was prepared by dissolving the sodium salt (Sigma-Aldrich) in buffer. The solutions were filtered two times through a 0.7 μm polycarbonate filter. Stock solutions of the complexes (~1 mM) were prepared by dissolving the chloride salts in buffer. Concentrations were determined spectrophotometric using extinction coefficients: ε_{258} = 6600 M^{-1} cm^{-1} per nucleotide for ctDNA, ε_{260} = 6600 M^{-1} cm^{-1} per nucleotide for AT-DNA, ε_{371} = 16 900 M^{-1} cm^{-1} for Ru-tpy and ε_{444} = 16 100 M^{-1} cm^{-1} for Ru(bpy)$_2$dppz^{2+} (Ru-bpy). For ITC measurements the DNA solution was dialyzed against pure buffer for at least 48 hours at 8 °C. Ruthenium complex solutions of appropriate concentrations were prepared by dilution of the stock solutions in the dialysate. The dialysis membrane used had a molecular weight cut-off of 3.5–5 kDa (Spectra-Por® Float-A-Lyzer® G2, Sigma Aldrich).

Δ- and Λ-[Ru(bpy)$_2$dppz]Cl$_2$ used in this study were prepared as previously reported.[11a]

Other chemicals were purchased from Sigma-Aldrich and used without purification.

Synthesis of [Ru(tpy)(py)dppz]Cl$_2$

The synthetic route for preparation of [Ru(tpy)(py)dppz]Cl$_2$ is shown in Scheme 2. The procedure for preparation of Ru(tpy)-Cl$_3$ and [Ru(tpy)(dppz)Cl]Cl are in accordance to the methods previously reported by Zhou *et al.* and Leising *et al.*, respectively.[7a,14] [Ru(tpy)(dppz)(py)](PF$_6$)$_2$ was synthesized using the method previously described by Zhou *et al.* with some modifications. A portion of 0.0557 g of [Ru(tpy)(dppz)Cl]Cl and 0.0270 g of AgNO$_3$ were refluxed in 20 mL of ethanol–water (1 : 1) for 3 h under N$_2$(g). The solution was filtered after cooling and the filtrate was refluxed again under N$_2$ (g) for another 4 h, with 0.0101 g pyridine (py) added. The solution was left in a fridge over night for cooling. The next day the product was precipitated using KPF$_6$ dissolved in MilliQ water, left for a few hours, collected on a filter, and washed with ethanol–ether (1 : 2). Purification of [Ru(tpy)(dppz)(py)](PF$_6$)$_2$ was done using column chromatography with CH$_3$CN and neutral Al$_2$O$_3$. The eluate containing the pure orange product was collected leaving a dark purple residue layer on top of the column.

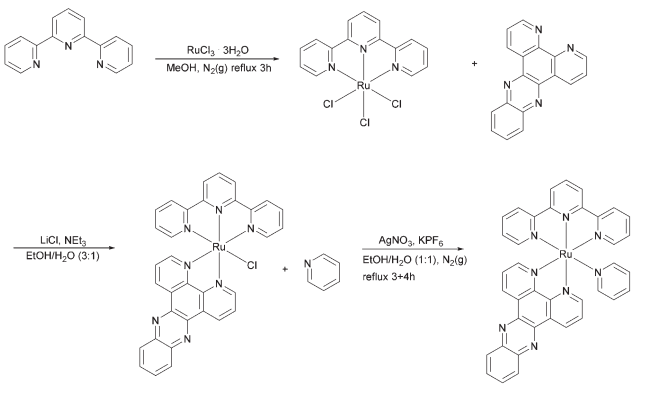

Scheme 2 Synthesis of Ru-tpy.

To replace the hexafluorophosphate anion with chloride, the CH$_3$CN solution of [Ru(tpy)(dppz)(py)](PF$_6$)$_2$ was reduced to ~1 mL evaporating with a stream of N$_2$ under mild heating, where after 0.5 g of ([CH$_3$(CH$_2$)$_3$]$_4$NCl), dissolved in 1 mL of acetone, was added in increasing portions while stirring until the solution was only weakly yellow and the precipitation complete. The product was collected by a sintered glass filter and washed first with acetone and then with diethyl ether to yield [Ru(tpy)(dppz)(py)]Cl$_2$ as a brown powder (36%, calculated from the starting material, Ru(tpy)Cl$_3$). UV/vis (in water; λ_{max} in nm, $\varepsilon/10^3$ M^{-1} cm^{-1} enclosed in parenthesis): 475(12.1), 372(16.9), 310(45.4), 275(69.2). ^{1}H NMR (as PF$_6$ salt, 400 MHz, acetone-d_6): δ 10.03 (dd, J = 8.2, 1.3 Hz, 1H), 9.56–9.52 (m, 1H), 9.48 (dd, J = 5.4, 1.4 Hz, 1H), 8.94 (t, J = 8.0 Hz, 2H), 8.84–8.71 (m, 2H), 8.59–8.42 (m, 4H), 8.26–8.11 (m, 9H), 8.04–7.94 (m, 2H), 7.76 (ddd, J = 8.2, 5.5, 0.8 Hz, 1H), 7.49–7.42 (m, 3H). The ^{1}H NMR spectrum of Ru-tpy (see Fig. S8 in ESI†) was in accordance with previous results by Zhou *et al.* (2009)[7a] and showed no significant impurities.

Spectroscopy

Absorption spectra were measured on a Varian Cary 4000 UV/vis spectrophotometer (path length = 1 cm). The reverse absorption titration spectra for Ru-tpy were measured with a constant concentration of 5 μM Ru-tpy in buffer. The stock solution of AT-DNA (with 5 μM of Ru-tpy to avoid dilution) added directly in the cuvette (path length = 1 cm) in aliquots up to a concentration of 80 μM nucleotides.

Linear dichroism spectra (LD) were measured on a Chirascan LD spectropolarimeter on samples oriented in an outer-rotating Couette flow cell with a 1 mm path length at a rate of 1000 rpm. The spectra of the same samples were recorded without rotation for baseline contribution and were subsequently subtracted from the LD spectra. The concentration of ctDNA used in the measurements was 266 μM nucleotides and mixed with complex solution with appropriate concentration to obtain desired [Ru]/[base pairs] ratios. Circular dichroism (CD) spectra were recorded on a Chirascan CD spectropolarimeter similarly as the absorption spectra. Five CD spectra were averaged for each sample. To be consistent with the absorption and ITC measurements, AT-DNA was used for the CD measurements (~138 μM nucleotides).

Calorimetric data was obtained using an ITC200 isothermal titration calorimeter (Microcal) controlled by Origin 7.0 software. The ruthenium complexes (~600 μM) were loaded in a syringe (40 μL) and titrated in 2 μl aliquots into 206 μl of AT-DNA in 150 mM NaCl aqueous solution (~340 μM nucleotides). By integrating the power required to maintain the reference and sample cells at the same temperature it is possible to obtain a direct measurement of the heat generated or absorbed when complex and DNA interact. The experimental raw data consists of a series of heat flow peaks, and each peak

corresponds to one injection of complex. These heat flow spikes are integrated with respect to time, which gives the total heat exchanged per mole injectant, plotted against the ratio [Ru]/[base pairs]. The primary ITC data was corrected for the heat of ligand dilution by subtracting the average heat per injection of complex titrated into buffer. There was negligible heat arising from DNA dilution. The experiments were performed at 20 °C, 25 °C and 30 °C.

^{1}H NMR spectrum of [Ru(tpy)(py)dppz](PF$_6$)$_2$ in acetone-d_6 was recorded on an Agilent 400 MHz spectrophotometer.

Theory and methods

Analysis of LD spectra

The isotropic absorption spectrum A_{iso} of a sample can be considered as a simple sum of component spectral envelopes e_i, each such envelope itself being a collecting all electronic transitions with a common polarisation direction relative to the molecular coordinate system:

$$A_{iso} = \sum_i e_i \quad (1)$$

Then, the linear dichroism spectrum LD will be a weighted sum of the same component spectral envelopes:

$$LD = \sum_i w_i e_i \quad (2)$$

there for an effectively uniaxial oriented system (*e.g.* DNA oriented by the shear flow in a Couette cell) the weights w_i are determined by the orientation of the polarization direction characteristic for the electronic transition dipole moments of e_i relative to the macroscopic orientation axis of the system:

$$w_i = \gamma \frac{3}{2} S(3\cos^2\theta_i - 1) \quad 0 \le S \le 1 \quad (3)$$

where γ is the ratio of the optical path-length of the LD to the absorption measurement, θ_i is the angle between the transition dipole moment direction of envelope e_i and the orientation axis of the molecular system (in our case the DNA helix axis), and the orientation factor S describes the degree of alignment of the molecular system orientation axis relative to the macroscopic orientation axis, with S = 0 for an unoriented and S = 1 for a perfectly aligned sample.

The reduced linear dichroism LD^r value at a certain wavelength is defined as the ratio of the linear dichroism value over the isotropic absorbance value:

$$LD^r = \frac{LD}{A_{iso}} \quad (4)$$

In wavelength regions where a single component spectral envelope e_i dominates the absorption spectrum, the LD^r curve will be essentially constant and take the value w_i, *e.g.* as observed around the 260 nm band of B-DNA. Since θ for the in-plane polarized $\pi\rightarrow\pi^*$ nucleobase transitions here is close to 90°, the orientation factor S_0 for ligand-free DNA can readily be calculated from the LD^r value.

$$LD^r_{260} = w = -\gamma \frac{3}{2} S_0 \quad (5)$$

However, in most cases, and in particular for 3D-chromophores like ruthenium polypyridyl complexes, component spectral envelopes overlap substantially over the whole range of the spectrum, and the LD^r curve will vary strongly with wavelength. Deconvolution of the experimental A_{iso} and LD spectra into component envelopes, and thereby determining the weights w_i, can in favorable cases be accomplished by the TEM-method.[5a,15] For a system with two component envelope spectra, having distinct characteristic absorption band features and distinct weights, the TEM-method in matrix notation can be formulated as the solution of the combined eqn (1) and (2):

$$[\mathbf{a} \quad \mathbf{b}] \begin{bmatrix} 1 & w_1 \\ 1 & w_2 \end{bmatrix}^{-1} = [\mathbf{e}_1 \quad \mathbf{e}_2] \quad (6)$$

where **a**, **b**, $\mathbf{e_1}$ and $\mathbf{e_2}$ are column vectors corresponding to the isotropic absorption, linear dichroism and the two component envelope spectra, respectively. The variables w_1 and w_2 in eqn (6) are varied until, as determined by visual inspection, the characteristic features of component $\mathbf{e_2}$ have vanished in component $\mathbf{e_1}$ and *vice versa*.

The orientation factor S is required for the angular orientation to be determined from the weights w_i. For a dye that (a) is strongly bound to DNA; (b) has significant absorption at wavelengths >300 nm (where the DNA is transparent); and (c) has, within a certain range of [dye]/[DNA] ratios, invariant binding geometry and invariant absorption spectrum; S can readily be obtained as follows:

Let two LD spectra with different [dye]/[DNA] ratios (within the invariant range) be column vectors $\mathbf{L_1}$ and $\mathbf{L_2}$, and $\mathbf{L_0}$ be the LD spectrum of a sample with DNA only. Then, if condition (c) is fulfilled, the three columns are linearly dependent, thus scalars α and β can be found so that $\alpha\mathbf{L_1} + \beta\mathbf{L_2} = \mathbf{L_0}$; in matrix notation:

$$\mathbf{Mx} = \mathbf{L_0} \quad (7)$$

where $\mathbf{M} = [\mathbf{L_1}\ \mathbf{L_2}]$ and $\mathbf{x} = [\alpha; \beta]$. Solving eqn (7) by a least square projection gives α and β:

$$(\mathbf{M^T M})^{-1}\mathbf{M^T L_0} = \mathbf{x} \quad (8)$$

When condition (a) is fulfilled, practically all added dye can be considered to be bound; and with the DNA concentration being equal in the three samples, the vectors can be written as:

$$\mathbf{L_0} = \gamma S_0 \mathbf{d} \quad \mathbf{L_1} = \gamma S_1(\mathbf{d} + c_1\mathbf{b}) \quad \mathbf{L_2} = \gamma S_2(\mathbf{d} + c_2\mathbf{b}) \quad (9)$$

where (with γ = 1), **d** is the LD spectrum at perfect orientation of DNA only, **b** is the LD spectrum at perfect orientation of bound dye at unit concentration, and c_1 and c_2 are

the two known total dye concentrations. Since condition (b) assures that **d** is zero and **b** is non-zero for wavelengths > 300 nm, the following two equations are obtained by inserting eqn (9) in (7):

$$\alpha S_1 + \beta S_2 = S_0 \quad c_1\alpha S_1 + c_2\beta S_2 = 0 \tag{10}$$

Since γS_0 can be evaluated from eqn (5), S_1 and S_2 can be obtained from known quantities after solving the two equations in (10):

$$S_1 = \frac{S_0 c_2}{\alpha(c_2 - c_1)} \quad S_2 = \frac{S_0 c_1}{\beta(c_2 - c_1)} \tag{11}$$

Analysis of binding isotherms

Although global fitting of calorimetric and excited state lifetime data for Δ- and Λ-Ru-bpy and their 1,10-phenanthroline analogues required a fairly complicated binding model comprising a symmetrical and a pair of unsymmetrical intercalation geometries (Model 3), fits to calorimetric data only were found to be satisfactory with a model with a single binding geometry.[10] This model, the classical McGhee–von Hippel single ligand cooperative binding model was used also in this work, and involves three adjustable parameters: the thermodynamic binding constant K, the binding site coverage parameter n and the cooperativity factor y.[16] Given values of these three parameters (assumed to be constant in the small temperature range used here), and total concentrations of binding sites $[B]_{tot}$ (*i.e.* base pairs) and DNA-ligand $[L]_{tot}$ (*i.e.* ruthenium complex) for each step of the titration, the mass-balance equations were solved iteratively with a Newton–Raphson procedure, to give consistent binding densities θ and free ligand concentrations $[L]_{free}$, as well as the conditional probabilities p_{ij}, as previously described.[10,17]

Calorimetric titration

The ITC data obtained at a certain temperature was assumed to be composed of three components:

$$\mathrm{ITC}(i) = (\Delta H^\circ_b)\Delta\mathbf{b}(i) + (\Delta H^\circ_{nn})\Delta\mathbf{nn}(i) + \Delta H_{baseline} \tag{12}$$

where ΔH°_b is the standard binding enthalpy change, ΔH°_{nn} is the standard nearest neighbor interaction enthalpy change and $\Delta H_{baseline}$ is a small constant value. For titration data point i, the change in concentration of bound ligand $\Delta\mathbf{b}(i)$ is calculated as $[B]_{tot}(i)[\theta(i) - \theta(i-1)]$ and the change in concentration of nearest neighbors $\Delta\mathbf{nn}(i)$ is calculated as $[B]_{tot}(i)[\theta(i)p_{22}(i) - \theta(i-1)p_{22}(i-1)]$, where p_{22} is the conditional probability that a bound ligand is followed by another bound ligand on the DNA lattice. The ΔH values were determined by projecting the matrix with the ITC data as columns, one for each temperature, on the space spanned by the **Δb**, **Δnn** and a constant vector. The simulated ITC curves were then calculated with eqn (12) and the goodness-of-fit determined as the Euclidian norm of the difference between the measured and simulated data matrices.

Spectroscopic titration

The absorption spectra were arranged in data matrix **M** as columns with w elements corresponding to the wavelengths recorded; the columns corresponding to the t titration steps. Singular value decomposition, using the *svd* command in the MATLAB software, factorized the data matrix into two matrices of orthonormal columns **U** and **V**, and a diagonal matrix **S** with the singular values $s_1 \geq s_2 \geq s_3 \cdots \geq 0$ along the diagonal. Keeping only the m singular values that are significantly larger than zero make it possible to simplify the factorization:

$$\mathbf{M} = \mathbf{USV}^\mathbf{T} = \underline{\boldsymbol{USV}}^\mathbf{T} + \mathbf{N} \tag{13}$$

where $\boldsymbol{S}$ is the upper m by m submatrix of **S**; $\underline{\boldsymbol{U}}$ and $\underline{\boldsymbol{V}}$ are the first m columns of **U** and **V**, respectively, and **N** is a matrix of small elements, ideally corresponding only to the noise in the measurements. Assuming thus that the titration involves m different absorbing species, with absorption spectra in w by m matrix **A** and concentrations in t by m matrix **C**, the factorization can now be written as

$$\mathbf{M} - \mathbf{N} = \underline{\boldsymbol{USV}}^\mathbf{T} = \mathbf{AC}^\mathbf{T} = \underline{\boldsymbol{U}}[\mathbf{RR}^{-1}]\underline{\boldsymbol{SV}}^\mathbf{T} = [\underline{\boldsymbol{U}}\mathbf{R}][\mathbf{R}^{-1}\underline{\boldsymbol{SV}}^\mathbf{T}] \tag{14}$$

where **R** is a non-singular m by m matrix. Since $\mathbf{A} = \underline{\boldsymbol{U}}\mathbf{R}$ and $\mathbf{C} = \underline{\boldsymbol{VS}}(\mathbf{R}^{-1})^\mathbf{T}$, any theoretical binding model, which can calculate a matrix $\mathbf{C}_m$ of concentrations of m species, can be evaluated for consistency with the data by finding the **R** that is the least square projection of $\boldsymbol{VS}$ on the space spanned by $\mathbf{C}_m$:

$$\mathbf{R}^\mathbf{T} = (\mathbf{C}_m{}^\mathbf{T}\mathbf{C}_m)^{-1}\mathbf{C}_m{}^\mathbf{T}\underline{\boldsymbol{VS}} \tag{15}$$

By varying the adjustable parameters of the theoretical model, $\mathbf{C}_m$ is varied to minimize the norm of the residual $\underline{\boldsymbol{VS}} - \mathbf{C}_m\mathbf{R}^\mathbf{T}$ while keeping the specie spectra in $\mathbf{A} = \underline{\boldsymbol{U}}\mathbf{R}$ physically reasonable (non-negative in the case of absorption spectra). In the present case, the concentration matrix $\mathbf{C}_m$ was constructed with three columns corresponding to free ligand, bound ligand with a neighboring free binding site, calculated as $[B]_{tot}\theta(1 - p_{22})$, and bound ligand adjacent to another bound ligand, calculated as $[B]_{tot}\theta p_{22}$.

Conclusion

The angular orientation of the dppz and tpy ligands as determined by LD and CD spectroscopies, strongly indicate that Ru-tpy binds from the minor groove by intercalating the dppz ligand between the base pairs, as has previously been determined for the isomeric complexes Δ- and ΛRu-bpy. The strong hypochromicity in the dppz absorption band is almost identical in magnitude to that of ΔRu-bpy, indicating that the alignment in the intercalation pocket is similar, too.

A simple cooperative binding model with one symmetrical binding geometry provide an excellent fit to data for calorimetric and absorption titrations of Ru-tpy into AT-DNA. The intrinsic intercalation has an equilibrium constant of 10^6 M^{-1}, close to that of Δ-Ru-bpy, and is associated with a small endothermic enthalpy change of +3 kJ M^{-1}. The cooperativity

factor is 2.8, and the associated neighbor interaction enthalpy is exothermic, −10.2 kJ M^{-1}; these values being in-between those of Δ- and Λ-Ru-bpy, and consistent with a slight preference of a one-sided arrangement of tpy-ligands of complexes consecutively bound to DNA.

Acknowledgements

The authors want to express their gratitude to Vetenskapsrådet (grant VR 2012-1661) and Chalmers Area of Advance Nano for funding, and COST Action CM1105 for providing a forum for stimulating discussions.

Notes and references

1 S. M. Cohen and S. J. Lippard, *Prog. Nucleic Acid Res. Mol. Biol.*, 2001, **67**, 93–130.
2 (*a*) J. K. Barton, A. T. Danishefsky and J. M. Goldberg, *J. Am. Chem. Soc.*, 1984, **106**, 2172–2176; (*b*) J. K. Barton, J. M. Goldberg, C. V. Kumar and N. J. Turro, *J. Am. Chem. Soc.*, 1986, **108**, 2081–2088.
3 (*a*) Y. Jenkins, A. E. Friedman, N. J. Turro and J. K. Barton, *Biochemistry*, 1992, **31**, 10809–10816; (*b*) C. Hiort, P. Lincoln and B. Nordén, *J. Am. Chem. Soc.*, 1993, **115**, 3448–3454; (*c*) A. E. Friedman, J. C. Chambron, J. P. Sauvage, N. J. Turro and J. K. Barton, *J. Am. Chem. Soc.*, 1990, **112**, 4960–4962.
4 C. G. Hartinger, S. Zorbas-Seifried, M. A. Jakupec, B. Kynast, H. Zorbast and B. K. Keppler, *J. Inorg. Biochem.*, 2006, **100**, 891–894.
5 (*a*) P. Lincoln, A. Broo and B. Nordén, *J. Am. Chem. Soc.*, 1996, **118**, 2644–2653; (*b*) R. Hartshorn and J. Barton, *J. Am. Chem. Soc.*, 1992, **114**, 5919–5925; (*c*) I. Haq, P. Lincoln, D. C. Suh, B. Nordén, B. Z. Chowdry and J. B. Chaires, *J. Am. Chem. Soc.*, 1995, **117**, 4788–4796; (*d*) H. Song, J. T. Kaiser and J. K. Barton, *Nat. Chem.*, 2012, **4**, 615–620; (*e*) J. P. Hall, D. Cook, S. R. Morte, P. McIntyre, K. Buchner, H. Beer, D. J. Cardin, J. A. Brazier, G. Winter, J. M. Kelly and C. J. Cardin, *J. Am. Chem. Soc.*, 2013, **135**, 12652–12659; (*f*) H. Niyazi, J. P. Hall, K. O'Sullivan, G. Winters, T. Sorenson, J. M. Kelly and C. J. Cardin, *Nat. Chem.*, 2012, **4**, 621–628.
6 (*a*) H. H. Thorp, *J. Inorg. Organomet. Polym.*, 1993, **3**, 41–57; (*b*) J. G. Goll and H. H. Thorp, *Inorg. Chim. Acta*, 1996, **242**, 219–223; (*c*) P. J. Carter, C. C. Cheng and H. H. Thorp, *J. Am. Chem. Soc.*, 1998, **120**, 632–642; (*d*) B. T. Farrer and H. H. Thorp, *Inorg. Chem.*, 2000, **39**, 44–49; (*e*) N. Grover, N. Gupta, P. Singh and H. H. Thorp, *Inorg. Chem.*, 1992, **31**, 2014–2020.
7 (*a*) Q. X. Zhou, F. Yang, W. H. Lei, J. R. Chen, C. Li, Y. J. Hou, X. C. Ai, J. P. Zhang, X. S. Wang and B. W. Zhang, *J. Phys. Chem. B*, 2009, **113**, 11521–11526; (*b*) D. Ossipov, S. Gohil and J. Chattopadhyaya, *J. Am. Chem. Soc.*, 2002, **124**, 13416–13433.
8 (*a*) M. Frasconi, Z. Liu, J. Lei, Y. Wu, E. Strekalova, D. Malin, M. W. Ambrogio, X. Chen, Y. Y. Botros, V. L. Cryns, J.-P. Sauvage and J. F. Stoddart, *J. Am. Chem. Soc.*, 2013, **135**, 11603–11613; (*b*) A. Bahreman, B. Limburg, M. A. Siegler, R. Koning, A. J. Koster and S. Bonnet, *Chem. – Eur. J.*, 2012, **18**, 10271–10280; (*c*) S. Bonnet, B. Limburg, J. D. Meeldijk, R. Gebbink and J. A. Killian, *J. Am. Chem. Soc.*, 2011, **133**, 252–261.
9 (*a*) K. K. Patel, E. A. Plummer, M. Darwish, A. Rodger and M. J. Hannon, *J. Inorg. Biochem.*, 2002, **91**, 220–229; (*b*) C. W. Jiang, H. Chao, H. Li and L. N. Ji, *J. Inorg. Biochem.*, 2003, **93**, 247–255; (*c*) H. Chao, W. J. Mei, Q. W. Huang and L. N. Ji, *J. Inorg. Biochem.*, 2002, **92**, 165–170.
10 J. Andersson, L. H. Fornander, M. Abrahamsson, E. Tuite, P. Nordell and P. Lincoln, *Inorg. Chem.*, 2013, **52**, 1151–1159.
11 (*a*) P. Lincoln and B. Nordén, *J. Phys. Chem. B*, 1998, **102**, 9583–9594; (*b*) S. Vasudevan, J. A. Smith, M. Wojdyla, A. DiTrapani, P. E. Kruger, T. McCabe, N. C. Fletcher, S. J. Quinn and J. M. Kelly, *Dalton Trans.*, 2010, **39**, 3990–3998; (*c*) T. Very, S. Despax, P. Hébraud, A. Monari and X. Assfeld, *Phys. Chem. Chem. Phys.*, 2012, **14**, 12496–12504.
12 (*a*) R. Siebert, F. Schlütter, A. Winter, M. Presselt, H. Görls, U. S. Schubert, B. Dietzek and J. Popp, *Cent. Eur. J. Chem.*, 2011, **9**, 990–999; (*b*) T. K. Aldridge, E. M. Stacy and D. R. McMillin, *Inorg. Chem.*, 1994, **33**, 722–727.
13 (*a*) R. Lyng, A. Rodger and B. Nordén, *Biopolymers*, 1991, **31**, 1709–1720; (*b*) R. Lyng, A. Rodger and B. Nordén, *Biopolymers*, 1992, **32**, 1201–1214.
14 R. A. Leising, S. A. Kubow, M. R. Churchill, L. A. Buttrey, J. W. Ziller and K. J. Takeuchi, *Inorg. Chem.*, 1990, **29**, 1306–1312.
15 J. Michl and E. Thulstrup, *Spectroscopy with Polarized Light*, VCH Publishers, New York, 1986, p. 120.
16 J. D. McGhee and P. H. V. Hippel, *J. Mol. Biol.*, 1974, **86**, 469–489.
17 P. Lincoln, *Chem. Phys. Lett.*, 1998, **288**, 647–656.

Electronic Supplementary Material (ESI) for Dalton Transactions.

Supplementary Information

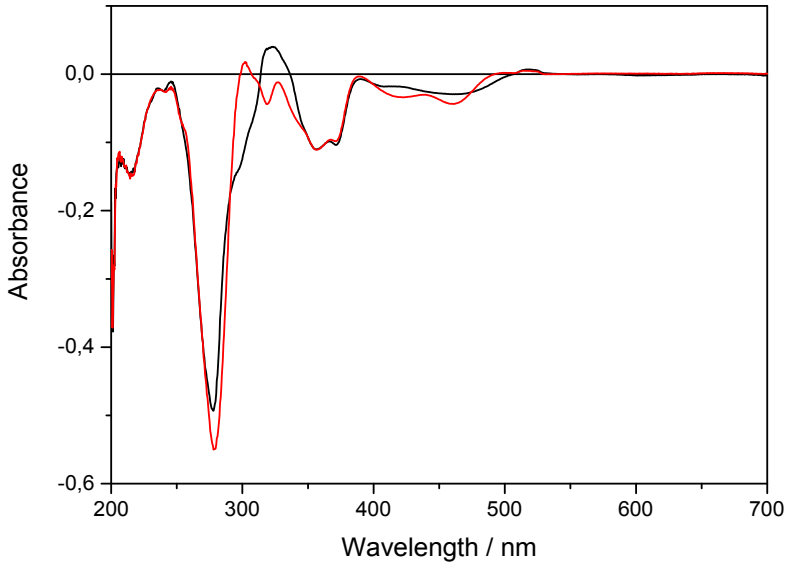

Fig. S 1 Difference spectrum (Ru_{bound} – (Ru_{free} + DNA)) of Ru-tpy (black) and ΔRu-bpy (red) in 150 mM NaCl solution at 25°C.

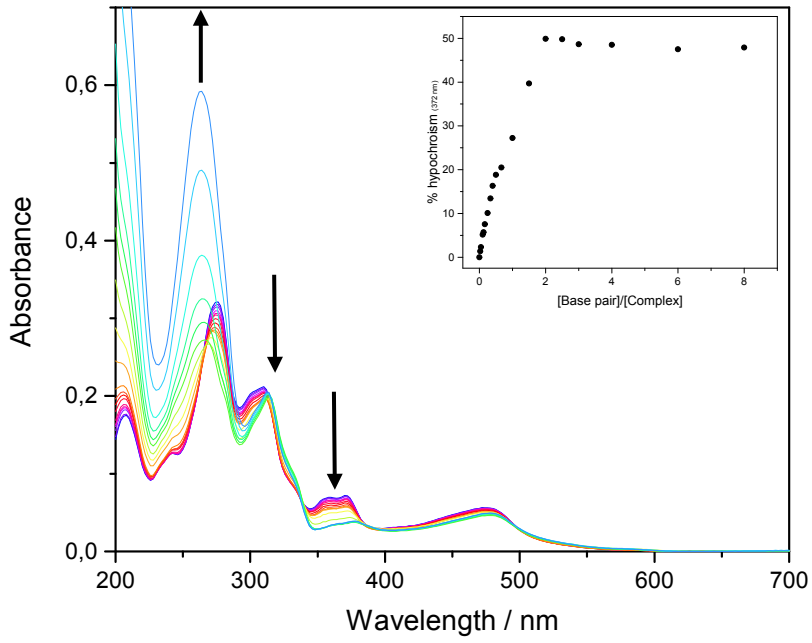

Fig. S 2 Reverse absorption spectral titration carried out for Ru-tpy (5 μM) by addition of AT-DNA in a 150 mM NaCl solution at 25°C. The spectra follows the addition of 0-8 [base pairs] / [Ru]. The arrows indicate the course of reaction as increasing amounts of AT-DNA is added to the solution. To avoid dilution equal amounts of 5 μM Ru-tpy was added simultaneously. The increasing hypochroism at 372 nm upon addition of AT-DNA is depicted in the inset of Fig. S 2.

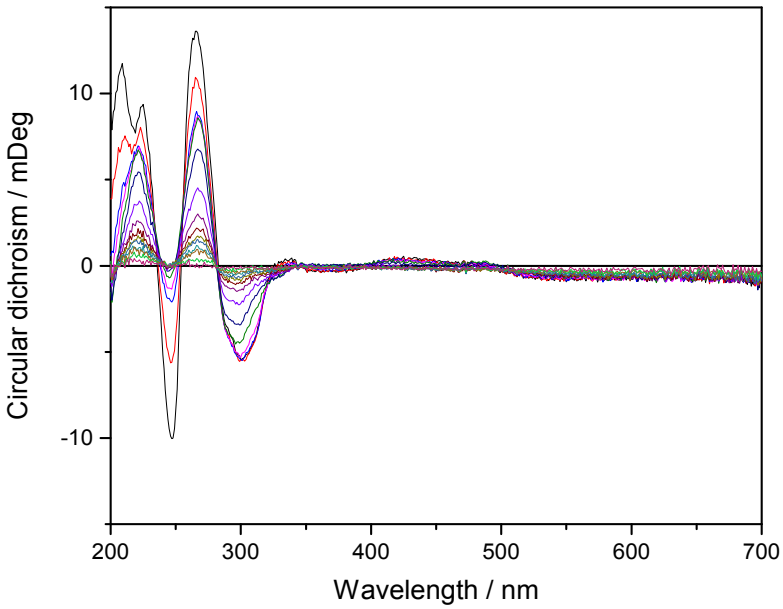

Fig. S 3 Reverse circular dichroism titration of Ru-tpy (5 μM) with AT-DNA in a 150 mM NaCl aqueous solution. The spectra follows the addition of 0-7 base pairs per complex.

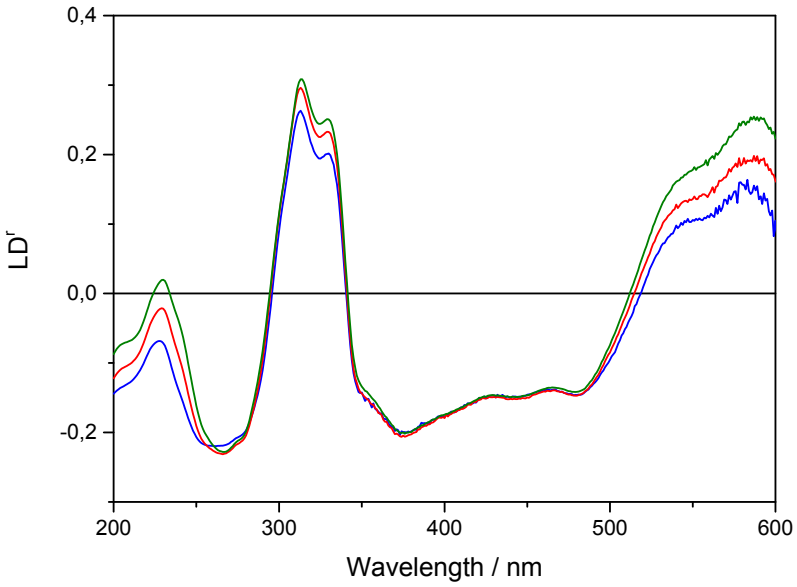

Fig. S 4 Reduced Linear dichroism spectra of Ru-tpy in the presence of ctDNA in a 150 mM NaCl aqueous solution at [base pairs] / [Ru] ratios of 8 (blue), 4 (red) and 2 (green) in 10 mM NaCl solution. The concentration of ctDNA is 270 μM nucleotides.

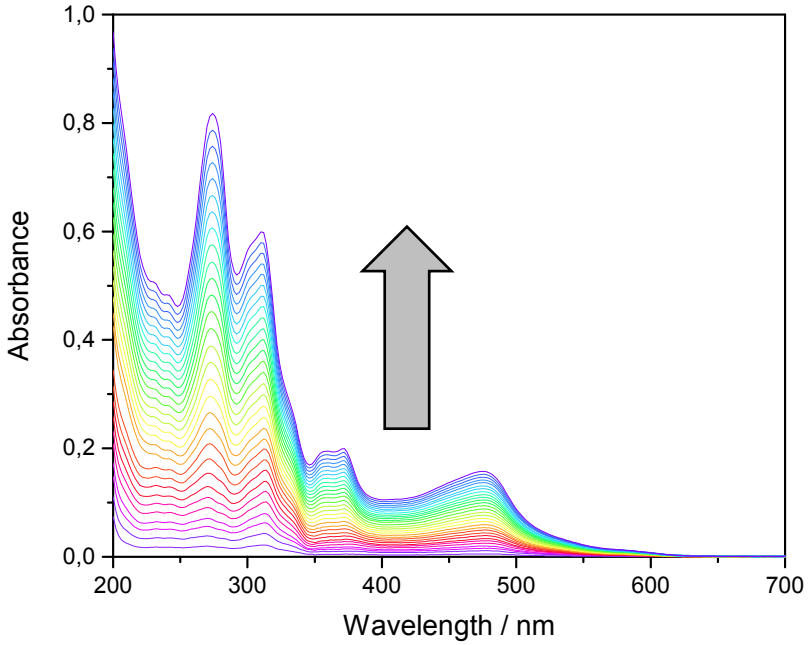

Fig. S 5 Absorption spectral titration carried out for AT-DNA (12 μM nucleotides) by addition of Ru-tpy in a 150 mM NaCl solution at 25°C. The spectra follows the addition of 0-2 [Ru] / [complex]. The arrow indicate the course of reaction as increasing amounts of Ru-tpy is added to the solution. To avoid dilution equal amounts of 12 μM AT-DNA was added simultaneously.

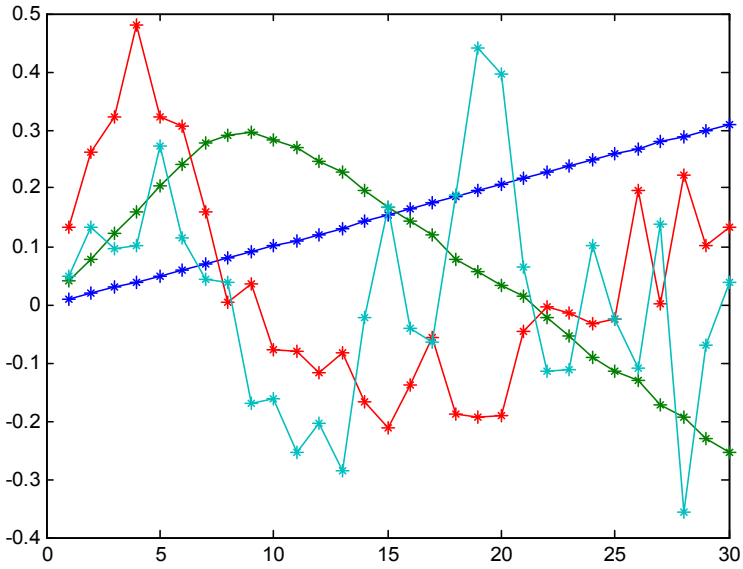

Fig. S 6 The first 4 columns of V plotted against row number. Blue: v1 (s1=100); green: v2 (s2=2.45); red: v3 (s3=0.23); light blue: v4 (s4=0.18).

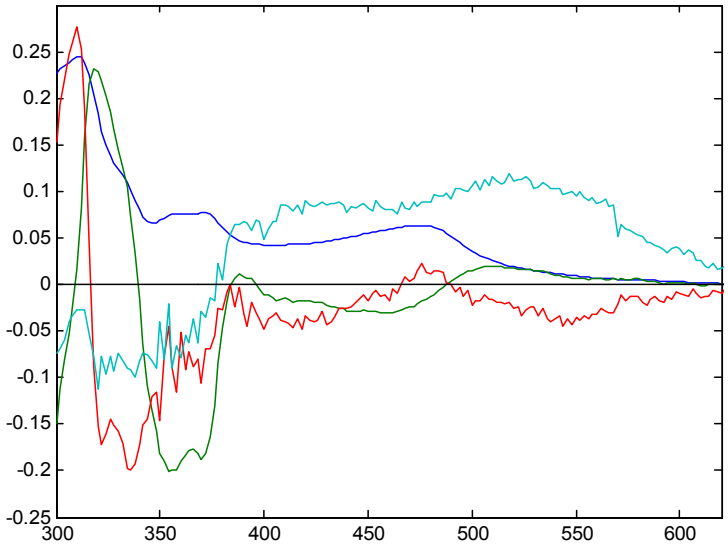

Fig. S 7 The first 4 columns of U plotted against wavelength. Blue: u1 (s1=100); green: u2 (s2=2.45); red: u3 (s3=0.23); light blue: u4 (s4=0.18)

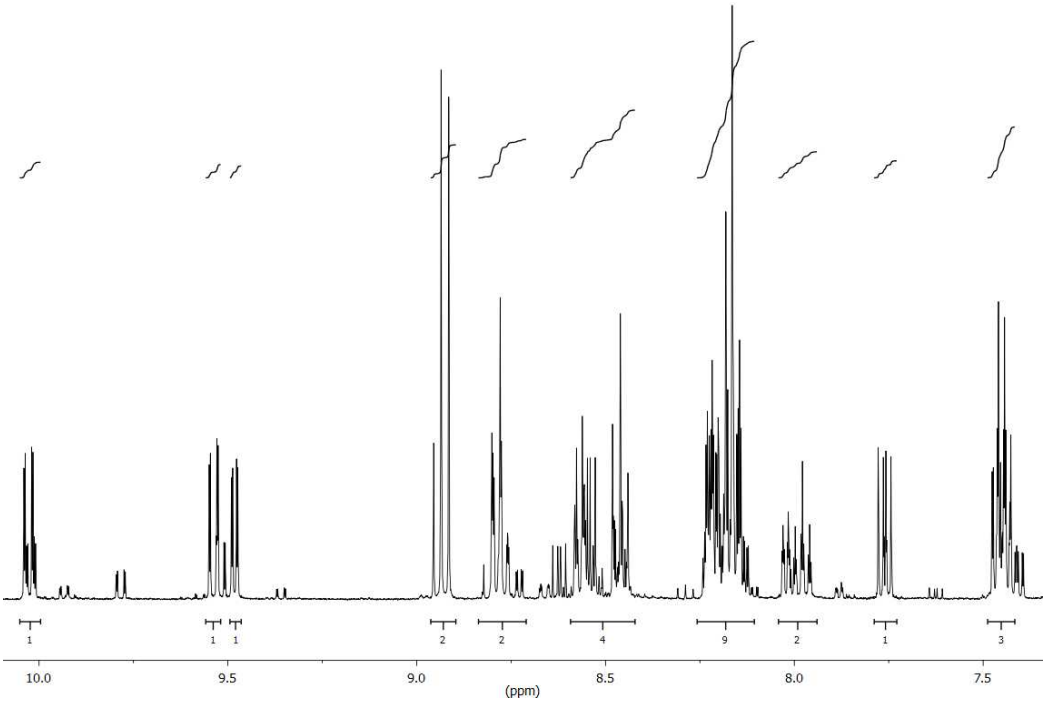

Fig. S 8 ^{1}H NMR spectrum of [Ru(tpy)(py)dppz]$(PF_6)_2$ dissolved in acetone-d_6.

Paper II

Volume 20 | Number 12 | 28 March 2018 | Pages 7899–8360

PCCP

Physical Chemistry Chemical Physics

rsc.li/pccp

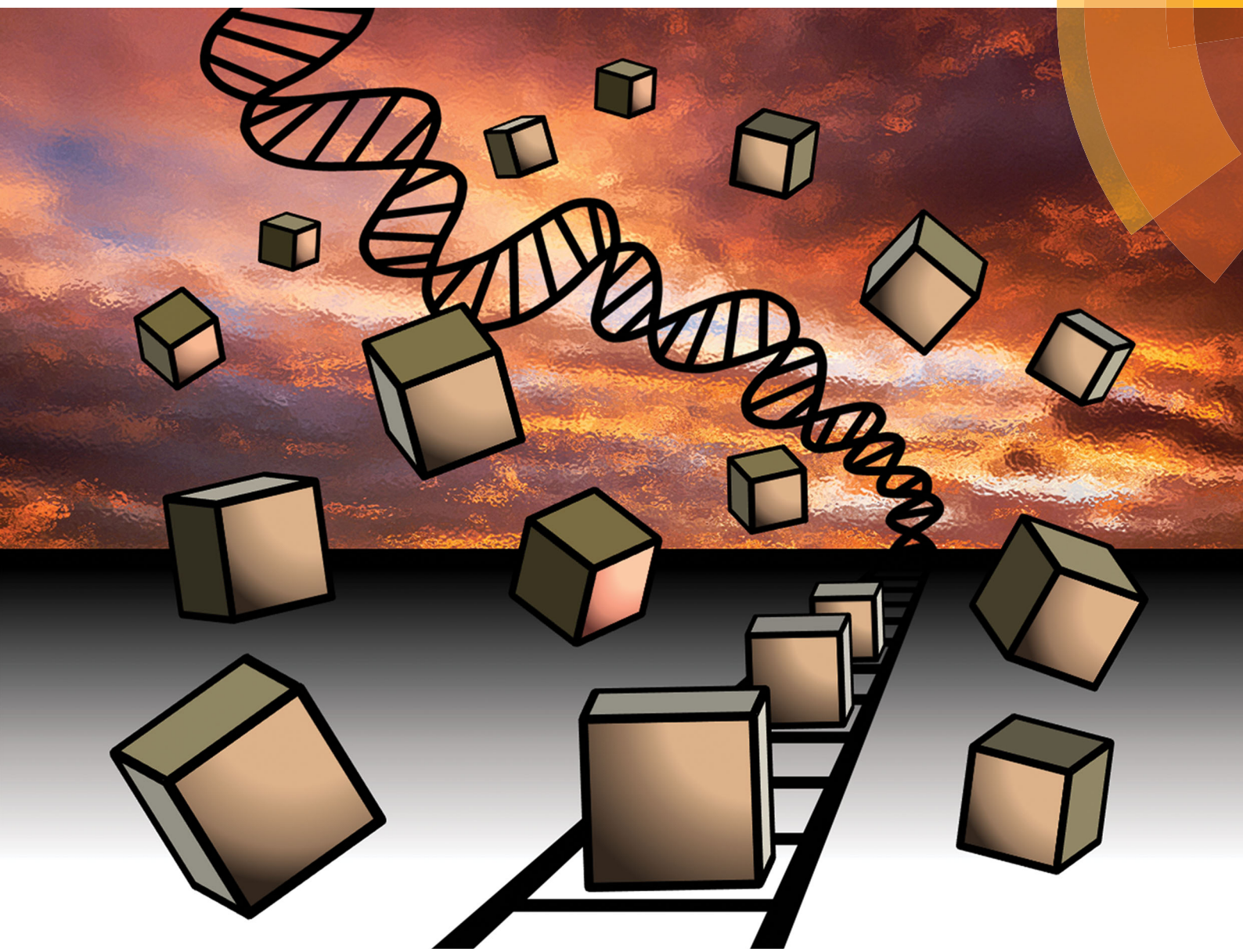

ISSN 1463-9076

ROYAL SOCIETY OF CHEMISTRY

PAPER

Anna K. F. Mårtensson and Per Lincoln

Competitive DNA binding of $Ru(bpy)_2dppz^{2+}$ enantiomers studied with isothermal titration calorimetry (ITC) using a direct and general binding isotherm algorithm

PCCP

PAPER

View Article Online
View Journal | View Issue

Cite this: *Phys. Chem. Chem. Phys.*, 2018, **20**, 7920

Competitive DNA binding of $Ru(bpy)_2dppz^{2+}$ enantiomers studied with isothermal titration calorimetry (ITC) using a direct and general binding isotherm algorithm†

Anna K. F. Mårtensson and Per Lincoln*

Received 13th May 2017,
Accepted 12th December 2017

DOI: 10.1039/c7cp03184j

rsc.li/pccp

While isothermal titration calorimetry (ITC) is widely used and sometimes referred to as the "gold standard" for quantitative measurements of biomolecular interactions, its usage has so far been limited to the analysis of the binding to isolated, non-cooperative binding sites. Studies on more complicated systems, where the binding sites interact, causing either cooperativity or anti-cooperativity between neighboring bound ligands, are rare, probably due to the complexity of the methods currently available. Here we have developed a simple algorithm not limited by the complexity of a binding system, meaning that it can be implemented by anyone, from analyzing systems of simple, isolated binding sites to complicated interactive multiple-site systems. We demonstrate here that even complicated competitive binding calorimetric isotherms can be properly analyzed, provided that ligand–ligand interactions are taken into account. As a practical example, the competitive binding interactions between the two enantiomers of $Ru(bpy)_2dppz^{2+}$ (Ru-bpy) and $poly(dAdT)_2$ (AT-DNA) are analyzed using our new algorithm, which provided an excellent global fit for the ITC experimental data.

Introduction

When studying the binding interactions between a ligand and a macromolecule, isothermal titration calorimetry (ITC) has many advantages. It is a powerful, high-precision tool that is often referred to as the "gold standard" for quantitative measurements of biomolecular interactions, and the only direct thermodynamic method that enables full thermodynamic characterization (stoichiometry, association constant, enthalpy and entropy of binding) of the interaction after a single titration experiment. However, the currently available analysis software is generally limited to the analysis of multiple binding systems with isolated (*i.e.* non-interactive) binding sites, and cannot adequately take into account cooperative or anti-cooperative interactions inherent in the binding of large ligands to DNA.[1]

In our previous ITC studies on ruthenium complexes intercalating into DNA, a generalized McGhee–von Hippel binding isotherm algorithm was utilized to account for binding site interactions.[2,3] However, the algorithm employed[4] in our earlier work involves two nested iterations: the inner iteration for solving the secular equations, the outer for solving the mass-balance equations. This algorithm has never got a wide-spread use, not unlikely due to its complexity and limited efficiency. Moreover, it is limited to describe interactions between 1 : 1 binding site : ligand equilibria.

Here we present a much improved and simplified algorithm, which iterates the mass balance equations directly with just 14 lines of the MATLAB code (see the ESI†). The new method is very general, and is no longer limited to just the nearest-neighbor interactions between bound ligands, since higher than 1 : 1 binding site : ligand equilibria can be treated just as easy. While this method can be utilized for modelling ligand binding to any type of linear biopolymers (such as actin, myosin or tubulin), we anticipate that the most frequent usage would be for studying the binding affinity of ligands to the closely spaced binding sites of DNA.

The intercalation ability of ligands to DNA is commonly determined by ethidium bromide displacement assays.[5–8] This method was scrutinized in a recent study, using ITC as an alternative non-label method.[9] However, the study focused on whether ethidium bromide displacement ability could automatically be interpreted as the intercalation potential of small molecules, not addressing the issue with ligand–ligand interactions. Most often, ITC experiments included in competitive binding studies are limited to the determination of thermodynamic parameters, ignoring ligand–ligand interactions. There are a few notable examples of ITC data analysis methods that are capable of adequately analysing more complex

Department of Chemistry and Chemical Engineering, Chalmers University of Technology, SE-41296 Gothenburg, Sweden. E-mail: lincoln@chalmers.se

† Electronic supplementary information (ESI) available. See DOI: 10.1039/c7cp03184j

ligand–macromolecule systems. One such example is the AFFINImeter software (S4SD), which is capable of the global fitting of non-standard binding models, such as competing ligands to a multiple site receptor. However, while several case studies are available exemplifying the resourcefulness of the method,[10] a binding system of a repetitive one-dimensional lattice of closely spaced binding sites (*e.g.* DNA) is not included. Perhaps for that reason, nearest-neighbor cooperativity is not addressed either. In addition, Buurma and Haq have developed a general software package, denoted IC-ITC, capable of analysing ITC data with a model including two independent binding sites and taking ligand self-aggregation into account.[11]

To exemplify the practical usage of our algorithm, we have conducted a series of competitive ITC experiments titrating enantiopure $Ru(bpy)_2dppz^{2+}$ (Ru-bpy; bpy = 2,2′-bipyridine; dppz = dipyrido[3,2-*a*:2′,3′-*c*]phenazine) into a solution of poly(dAdT)$_2$ (AT-DNA). Ru-bpy is an intercalating Ru(II) polypyridyl complex with a strong binding affinity to DNA (and a slight preference towards A–T base pairs). The complex has an octahedral coordination geometry resulting in two possible configurations, a right-handed (Δ) and a left-handed (Λ) propeller-like structure (Fig. 1).

It is well-established that it is the dppz moiety that intercalates between the base pairs of the DNA helix using both spectroscopic and biophysical methods as well as using X-ray crystallography.[12–20] However, while the intercalating properties of Ru(II) polypyridyl complexes are certainly important, it is becoming more and more apparent that the molecular structure of the ancillary ligands has a strong influence on the binding characteristics of a complex,[21–25] including complex–complex interactions.[2,3,26] It has often been neglected to take into account the cooperative and anti-cooperative behaviour of DNA-bound dppz-based Ru-centred structures when analysing the complex-DNA interactions.

Only recently have high-resolution structures and calorimetric studies emerged that have revealed nearest-neighbor interactions as a possible explanation to the complicated thermodynamic profiles of these complexes.[2,3,16–19,26,27] The non-classical ITC curves previously reported for $Ru(L)_2dppz^{2+}$ complexes (L = bpy or phen (phen = 1,10-phenanthroline)) have been attributed to an additional enthalpy contribution from neighboring complexes on the DNA as saturation of binding sites increases.[2,3] DNA, being a right-handed helical structure, would assumingly interact differently with the Δ and Λ-enantiomers of tri-bidentate complexes, and previous results obtained using calorimetry do indeed indicate the Δ-form of both Ru-bpy and Ru-phen to have a stronger binding affinity towards DNA.[2,14]

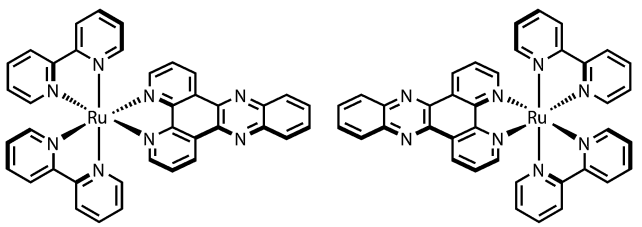

Fig. 1 Structures of Λ-(left) and Δ-$Ru(bpy)_2dppz^{2+}$ (right).

Analysis of a single enantiomer – DNA ITC titration with a simple neighbor interaction lattice model requires 3 binding parameters (the intrinsic binding constant K, the cooperativity parameter y_{aa} and n, the number of basepairs covered by the bound ligand) and two enthalpy parameters (the intrinsic binding enthalpy ΔH_a° and ligand–ligand interaction enthalpy ΔH_{aa}°), thus determining the thermodynamic characteristics of Δ- and ΛRu-bpy binding requires (6 + 4) fitting parameters.[3] By augmenting the dataset with two continued titrations, in which one enantiomer is titrated into DNA saturated with the opposite enantiomer, the consistency of the model can be scrutinized by performing a global analysis of all 4 titrations with only two additional fitting parameters (y_{ab} and ΔH_{ab}°).

Recently, Mikek *et al.* showed that the non-classical ITC curves, which arise upon titration of a 25-bp DNA oligomer duplex with ruthenium dppz complexes, can be excellently fitted with a two independent site binding model with 4 binding parameters (K_1, K_2, f_1 and f_2) and 2 enthalpy parameters (ΔH_1° and ΔH_2°) per titration.[28] Since the binding site fractions f_1 and f_2 were found to be reasonably similar for both enantiomers, one could envisage that a global analysis with the two independent site model on the augmented data set could provide an alternative interpretation to the lattice based models.

Our previous ITC studies on binding of $Ru(L)_2dppz^{2+}$ complexes to poly(dAdT)$_2$ have modeled the DNA as a homopolymer of identical intercalation pockets.[2,3] Crystallographic studies from the Cardin group have convincingly shown that the Λ-enantiomer of $Ru(L)_2dppz^{2+}$ type complexes strongly prefers 5′-TA-3′ to 5′-AT-3′.[17] Thus, it is further of considerable interest to investigate a more realistic binding model, in which the two alternating intercalation pockets of poly(dAdT)$_2$ are explicitly accounted for.

Experimental

Materials and sample preparation

All experiments were performed in an aqueous buffer solution (pH = 7.0) containing 150 mM NaCl and 1 mM cacodylate (dimethylarsinic acid sodium salt). A stock solution of poly(dAdT)$_2$ (AT-DNA) ($\sim$5 mM nucleotides) was prepared by dissolving the sodium salt (Sigma-Aldrich) in buffer. Stock solutions of the complexes ($\sim$1 mM) were prepared by dissolving the chloride salts in buffer. Concentrations were determined spectrophotometrically using extinction coefficients: ε_{260} = 6600 M^{-1} cm^{-1} per nucleotide for AT-DNA, and ε_{444} = 16 100 M^{-1} cm^{-1} for $Ru(bpy)_2dppz^{2+}$. For ITC measurements the DNA solution was dialyzed against pure buffer for at least 48 hours at 8 °C. Ruthenium complex solutions of appropriate concentrations were prepared by dilution of the stock solutions in the dialysate. The dialysis membrane used had a molecular weight cut-off of 3.5–5 kDa (Spectra-Por® Float-A-Lyzer® G2, Sigma-Aldrich).

Enantiopure Δ- and Λ-$[Ru(bpy)_2dppz]Cl_2$ used in this study were prepared as previously reported.[20]

Other chemicals were purchased from Sigma-Aldrich and used without purification.

Absorption spectra were measured on a Varian Cary 4000 UV/vis spectrophotometer (path length = 1 cm).

Isothermal titration calorimetry

Isothermal titration calorimetry (ITC) is a high-precision tool where the heat produced or absorbed upon addition of the complex to a DNA solution enables direct assessment of the binding free energy by integrating the power required to maintain the reference and sample cells at the same temperature. The experimental raw data consist of a series of heat flow peaks, and each peak corresponds to one injection of complex. These heat flow spikes are integrated with respect to time, which gives the total heat exchanged per mole injectant plotted against the ratio [Ru]/[base pairs].

Calorimetric data were obtained using an ITC200 isothermal titration calorimeter (Microcal) controlled by Origin 7.0 software. The ITC profiles of the Δ and Λ enantiomers of Ru-bpy were obtained by a single injection of 1 μl followed by 19 sequential titrations in 2 μl aliquot injections of complex from a syringe stock solution (~470 μM) into the sample cell (206 μl) loaded with AT-DNA in 150 mM NaCl aqueous solution (~300 μM nucleotides). This was subsequently followed by an additional 20 sequential additions (single injection of 1 μl followed by 19 injections of 2 μl aliquots) of the opposite enantiomer into the sample cell now loaded with AT-DNA saturated by the first complex. All ITC experiments were performed at 25 °C. The injection spacing was 180 s, the syringe rotation was 750 rpm, and there was an initial delay of 120 s prior to the first injection. The concentration ranges used for the complex and DNA were set to span mixing ratios of [Ru]/[base pairs] from 0.08 to 0.6 for the first titration and from 0.7 to 1.4 for the second titration. The primary ITC data were corrected for the heat of complex dilution by subtracting the average heat per injection of the complex titrated into buffer. There was negligible heat arising from DNA dilution. The raw ITC data peaks were automatically integrated using the Origin 7.0 software. For improved accuracy of the integration, the integration range for each heat peak was narrowed to include ~2/3 of the original range, thus reducing the background noise from the baseline.

Results

Derivation of the general binding isotherm algorithm

The problem of modelling binding equilibria between a set of ligands and an infinite one-dimensional lattice of identical binding site units is advantageously treated with the statistical thermodynamics of linear hetero-polymers, which can conveniently be cast into matrix equations. The binding site unit itself can be defined to consist of one or several polymer subunits, and may provide one or several distinct ligand binding sites. The mathematical equivalence between the partition function and Markov chain formalisms have been demonstrated earlier,[4] and although we here will use a variant of the elegant formulation by Chen of the ligand binding problem using the former formalism,[29] the derivation uses the probabilistic Markov chain approach, implicit in the classical paper by McGhee and von Hippel.[30]

In the most general case, at equilibrium with L different ligands A ($A = 1,\ldots L$), the initial homo-polymer of bare binding-site units has been converted into a hetero-polymer with $N + 1$ different types of elementary units i ($i = 0, 1\ldots N$), where the unit 0 is the bare binding site unit, and the other N elementary units i are composed of n_i consecutive binding site units and $\sum_A m_{iA}$ ligands. We denote n_i the length, and m_{iA} the stoichiometric coefficient with respect to the ligand A, of the elementary unit i. At equilibrium, each elementary unit is further characterized by its binding density θ_i and its binding potential x_i. The probability that a randomly chosen binding site unit is in the elementary unit i is given by $n_i\theta_i$, and the binding densities thus give the total concentration of the bound ligand A:

$$A_{\text{bound}} = B_0 \sum_{i=1} m_{iA}\theta_i \tag{1}$$

where B_0 is the total concentration of binding site units.

The binding potential is a function of the intrinsic binding constant K_i (the equilibrium constant for the formation of elementary unit i from free ligands and n_i consecutive bare binding site units in the absence of interactions with neighbor units) and the free ligand concentrations A_{free}:

$$x_i = K_i \Pi_A A_{\text{free}}^{m_{iA}} \tag{2}$$

the binding potential for unit 0 being defined as unity, $x_0 = 1$.

The interactions between neighboring elementary units are given by a set of non-negative cooperativity constants y_{ij} that are elements of the cooperativity matrix $\mathbf{Y} = [y_{ij}]$, $i,j = 0, 1,\ldots N$. The product of the cooperativity constant y_{ij} and the intrinsic binding constants K_i and K_j gives the equilibrium constant K_{ij} for formation of the two consecutive units i and j from free ligands and $n_i + n_j$ consecutive bare binding sites in the absence of other neighbor interactions:

$$K_{ij} = K_i K_j y_{ij} \tag{3}$$

$y_{ij} > 1$ indicates a favorable (cooperative), $y_{ij} < 1$ an unfavorable (anti-cooperative) and $y_{ij} = 1$ no interaction between units i and j. The interaction between two bare binding sites is always non-cooperative by definition, hence $y_{00} \equiv 1$, and in most cases, all cooperativity parameters involving a bare binding site unit, y_{0i} and y_{i0}, are set to 1. In some binding models zero elements, $y_{ij} = 0$, are used to exclude certain sequences of elementary units; however, to provide a physically meaningful model, $\mathbf{Y} \geq 0$ must be a primitive nonnegative matrix, *i.e.* there is a power of $\mathbf{Y}$ which is positive: $\mathbf{Y}^{\mathbf{p}} > 0$ for some $p \geq 1$.[31]

Defining matrix $\mathbf{M} = [m_{iA}]$ and column vectors $\mathbf{x} = [x_i]$, $\boldsymbol{\theta} = [\theta_i]$, $\mathbf{k} = [K_i]$, $\mathbf{c_f} = [A_{\text{free}}]$ and $\mathbf{c_b} = [A_{\text{bound}}]$ ($i = 1,\ldots N$; $A = 1,\ldots L$), eqn (1) and (2) can be expressed in matrix notation:

$$\mathbf{c_b} = B_0 \mathbf{M}^{\mathbf{T}} \boldsymbol{\theta} \tag{4}$$

$$\mathbf{x} = \exp[\ln(\mathbf{k}) + \mathbf{M}\ln(\mathbf{c_f})] \tag{5}$$

where the superscript $^{\mathbf{T}}$ denotes matrix transposition; and ln and exp denote elementwise operation of the natural logarithm and exponential functions, respectively.

Given that an N by N non-singular transformation matrix $\mathbf{T}$ can be constructed such that the product $\mathbf{TM}$ has only 0 and 1 as elements, with exactly one 1 in each row but no zero columns; N mass balance equations can be set up:

$$\mathbf{TMc}_0 = \exp(\mathbf{T}[\ln(\mathbf{x}) - \ln(\mathbf{k})]) + B_0\mathbf{TMM}^{\mathbf{T}}\boldsymbol{\theta} \quad (6)$$

where $\mathbf{c_0} = [A_{\text{total}}]$ is a column vector with the total concentrations of the L ligands as elements.

In order to solve eqn (6), the relation between $\mathbf{x}$, $\boldsymbol{\theta}$ and $\mathbf{Y}$ has to be made explicit. Given any positive N vector $\mathbf{r}$, $\mathbf{Y}$ can be transformed into a stochastic matrix $\mathbf{P}$ with the constant row sum of 1:

$$\mathbf{P} = D(\mathbf{s})\mathbf{Y}D([1; \mathbf{r}]) \quad (7)$$

where $D(\mathbf{s})$ denotes a diagonal matrix which has the elements of vector $\mathbf{s}$ along the diagonal and is zero elsewhere. The elements s_i of the $N + 1$ vector $\mathbf{s}$ normalize each row sum to unity:

$$s_i = (y_{i0} + \mathbf{y}_i^{\mathbf{T}}\mathbf{r})^{-1}, \quad i = 0, 1, \ldots N \quad (8)$$

where $\mathbf{y}_i^{\mathbf{T}}$ is the $(i + 1)$th row of $\mathbf{Y}$, except for the first element y_{i0}. Thus

$$p_{ij} = s_i y_{ij} r_j \quad (9)$$

and the element p_{ij} of $\mathbf{P}$ gives the conditional probability that the elementary unit i is followed by the elementary unit j.

Following the probabilistic approach of McGhee and von Hippel, the binding potential x_i can, in the absence of neighbor interactions, be equated to the quotient between the probability of finding the elementary unit i, preceded by the elementary unit a and followed by the unit b, and the probability of finding a and b enclosing n_i consecutive bare binding site units:

$$x_i = \frac{p_{ai}p_{ib}}{p_{a0}p_{00}^{n_i-1}p_{0b}} \quad (10)$$

McGhee and von Hippel use eqn (10) and take a and b as the bare binding site units with $y_{0i} = y_{i0} = 1$, in which case $x_i = p_{ai}p_{ib}/p_{00}^{n_i+1}$. For the general case, inserting $p_{ij} = s_i y_{ij} r_j$, in eqn (10) and using that $y_{00} = r_0 = 1$, gives

$$\begin{aligned} x_i &= \frac{(s_a y_{ai} r_i)(s_i y_{ib} r_b)}{(s_a y_{a0} r_0)(s_0 y_{00} r_0)^{n_i-1}(s_0 y_{0b} r_b)} \\ &= s_i r_i s_0^{-n_i}\left(\frac{y_{ai}y_{ib}}{y_{a0}y_{0b}}\right) \end{aligned} \quad (11)$$

The binding potential x_i is defined from the equilibrium for the formation of elementary unit i from free ligands and n_i consecutive bare binding site units in the hypothetical absence of interactions with neighbor units. Thus, the factor involving the cooperativity parameters on the right side of eqn (11) can be set to 1 to give

$$x_i = s_i r_i s_0^{-n_i} \quad (12)$$

As long as $\mathbf{Y}$ is primitive, eqn (12) is valid whatever value taken by the cooperativity parameters involving the elementary unit i. When $\mathbf{Y}$ is primitive, $\mathbf{P}$ will be as well since $\mathbf{r} > 0$. The theorem of Frobenius states that a primitive non-negative square matrix has only one strictly positive right-hand eigenvector, and that the corresponding dominant eigenvalue is a simple root of the characteristic equation, equal to the spectral radius of the matrix and exceeds all the other eigenvalues in modulus.[31]

For any primitive stochastic matrix, the constant $N + 1$ vector $\mathbf{e} = [1]$ is the right-hand eigenvector corresponding to the dominant eigenvalue 1:

$$\mathbf{Pe} = \mathbf{e} \quad (13)$$

Let the left-hand eigenvector corresponding to the dominant eigenvalue 1 be the positive row vector $\mathbf{f}^{\mathbf{T}}$, thus

$$\mathbf{f}^{\mathbf{T}}\mathbf{P} = \mathbf{f}^{\mathbf{T}} \quad (14)$$

When normalized so that $\mathbf{f}^{\mathbf{T}}\mathbf{e} = 1$, $\mathbf{f}$ gives the limiting probabilities of the Markov chain defined by $\mathbf{P}$; *i.e.* for an infinitely long heteropolymer, f_i is the absolute probability that an elementary unit picked at random is the elementary unit i. However, elementary units may be of different lengths n_i, and it is convenient to normalize $\mathbf{f}$ with respect to the length of each unit:

$$\mathbf{f}^{\mathbf{T}}[1; \mathbf{n}] = 1 \quad (15)$$

When $\mathbf{f}$ is so normalized, the first element, $f_0 = 1 - \boldsymbol{\theta}^{\mathbf{T}}\mathbf{n}$, will be the absolute probability that a lattice subunit picked at random is a bare binding site unit, and the other N elements in $\mathbf{f}$ will be the binding densities θ_i, thus

$$\mathbf{f}^{\mathbf{T}} = [(1 - \boldsymbol{\theta}^{\mathbf{T}}\mathbf{n})\ \boldsymbol{\theta}^{\mathbf{T}}] \quad (16)$$

Let $\mathbf{P}$ be partitioned as

$$\mathbf{P} = \begin{bmatrix} \mathbf{p}_{00} & \mathbf{p}_{01}^{\mathbf{T}} \\ \mathbf{p}_{10} & \mathbf{P}_{11} \end{bmatrix} \quad (17)$$

Insertion of eqn (16) and (17) in (14) gives $[(1 - \boldsymbol{\theta}^{\mathbf{T}}\mathbf{n})\mathbf{p}_{01}^{\mathbf{T}} + \boldsymbol{\theta}^{\mathbf{T}}\mathbf{P}_{11}]$ $= \boldsymbol{\theta}^{\mathbf{T}}$, which can be solved for $\boldsymbol{\theta}^{\mathbf{T}}$:

$$\boldsymbol{\theta}^{\mathbf{T}} = \mathbf{P}_{01}^{\mathbf{T}}\mathbf{V}^{-1}, \quad \mathbf{V} = (\mathbf{I} + \mathbf{np}_{01}^{\mathbf{T}} - \mathbf{P}_{11}) \quad (18)$$

where $\mathbf{I}$ is the identity matrix. Matrix $\mathbf{V}$ in eqn (18) can never become singular, since the spectral radius of any submatrix of a primitive, and thus irreducible, non-negative matrix is strictly smaller than that of the full matrix, hence the eigenvalues of $\mathbf{P_{11}}$ will all be less than 1.

Given cooperativity parameters in matrix $\mathbf{Y}$ and elementary unit lengths in column vector $\mathbf{n}$, the vectors of binding potentials $\mathbf{x}$ and binding densities $\boldsymbol{\theta}$ are thus functions of an N-vector $\mathbf{r} > 0$ through eqn (7), (8), (12) and (18). Given intrinsic binding constants $\mathbf{k}$, stoichiometric coefficients $\mathbf{M}$, total ligand concentrations $\mathbf{c}_0$ and total binding site concentration B_0, the mass balance eqn (6) can be rearranged to

$$\mathbf{q} = \exp(\mathbf{T}[\ln(\mathbf{x}) - \ln(\mathbf{k})]) + \mathbf{TM}\ (B_0\mathbf{M}^{\mathbf{T}}\boldsymbol{\theta} - \mathbf{c}_0) \quad (19)$$

where the mass balance error in N-vector $\mathbf{q}$ is a function of $\mathbf{r}$. The norm of the mass balance error $\mathbf{q}$ is conveniently minimized by iterating with the Newton–Raphson method:

$$\mathbf{r}_{n+1} = \mathbf{r}_n - \left(\frac{\delta \mathbf{q}}{\delta \mathbf{r}}\right)^{-1} \mathbf{q} \tag{20}$$

where subscript n is the number of the iteration step and it is understood that $\mathbf{q}$ and its derivatives are evaluated at $\mathbf{r}_n$. By elementwise evaluation of the elements of $(\delta\mathbf{q}/\delta\mathbf{r})$ we find that the derivatives of $\mathbf{x}$ and $\boldsymbol{\theta}$ can be separated:

$$\left(\frac{\delta \mathbf{q}}{\delta \mathbf{r}}\right) = D(\mathbf{a})\mathbf{T}D(\mathbf{x})^{-1}\left(\frac{\delta \mathbf{x}}{\delta \mathbf{r}}\right) + B_0\mathbf{T}\mathbf{M}\mathbf{M}^{\mathbf{T}}\left(\frac{\delta \boldsymbol{\theta}}{\delta \mathbf{r}}\right) \tag{21}$$

where $\mathbf{a} = \exp(\mathbf{T}[\ln(\mathbf{x}) - \ln(\mathbf{k})])$. In the common case that $\mathbf{T} = \mathbf{I}$, *i.e.* every elementary unit (except the bare binding site unit) contains only one bound ligand, $\mathbf{a}$ reduces to $D(\mathbf{k})^{-1}\mathbf{x}$ and eqn (21) simplifies to

$$\left(\frac{\delta \mathbf{q}}{\delta \mathbf{r}}\right) = D(\mathbf{k})^{-1}\left(\frac{\delta \mathbf{x}}{\delta \mathbf{r}}\right) + B_0\mathbf{M}\mathbf{M}^{\mathbf{T}}\left(\frac{\delta \boldsymbol{\theta}}{\delta \mathbf{r}}\right) \tag{22}$$

The derivative of s_i with respect to r_k is readily obtained from eqn (8):

$$\frac{\delta s_i}{\delta r_k} = -s_i^2 y_{ik} = -s_i p_{ik} r_k^{-1} \tag{23}$$

Thus, from eqn (12)

$$\frac{\delta x_i}{\delta r_k} = \frac{\delta(s_i r_i s_0^{-n_i})}{\delta r_k} = -x_i p_{ik} r_k^{-1} + x_i r_k^{-1}\partial_{ik} + x_i n_i p_{0k} r_k^{-1} \tag{24}$$

where ∂_{ik} is 1 only when $i = k$ and zero otherwise. Assembling the matrix from the elements given by eqn (24) gives:

$$\left(\frac{\delta \mathbf{x}}{\delta \mathbf{r}}\right) = D(\mathbf{x})\mathbf{V}D(\mathbf{r})^{-1} \tag{25}$$

where $\mathbf{V}$ was defined in eqn (18). The derivatives of $\boldsymbol{\theta}^{\mathbf{T}}$ involve derivatives of submatrices of $\mathbf{P}$, and are thus best evaluated row-wise from eqn (18):

$$\begin{aligned}\left(\frac{\delta \boldsymbol{\theta}^{\mathrm{T}}}{\delta r_k}\right) &= \left(\frac{\delta \mathbf{p}_{01}{}^{\mathrm{T}}}{\delta r_k}\right)^{-1}\mathbf{V}^{-1} - \mathbf{p}_{01}^{\mathbf{T}}\mathbf{V}^{-1}\left(\frac{\delta \mathbf{V}}{\delta r_k}\right)\mathbf{V}^{-1} \\ &= \left[\left(\frac{\delta \mathbf{p}_{01}^{\mathbf{T}}}{\delta r_k}\right)^{-1} - \boldsymbol{\theta}^{\mathbf{T}}\left(\frac{\delta \mathbf{V}}{\delta r_k}\right)\right]\mathbf{V}^{-1}\end{aligned} \tag{26}$$

where the derivatives of $\mathbf{V}$ follow directly from the definition of $\mathbf{V}$ in eqn (18):

$$\left(\frac{\delta \mathbf{V}}{\delta r_k}\right) = -\mathbf{n}\left(\frac{\delta \mathbf{p}_{01}^{\mathbf{T}}}{\delta r_k}\right)^{-1} + \left(\frac{\delta \mathbf{P}_{11}}{\delta r_k}\right) \tag{27}$$

Insertion of eqn (27) in (26) gives:

$$\begin{aligned}\left(\frac{\delta \boldsymbol{\theta}^{\mathbf{T}}}{\delta r_k}\right) &= \left[(1 - \boldsymbol{\theta}^{\mathbf{T}}\mathbf{n})\left(\frac{\delta \mathbf{p}_{01}^{\mathbf{T}}}{\delta r_k}\right)^{-1} + \boldsymbol{\theta}^{\mathbf{T}}\left(\frac{\delta \mathbf{P}_{11}}{\delta r_k}\right)\right]\mathbf{V}^{-1} \\ &= \mathbf{f}^{\mathbf{T}}\left(\frac{\delta \mathbf{P}_1}{\delta r_k}\right)\mathbf{V}^{-1}\end{aligned} \tag{28}$$

where the left-hand eigenvector $\mathbf{f}^{\mathbf{T}}$ is given by eqn (16) and $\mathbf{P_1}$ is the rectangular submatrix obtained from $\mathbf{P}$ by omitting the first column. The derivative of p_{ij} with respect to r_k is

$$\begin{aligned}\frac{\delta p_{ij}}{\delta r_k} &= \frac{\delta\left(s_i y_{ij} r_j\right)}{\delta r_k} = s_i y_{ij}\partial_{jk} - s_i p_{ik} y_{ij} r_j r_k^{-1} \\ &= \left(p_{ik}\partial_{jk} - p_{ik}p_{ij}\right) r_k^{-1}\end{aligned} \tag{29}$$

Insertion of eqn (29) in $\mathbf{f}^{\mathbf{T}}(\delta\mathbf{P}_1/\delta r_k)$ gives

$$\begin{aligned}\mathbf{f}^{\mathbf{T}}\left(\frac{\delta \mathbf{P}_1}{\delta r_k}\right) &= r_k^{-1}\left(\sum_i f_i p_{ik}\partial_{jk} - \sum_i p_{ik} f_i p_{ij}\right) \\ &= r_k^{-1}\left(\theta_k\partial_{jk} - \mathbf{p}_{\mathbf{k}}^{\mathbf{T}} D(\mathbf{f})\mathbf{P}_1\right)\end{aligned} \tag{30}$$

where f_i is the ith element of $\mathbf{f}$ $(i = 0, 1, \ldots N)$, $\mathbf{p_k}$ is the kth column of $\mathbf{P_1}$ $(k = 1, \ldots N)$ and thus $\sum_i f_i p_{ik} = \mathbf{f}^{\mathbf{T}}\mathbf{p}_{\mathbf{k}} = \theta_k$. Assembling the rows of eqn (30) into a matrix and transposing gives with eqn (28):

$$\left(\frac{\delta \boldsymbol{\theta}}{\delta \mathbf{r}}\right) = \left(\mathbf{V}^{\mathbf{T}}\right)^{-1}\mathbf{U}D(\mathbf{r})^{-1}, \quad \mathbf{U} = \left[D(\boldsymbol{\theta}) - \mathbf{P}_1^{\mathbf{T}} D(\mathbf{f})\mathbf{P}_1\right] \tag{31}$$

Insertion of eqn (25) and (31) in eqn (21) completes the iterative step for solution of the mass balance in eqn (19). In the ESI,† the code is given for the MATLAB program *GeneralAlgorithm* which solves the mass-balance for a single titration point using eqn (21). The code is also given for a series of programs *ITCalgorithmModelX* which show examples of how the *GeneralAlgorithm* can easily be implemented for global analysis of ITC titration data with various binding models. In addition, the code is given for the program *ITCalgorithmIndependent* which implements analysis using a model with 2 independent binding sites.

Isothermal titration calorimetry and model fitting

Fig. 2 shows raw ITC data of titration of AT-DNA with the enantiomers *Δ*Ru-bpy and *Λ*Ru-bpy. To the left, the ligand is titrated into AT-DNA only. In accordance with our previous results, further injections with the same enantiomer (not shown) gave only very small, constant heat values, indicating full saturation of the DNA.[2,3] However, when proceeding the titration by injecting the opposite enantiomer (Fig. 2, right) substantial enthalpy changes are observed, indicating that both enantiomers can displace each other on the DNA.

In the global fitting of these ITC isotherms, a data point i in the ITC isotherm is assumed to be a sum of intrinsic and neighbor interaction binding enthalpies:

$$\mathrm{ITC}(i) = \sum_a \left(\Delta H_a^{\circ}\right)\Delta a(i) + \sum_{ab} \Delta H_{ab}^{\circ}\Delta ab(i) + \Delta H_{\mathrm{baseline}} \tag{32}$$

where ΔH_a° is the standard enthalpy change for the formation of elementary unit a from free ligands and binding sites in the absence of interactions with neighbor units and ΔH_{ab}° is the standard enthalpy change of the interaction between neighbor elementary units a and b. $\Delta H_{\mathrm{baseline}}$ is a small constant, and is an approximation for various enthalpy contributions not

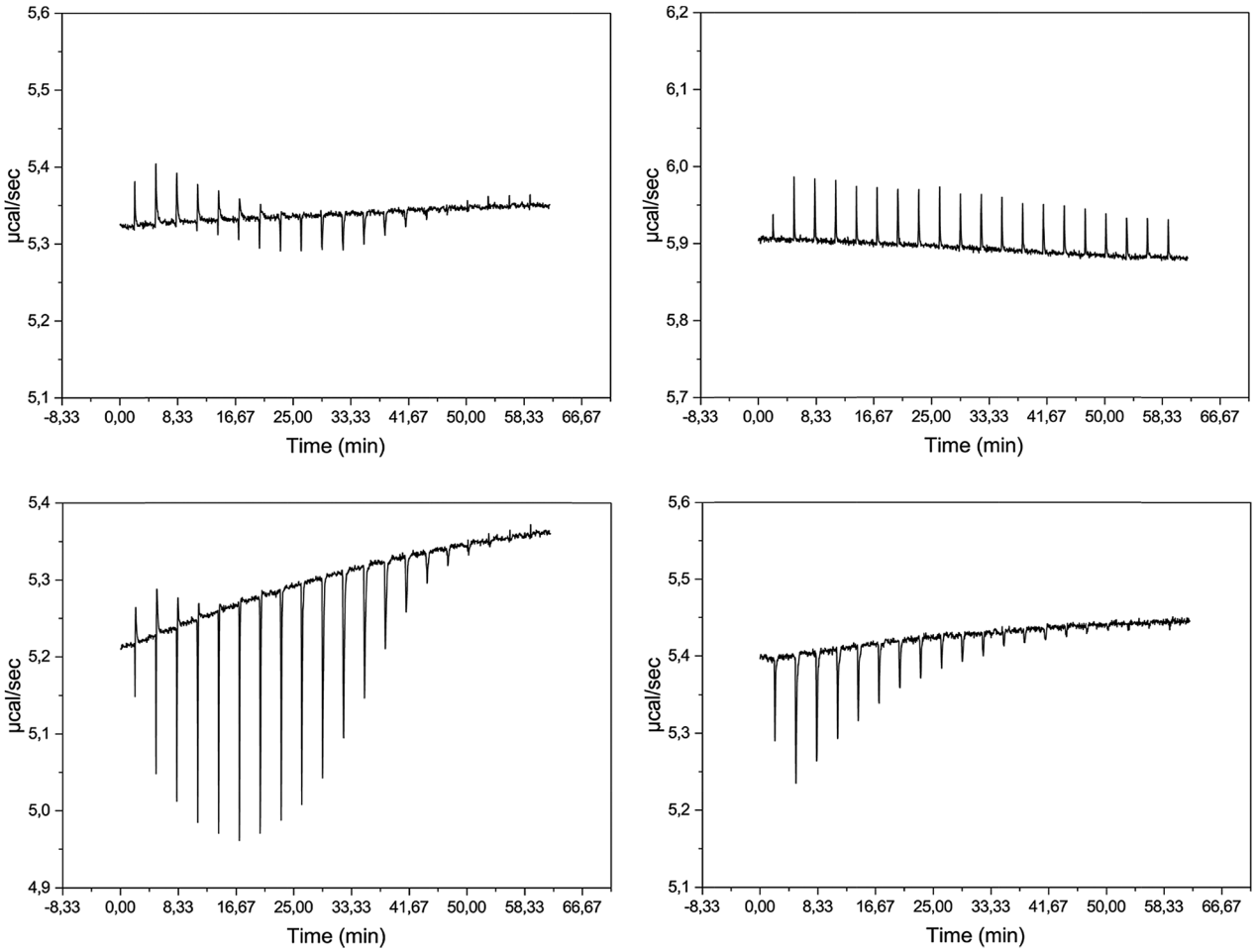

Fig. 2 ITC raw data for binding of the Δ and Λ enantiomers of Ru-bpy to AT-DNA alone (Δ: top left; Λ: bottom left) followed by a second titration of the opposite enantiomer to already complex-saturated AT-DNA (Δ into Λ-saturated DNA: top right; Λ into Δ-saturated DNA: bottom right) in 150 mM NaCl aqueous solution at 25 °C. Complex (~470 μM) was injected in 2 μl aliquots to the 206 μl cell containing the DNA (~300 μM nucleotides). For improved accuracy of the integration details the integration range was narrowed to ~2/3 of the original range.

included in the model and not corrected for by the subtraction of the heat of dilution. Examples of such possible contributions could be the different environment in the counter-ion distribution around the DNA compared to in buffer or weak association of the ruthenium complex cations with the saturated, but still negatively charged DNA.

For the titration data point i, $\Delta a(i)$, the change in the concentration (per mole of the injected ligand) of the elementary unit a from the preceding point $i-1$, is calculated as $B_0(i)\theta_a(i) - d_f B_0(i-1)\theta_a(i-1)$, and the change in concentration (per mole of injected ligand) of nearest-neighbors $\Delta ab(i)$ is calculated as $B_0(i)\theta_a(i)p_{ab}(i) - d_f B_0(i-1)\theta_a(i-1)p_{ab}(i-1)$, where, at data point i, $B_0(i)$ is the total concentration of binding site units divided with the mole amount of the injected ligand, and $p_{ab}(i)$ is the conditional probability that ligand a is directly followed by ligand b on the DNA lattice. The dilution factor d_f is calculated as $1 - V_{add}/V_{cell}$. The ΔH° values were determined by a least-square projection of the column matrix with all the ITC data on the space spanned by the **Δb** and **Δab** columns, and 4 constant columns corresponding to the 4 baselines. The elements of the constant columns were 1 for the corresponding titration and zero elsewhere. The simulated ITC curves were then calculated with eqn (32) and the RMSD goodness-of-fit determined as the Euclidian norm of the difference between the measured and simulated data matrices, divided by the square root of the number of data points (here 76). To facilitate comparison with other ITC studies, we here report nRMSD values, *i.e.* RMSD normalized by division with the mean of the absolute values of the data (the mean value being 3.316 kJ per mol injectant for this data set). The MATLAB program *ITCalgorithmModelX* (as shown in the ESI†) performs this calculation, and was used with the non-linear optimization MATLAB routine *fminsearch* to find the parameter values for the best global fit to the experimental ITC data.

We have considered 5 models, which are schematically depicted as lattice models in Fig. 3. Models 1–3 consider both intrinsic (ΔH_a°) and neighbor interaction (ΔH_{ab}°) reaction enthalpies. Model 1 is the classical model, which takes the lattice subunit to be one base pair and thus assumes all intercalation pockets on the DNA to be equal. The binding site

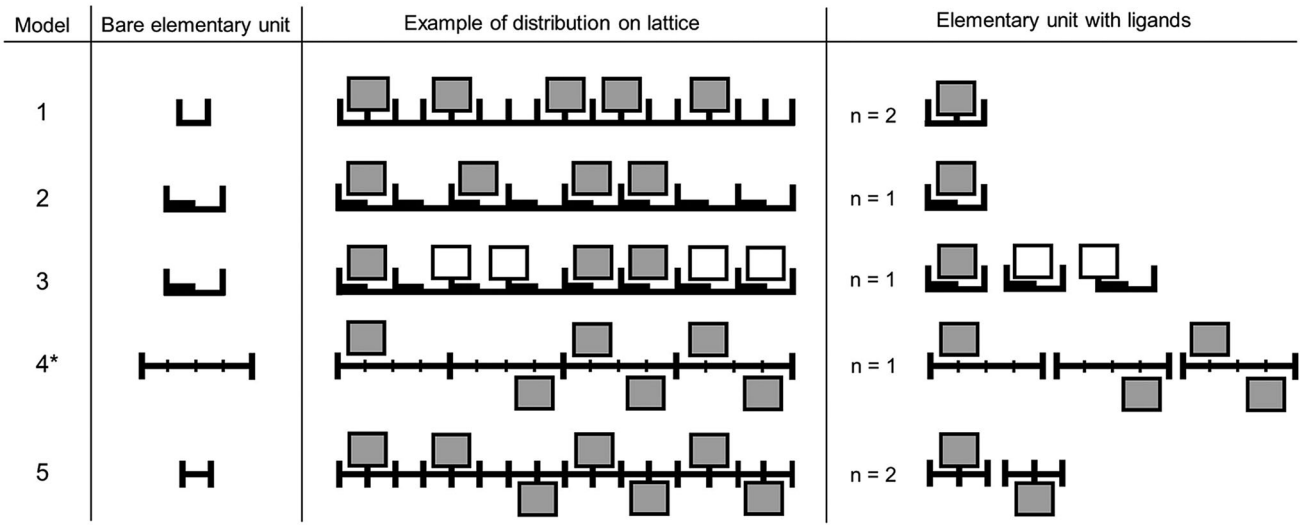

Fig. 3 Schematic illustration summarizing the 5 proposed lattice models of the DNA-ligand binding interactions.

coverage vector $\boldsymbol{n}$ is allowed to vary in the fit, but is expected to take a value close to 2, *i.e.* nearest-neighbor exclusion, as observed for binding of most intercalators to DNA. Models 2 and 3 take the lattice subunit to be 2 base pairs (and $\boldsymbol{n}$ close to 1); in model 2 the subunit is assumed to bind Δ or Λ only in one way, modelling a strict TA (or AT) selectivity for both enantiomers. In model 3, this selectivity is relaxed for Δ which is assumed to be able to bind in either of the intercalation pockets 1 or 2 of the lattice subunit, while Λ only binds in pocket 1. Nearest-neighbor exclusion is followed since Λ1 or Δ1 cannot be directly followed by Δ2 (see Fig. 3). Models 4 and 5 assume two binding modes for each enantiomer, and consider only intrinsic reaction enthalpies $\left(\Delta H_a^\circ\right)$. In model 4, the two binding modes are modelled as two independent binding sites, for which the fraction of the total concentration of base pairs is a freely adjustable parameter, *i.e.* no lattice model is involved. It is possible to construct a mathematically equivalent lattice model in the case the fractions of the two binding sites have the same value, as shown for model 4* in Fig. 3. The lattice subunit contains here 4 base pairs, all y_{ij} = 1, and a third type of elementary unit with two bound ligands is required, for which the intrinsic binding constant $K_3 = K_1K_2$. Model 4* gives numerically identical results to model 4 with only one value of the fraction parameter, but relaxing the independence of the two binding sites (by allowing the intrinsic binding constant of each of the 8 elementary units to vary independently) did only marginally improve the bad global fit. Although the location of the bound ligand(s) within the lattice subunit is arbitrary, Fig. 3 indicates a possible physical interpretation, where the two distinct sites of model 4* are assigned to intercalation from minor and major groove, respectively. Thus, model 4* can be interpreted as only permitting alternating minor and major groove intercalation for consecutive sequences of bound ligands. To simplify this idea, in model 5 two binding modes are defined, which must alternate in consecutive sequences, which hence only interact ($y_{ij} \neq 1$) for different mode neighbors. The best fit of this model was obtained when the lattice subunit was defined to be one base pair, as depicted in Fig. 3.

For each of the models, the number of fitting parameters (binding parameters, and for model 3 also the number of enthalpy parameters) was also gradually reduced from the full model by symmetry considerations or by assuming non-cooperativity. An overview of the goodness-of-fit of the different models is given in Fig. 4, which plots the relative RMSD of calculated and experimental ITC-data against the total number of fitting parameters. If non-cooperative binding is assumed for models 1–3 and 5 (all non-zero y_{ij} are set to 1), the RMSD increases by a factor of 2–5 compared to the best fit, as seen to the left in Fig. 4. While the non-interacting site model 4 makes a descent fit (nRMSD = 3.50%) when the fractions of site 1 and site 2 are allowed to have different values in all four different titrations (to the right in Fig. 4), restraining the 8 fractions of

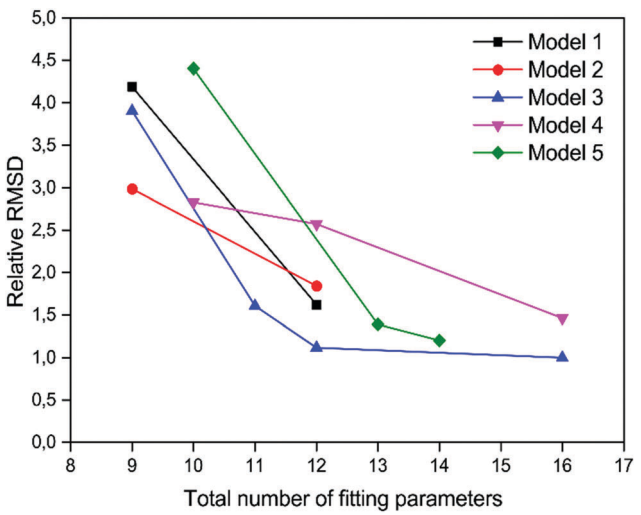

Fig. 4 Relative RMSD plotted against the total number of fitting parameters comparing the goodness-of-fit for all 5 models.

the global fit to take fewer different values makes the RMSD increase by a factor of about 2 (see Fig. S1 in the ESI†). On the other hand, for model 3 (total number of fitting parameters 9 + 7 = 16), which gives the lowest RMSD of all the models investigated here (nRMSD = 2.45%), the RMSD is only slightly increased (15%) if the binding and enthalpy parameters of Δ are constrained to be the same for the two base pair steps (total number of fitting parameters 7 + 5 = 12). Furthermore, for (7 + 5) parameter models 1–3, the best fit value of the $y\Delta\Delta$ cooperativity parameter was found to be close to one, and defining $y\Delta\Delta = 1$ (*i.e.* fitting only 6 + 5 parameters) increased the RMSD by less than 0.5%. Fig. 5 shows the excellent fit of the (6 + 5) parameter model 3 to the integrated peaks of the raw data in Fig. 2. Model 5 performs almost as well as model 3, but since it requires a larger number of binding parameters for a comparable RMSD, the best fit values of these are not further considered here.

An estimate for the sensitivity of the fitting parameters to changes in the model can be obtained from Table 1, which gives the values of the binding and enthalpy parameters, as well as the nRMSD, for the global fit of (6 + 5) parameter models 1–3. All three fits showed only small baseline enthalpy values, given in Table S1 in the ESI†.

Table 2 gives standard thermodynamic values from the (6 + 5) parameter fit of model 3. Given the 9-fold difference in the intrinsic binding constant, the almost identical corresponding ΔS°-values of Δ and Λ are striking, suggesting that the affinity difference is of purely enthalpic origin. However, the similarity in calculated entropy changes is better regarded as coincidental and provisional, since any small model-dependent change in the ΔH°-values would partition the free energy difference differently between enthalpy and entropy contributions.

Discussion

The general algorithm derived in this work allows quick evaluation of lattice binding models of widely varying complexity, and for the first time, mass balance equations for lattice models which, by defining multiple-ligand units, go beyond nearest-neighbor interactions, can be easily solved. As model complexity increases, however, so does the number of fitting parameters,

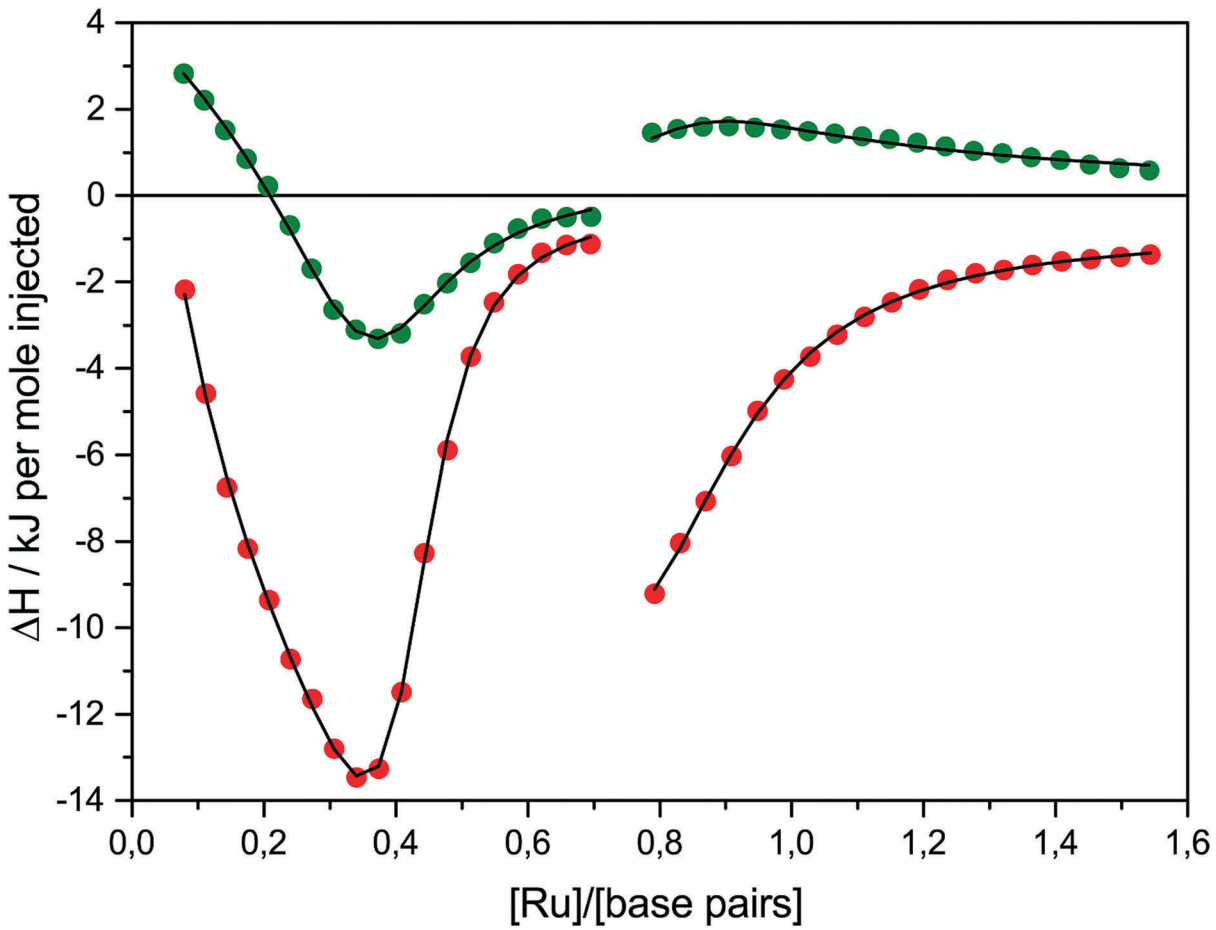

Fig. 5 ITC profiles with fitted traces of (6 + 5) parameter model 3 for the binding of the Δ- and ΛRu-bpy to AT-DNA alone (left) followed by a second titration of opposite enantiomer to already complex-saturated AT-DNA (right) in 150 mM NaCl aqueous solution at 25 °C. Symbols (Δ: green; Λ: red) indicate the normalized integrated heat absorbed or evolved upon sequential 2 μl injections of the complex (~470 μM) into the 206 μl cell containing the DNA (~300 μM nucleotides).

Table 1 Binding and enthalpy parameter values from global fitting of (6 + 5) parameter models to ITC data

Model		Δ	Λ		$\Delta\Delta$[a]	$\Lambda\Lambda$	$\Delta\Lambda$	$n\Delta$	$n\Lambda$	nRMSD[b] (%)	rRMSD[c]
1	K[d]	0.604	0.075	y	1	6.75	5.62	2.28	2.53	4.04	1.65
	ΔH_a°[e]	*3.43*	*5.05*	ΔH_{ab}°[e]	*−6.83*	*−17.68*	*−15.23*			(10.3)	(4.18)[f]
2	K	0.919	0.256	y	1	2.67	2.88	1.18[g]	1.25	4.48	1.83
	ΔH_a°	*4.77*	*3.89*	ΔH_{ab}°	*−5.87*	*−15.17*	*−14.14*			(7.72)	(3.14)
3	K	0.700	0.081	y	1	5.23	6.17	1.13	1.30	2.83	1.15
	ΔH_a°	*3.29*	*8.33*	ΔH_{ab}°	*−6.59*	*−19.61*	*−15.37*			(10.0)	(4.11)

[a] RMSD decreases less than 0.5% if $y\Delta\Delta$ is allowed to vary: best fit values 1.22 (1), 1.28 (2), 1.09 (3). [b] nRMSD: RMSD normalized by division with the mean of the absolute values of the ITC data. [c] rRMSD (relative RMSD): RMSD divided by the RMSD of the (9 + 7) parameter fit of model 3 (nRMSD 2.45%). [d] $K/10^6$ M^{-1}. [e] ΔH°/kJ mol^{-1}. [f] Enclosed in parentheses; nRMSD and rRMSD of the non-cooperative (4 + 5) parameter fit. [g] Models 2 and 3 define the lattice subunit to be 2 base pairs, hence for comparison with model 1 the n values should be multiplied by 2.

Table 2 Standard thermodynamic values (25 °C) from the fit of (6 + 5) parameter model 3

Equilibrium constant		ΔG°/kJ mol^{-1}	ΔH°/kJ mol^{-1}	ΔS°/J K^{-1} mol^{-1}
$K\Delta$	7.00×10^5 M^{-1}	−33.36	+3.29	+122.9
$K\Lambda$	8.10×10^4 M^{-1}	−28.02	+8.86	+121.9
$y\Delta\Delta$	1	0	−6.53	−22.9
$y\Lambda\Lambda$	5.23	−4.10	−19.16	−52.0
$y\Delta\Lambda$	6.17	−4.51	−15.37	−36.4
$K\Delta{\cdot}y\Delta\Delta$	7.00×10^5 M^{-1}	−33.36	−3.30	+100.8
$K\Lambda{\cdot}y\Lambda\Lambda$	4.82×10^5 M^{-1}	−32.12	−11.28	+69.9
$K\Delta{\cdot}y\Delta\Delta$[a]	9.19×10^5 M^{-1}	−34.04	−1.10	+110.5
$K\Lambda{\cdot}y\Lambda\Lambda$[a]	6.84×10^5 M^{-1}	−33.30	−11.28	+73.9

[a] (6 + 5) parameter model 2.

and the physical meaningfulness of their best-fit values might rapidly deteriorate if the range of experimental data in the global fit is too narrow. As the present study is intended to show examples of general global analysis of ITC data, we have deliberately excluded titration data sets made by other experimental methods.

Thus, the goal of this study is to find the binding model that gives a very good global fit to the ITC data with the smallest number of adjustable parameters. Since neither non-cooperative lattice-models (model 1–3 and 5) nor the restricted two independent site model 4 produced any reasonable global fit (see Fig. 4), we conclude that ligand–ligand interactions, whether direct or mediated by the DNA, are an absolute requirement to understand the behavior of the present system. Furthermore, since models 4 and 5, in which no neighbor interaction enthalpy is considered, require a considerably larger number of fitting parameters for acceptable fits, we conclude that for a minimal parameter model, the enthalpic contribution from ligand–ligand interactions has to be included.

Using model 1, the present dataset with extended competitive titrations gave only minor differences in intrinsic and homochiral interaction parameters compared to our earlier analysis of single titration Δ- and ΛRu-bpy ITC data.[3] However, the X-ray structure evidence for the ΛRu-bpy 5′-TA-3′ selectivity suggests that the assumption in model 1 of identical intercalation pockets in poly(dAdT)$_2$ is erroneous. Assuming that ΔRu-bpy shares the same selectivity, model 2 models poly(dAdT)$_2$ as consisting of repeating units of 2 base pairs, to which 5′-TA-3′ selective ligands can bind with essentially no overlap, but the fit is slightly worse (nRMSD = 4.48%) than with model 1 (4.04%). It should be noted that assuming ΔRu-bpy to be homo-chiral non-cooperative (*i.e.* reducing the binding parameters from 7 to 6 by setting $y_{\Delta\Delta} = 1$) had a negligible influence on the fit for models 1 and 2.

Relaxing this assumption in model 3, and allowing the 5′-TA-3′ and 5′-AT-3′ intercalation sites for ΔRu-bpy to have different values for the intrinsic binding constant and homo-chiral cooperativity parameter (9 + 7 fitting parameters, nRMSD 2.45%), gave the best fit of all models tried, although at the drawback of having 2 additional binding and 2 additional enthalpy parameters. Restricting the 5′-TA-3′ and 5′-AT-3′ intercalation sites for ΔRu-bpy to have the same fitting parameter values and setting $y_{\Delta\Delta} = 1$ gave only a slightly inferior fit (6 + 5 fitting parameters, nRMSD 2.83%). The better fit of the (6 + 5) parameter model 3 compared to the (6 + 5) parameter model 2 suggests that ΔRu-bpy can intercalate 5′-AT-3′ as well as 5′-TA-3′ steps, but in view of the good overall fit of both models, conclusive evidence will require independent experimental data for the sequence preferentiality of ΔRu-bpy.

Although binding parameters variate due to the fact that the stoichiometry of binding sites is differently defined, models 1–3 show the same overall pattern: Δ itself binds non-cooperatively and has a larger (3 to 9-fold) intrinsic binding constant than Λ; the latter, on the other hand, has a stronger (3 to 6-fold) cooperative binding, both with itself and with Δ. Notably, for all models 1–3, the hetero-chiral cooperativity parameter value is close to the homo-chiral value for Λ.

Also the enthalpy parameters show a similar overall pattern for models 1–3: the intrinsic binding is endothermic

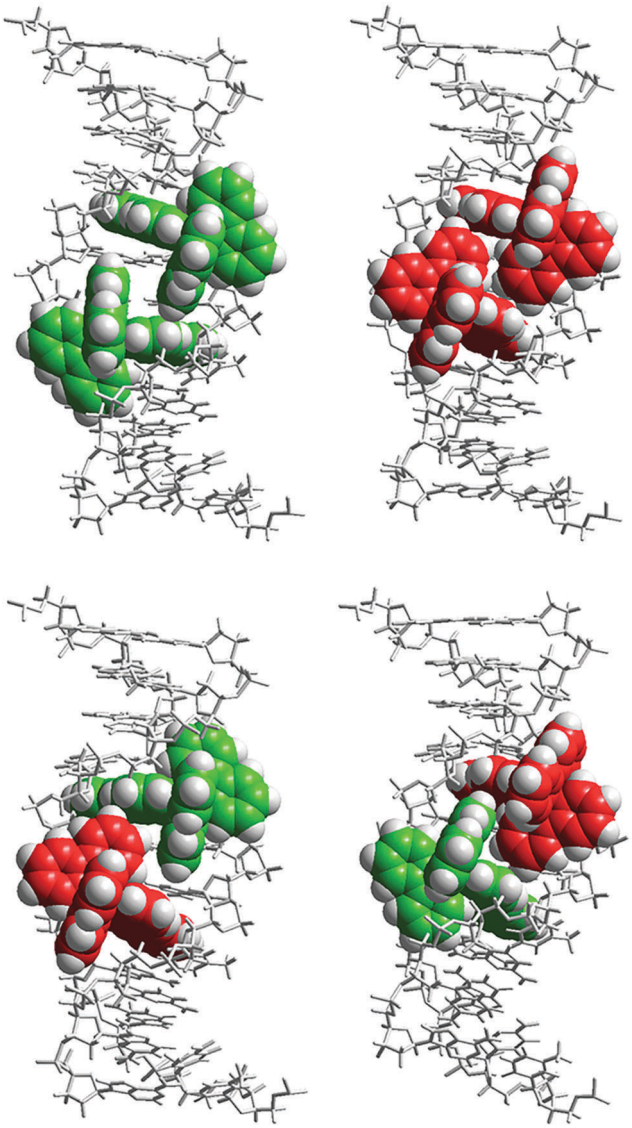

Fig. 6 Schematic illustration of the proposed nearest-neighbor interaction geometries for the *Δ* (green) and *Λ* (red) enantiomers of Ru-bpy when intercalated to DNA *via* the minor groove. The models were constructed by manual docking and subsequent energy minimization in a vacuum, using the AMBER 2 force field in the HyperChem 8.0 software package (HyperCube, Inc.).

(although the relative magnitude for the two enantiomers is clearly model sensitive), while the interaction enthalpies are exothermic, with *ΛΛ* about 2.7 and *ΔΛ* about 2.3 times that of *ΔΔ* for all three models. Comparing the enthalpy values with the associated standard free energy changes (see Table 2) clearly shows the endothermic intrinsic binding to be massively entropy driven, while the exothermic ligand–ligand interaction is nearly compensated for by a large entropy decrease.

The stronger homo-chiral cooperativity largely compensates for the smaller intrinsic binding constant for *Λ*, which for models 3 and 2 leads to a very similar ratio $K_{\Delta}y_{\Delta\Delta}/K_{\Lambda}y_{\Lambda\Lambda}$ = 1.4 ± 0.05. The value of the product of the intrinsic binding constant and the homo-chiral cooperativity parameter *Ky* is essentially the effective binding constant in the vicinity of saturation of the intercalation sites, where the curvature of the ITC curve changes rapidly. Hence, the value of *Ky*, and the value of the corresponding enthalpy change, can both be expected to be the best determined quantity form the fit to the data. Indeed, as seen in the last rows of Table 2, where models 2 and 3 are compared, these values show relatively small variations between the models Thus, we can draw the conclusion, independent of whether *Δ*Ru-bpy discriminates between the two base pair steps or not, that the binding of *Δ*Ru-bpy next to a bound *Δ*Ru-bpy is almost entirely driven by entropy, and that the binding of *Λ*Ru-bpy next to a bound *Λ*Ru-bpy is to about one third driven by enthalpy.

A simple allosteric explanation of the lower intrinsic binding constant and higher cooperativity for the *Λ* enantiomer would be that, due to the seemingly less good steric fit compared to the *Δ* enantiomer,[32] *Λ* pays a free energy penalty by widening the groove upon intercalation, which pays back for the second *Λ* enantiomer intercalating from the already widened groove. However, this simple allosteric model does not explain the hetero-chiral cooperativity, since by hypothesis the better fitting, non-cooperative *Δ* enantiomer does not need to widen the groove upon intercalation. Although allosteric interactions undoubtedly play an important role, we suggest that ligand–ligand interactions also make a significant contribution. Fig. 6 shows models of the different combinations of Ru-bpy enantiomers intercalating (from the minor groove, as suggested by X-ray structures) two base pairs apart on DNA. We can distinguish three essentially different types of arrangements of the close-by bipyridine moieties: *ΔΔ*: face to face; *ΛΛ*: edge to edge; *ΔΛ*: face to edge. These three types of arrangements can be expected to be significantly different with regard to direct, mainly enthalpic interactions such as pi-stacking and electrostatic repulsion, but also with respect to entropy-contributing effects of water solvation and the counter-ion distribution. We believe that it presently would be premature to attempt to do a more detailed correlation between structural differences and changes in the thermodynamic quantities.

Conclusions

By developing a new simple algorithm, no longer restricted by the complexity of the binding system and general enough to be implemented to any biopolymers, we have been able to demonstrate a method that can capture the most essential effects of the nearest-neighbor interactions between ligands. This has allowed us to critically examine different binding models for the analysis of competitive calorimetric binding isotherms for the enantiomers of $Ru(bpy)_2dppz^{2+}$, for which we find a significant hetero-chiral binding cooperativity. It is our hope that this method will contribute in the future search for better pharmacological therapeutics and biotechnological applications.

Conflicts of interest

There are no conflicts to declare.

Acknowledgements

The authors gratefully acknowledge Swedish Research Council (Vetenskapsrådet) grant 2012-1661 and 2016-05421 and Chalmers Area of Advance Nano for funding, as well as COST Action CM1105 for providing a forum for stimulating discussions.

Notes and references

1 V. H. Le, R. Buscaglia, J. B. Chaires and E. A. Lewis, *Anal. Biochem.*, 2013, **434**, 233–241.
2 J. Andersson, L. H. Fornander, M. Abrahamsson, E. Tuite, P. Nordell and P. Lincoln, *Inorg. Chem.*, 2013, **52**, 1151–1159.
3 A. K. F. Mårtensson and P. Lincoln, *Dalton Trans.*, 2015, **44**, 3604–3613.
4 P. Lincoln, *Chem. Phys. Lett.*, 1998, **288**, 647–656.
5 J. A. Hartley, K. Reszka, E. T. Zuo, W. D. Wilson, A. R. Morgan and J. W. Lown, *Mol. Pharmacol.*, 1988, **33**, 265–271.
6 A. Jamalian, A. Shafiee, B. Hemmateenejad, M. Khoshneviszadeh, R. Miri, A. Madadkar-Sobhani, S. Z. Bathaie and A. A. Moosavi-Movahedi, *J. Iran. Chem. Soc.*, 2011, **8**, 1098–1112.
7 G. Marverti, M. Cusumano, A. Ligabue, M. L. Di Pietro, P. A. Vainiglia, A. Ferrari, M. Bergomi, M. S. Moruzzi and C. Frassineti, *J. Inorg. Biochem.*, 2008, **102**, 699–712.
8 T. A. K. Prescott, I. H. Sadler, R. Kiapranis and S. K. Maciver, *J. Ethnopharmacol.*, 2007, **109**, 289–294.
9 A. Banerjee, J. Singh and D. Dasgupta, *J. Fluoresc.*, 2013, **23**, 745–752.
10 S4SD – AFFINImeter 2017, accessed 20 October 2017, https://www.affinimeter.com/site/.
11 N. J. Buurma and I. Haq, *J. Mol. Biol.*, 2008, **381**, 607–621.
12 P. Lincoln, A. Broo and B. Nordén, *J. Am. Chem. Soc.*, 1996, **118**, 2644–2653.
13 R. M. Hartshorn and J. K. Barton, *J. Am. Chem. Soc.*, 1992, **114**, 5919–5925.
14 I. Haq, P. Lincoln, D. C. Suh, B. Nordén, B. Z. Chowdhry and J. B. Chaires, *J. Am. Chem. Soc.*, 1995, **117**, 4788–4796.
15 A. E. Friedman, J. C. Chambron, J. P. Sauvage, N. J. Turro and J. K. Barton, *J. Am. Chem. Soc.*, 1990, **112**, 4960–4962.
16 H. Song, J. T. Kaiser and J. K. Barton, *Nat. Chem.*, 2012, **4**, 615–620.
17 H. Niyazi, J. P. Hall, K. O'Sullivan, G. Winter, T. Sorensen, J. M. Kelly and C. J. Cardin, *Nat. Chem.*, 2012, **4**, 621–628.
18 J. P. Hall, *et al.*, *J. Am. Chem. Soc.*, 2013, **135**, 12652–12659.
19 J. P. Hall, P. M. Keane, H. Beer, K. Buchner, G. Winter, T. L. Sorensen, D. J. Cardin, J. A. Brazier and C. J. Cardin, *Nucleic Acids Res.*, 2016, **44**, 9472–9482.
20 P. Lincoln and B. Nordén, *J. Phys. Chem. B*, 1998, **102**, 9583–9594.
21 J. G. Liu, B. H. Ye, H. Li, L. N. Ji, R. H. Li and J. Y. Zhou, *J. Inorg. Biochem.*, 1999, **73**, 117–122.
22 L. Wang, J. Z. Wu, G. Yang, T. X. Zeng and L. N. Ji, *Transition Met. Chem.*, 1996, **21**, 487–490.
23 J. G. Liu, Q. L. Zhang, X. F. Shi and L. N. Ji, *Inorg. Chem.*, 2001, **40**, 5045–5050.
24 B. Y. Wu, L. H. Gao, Z. M. Duan and K. Z. Wang, *J. Inorg. Biochem.*, 2005, **99**, 1685–1691.
25 D. Lawrence, V. G. Vaidyanathan and B. U. Nair, *J. Inorg. Biochem.*, 2006, **100**, 1244–1251.
26 A. W. McKinley, J. Andersson, P. Lincoln and E. M. Tuite, *Chem. – Eur. J.*, 2012, **18**, 15142–15150.
27 M. Scott Vandiver, *et al.*, *Inorg. Chem.*, 2010, **49**, 839–848.
28 C. G. Mikek, J. I. DuPont, V. R. Machha, J. C. White, L. R. Martin, N. Alatrash, F. M. MacDonnell and E. A. Lewis, *Eur. J. Inorg. Chem.*, 2017, 3953–3960.
29 Y. D. Chen, *Biopolymers*, 1990, **30**, 1113–1121.
30 J. D. McGhee and P. H. von Hippel, *J. Mol. Biol.*, 1974, **86**, 469–489, correction J. D. McGhee and P. H. von Hippel, *J. Mol. Biol.*, 1976, **103**, 679.
31 F. R. Gantmacher, *Applications of the theory of matrices*, Interscience Publishers, Inc., New York, 1959.
32 J. K. Barton, A. T. Danishefsky and J. M. Goldberg, *J. Am. Chem. Soc.*, 1984, **106**, 2172–2176.

Electronic Supplementary Material (ESI) for Physical Chemistry Chemical Physics.

Supplementary Materials

Competitive DNA binding of $Ru(bpy)_2dppz^{2+}$ enantiomers studied with isothermal titration calorimetry (ITC) using a direct and general binding isotherm algorithm

Anna K. F. Mårtensson and Per Lincoln

Contents: Page

Table S1

Baseline enthalpy values (kJ mol^{-1}) for the fit of (6+5) parameter Model 1-3

Titration	Model 1	Model 2	Model 3
1) Δ in AT	0.42315	-0.10353	0.46363
2) Λ in AT	0.20343	-0.084847	-0.21065
3) Δ in AT + Λ	-0.028274	-0.27608	0.089987
4) Λ in AT + Δ	-0.52783	-0.47468	-0.74829

Note that in the following programs, the total concentration of binding sites, denoted B_0 in the main text, is now denoted D0.

GeneralAlgorithm.m

```
function [conc,x,f,P,r]=GeneralAlgorithm(C0,M,T,Y,K,n,r)
%General algortihm for solving the mass balance for
%ligands interacting with a linear polymer of identical binding site units
%D with explicit nearest neighbor interaction.

%INPUT:
%CO=[D0 A0 B0...] 1x(1+L) vector with total concentration of
%binding site units D and L ligands A, B...
%M = mxL matrix of the stoichiometric coefficients for the m ligand-
containg elementary
%units.
%T = mxm non-singular matrix transforming M such that in the product T*M no
column is
%zero, and each row only contains one 1, the rest being zeros.
%Y =(m+1)x(m+1)matrix containg the cooperativity parameters for nearest
%neighbor interactions between the elementary units, the first row and
%column being the interactions with the ligand-free elementary unit.
%K = Intrinsic binding constants of the elementary units.
%n = Number of binding site units made inaccesible by formation of the
elementary unit.
%r = Guess for vector r

%OUTPUT
%conc = [[Afree; Bfree ...][ Abound; Bbound ...]]
%x = binding potentials of elementary units
%f = binding densities of elementary units
%P = matrix of conditional probabilities
%r = vector r that solves the mass balance equations

[m,l]=size(M);
lnK=log(K);
TMM=T*M*M';
L0=T*M*C0(2:end,1); %free ligand concentrations
D0=C0(1);
q=1;
    while norm(q)>1e-9;
       s=1./(Y*[1;r]);
       P=diag(s)*Y*diag([1;r]);
       v=eye(m)-P(2:end,2:end)+n'*P(1,2:end);
       f=inv(v')*P(1,2:end)';
       x=s(2:end).*r./(s(1).^n');
       etl=exp(T*(log(x)-lnK));
       q=etl+D0*TMM*f-L0;
       u=inv(v')*(diag(f)-P(:,2:end)'*diag([1-n*f;f])*P(:,2:end));
       dqdr=(D0*TMM*u+diag(etl)*T*v);
        dr=diag(r)*(dqdr\q);
       while min(r-dr)<=0    %ensures that r remains positive
           dr=dr/3;
       end
       r=r-dr;
    end
       conc=[etl D0*TMM*f];
```

ITCalgorithmModel3.m

```
function [err,sim,heat,conc]=ITCalgorithmModel3(par,totdata,inj)
%Calculates ITC curve for binding of two ligands La and Lb
%with a lattice binding model in which
%A forms symmetrical subunits A1 and A2 (here with identical properties),
when binding
%to an infinite chain of alternating binding sites 1 and 2, and B only
%binds to site 1.
%This code is (7+5) parameter Model 3; can easily be converted to Model 1
%or Model 2, see comments on line 32-33 and 40.

%INPUT:
%par=[1) Ka 2) Kb 3) yAA  4) yBB 5) yAB 6) na 7) nb]
%For (9+7) parameter Model 3, Ka2 and yA2A2 are included in par
%and inserted into the appropriate matrices below.
%totdata=[ITC-data D0 La0 Lb0] (4*20) X 4 matrix with data and total
%concentrations of basepairs and ligands, preferably with total
concentrations of Ln in increasing order
%inj=[inj1 inj2 inj3 inj4] injN = mol injectant/Vcell for titration N

%OUTPUT:
%err is the least square error
%sim = [ITC-data   simulated data]
%heat=[bl1 bl2 bl3 bl4 bl5 dHa dHb dHaa dHbb dHab]; bln is baseline value
%for titration n, dHa etc. enthalpy changes per mol

data=totdata([2:20 22:40 42:60 62:80],1);
o=ones([19,1]);
e4=eye([4,4]);
bl=[o*e4(1,:);o*e4(2,:);o*e4(3,:);o*e4(4,:)];
dc=[];
K=par([1 1 2])';
%K(2)=1e-9;  %Effectively removes A binding to site 2, converting Model 3
to Model 2 (when ff=0.5) or
%to Model 1 (when ff=1).
Y=[1 1 1 1  ;1 par(3) 0 par(5);1 1 par(3) 1 ;1 par(5) 0 par(4)];
n=par([6 6 7]);
C0=totdata(:,2:4);
conc=[];
M=[1 0;1 0;0 1];
T=eye(3);
ff=.5;  %Fraction of binding site unit per basepair, set to 1 for Model 1

if min(par(1:7))<=0 %Ensures the variables stay positive
    err=1e6;
else
dc=[];
C0=totdata(:,2:4);
conc=[];
    r=[.1 .1]'; % For titrations 1 and 2, the appropriate submatrices are
defined; here La only
    Kt=K(1:2);
    Mt=M(1:2,1);
    Tt=T(1:2,1:2);
    nt=n(1:2);
    Yt=Y(1:3,1:3);
 for t=C0(1:20,:)';
    t(1)=t(1)*ff;
```

```
    t=t(1:2);

    [C,x,f,P,r]=GeneralAlgorithm(t,Mt,Tt,Yt,Kt,nt,r);
    PP=t(1)*diag(f)*P(2:3,2:3);
    conc=[conc;(t(1)*[1 1]*f)' 0 PP(1,1)+PP(2,2) 0 0];
    %Note that the assumed identical La contributions are summed together

 end
    r=[.1 ]';   %Lb only

    Kt=K(3);
    Mt=M(3,2);
    Tt=T(3,3);
    nt=n(3);
    Yt=Y([1 4],[1 4]);
for t=C0(21:40,:)';
    t(1)=t(1)*ff;
    t=t([1 3]);
    [C,x,f,P,r]=GeneralAlgorithm(t,Mt,Tt,Yt,Kt,nt,r);
    PP=t(1)*diag(f)*P(2,2);
    conc=[conc;0  (t(1)*f)' 0  PP(1,1) 0 ];

end
r=[.1 .1 .1 ]';
for t=C0(41:60,:)'; %La into Lb + DNA
    t(1)=t(1)*ff;

    [C,x,f,P,r]=GeneralAlgorithm(t,M,T,Y,K,n,r);
    PP=t(1)*diag(f)*P(2:4,2:4);
    conc=[conc;(t(1)*[1 1 0;0 0 1]*f)' PP(1,1)+PP(2,2) PP(3,3) PP(1,3)*2 ];
end
r=[.1 .1 .1 ]';   %Lb into La + DNA
for t=C0(61:80,:)';
    t(1)=t(1)*ff;

    [C,x,f,P,r]=GeneralAlgorithm(t,M,T,Y,K,n,r);
    PP=t(1)*diag(f)*P(2:4,2:4);
    conc=[conc;(t(1)*[1 1 0;0 0 1]*f)' PP(1,1)+PP(2,2) PP(3,3) PP(1,3)*2 ];

end
          %Calculated concentration changes per mol injectant
          %corrected for dilution:
    dc=[dc;[conc(2:20,:)-conc(1:19,:)*204/206]/inj(1)];
    dc=[dc;[conc(22:40,:)-conc(21:39,:)*204/206]/inj(2)];
    dc=[dc;[conc(42:60,:)-conc(41:59,:)*204/206]/inj(3)];
    dc=[dc;[conc(62:80,:)-conc(61:79,:)*204/206]/inj(4)];

    dc=[bl dc];

    heat=pinv(dc)*data;
    sim=dc*heat;

    err=norm(data-sim,'fro');

    sim=[data sim];
end
```

ITCalgorithmIndependent.m

```
function [err,sim,heat]=ITCalgorithmIndependent(par,totdata,inj)
%Calculates ITC curve for competitive binding of two ligands La
%and Lb to two types of independent, non-overlapping binding sites X and Y.
%The fractions fX and fY can take independent values for each of the four
%titrations, or at wish be restricted to fewer independent values.
%
%INPUT:
%par=[1) Kax 2) Kay  3) Kbx 4) Kby 5) fraction;
%fraction can be one variable, as in the present case, or up to 8 variables
in the unrestricted case.
%totdata=[ITC-data D0 La0 Lb0] (4*20) X 4 matrix with data and total
%concentrations of basepairs and ligands, preferably with total
%concentrations of Ln in increasing order.
%The data are assumed to be ordered as only La, only Lb, La into Lb, Lb
%into La
%inj=[inj1 inj2 inj3 inj4] injN = mol injectant/Vcell for titration N

%OUTPUT:
%err is the least square error
%sim = [ITC-data   simulated data]
%heat=[bl1 bl2 bl3 bl4 dHax dHay dHbx dHby]; bli is baseline value for
%titration i, dHax etc. enthalpy changes per mol, same units as in ITC-data

data=totdata([2:20 22:40 42:60 62:80],1);   %The column of ITC-data
o=ones([19,1]);
C0=totdata(:,2:4);  %The 3 columns of total concentrations
e4=eye([4,4]);
bl=[o*e4(1,:);o*e4(2,:);o*e4(3,:);o*e4(4,:)];

fraction=par(5)*[[1 1 1 1];[1 1 1 1]];
%fraction=[par([5 7 9 11]);par([6 8 10 12])]; %Unrestricted case, first row
%X-fractions, second row Y-fractions
conc=[];
Kx=par([1 2]);
Ky=par([3 4]);
dc=[];
if min(par(1:5))<=0  %All variable values should be positive, here 5
variables are varied.
    err=1e6;
else

 f=fraction(:,1);
 L=[.1]; %Guess for free ligand concentration
 for t=C0(1:20,:)'; % La only titration
    D0=t(1);  %basepair concentration.
    L0=t(2)'; %Ligand total concentration
    q=1;
    kx=Kx(1);
    ky=Ky(1);
    while norm(q)>1e-9;
       q=(kx*L/(1+kx*L)*f(1)+ky*L/(1+ky*L)*f(2))*D0+L-L0;
       dqdL=(kx/(1+kx*L)*f(1)+ky/(1+ky*L)*f(2)-
(f(1)*L*kx^2/((1+kx*L)^2))+f(2)*L*ky^2/((1+ky*L)^2))*D0+1;
       dL=q*inv(dqdL);
       L=L-dL;
    end
    conc=[conc;[f(1)*kx*L/(1+kx*L) 0 f(2)*ky*L/(1+ky*L) 0]*D0];
```

```
 end
    f=fraction(:,2);
 L=[.1];
 for t=C0(21:40,:)';    %Only Lb titration
    D0=t(1);
    L0=t(3)';
    q=1;
    kx=Kx(2);
    ky=Ky(2);
    while norm(q)>1e-9;
       q=(kx*L/(1+kx*L)*f(1)+ky*L/(1+ky*L)*f(2))*D0+L-L0;
       dqdL=(kx/(1+kx*L)*f(1)+ky/(1+ky*L)*f(2)-
(f(1)*L*kx^2/((1+kx*L)^2))+f(2)*L*ky^2/((1+ky*L)^2))*D0+1;
       dL=q*inv(dqdL);
       L=L-dL;
    end
    conc=[conc;[0 f(1)*kx*L/(1+kx*L) 0 f(2)*ky*L/(1+ky*L)]*D0];

 end
 f=fraction(:,3);
 L=[.1 .1];
 for t=C0(41:60,:)';%lLa into Lb
    D0=t(1);
    L0=t(2:3)';
    q=1;
    while norm(q)>1e-9;
       q=(Kx.*L/(1+Kx*L')*f(1)+Ky.*L/(1+Ky*L')*f(2))*D0+L-L0;
       dqdL=(diag(Kx)/(1+Kx*L')*f(1)+diag(Ky)/(1+Ky*L')*f(2)-
(f(1)*(diag(L)*Kx'*Kx/((1+Kx*L')^2))+f(2)*(diag(L)*Ky'*Ky/((1+Ky*L')^2))))*
D0+eye(2);
       dL=q*inv(dqdL');
       L=L-dL;
    end
    conc=[conc;[f(1)*Kx.*L/(1+Kx*L') f(2)*Ky.*L/(1+Ky*L')]*D0];

 end

 f=fraction(:,4);
 L=[.1 .1];
for t=C0(61:80,:)'; %Lb into La
    D0=t(1);
    L0=t(2:3)';
    q=1;
    while norm(q)>1e-9;
       q=(Kx.*L/(1+Kx*L')*f(1)+Ky.*L/(1+Ky*L')*f(2))*D0+L-L0;
       dqdL=(diag(Kx)/(1+Kx*L')*f(1)+diag(Ky)/(1+Ky*L')*f(2)-
(f(1)*(diag(L)*Kx'*Kx/((1+Kx*L')^2))+f(2)*(diag(L)*Ky'*Ky/((1+Ky*L')^2))))*
D0+eye(2);
       dL=q*inv(dqdL');
       L=L-dL;
    end
    conc=[conc;[f(1)*Kx.*L/(1+Kx*L') f(2)*Ky.*L/(1+Ky*L')]*D0];

end

   dc=[dc;[conc(2:20,:)-conc(1:19,:)*204/206]/inj(1)]; %Calculated
concentration changes per mol injectant
    dc=[dc;[conc(22:40,:)-conc(21:39,:)*204/206]/inj(2)]; %corrected for
dilution
    dc=[dc;[conc(42:60,:)-conc(41:59,:)*204/206]/inj(3)];
```

```
    dc=[dc;[conc(62:80,:)-conc(61:79,:)*204/206]/inj(4)];
    dc=[bl dc];

    heat=pinv(dc)*data;
    sim=dc*heat;

   err=norm(data-sim,'fro');

    sim=[data sim];
end
```

ITCalgorithmModel4:

```
function [err,sim,heat]=ITCalgorithmModel4(par,totdata,inj)
%Uses the lattice model to calculates the ITC curve for binding of two
ligands La
%and Lb to two independent binding sites X and Y, which fractions are equal

%INPUT:
%par=[1) Ka1 2) Kb1 3) Ka2 4) Kb2 5) fraction ]

%totdata=[ITC-data D0 La0 Lb0] (4*20) X 4 matrix with data and total
%concentrations of basepairs and ligands, preferably with total
concentrations of Ln in increasing order

%inj=[inj1 inj2 inj3 inj4] injN = mol injectant/Vcell for titration N

%OUTPUT:
%err is the least square error

%sim = [ITC-data   simulated data]

%heat=[bl1 bl2 bl3 bl4 dHaX dHbX dHaY dHbY]; bln is baseline value for
%titration n, dHaX etc. enthalpy changes per mol, same units as in ITC-data

data=totdata([2:20 22:40 42:60 62:80],1);
o=ones([19,1]);
e4=eye([4,4]);
bl=[o*e4(1,:);o*e4(2,:);o*e4(3,:);o*e4(4,:)];
dc=[];
C0=totdata(:,2:4);
conc=[];

ff=par(5); %Fraction of binding site per base-pair.


Y=ones([9,9]); %No cooperativity in this case
K=[par(1:4) par(1)*par(3) par(2)*par(4) par(1)*par(4) par(2)*par(3)]'; %To
comply with the 2 independent site model

n=ones([1,8]);  %Binding site coverage is unity
mm=[eye(4);[1 0 1 0;0 1 0 1;1 0 0 1;0 1 1 0] ];     %Matrix of elementary
unit composition in terms of LaX, LbX, LaY and LbY
M=mm*[1 0 1 0;0 1 0 1]';
T=eye(8);
T(5,5)=.5;
T(6,6)=.5;
T(7,2)=-1;
T(8,1)=-1;

if min(par(1:5))<=0  %Ensures that the variables stays positive
    err=1e6;
else

    r=[.1 .1 .1]';  %For each of the 4 titrations, appropriate submatrices
are constructed. Here La only titration.
    Kt=K([1 3 5]);
    Mt=M([1 3 5],1);
    Tt=T([1 3 5],[1 3 5]);
```

```
    nt=n([1 3 5]);
    Yt=Y([1 2 4 6],[1 2 4 6]);
    mmt=mm([1 3 5],:);
 for t=C0(1:20,:)';
    t(1)=t(1)*ff;
    t=t(1:2);
    [C,x,f,P,r]=GeneralAlgorithm(t,Mt,Tt,Yt,Kt,nt,r);
    conc=[conc;t(1)*f'*mmt ];
 end

    r=[.1 .1 .1]';  %Lb only titration
    Kt=K([2 4 6]);
    Mt=M([2 4 6],2);
    Tt=T([2 4 6],[2 4 6]);
    nt=n([2 4 6]);
    Yt=Y([1 3 5 7],[1 3 5 7]);
    mmt=mm([2 4 6],:);
 for t=C0(21:40,:)';
    t(1)=t(1)*ff;
    t=t([1 3]);
    [C,x,f,P,r]=GeneralAlgorithm(t,Mt,Tt,Yt,Kt,nt,r);
    conc=[conc;t(1)*f'*mmt ];
 end

r=[.1 .1 .1 .1 .1 .1 .1 .1]';   %La into Lb, the full matrices are used.
for t=C0(41:60,:)';
    t(1)=t(1)*ff;
    [C,x,f,P,r]=GeneralAlgorithm(t,M,T,Y,K,n,r);
     conc=[conc;t(1)*f'*mm ];
end

r=[.1 .1 .1 .1 .1 .1 .1 .1]';   %Lb into La
for t=C0(61:80,:)';
    t(1)=t(1)*ff;
    [C,x,f,P,r]=GeneralAlgorithm(t,M,T,Y,K,n,r);
     conc=[conc;t(1)*f'*mm ];
end
    %Calculated concentration changes per mol injectant
    %corrected for dilution
    dc=[dc;[conc(2:20,:)-conc(1:19,:)*204/206]/inj(1)];
    dc=[dc;[conc(22:40,:)-conc(21:39,:)*204/206]/inj(2)];
    dc=[dc;[conc(42:60,:)-conc(41:59,:)*204/206]/inj(3)];
    dc=[dc;[conc(62:80,:)-conc(61:79,:)*204/206]/inj(4)];
    dc=[bl dc];

    heat=pinv(dc)*data;
    sim=dc*heat;

    err=norm(data-sim,'fro');

    sim=[data sim];
end
```

Analysis of the ITC data:

The total concentrations in *TotData* are calculated from the concentration of injectant stock solution, volume added (2 μL) and the initial content of the cell and its volume (206 μL). For each injection, the injectant is assumed to displace 2 μL of the content in the cell before mixing. *Inj* is the concentration resulting from one 2 μL addition of injectant into a cell filled with buffer, and used to normalize the species concentrations calculated to the ITC-data in the first column. All concentrations are given in μM. See further comments in the program 'ITCalgorithm' above.

Indata:

TotData =

3.5673	148.8010	6.9029	0.0000
2.8297	147.3563	11.4378	0.0000
2.2158	145.9257	15.9287	0.0000
1.5232	144.5089	20.3760	0.0000
0.8603	143.1059	24.7801	0.0000
0.2285	141.7165	29.1415	0.0000
-0.6821	140.3406	33.4605	0.0000
-1.6861	138.9781	37.7376	0.0000
-2.6287	137.6288	41.9732	0.0000
-3.0987	136.2926	46.1676	0.0000
-3.3115	134.9694	50.3213	0.0000
-3.1798	133.6590	54.4347	0.0000
-2.5041	132.3613	58.5081	0.0000
-2.0208	131.0763	62.5420	0.0000
-1.5544	129.8037	66.5368	0.0000
-1.0936	128.5435	70.4927	0.0000
-0.7567	127.2955	74.4103	0.0000
-0.5287	126.0596	78.2898	0.0000
-0.4940	124.8357	82.1316	0.0000
-0.4883	123.6237	85.9362	0.0000
0.3559	148.8010	0.0000	6.8738
-2.1600	147.3563	0.0000	11.3896
-4.5524	145.9257	0.0000	15.8615
-6.7236	144.5089	0.0000	20.2900
-8.1363	143.1059	0.0000	24.6756
-9.3413	141.7165	0.0000	29.0185
-10.7015	140.3406	0.0000	33.3193
-11.6217	138.9781	0.0000	37.5784
-12.7751	137.6288	0.0000	41.7961
-13.4433	136.2926	0.0000	45.9728
-13.2426	134.9694	0.0000	50.1090
-11.4619	133.6590	0.0000	54.2050
-8.2448	132.3613	0.0000	58.2613
-5.8635	131.0763	0.0000	62.2781
-3.6970	129.8037	0.0000	66.2560
-2.4371	128.5435	0.0000	70.1953

-1.7974	127.2955	0.0000	74.0963
-1.2967	126.0596	0.0000	77.9595
-1.1205	124.8357	0.0000	81.7851
-1.1004	123.6237	0.0000	85.5736
0.9546	121.8234	6.9029	84.3274
1.5000	120.6406	11.4378	83.5087
1.5933	119.4693	15.9287	82.6979
1.6437	118.3094	20.3760	81.8950
1.6524	117.1608	24.7801	81.0999
1.6227	116.0233	29.1415	80.3125
1.5730	114.8969	33.4605	79.5328
1.5407	113.7814	37.7376	78.7606
1.4867	112.6767	41.9732	77.9960
1.4239	111.5828	46.1676	77.2387
1.3592	110.4994	50.3213	76.4888
1.2688	109.4266	54.4347	75.7462
1.1883	108.3642	58.5081	75.0108
1.0863	107.3121	62.5420	74.2826
1.0232	106.2703	66.5368	73.5614
0.9363	105.2385	70.4927	72.8472
0.8703	104.2168	74.4103	72.1399
0.7674	103.2050	78.2898	71.4395
0.6834	102.2030	82.1316	70.7459
0.6225	101.2107	85.9362	70.0591
-9.5212	121.8234	84.6847	6.8738
-9.2077	120.6406	83.8625	11.3896
-8.0398	119.4693	83.0483	15.8615
-7.0590	118.3094	82.2420	20.2900
-6.0224	117.1608	81.4435	24.6756
-4.9818	116.0233	80.6528	29.0185
-4.2492	114.8969	79.8698	33.3193
-3.7254	113.7814	79.0944	37.5784
-3.2104	112.6767	78.3265	41.7961
-2.8004	111.5828	77.5660	45.9728
-2.4630	110.4994	76.8129	50.1090
-2.1631	109.4266	76.0672	54.2050
-1.9390	108.3642	75.3287	58.2613
-1.7970	107.3121	74.5973	62.2781
-1.7187	106.2703	73.8731	66.2560
-1.6006	105.2385	73.1559	70.1953
-1.5198	104.2168	72.4456	74.0963
-1.4685	103.2050	71.7422	77.9595
-1.4097	102.2030	71.0457	81.7851
-1.3651	101.2107	70.3560	85.5736

Inj =

4.6019	4.5825	4.6019	4.5825

MATLAB Command Window:

```
>> options=optimset('Display','Iter','MaxIter',4000,'MaxFunEvals',8000,'TolX',1e-6,'TolFun',1e-6);
```

(7+5) parameter Model 3

```
>> [Err,Sim,Heat]=ITCalgorithmModel3(Par,TotData,Inj)

>> Par=fminsearch('ITCalgorithmModel3',[ 1  0.1  1  5  5  1.1  1.3],options,TotData,Inj)
```

After 35 seconds (722 iterations / 1127 evaluations of 'ITCalgortithmModel3'), convergence criteria are satisfied and

```
Par =

    0.6478    0.0871    1.0918    5.0097    5.9443    1.1374    1.2942

>> [Err,Sim,Heat]=ITCalgorithm(Par,TotData,Inj)

Err =

    0.8155


Sim =

    2.8297    2.8322
    2.2158    2.2557
    1.5232    1.6102
    0.8603    0.8886
    0.2285    0.0881
   -0.6821   -0.7817
   -1.6861   -1.6821
   -2.6287   -2.5191
   -3.0987   -3.1242
   -3.3115   -3.3150
   -3.1798   -3.0614
   -2.5041   -2.5475
   -2.0208   -1.9960
   -1.5544   -1.5225
   -1.0936   -1.1504
   -0.7567   -0.8660
   -0.5287   -0.6487
   -0.4940   -0.4809
   -0.4883   -0.3495
   -2.1600   -2.2965
   -4.5524   -4.6329
   -6.7236   -6.4670
   -8.1363   -8.0184
   -9.3413   -9.3977
```

-10.7015	-10.6599
-11.6217	-11.8149
-12.7751	-12.8037
-13.4433	-13.4215
-13.2426	-13.1845
-11.4619	-11.4535
-8.2448	-8.4612
-5.8635	-5.6108
-3.6970	-3.6860
-2.4371	-2.5319
-1.7974	-1.8380
-1.2967	-1.4028
-1.1205	-1.1164
-1.1004	-0.9195
1.5000	1.3515
1.5933	1.5931
1.6437	1.7416
1.6524	1.7752
1.6227	1.7211
1.5730	1.6243
1.5407	1.5166
1.4867	1.4130
1.4239	1.3188
1.3592	1.2348
1.2688	1.1603
1.1883	1.0942
1.0863	1.0353
1.0232	0.9825
0.9363	0.9350
0.8703	0.8919
0.7674	0.8526
0.6834	0.8167
0.6225	0.7836
-9.2077	-9.1190
-8.0398	-8.1612
-7.0590	-7.0409
-6.0224	-5.9605
-4.9818	-5.0206
-4.2492	-4.2490
-3.7254	-3.6341
-3.2104	-3.1495
-2.8004	-2.7678
-2.4630	-2.4652
-2.1631	-2.2231
-1.9390	-2.0273
-1.7970	-1.8673
-1.7187	-1.7351
-1.6006	-1.6247
-1.5198	-1.5317
-1.4685	-1.4526
-1.4097	-1.3848
-1.3651	-1.3262

Heat =

```
    0.4159
   -0.2019
    0.0503
   -0.7214
    3.4328
    8.0063
   -6.5616
  -19.2850
  -15.3134
```

(5+4) Parameter Model 4

>> ParInd=fminsearch('ITCalgorithmIndependent',[2 2 1 1 .2],options,TotData,inj)

After 13 seconds (428 iterations / 712 evaluations of 'ITCalgortithmIndependent'), convergence criteria are satisfied, the error is 2.1216 and

ParInd =

```
    0.9017    1.4730    0.7276    1.3105    0.2079
```

(5+4) Parameter Model 4*

>> ParModel4=fminsearch('ITCalgorithmModel4',[2 2 1 1 .2],options,TotData,inj)

After 30 seconds (420 iterations / 703 evaluations of 'ITCalgortithmModel4'), convergence criteria are satisfied, the error is 2.1216 and

ParModel4 =

```
    0.9017    1.4730    0.7276    1.3105    0.2079
```

[Err4,Sim4,Heat4]=ITCalgorithmModel4(ParModel4,TotData,Inj)

Err4 =

```
    2.1216
```

Sim4 =

```
    2.8297    3.2909
    2.2158    2.4080
    1.5232    1.5269
    0.8603    0.6543
```

0.2285	-0.1992
-0.6821	-1.0166
-1.6861	-1.7699
-2.6287	-2.4126
-3.0987	-2.8717
-3.3115	-3.0540
-3.1798	-2.8981
-2.5041	-2.4675
-2.0208	-1.9469
-1.5544	-1.4952
-1.0936	-1.1621
-0.7567	-0.9317
-0.5287	-0.7739
-0.4940	-0.6644
-0.4883	-0.5867
-2.1600	-2.9630
-4.5524	-4.5572
-6.7236	-6.1438
-8.1363	-7.7100
-9.3413	-9.2349
-10.7015	-10.6822
-11.6217	-11.9861
-12.7751	-13.0214
-13.4433	-13.5500
-13.2426	-13.1635
-11.4619	-11.4283
-8.2448	-8.5654
-5.8635	-5.7166
-3.6970	-3.6968
-2.4371	-2.4671
-1.7974	-1.7358
-1.2967	-1.2875
-1.1205	-1.0000
-1.1004	-0.8075
1.5000	1.3615
1.5933	1.4045
1.6437	1.4241
1.6524	1.4272
1.6227	1.4185
1.5730	1.4014
1.5407	1.3782
1.4867	1.3508
1.4239	1.3205
1.3592	1.2881
1.2688	1.2546
1.1883	1.2204
1.0863	1.1859

1.0232	1.1514
0.9363	1.1172
0.8703	1.0835
0.7674	1.0503
0.6834	1.0178
0.6225	0.9861
-9.2077	-8.8329
-8.0398	-7.7102
-7.0590	-6.7332
-6.0224	-5.8861
-4.9818	-5.1535
-4.2492	-4.5206
-3.7254	-3.9739
-3.2104	-3.5016
-2.8004	-3.0929
-2.4630	-2.7389
-2.1631	-2.4315
-1.9390	-2.1641
-1.7970	-1.9309
-1.7187	-1.7269
-1.6006	-1.5482
-1.5198	-1.3910
-1.4685	-1.2525
-1.4097	-1.1301
-1.3651	-1.0217

Heat4 =

-0.3016
-0.1824
-0.0516
0.0726
56.3874
179.2164
-57.6632
-200.5562

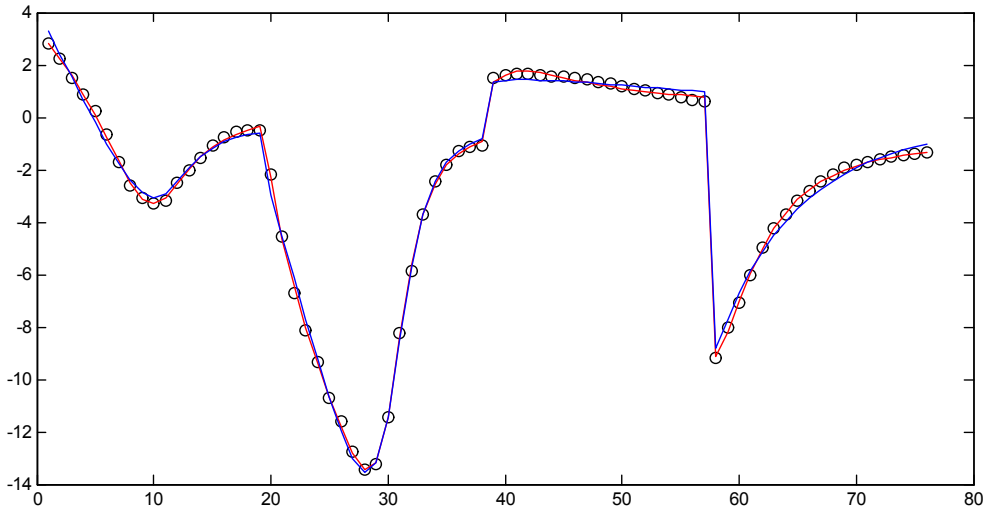

Figure S1: Fit of (7+5) parameter Model 3 (red) and (5+4) parameter model 4* (blue) to the ITC data. Note that in addition to an inferior fit, the enthalpy values obtained from Model 4 are of an unrealistically high magnitude.

Paper III

PCCP

PAPER

View Article Online
View Journal

Cite this: DOI: 10.1039/c8cp01151f

Effects of methyl substitution on DNA binding enthalpies of enantiopure Ru(phenanthroline)$_2$dipyridophenazine^{2+} complexes†

Anna K. F. Mårtensson and Per Lincoln*

Received 20th February 2018,
Accepted 1st April 2018

DOI: 10.1039/c8cp01151f

rsc.li/pccp

Isothermal titration calorimetry (ITC) has been utilized to investigate the effect of methyl substituents on the intercalating dppz ligand of the enantiomers of the parent complex Ru(phen)$_2$dppz^{2+} (phen = 1,10-phenanthroline; dppz = dipyrido[3,2-*a*:2′,3′-*c*]phenazine) on DNA binding thermodynamics. The methylated complexes (10-methyl-dppz and 11,12-dimethyl-dppz) have large, concentration-dependent, positive heats of dilution, and a strong endothermic background is also apparent in the ITC-profiles from titration of methylated complexes into poly(dAdT)$_2$, which make direct comparison between complexes difficult. By augmenting a simple cooperative binding model with one equilibrium for complex self-aggregation in solution and one equilibrium for complex aggregation on saturated DNA, it was possible to find an excellent global fit to the experimental data with DNA affinity parameters restricted to be equal for all Δ-enantiomers as well as for all Λ-enantiomers. In general, enthalpic differences, compared to the unsubstituted complex, were small and less than 4 kJ mol^{-1}, except for the heat of intercalation of Δ-10-methyl-dppz (−11,6 kJ mol^{-1}) and Λ-11,12-dimethyl-dppz (+4.3 kJ mol^{-1}).

Introduction

Since the mid-1980s, there have been extensive studies on ruthenium(II) polypyridyl complexes.[1–5] Along with their interesting photophysical properties, ruthenium complexes have been shown to have various useful interacting properties, such as acting as DNA probes[6] or inducing DNA cleavage.[7] Extending one of the planar ligands of the complex will facilitate intercalation between the base pairs, the most studied examples being ruthenium complexes possessing a dppz moiety (dppz = dipyrido[3,2-*a*:2′,3′-*c*]phenazine). Originally denoted "light-switch complexes", tris-bidentate complexes of the general structure Ru(L)$_2$dppz^{2+} (L = phen(1,10-phenanthroline) or bpy (2,2′-bipyridine)) will display a massive increase in the quantum yield when intercalated to DNA,[6,8–10] owing to the hydrophobic environment between the base pairs protecting the dppz moiety from hydrogen bonding with the solvent water molecules.[11,12]

By introducing small changes into the molecular structure of the complex, it is possible to modify the photophysical properties and also the DNA binding affinity and specificity. Consequently, there have been numerous reports on ruthenium complexes with substituents on both the ancillary and the intercalating ligands.[13–18] By adding methyl groups on the outermost benzene ring of the dppz ligand in Ru(phen)$_2$dppz^{2+} the steric consequences might alter the binding motifs of the complex. Previous studies observed a significant lengthening of the excited state lifetimes of dppz-based ruthenium complexes with methyl substitutions in the 10-position and in the 11,12-positions of the dppz moiety, which was attributed to a steric interference of the hydration cage around the complex.[6,19] The structurally similar complex Ru(TAP)$_2$dppz^{2+} (TAP = 1,4,5,8-tetraazaphenanthrene) has been reported to bind more strongly to DNA when methyl-substituted in the 11,12-position of the dppz moiety.[20] Methyl substituents in the 11,12-positions of the dppz moiety of Cr(phen)$_2$dppz^{3+} also increased the binding affinity of the parent complex.[21] In contrast, methyl substituted dpq (dpq = dipyrido[3,2-*f*:2′,3′-*h*]-quinoxaline), a close analogue of dppz, has shown a decrease in DNA binding strength compared to its parent complex Ru(phen)$_2$dpq^{2+}, which was attributed to steric hindrance of the bulky methyl groups.[22] Clearly, methyl substituents may alter the binding properties of intercalative complexes, but there are still many questions on the underlying binding mechanism that have been left unanswered. Also, many of the previous studies have limited themselves to unresolved ruthenium complexes. This is unfortunate as it has been demonstrated on numerous occasions by various experimental methods that DNA binding is highly influenced by the chirality of

Department of Chemistry and Chemical Engineering, Chalmers University of Technology, SE-41296 Gothenburg, Sweden. E-mail: lincoln@chalmers.se

† Electronic supplementary information (ESI) available. See DOI: 10.1039/c8cp01151f

tris-bidentate ruthenium complexes with the right-handed Δ-form generally having a stronger affinity to DNA than the Λ-form.[1,18,23–27]

Isothermal titration calorimetry (ITC) is a high-precision tool used for the thermodynamic characterization of ligand binding to a macromolecule (*e.g.* DNA) and is the only thermodynamic method that directly measures all energetics associated with the ligand–macromolecule interaction process.[28–30] Aliquots of the ligand are added to a solution of the macromolecule and the resulting heat effects observed can then be analysed for quantitative characterization of the energetic processes associated with the binding reaction. As the titration progresses, the binding sites on the macromolecule become increasingly occupied and at the end of the titration, only a small heat change caused by ligand dilution and other non-specific effects will be registered. In most cases this is corrected for by simply subtracting the average heat of dilution from a blank titration of ligand into buffer. However, if the blank titration shows a large non-constant heat of dilution it cannot simply be dismissed by subtraction. As an effect of the highly concentrated titrant solution, the ligands may self-aggregate to form oligomers, which partly dissociate when added to the macromolecule solution.[31,32] Being another equilibrium process involving the free ligand in solution, the self-aggregation needs to be included in the analysis of the ligand–DNA interaction.

Intercalating dppz-based ruthenium complexes have previously been demonstrated to either facilitate or hinder the adjacent binding of neighboring complexes along the DNA polymer.[27,33] In addition, the binding sites on a DNA polymer are in such close proximity of each other that each intercalated ruthenium complex covers more than one binding site. Based on the classical McGhee and von Hippel model, where DNA is treated as a one-dimensional lattice of binding sites,[34] we have recently developed a general algorithm that can be utilized for the model fitting of binding interactions between ligands and linear biopolymers.[35]

In this study, we seek to thermodynamically characterize the DNA binding of $Ru(phen)_2dppz^{2+}$ with methyl groups substituted in the 10-position or the 11,12-positions of the dppz moiety (Fig. 1). In order to avoid the effects of DNA sequence heterogeneity, we chose to use poly(dAdT)$_2$ (AT-DNA) for the ligand–DNA interaction. Since the methylated complexes show a pronounced non-constant heat of dilution, this has been included in the analysis.

Experimental

Materials and sample preparation

All experiments were performed in aqueous solution (pH = 7.0) containing 150 mM NaCl and 1 mM cacodylate (dimethylarsinic acid sodium salt). A stock solution of poly(dAdT)$_2$ (AT-DNA) (~5 mM nucleotides) was prepared by dissolving the sodium salt (Sigma-Aldrich) in buffer. Stock solutions of the complexes (~1 mM) were prepared by dissolving the chloride salts in buffer. Concentrations were determined spectrophotometrically using extinction coefficients: ε_{260} = 6600 M^{-1} cm^{-1} per nucleotide for AT-DNA and ε_{440} = 20 000 M^{-1} cm^{-1} for the ruthenium complexes. For ITC measurements the DNA solution was dialyzed against pure buffer for at least 48 hours at 8 °C. Ruthenium complex solutions of appropriate concentrations were prepared by dilution of the stock solutions in the dialysate. The dialysis membrane used had a molecular weight cut-off of 3.5–5 kDa (Spectra-Por® Float-A-Lyzer® G2, Sigma-Aldrich).

The enantiopure Δ- and Λ-$[Ru(phen)_2dppz]Cl_2$, $[Ru(phen)_2dppzCH_3]Cl_2$ and $[Ru(phen)_2dppz(CH_3)_2]Cl_2$ (here denoted **1**, **2** and **3**, respectively) used in this study were synthesized and resolved as previously reported.[23,36]

Other chemicals were purchased from Sigma-Aldrich and used without purification.

Absorption spectra were measured on a Varian Cary 4000 UV/vis (Agilent Technologies) spectrophotometer (path length = 1 cm).

Isothermal titration calorimetry

During an isothermal titration calorimetry (ITC) experiment, the heat produced or absorbed upon addition of the complex to a DNA solution enables direct assessment of the binding free energy by integrating the power required to maintain the reference and sample cells at the same temperature. The experimental raw data consist of a series of heat flow peaks and each peak corresponds to one injection of the ruthenium complex. These heat flow peaks are then integrated with respect to time, to give the total heat exchanged per mole injectant plotted against the ratio [Ru complex]/[base pairs].

Calorimetric data were obtained using a MicroCal iTC200 isothermal titration calorimeter (Malvern) controlled by Origin 7.0 software. The ITC profiles of the resolved ruthenium complexes were obtained by a single injection of 1 μl followed by 19 sequential injections of 2 μl aliquots of stock solution (~590 μM) of the complex from a syringe into the sample cell

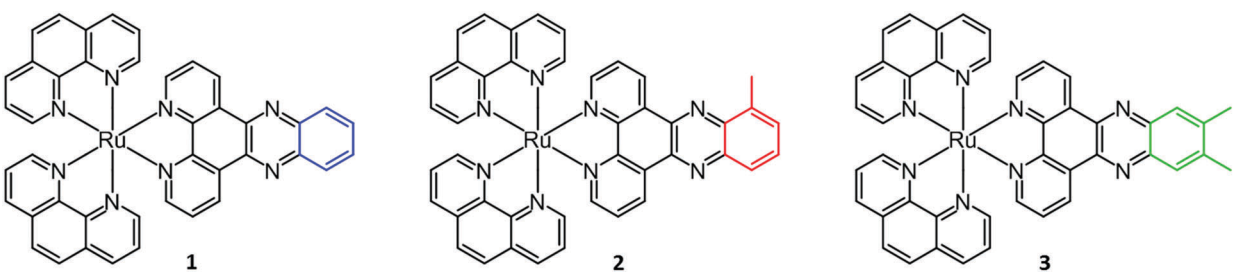

Fig. 1 Structures of ruthenium complexes $Ru(phen)_2dppz^{2+}$ (**1**), $Ru(phen)_2dppzCH_3^{2+}$ (**2**) and $Ru(phen)_2dppz(CH_3)_2^{2+}$ (**3**).

(206 μl) loaded with AT-DNA in 150 mM NaCl aqueous buffer solution (~312 μM nucleotides) or with buffer alone. All ITC experiments were performed at 25 °C. The injection spacing was 180 s, the syringe rotation was 750 rpm and there was an initial delay of 120 s prior to the first injection. The raw ITC data peaks were automatically integrated using the Origin 7.0 software. For improved accuracy of the integration, the integration range for the spacing between each heat peak was narrowed, thus reducing the background noise from the baseline.

Analysis of binding isotherms

For the analysis of the ITC-data we have used the classical McGhee–von Hippel DNA binding model, which assumes identical intercalation pockets in-between each base pair. In this model, the DNA ligand is characterized by an intrinsic binding constant K (for binding without neighbor interactions), a cooperativity parameter y (for cooperative binding interactions with neighbors, $y > 1$, for anti-cooperative neighbor interactions $0 < y < 1$) and the number n of binding sites made inaccessible by the binding of one ligand. We have previously described an efficient algorithm for solving the mass balance for a general McGhee–von Hippel system,[35] and here we have also incorporated a ligand solution oligomerization equilibrium $m\,\mathrm{L} \rightarrow \mathrm{L}_m$ into the mass balance (for details of the implementation, see the program code in ESI†). The thermodynamic constant for this equilibrium is

$$K_m = \frac{[\mathrm{L}_m]}{[\mathrm{L}]^m} \cdot C^{\circ(m-1)} \quad (1)$$

(where, as described elsewhere in this paper, equilibrium constants are unit-less and refer to the standard state concentration C° = 1 mol per liter). To be able to compare oligomerization constants with different m, the value of the effective dimerization constant $K_{\mathrm{m}}^{1/(\mathrm{m}-1)}$ was calculated.

Two different intercalation pockets, TA/TA and AT/AT, alternate in the AT-DNA used for this study. However, for simplicity, the present model considers them to be equal, and thus n is expected to be close to 2 as for classical intercalation.

Furthermore, each intercalated ligand is also assumed to be able to become an external binding site for an additional ligand, characterized by an external binding constant K_{ext}, which we have arbitrarily set as 10^4 for all ligands. The effect of external binding on the mass balance has been neglected, since K_{ext} used will be at least 100 times less than the effective ligand intercalation binding constant, which is in the range between Ky and Ky^2 when the free ligand concentration starts to rise as a consequence of increasing intercalation site saturation.

Results

Isothermal titration calorimetry and model fitting

The raw ITC data of the enantiomers of complexes **1**, **2** and **3** are shown in Fig. S1(Δ) and S2(Λ) of ESI.† To the left side of the figures, the ligand is titrated into AT-DNA, and to the right, the ligand is titrated into pure buffer. The ITC profiles obtained deviate strongly from the standard sigmoidal shape typically expected from a ligand–macromolecule binding system with a single type of non-overlapping binding sites. This is consistently observed for both enantiomers of complexes **1**–**3**. As previously suggested by us, this indicates a more complicated ligand–macromolecule binding system with at least two different types of binding interactions present.[27,33,35] The Λ-enantiomers share the common feature of showing a more exothermic ITC profile than their Δ counterpart. All complexes show a non-constant heat of dilution, which is small for the unsubstituted complex **1**, but very prominent for methylated complexes **2** and **3**. Moreover, upon saturation at the end of the titration, when almost all binding sites on the DNA strand are occupied by ligands, the methyl substituted complexes **2** and **3** both show much more intense endothermal heat peaks, compared to the parent complex **1**, which cannot be explained by heat of dilution only. To account for the phenomena in a physically meaningful way, here we have explicitly considered the heat of aggregation in solution as well as of external ligand binding to saturated DNA, rather than to introduce constant base-line terms in the model.

Linear dichroism studies in solution do not indicate significant binding geometry differences between **1**, **2** and **3** for either enantiomer,[19] and high resolution X-ray crystal structures of the Λ-enantiomers show virtually identical intercalation geometries irrespective of methyl substituents.[20] Thus, it seemed reasonable to attempt a global fit to the ITC data assuming identical intercalation equilibrium constants K and neighbor interaction parameters y for each set of enantiomers, while allowing the binding site coverage parameter n to vary freely.

Aside from the intrinsic (ΔH_K°) and neighbor interaction (ΔH_y°) reaction enthalpies, this model also considers the oligomer dissociation (ΔH_m°) as well as the external DNA association ($\Delta H_{\mathrm{ext}}^\circ$) enthalpy. As can be seen in Fig. 2, it is possible to find a very good global fit to the integrated peaks of the raw data in Fig. S1 and S2 (ESI†) which gave nRMSD = 7.3% (nRMSD: normalized root-mean-square-deviation, the Euclidian norm of the residual divided by the Euclidian norm of the data). In fact, allowing K and y to vary freely gave only a slightly lower nRMSD (6.4%), indicating that the assumption of similar binding affinity parameters for each set of enantiomers was consistent with the data.

Table 1 gives the best global fit binding parameter values, showing that the Δ-enantiomer is anti-cooperative in its nearest-neighbor interactions while the Λ-enantiomer is cooperative. It is worth noting that although the intrinsic binding constant K differs by more than two orders of magnitude between the enantiomers, the effective binding constant close to saturation, Ky^2, is rather similar: $Ky^2 = 5.9 \times 10^6$ for Δ and 3.2×10^6 for Λ.

Interestingly, the Λ-enantiomers all have larger binding site coverage parameters n compared to Δ. While the difference is small for complexes **1** and **3**, it is prominent for complex **2**.

The self-aggregation (expressed as the effective dimerization constant $K_m^{1/(m-1)}$ in Table 1) increases with the number of methyl groups, but the effective dimerization enthalpy $\Delta H_m^\circ/(m-1)$ remains relatively constant as shown in Table 2. The external binding contribution to the ITC-signal $\Delta H_{\mathrm{ext}}^\circ$ becomes more

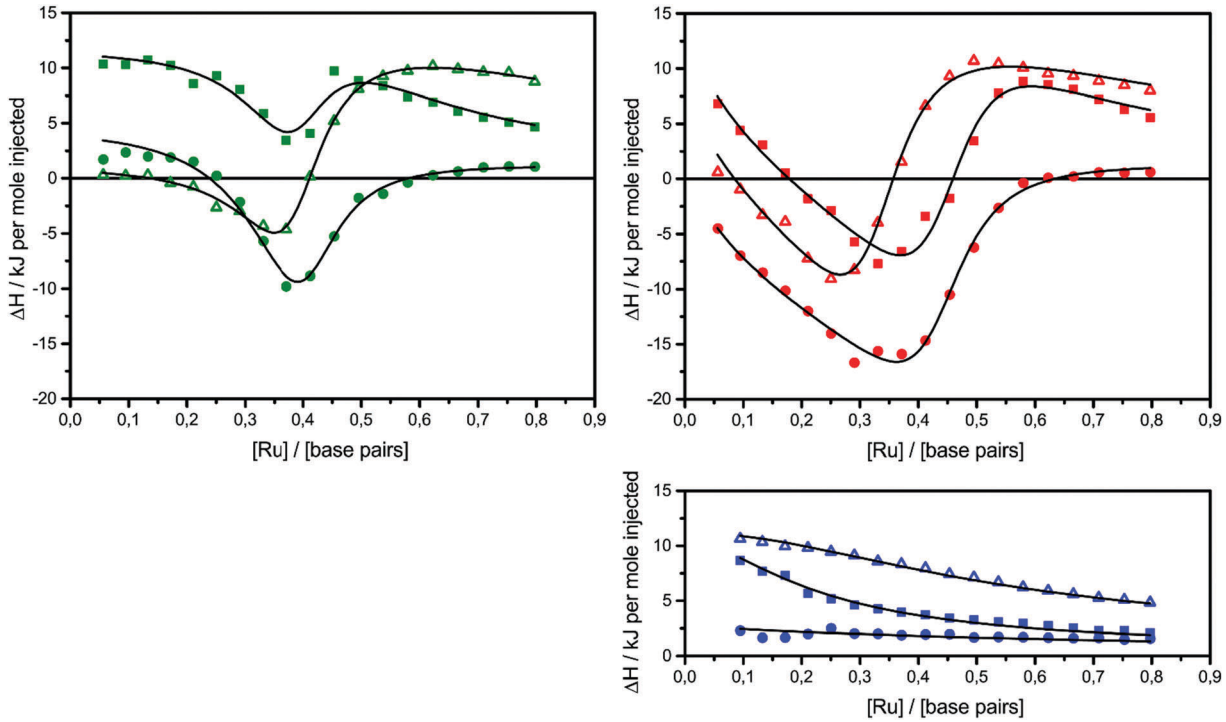

Fig. 2 ITC profiles with fitted traces for the titrations of the Δ-enantiomers (top left) and the Λ-enantiomers (top right) into poly(dAdT)$_2$. The symbols (circle: 1; triangle: 2; square: 3) indicate the normalized heat absorbed or evolved upon 2 μl injections of the complex (~590 μM) into the 206 μl cell containing DNA (~320 μM nucleotides). The bottom right graph shows the averaged titration of both enantiomers into pure buffer. All titrations were performed in 150 mM NaCl aqueous solution at 25 °C.

Table 1 Binding parameter values from global fit to ITC-data (enantiomer-common fit values in italics)

	$K_\Delta/10^6$	$y_{\Delta\Delta}$	n_Δ	$K_\Lambda/10^6$	$y_{\Lambda\Lambda}$	n_Λ	$K_m^{1/(m-1)}$	m
1	*41*	*0.38*	2.17	*0.28*	*3.4*	2.29	400	2.0
2	*41*	*0.38*	2.25	*0.28*	*3.4*	2.99	3300	3.0
3	*41*	*0.38*	2.24	*0.28*	*3.4*	2.25	8900	2.7

Table 2 Enthalpy values from fit to ITC-data (in kJ mol^{-1})

	Δ			Λ		
	1	**2**	**3**	**1**	**2**	**3**
$\Delta H_m^\circ(m-1)$	−19.5	−26.8	−21.8	−19.5	−26.8	−21.8
ΔH_K°	+1.2	−10.4	+0.4	−4.5	−6.1	−0.2
ΔH_y°	−7.7	−4.3	−4.4	−13.7	−14.8	−16.3
ΔH_{ext}°	−1.0	+2.1	+2.4	−0.5	+5.1	+9.2

prominent upon methylation, in particular for the Λ-enantiomers, but the weak binding makes it impossible to partition this trend into external binding affinity and external binding enthalpy. However, the distinct diastereomeric differences for **2** and, in particular, for **3** suggest that the distal benzene ring of the dppz of one complex and the phenanthroline of another are important for the external binding mode. By electrostatic arguments, it appears most likely that this interaction occurs in the groove opposite to where the Ru(phen)$_2$-moieties of the intercalated complexes reside, *i.e.* that it is the phenanthrolines of the externally bound complexes that interacts with the methyl groups of the intercalated ones.

The differences in the intercalation enthalpy (ΔH_K°) between the enantiomers of the same complex show no clear trend, but the neighbor interaction enthalpy (ΔH_y°) for Λ is about 2–3 times more exothermic than that of Δ. (As an example, the different enthalpy contributions are illustrated for complex **2** in Fig. S3 of ESI.†)

Table 3 highlights the differences in the enthalpy values due to methyl substitution. The much more exothermic intercalation for the Δ-enantiomer of **2** compared to **1** stands out as the most significant effect, followed by the less exothermic intercalation of the Λ-enantiomer of **3** and the less exothermic neighbor interaction enthalpies of the Δ-enantiomers of **2** and **3**.

Table 4 gives the free energy changes and entropy contributions calculated from the data in Tables 1 and 2. Since the free energy changes were assumed to depend on chirality only, differences in $T\Delta S^\circ$ between different complexes directly reflect the enthalpy changes in Table 3. However, these are small enough not to change the overall pattern: intercalation is in all cases predominantly entropy driven, and most so for Δ-enantiomers;

Table 3 Changes in enthalpy values due to methyl substitution (in kJ mol^{-1})

Complex	$\Delta(\Delta H_{K\Delta}^\circ)$	$\Delta(\Delta H_{y\Delta}^\circ)$	$\Delta(\Delta H_{K\Lambda}^\circ)$	$\Delta(\Delta H_{y\Lambda}^\circ)$
2	−11.6	+3.4	−1.6	−1.1
3	−0.8	+3.3	+4.3	−2.6

Table 4 Derived thermodynamic parameters from global fit (in kJ mol^{-1} at 25 °C)

	$\Delta G^{\circ}_{K\Delta} = -43.5$	$\Delta G^{\circ}_{y\Delta} = +2.4$	$\Delta G^{\circ}_{K\Lambda} = -31.1$	$\Delta G^{\circ}_{y\Lambda} = -3.0$
	$T\Delta S^{\circ}_{K\Delta}$	$T\Delta S^{\circ}_{K\Lambda}$	$T\Delta S^{\circ}_{y\Delta}$	$T\Delta S^{\circ}_{y\Lambda}$
1	+44.7	+26.6	−10.1	−10.7
2	+33.1	+25.0	−6.7	−11.8
3	+43.9	+30.9	−6.8	−13.3

the neighbor interaction on the other hand, in all cases, has a large unfavorable entropy.

Discussion

Adding methyl substituents on the distant benzene ring of the intercalating dppz ligand in the parent complex $Ru(phen)_2dppz^{2+}$ increases the hydrophobicity of the complex causing an increased self-aggregation of dimer/trimer structures. This in turn results in a high non-constant heat of dilution when the ligand is added to the macromolecule solution. This additional enthalpy change is in the majority of ITC-studies simply subtracted from the experimental data, but here the magnitude of the heat change is too large not to be included in the analysis.

For any binding model to be of practical use, a large number of fitting parameters is not acceptable. Here, we demonstrate an algorithm making it possible to fit experimental data of complicated ligand–macromolecule systems using only a minimum of additional parameters. In order not to over-interpret the data, we have limited the binding model to be the simplest possible. Thus effects due to AT/AT and TA/TA-differences, possible different groove-locations and different intercalation geometries are all neglected. Furthermore, we test the hypothesis that methyl substitution does significantly alter K and y for a given enantiomer.

When the self-aggregation and external binding effects had been accounted for, the seemingly disparate ITC-curves of **1**, **2** and **3** (Fig. 2) were indeed found to be consistent with the same binding affinity for all Δ and all Λ enantiomers, *i.e.* all differences due to methylation could satisfactorily be accounted for as differences in the binding site coverage (n) and the binding and the interacting enthalpy values. This suggests that methylation on the distant benzene ring does not dramatically alter the binding affinity characteristics typical for the enantiomers.

The graphs of concentration changes in the total bound ligand and the neighboring bound ligand, respectively, for Δ and Λ are depicted for **1** in Fig. 3. The more cooperative binding of Λ becomes apparent in the initial part of the interaction curve; the convex shape is due to the facilitated binding of additional ligands. Δ-enantiomers, in contrast, have a concave initial shape due to the anti-cooperative behavior of the ligands. Since the fitting model needs to produce a close coincidence of the Δ and Λ-curves at the end of the titrations, the intrinsic binding constant K has to be correspondingly higher for the anti-cooperative Δ-enantiomer than for Λ.

X-ray structures by Hall *et al.* have demonstrated the $Ru(TAP)_2dppz$ analogues of Λ-**1**, -**2** or -**3** to intercalate with

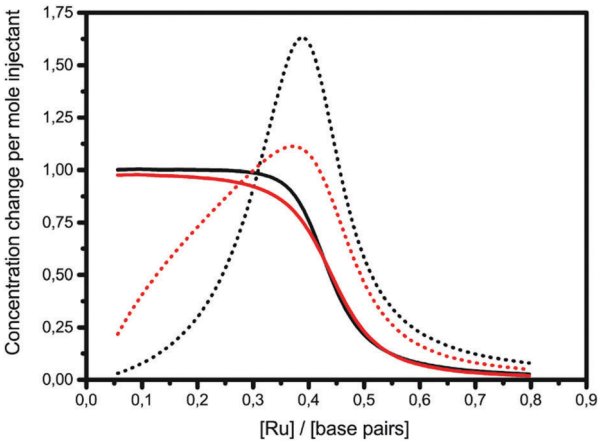

Fig. 3 ITC titrations with complex **1** into poly(dAdT)$_2$ with the changes in the concentration of the total bound ligand (solid line) and the neighboring bound ligand (dotted line) (black: Δ; red: Λ).

the same depth and the same angular orientation.[20] The X-ray structure further showed that the 10-methyl group on dppz efficiently protects the exposed dppz aza-nitrogen from interaction with water, consistent with the observation by Olofsson *et al.* that methyl substitution in the 10-position gave longer luminescence lifetimes for both enantiomers, in polyol solution as well as when intercalated to DNA.[19] Fig. 4 (left) shows a model of three Δ-**2** complexes consecutively intercalated (from the minor groove, as per the suggestion from X-ray structures) two base pairs apart from each other. A more hydrophobic environment around the 10-methyl group, as suggested by the model, than for the methyl groups of the 11,12-disubstituted derivative Δ-**3** (Fig. 4 (right)) might account for the significantly more exothermic intercalation enthalpy of Δ-**2**. If this is the case,

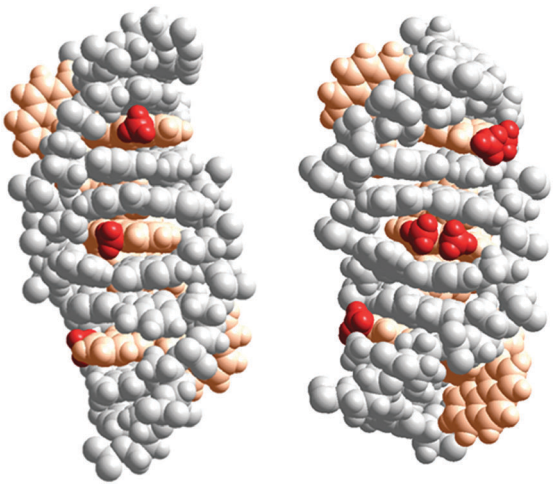

Fig. 4 Schematic illustration of the proposed interaction geometries for Δ-**2** (left) and Δ-**3** (right) intercalated into DNA. The model was constructed by manual docking and subsequent energy minimization in vacuum, using the Amber 2 force field in the HyperChem 8.0 software package (HyperCube, Inc.). The ruthenium(II) ions together with the ancillary and intercalating ligands are colored orange, while the methyl substituents are colored red for easier identification.

the environment around the methyl group of the corresponding enantiomer Λ-**2** is expected to be different, perhaps due to a different intercalation depth or different angular orientation in the intercalation pocket.

Conclusions

The addition of methyl substituents on the intercalating dppz moiety of ruthenium(II) polypyridyl complexes results in non-constant heat of dilution when titrated into a DNA solution. These heat peaks are too strong to simply be subtracted from the intrinsic binding enthalpy and must be included in the analysis. By incorporating the oligomer dissociation as well as the external DNA association enthalpy changes into our general mass balance solving algorithm, we have here demonstrated how complicated binding systems with a large background enthalpy change can still be properly fitted into a binding model, without the need to add unnecessary many parameters. A satisfactory global fit was found when assuming the binding affinities for each enantiomer of both non-methylated and methylated dppz-Ru to be equal, while only allowing the binding site size to vary freely.

Conflicts of interest

There are no conflicts to declare.

Acknowledgements

The authors gratefully acknowledge Swedish Research Council (Vetenskapsrådet) grant 2016-05421 and Chalmers Area of Advance Nano for funding, as well as COST Action CM1105 for providing a forum for stimulating discussions.

Notes and references

1 J. K. Barton, A. T. Danishefsky and J. M. Goldberg, *J. Am. Chem. Soc.*, 1984, **106**, 2172–2176.
2 C. V. Kumar, J. K. Barton and N. J. Turro, *J. Am. Chem. Soc.*, 1985, **107**, 5518–5523.
3 J. K. Barton, J. M. Goldberg, C. V. Kumar and N. J. Turro, *J. Am. Chem. Soc.*, 1986, **108**, 2081–2088.
4 A. Yamagishi, *J. Chem. Soc., Chem. Commun.*, 1983, 572–573.
5 J. M. Kelly, A. B. Tossi, D. J. McConnell and C. Ohuigin, *Nucleic Acids Res.*, 1985, **13**, 6017–6034.
6 R. M. Hartshorn and J. K. Barton, *J. Am. Chem. Soc.*, 1992, **114**, 5919–5925.
7 J. M. Kelly, D. J. McConnell, C. Ohuigin, A. B. Tossi, A. K. D. Mesmaeker, A. Masschelein and J. Nasielski, *J. Chem. Soc., Chem. Commun.*, 1987, 1821–1823.
8 A. E. Friedman, J. C. Chambron, J. P. Sauvage, N. J. Turro and J. K. Barton, *J. Am. Chem. Soc.*, 1990, **112**, 4960–4962.
9 A. E. Friedman, C. V. Kumar, N. J. Turro and J. K. Barton, *Nucleic Acids Res.*, 1991, **19**, 2595–2602.
10 Y. Jenkins, A. E. Friedman, N. J. Turro and J. K. Barton, *Biochemistry*, 1992, **31**, 10809–10816.
11 B. Önfelt, P. Lincoln, B. Nordén, J. S. Baskin and A. H. Zewail, *Proc. Natl. Acad. Sci. U. S. A.*, 2000, **97**, 5708–5713.
12 C. G. Coates, J. Olofsson, M. Coletti, J. J. McGarvey, B. Önfelt, P. Lincoln, B. Nordén, E. Tuite, P. Matousek and A. W. Parker, *J. Phys. Chem. B*, 2001, **105**, 12653–12664.
13 J. G. Liu, B. H. Ye, H. Li, L. N. Ji, R. H. Li and J. Y. Zhou, *J. Inorg. Biochem.*, 1999, **73**, 117–122.
14 J. G. Liu, Q. L. Zhang, X. F. Shi and L. N. Ji, *Inorg. Chem.*, 2001, **40**, 5045–5050.
15 L. Wang, J. Z. Wu, G. Yang, T. X. Zeng and L. N. Ji, *Transition Met. Chem.*, 1996, **21**, 487–490.
16 B. Y. Wu, L. H. Gao, Z. M. Duan and K. Z. Wang, *J. Inorg. Biochem.*, 2005, **99**, 1685–1691.
17 D. Lawrence, V. G. Vaidyanathan and B. U. Nair, *J. Inorg. Biochem.*, 2006, **100**, 1244–1251.
18 P. U. Maheswari, V. Rajendiran, M. Palaniandavar, R. Parthasarathi and V. Subramanian, *J. Inorg. Biochem.*, 2006, **100**, 3–17.
19 J. Olofsson, L. M. Wilhelmsson and P. Lincoln, *J. Am. Chem. Soc.*, 2004, **126**, 15458–15465.
20 J. P. Hall, H. Beer, K. Buchner, D. J. Cardin and C. J. Cardin, *Organometallics*, 2015, **34**, 2481–2486.
21 S. Vasudevan, J. A. Smith, M. Wojdyla, A. DiTrapani, P. E. Kruger, T. McCabe, N. C. Fletcher, S. J. Quinn and J. M. Kelly, *Dalton Trans.*, 2010, **39**, 3990–3998.
22 K. O'Donoghue, J. C. Penedo, J. M. Kelly and P. E. Kruger, *Dalton Trans.*, 2005, 1123–1128.
23 C. Hiort, P. Lincoln and B. Nordén, *J. Am. Chem. Soc.*, 1993, **115**, 3448–3454.
24 I. Haq, P. Lincoln, D. Suh, B. Nordén, B. Z. Chowdhry and J. B. Chaires, *J. Am. Chem. Soc.*, 1995, **117**, 4788–4796.
25 P. Lincoln, A. Broo and B. Nordén, *J. Am. Chem. Soc.*, 1996, **118**, 2644–2653.
26 P. Lincoln and B. Nordén, *Chem. Commun.*, 1996, 2145–2146.
27 J. Andersson, L. H. Fornander, M. Abrahamsson, E. Tuite, P. Nordell and P. Lincoln, *Inorg. Chem.*, 2013, **52**, 1151–1159.
28 I. Jelesarov and H. R. Bosshard, *J. Mol. Recognit.*, 1999, **12**, 3–18.
29 T. Wiseman, S. Williston, J. F. Brandts and L. N. Lin, *Anal. Biochem.*, 1989, **179**, 131–137.
30 J. E. Ladbury and B. Z. Chowdhry, *Chem. Biol.*, 1996, **3**, 791–801.
31 K. Luke, D. Apiyo and P. Wittung-Stafshede, *Biophys. J.*, 2005, **89**, 3332–3336.
32 A. Velazquez-Campoy, S. A. Leavitt and E. Freire, *Methods Mol. Biol.*, 2004, **261**, 35–54.
33 A. K. F. Mårtensson and P. Lincoln, *Dalton Trans.*, 2015, **44**, 3604–3613.
34 J. D. McGhee and P. H. V. Hippel, *J. Mol. Biol.*, 1974, **86**, 469–489.
35 A. K. F. Mårtensson and P. Lincoln, *Phys. Chem. Chem. Phys.*, 2018, **20**, 7920–7930.
36 P. Lincoln and B. Nordén, *J. Phys. Chem. B*, 1998, **102**, 9583–9594.

Supporting information

Table of Contents

Figures

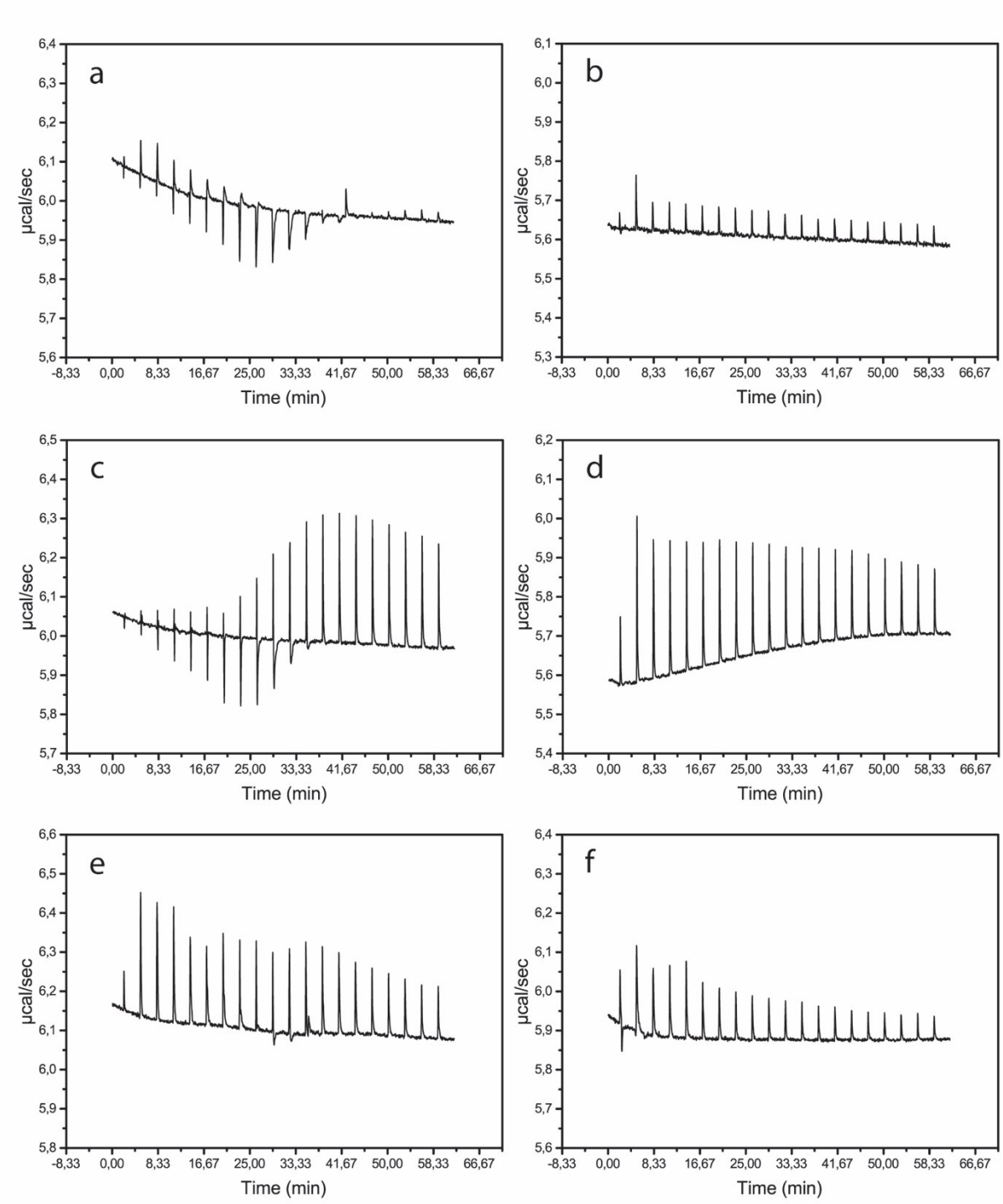

Figure S1 ITC raw data for the titration of the Δ-enantiomer of (a) **1** to AT-DNA; (b) **1** to buffer; (c) **2** to AT-DNA; (d) **2** to buffer; (e) **3** to AT-DNA; (f) **3** to buffer. All titrations were performed in 150 mM NaCl aqueous solution at 25°C. Complex (~590 µM) was injected in 2 µl aliquots to the 206 µl cell containing the DNA (~320 µM nucleotides).

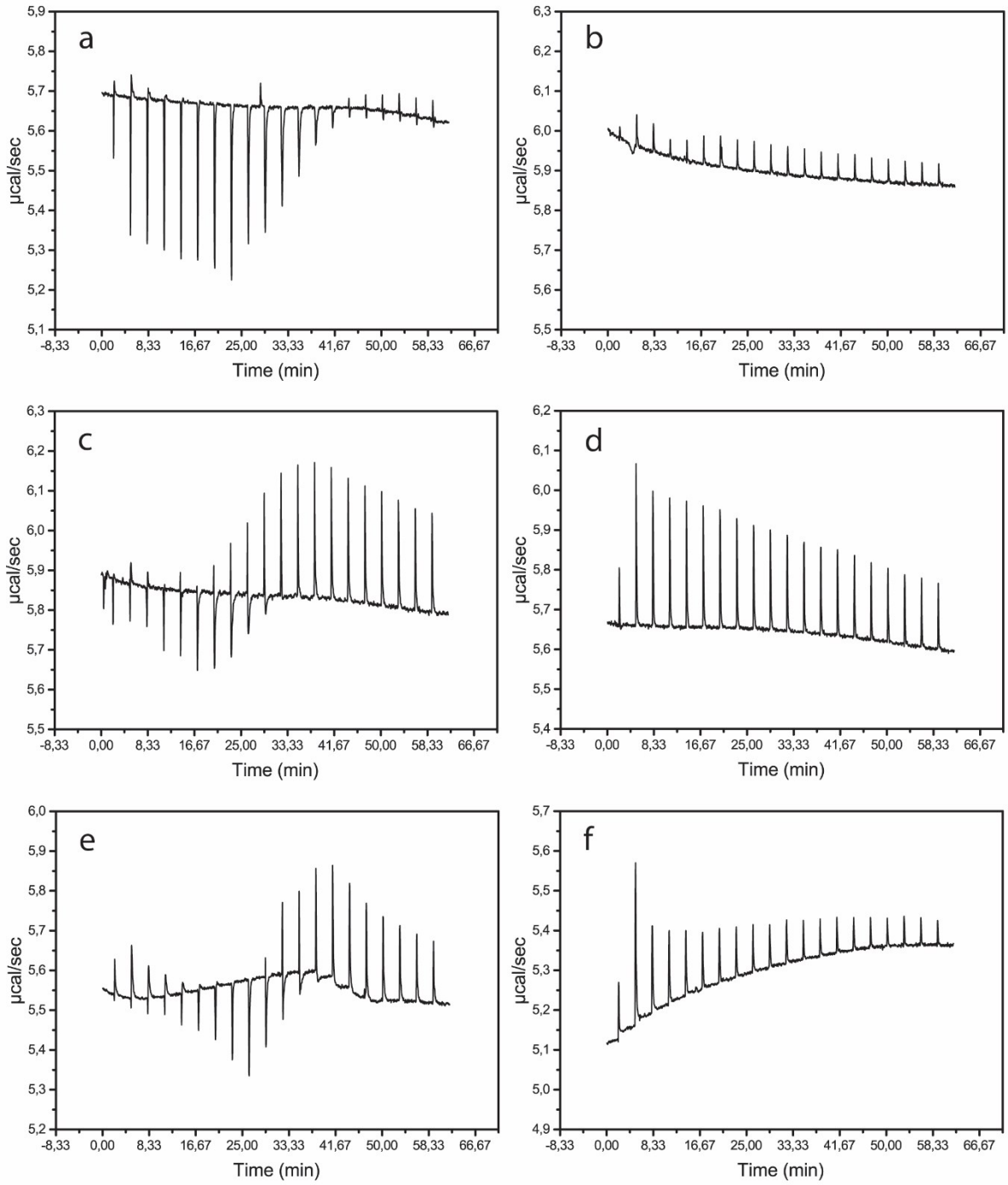

Figure S2 ITC raw data for the titration of the Λ-enantiomer of (a) **1** to AT-DNA; (b) **1** to buffer; (c) **2** to AT-DNA; (d) **2** to buffer; (e) **3** to AT-DNA; (f) **3** to buffer. All titrations were performed in 150 mM NaCl aqueous solution at 25°C. Complex (~590 µM) was injected in 2 µl aliquots to the 206 µl cell containing the DNA (~320 µM nucleotides).

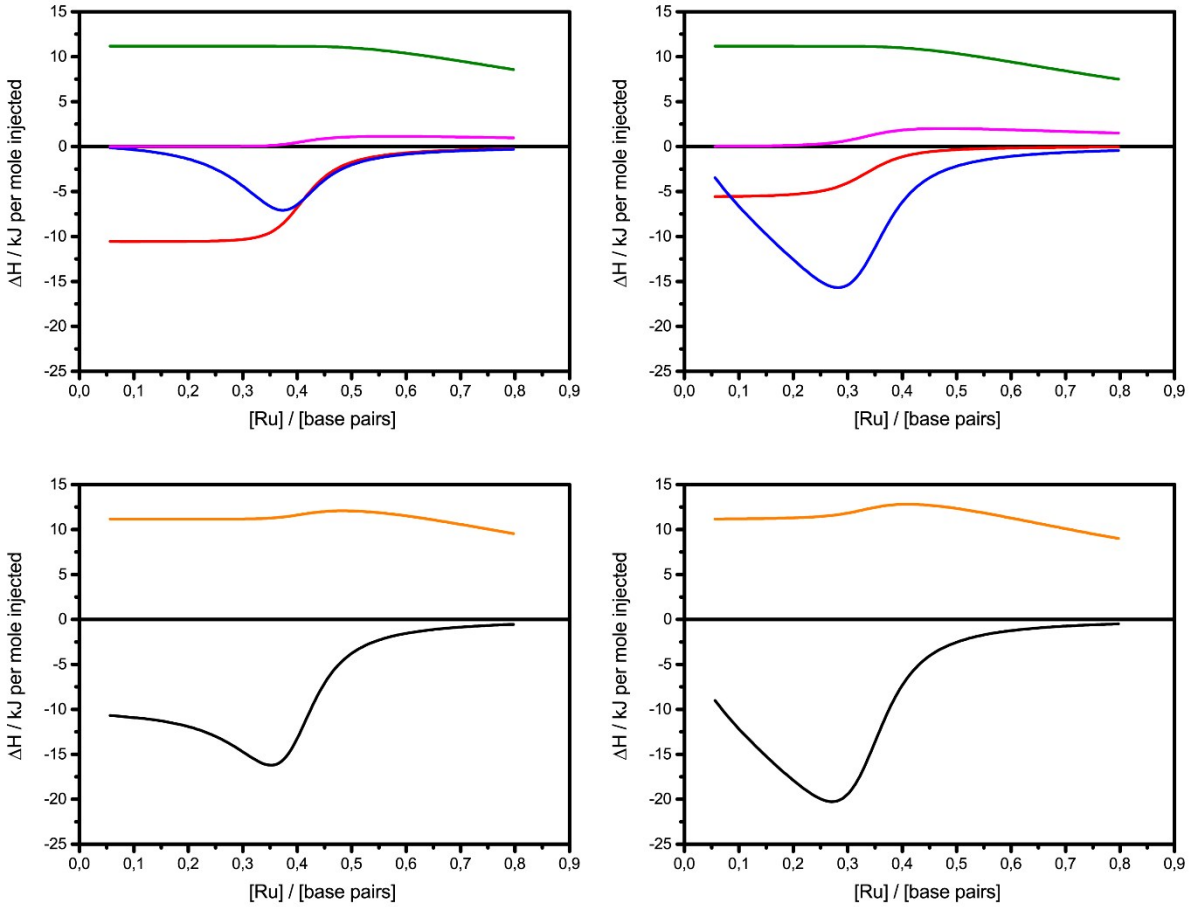

Figure S3 ITC profiles with fitted traces for the titrations of Δ-**2** (left) and Λ-**2** (right) to poly(dAdT)$_2$. Each trace show the different contributions of enthalpy change for the ligand-DNA binding interaction; Green: dilution of free ligand; Red: intercalation; Blue: neighbor interactions; Magenta: external binding; Orange: background (dilution + external); Black: ITC signal with background enthalpy removed.

Programs

ITCalgorithmDeltaLambda

```
function [err,err0,sim,heat]=ITCalgorithmDeltaLambda(tpar,totdata1,totdata2,A0)
%Calculates the ITC curves for binding of enantiomer ligands La and Lb
%that form single symmetrical subunits when binding
%to an infinite chain of identical binding sites D using
%the combined SGF-McGhee von Hippel approach. The oligomerization of L in solution
%and the further binding of L to the saturated lattice are both taken into account.

%INPUT:
%tpar=[1) Ka  2) yAA 3) na 4) Kb 5) yBB 6) nb 7) Km 8) m-2]
%there Km is the equilibrium constant for oligomerization: m L <-> Lm

%totdata1=[ITC-dilution ITC-data D0 La] Delta enantiomer data
%totdata1=[ITC-dilution ITC-data D0 Lb] Lambda enantiomer data
%(4*19) X 4 matrix with data and total
%concentrations, preferably with total concentrations of L in increasing order

%A0 = concentration in injectant stock solution

%OUTPUT:
%err = least square error of fit to data including penalty for very high
%entalpy and parameter values
%err0 = least square error of fit to data
%sim = [ITC-data  simulated data]

%heat = calculated heat of reaction

if min(tpar)<=0
    err=1e6;
else
Km=tpar(7)/1000;
m=tpar(8)+2;
data=[(totdata1(2:end,1)+totdata2(2:end,1))/2;totdata1(2:end,2);totdata2(2:end,2)];
%The dilution data for La and Lb are averaged.

L=1;
q=1;
while norm(q)>1e-10
    q=L+m*Km*L^m-A0;
    dqdL=1+m^2*Km*L^(m-1);
    dL=q/dqdL;
    while norm(L-dL)<=0
        dL=dL/3;
    end
    L=L-dL;
end
    M0=Km*L^m;


%Dilution
tot=totdata1(:,4);
C=[];
for t=tot'
    L=1;
q=1;
while norm(q)>1e-10
    q=L+m*Km*L^m-t;
    dqdL=1+m^2*Km*L^(m-1);
    dL=q/dqdL;
    while norm(L-dL)<=0
        dL=dL/3;
    end
    L=L-dL;
end
    C=[C;Km*L^m];
end
dc0=C(2:end,1)-(204*C(1:end-1,1)+2*M0)/206;
dc1=dc0/(2*A0/206);

%Delta:
par=tpar(1:3);
K=par(1);
Y=[1 1 ;1 par(2)];
```

```
n=par(3);
C0=totdata1(:,3:4);
r=0.01;
conc=[];
for t=C0';
    D0=t(1);
    L0=t(2);
    q=1;
    while norm(q)>1e-9;
       s=1./(Y*[1;r]);
       P=diag(s)*Y*diag([1;r]);
       v=1-P(2,2)+n*P(1,2);
       f=inv(v)*P(1,2);
       x=s(2)*r/(s(1)^n);
       q=x/K+f*D0+m*Km*(x/K)^m-L0;
       u=inv(v)*(f-P(:,2)'*diag([1-n*f;f])*P(:,2));
       dqdr=(D0*u+(x/K)*(1+m^2*Km*(x/K)^(m-1))*v)/r;
       dr=q/dqdr;
       while min(r-dr)<=0
             dr=dr/3;
       end
       r=r-dr;
    end
    conc=[conc;[(Km*(x/K)^m)-M0 D0*f*[1 P(2,2) 0.001*x/K] ]];
end
dc2=[conc(2:end,:)-conc(1:end-1,:)*204/206]/(2*A0/206);

%Lambda:
par=tpar(4:6);
K=par(1);
Y=[1 1 ;1 par(2)];
n=par(3);
C0=totdata2(:,3:4);
r=0.01;
conc=[];
for t=C0';
    D0=t(1);
    L0=t(2);
    q=1;
    while norm(q)>1e-9;
       s=1./(Y*[1;r]);
       P=diag(s)*Y*diag([1;r]);
       v=1-P(2,2)+n*P(1,2);
       f=inv(v)*P(1,2);
       x=s(2)*r/(s(1)^n);
       q=x/K+f*D0+m*Km*(x/K)^m-L0;
       u=inv(v)*(f-P(:,2)'*diag([1-n*f;f])*P(:,2));
       dqdr=(D0*u+(x/K)*(1+m^2*Km*(x/K)^(m-1))*v)/r;
       dr=q/dqdr;
       while min(r-dr)<=0
             dr=dr/3;
       end
       r=r-dr;
    end
    conc=[conc;[(Km*(x/K)^m)-M0 D0*f*[1 P(2,2) 0.001*x/K] ]];
end
dc3=[conc(2:end,:)-conc(1:end-1,:)*204/206]/(2*A0/206);

ze1=zeros(size(dc1(:,1)));

dc=[ dc1 ze1 ze1 ze1 ze1 ze1 ze1;dc2 ze1 ze1 ze1 ;dc3(:,1) ze1 ze1 ze1 dc3(:,2:4)];

heat=pinv(dc)*data;
    sim=dc*heat;
    err0=norm(data-sim,'fro');
    err=err0;
    err=err+norm(tpar)/220;         %Penalty for guess with very high parameter values
    err=err+norm(heat,'fro')/75;  %Penalty for guess that result in very high enthalpy values
    sim=[data sim];
end
```

GlobalITC

```
function [err,err0,sim,heat,terr,terr0,tvar]=GlobalITC(var,d1,d2,d3,d4,d5,d6,A0)
%Global fit of 3 ITC titrations of Delta and Lambda enantiomers of 3
%different compounds, sharing the same KD, KL, yDD and yLL binding parameters. n-values
%are allowed to vary between the 3 pairs of enantiomers, while heat of dilution is
%the same for Delta and Lambda.
%No:   1  2  3   4  5   6  7  8  9 10  11  12   13   14   15   16
%var=[KD KL yDD yLL n1 n2 n3 n4 n5 n6 Km12 Km34 Km56 m12  m34  m56  ]
%A0=stock solution conc för 1-6
if min(var)<=0
    err=1e6;
else
[err1,err01,sim1,heat1]=ITCalgorithmDeltaLambda(var([1 3 5 2 4 6 11 14]),d1,d2,A0);

[err2,err02,sim2,heat2]=ITCalgorithmDeltaLambda(var([1 3 7 2 4 8 12 15]),d3,d4,A0);

[err3,err03,sim3,heat3]=ITCalgorithmDeltaLambda(var([1 3 9 2 4 10 13 16]),d5,d6,A0);
terr=[err1 err2 err3];
terr0=[err01 err02 err03];
err=norm(terr);
err0=norm(terr0);
sim=[sim1;sim2;sim3];
heat=[heat1 heat2 heat3];
tvar=[var([1 3 5 2 4 6 11 14]);var([1 3 7 2 4 8 12 15]);var([1 3 9 2 4 10 13 16])];
end
```

MATLAB workspace

The initial guess for this global fit is based on fits of individual datasets using ITCalgorithmDeltaLambda. The search is restarted until no further reduction of the error is noted.

For information on what the numerical values etc. represent, see comments in the programs above or MATLAB documentation.

```
>> options=optimset('Display','Iter','MaxIter',24000,'MaxFunEvals',48000,'TolX',1e-6,'TolFun',1e-6);
>> Initguess=[10 1 1 3 2 2 2 2.5 2 2 .5 .01 .4 .01 1 .5];
>> tic;Bestfit=fminsearch('GlobalITC',Initguess,options,D1,L1,D2,L2,D3,L3,595);toc
…
13692      17930       8.26786       shrink
Optimization terminated:
 the current x satisfies the termination criteria using OPTIONS.TolX of 1.000000e-06
 and F(X) satisfies the convergence criteria using OPTIONS.TolFun of 1.000000e-06
Elapsed time is 332.361541 seconds.
>> tic;Bestfit=fminsearch('GlobalITC', Bestfit,options,D1,L1,D2,L2,D3,L3,595);toc
…
8463      11179       8.21745       shrink
Optimization terminated:
 the current x satisfies the termination criteria using OPTIONS.TolX of 1.000000e-06
 and F(X) satisfies the convergence criteria using OPTIONS.TolFun of 1.000000e-06
Elapsed time is 204.539907 seconds.
>> tic;Bestfit=fminsearch('GlobalITC',Bestfit,options,D1,L1,D2,L2,D3,L3,595);toc
…
8167      10802       8.19854       shrink
Optimization terminated:
 the current x satisfies the termination criteria using OPTIONS.TolX of 1.000000e-06
 and F(X) satisfies the convergence criteria using OPTIONS.TolFun of 1.000000e-06
Elapsed time is 196.558224 seconds.
>> tic;Bestfit=fminsearch('GlobalITC',Bestfit,options,D1,L1,D2,L2,D3,L3,595);toc
…
2745       3756       8.19836       shrink
Optimization terminated:
 the current x satisfies the termination criteria using OPTIONS.TolX of 1.000000e-06
 and F(X) satisfies the convergence criteria using OPTIONS.TolFun of 1.000000e-06
Elapsed time is 72.861021 seconds.
>> tic;Bestfit=fminsearch('GlobalITC',Bestfit,options,D1,L1,D2,L2,D3,L3,595);toc
```

…

482 856 8.19836 reflect

Optimization terminated:

the current x satisfies the termination criteria using OPTIONS.TolX of 1.000000e-06

and F(X) satisfies the convergence criteria using OPTIONS.TolFun of 1.000000e-06

Elapsed time is 16.680446 seconds.

>> [err,err0,sim,heat,terr,terr0,tvar]=GlobalITC(Bestfit,D1,L1,D2,L2,D3,L3,595);

>> err0

err0 =

6.1998

>> Bestfit

Bestfit =

Columns 1 through 8

41.389 0.27884 0.38022 3.4107 2.166 2.2949 2.2537 2.9887

Columns 9 through 16

2.235 2.2463 0.40589 0.0098819 0.36508 1.7433e-22 1.0198 0.67749

>> heat

heat =

-19.497 -53.73 -37.039

1.1894 -10.448 0.41634

-7.7106 -4.2695 -4.3563

-9.9474 20.846 23.757

-4.5145 -6.1307 -0.22318

-13.682 -14.811 -16.324

-4.7473 50.509 92.476

Indata matrices:

Column order: Titration into buffer Titration into AT [Base pair]/µM [Complex]/µM

Δ-$Ru(phen)_2dppz^{2+}$

D1 =

3.7566 1.7417 153.74 8.67

2.2114 2.3686 152.26 14.39

2.1588 1.9945 150.79 20.04

2.1218 1.9235 149.33 25.64

2.0451 1.5358 147.89 31.18

2.0713 0.25638 146.46 36.67

2.0021 -2.139 145.04 42.1

1.9833	-5.6969	143.64	47.47
1.9416	-9.7722	142.25	52.79
1.9244	-8.8324	140.87	58.05
1.7454	-5.2572	139.5	63.25
1.61	-1.7669	138.15	68.4
1.6451	-1.3845	136.81	73.49
1.6068	-0.35549	135.48	78.52
1.5799	0.3018	134.17	83.5
1.5607	0.64449	132.86	88.42
1.5472	1.0198	131.57	93.28
1.5006	1.0894	130.29	98.09
1.4047	1.0863	129.02	102.84

Λ-Ru(phen)$_2$dppz^{2+}

L1 =

3.6679	-4.4849	153.74	8.67
2.4308	-6.9631	152.26	14.39
1.2044	-8.4961	150.79	20.04
1.2727	-10.139	149.33	25.64
1.9543	-11.975	147.89	31.18
2.9779	-14.014	146.46	36.67
2.0697	-16.678	145.04	42.1
2.0657	-15.619	143.64	47.47
1.8531	-15.893	142.25	52.79
1.9834	-14.655	140.87	58.05
2.2098	-10.472	139.5	63.25
1.791	-6.2251	138.15	68.4
1.8303	-2.6333	136.81	73.49
1.8249	-0.37025	135.48	78.52
1.7614	0.11584	134.17	83.5
1.7011	0.22984	132.86	88.42
1.7606	0.6107	131.57	93.28
1.5178	0.55798	130.29	98.09
1.7619	0.62827	129.02	102.84

Δ-Ru(phen)$_2$(10-methyl-dppz)$^{2+}$

D2 =

12.416	0.31566	153.74	8.67

10.517	0.24837	152.26	14.39
10.162	0.30629	150.79	20.04
9.8768	-0.40978	149.33	25.64
9.7437	-0.75786	147.89	31.18
9.4239	-2.6523	146.46	36.67
8.9994	-2.9636	145.04	42.1
8.4868	-4.3023	143.64	47.47
8.1519	-4.6395	142.25	52.79
7.9208	0.15112	140.87	58.05
7.3004	5.2111	139.5	63.25
7.2236	8.1081	138.15	68.4
6.7909	9.2696	136.81	73.49
6.3102	9.7464	135.48	78.52
6.1268	10.187	134.17	83.5
5.8662	9.8917	132.86	88.42
5.6248	9.6414	131.57	93.28
5.268	9.5963	130.29	98.09
5.0021	8.7626	129.02	102.84

Λ-Ru(phen)$_2$(10-methyl-dppz)$^{2+}$

L2 =

12.855	0.60192	153.74	8.67
10.758	-0.96573	152.26	14.39
10.553	-3.284	150.79	20.04
10.035	-3.8993	149.33	25.64
9.8803	-7.235	147.89	31.18
9.5248	-9.0557	146.46	36.67
9.2223	-8.2744	145.04	42.1
8.6871	-3.9809	143.64	47.47
8.5194	1.559	142.25	52.79
8.0096	6.6224	140.87	58.05
7.5553	9.3006	139.5	63.25
7.0243	10.702	138.15	68.4
6.5891	10.453	136.81	73.49
6.1541	10.094	135.48	78.52
5.6981	9.5558	134.17	83.5
5.3517	9.3407	132.86	88.42
4.9173	8.9005	131.57	93.28

4.8942	8.5054	130.29	98.09
4.6641	8.0139	129.02	102.84

Δ-Ru(phen)$_2$(11,12-dimethyl-dppz)$^{2+}$

D3 =

10.58	10.371	153.74	8.67
7.1918	10.341	152.26	14.39
7.8112	10.743	150.79	20.04
7.6949	10.25	149.33	25.64
5.5588	8.6108	147.89	31.18
4.9684	9.3071	146.46	36.67
4.5578	8.0644	145.04	42.1
4.1777	5.9082	143.64	47.47
3.8389	3.4691	142.25	52.79
3.4636	4.1023	140.87	58.05
3.3941	9.7325	139.5	63.25
3.0645	8.8561	138.15	68.4
2.9066	8.3933	136.81	73.49
2.8998	7.409	135.48	78.52
2.6279	6.9091	134.17	83.5
2.4923	6.1043	132.86	88.42
2.3662	5.5711	131.57	93.28
2.3631	5.1123	130.29	98.09
2.239	4.6724	129.02	102.84

Λ-Ru(phen)$_2$(11,12-dimethyl-dppz)$^{2+}$

L3 =

17.21	6.8366	153.74	8.67
10.192	4.4014	152.26	14.39
7.5429	3.0983	150.79	20.04
6.9045	0.57154	149.33	25.64
5.8226	-1.795	147.89	31.18
5.4285	-2.8647	146.46	36.67
4.7281	-5.7139	145.04	42.1
4.3836	-7.6943	143.64	47.47
4.1021	-6.5846	142.25	52.79
3.9974	-3.3864	140.87	58.05
3.4657	-1.755	139.5	63.25

3.4623	3.4692	138.15	68.4
3.2753	7.7886	136.81	73.49
2.9811	8.8617	135.48	78.52
2.8622	8.5585	134.17	83.5
2.6108	8.1266	132.86	88.42
2.2241	7.2354	131.57	93.28
2.2353	6.3073	130.29	98.09
1.9823	5.5744	129.02	102.84

Paper IV

Diastereomeric crowding effects in the competitive DNA intercalation of Ru(phenanthroline)$_2$dipyridophenazine^{2+} enantiomers.

Anna K. F. Mårtensson and Per Lincoln*

Department of Chemistry and Chemical Engineering

Chalmers University of Technology, SE-41296 Gothenburg

*lincoln@chalmers.se

Abstract

The biexponential excited-state emission decay characteristic of DNA intercalating tris-bidentate dppz-based ruthenium complexes of the general form Ru(L)$_2$dppz^{2+} has previously been explained by a binding model with two distinct geometry orientations of the bound ligands. However, it has been found that upon DNA binding of Ru(phen)$_2$dppz^{2+} the fractions of short and long lifetimes are strongly dependent of environmental factors such as salt concentration and, in particular, temperature. Using competitive isothermal titration calorimetry (ITC) to evaluate the current binding model of Ru(phen)$_2$dppz^{2+} enantiomers interacting with poly(dAdT)$_2$, we found that rather than assigning each excited-state lifetime to a specific geometric orientation, each intercalated complex should be seen as being in equilibrium with a short and long lifetime state, which may be altered by neighboring bound ligands affecting each other. In addition, as the titration progresses and the binding sites on the DNA polymer become increasingly occupied, a general resistance for the saturation of the binding sites is observed suggesting diastereomeric crowding of the neighboring bound ligands.

Introduction

The discovery of the "light-switch" complex, Ru(bpy)$_2$dppz^{2+} (Ru-bpy; bpy = 2,2'-bipyridine; dppz = dipyrido[3,2-*a*:2',3'-*c*]phenazine) by Barton and Sauvage almost 30 years ago was soon followed by Ru(phen)$_2$dppz^{2+} (Ru-phen; phen = 1,10-phenanthroline) (Fig. 1) and initiated the synthesis of many variations of dppz-based ruthenium-centered tris-bidentate structures.[1-3] Having interesting photophysical properties together with strong binding affinity to DNA and a slight selectivity towards A-T base pairs have made these DNA intercalative complexes attractive candidates for new pharmacological therapeutics and biosensors.[4-5] The

luminescence of these complexes, attributed to a dppz-localized ^{3}MLCT excited state[6-10], is effectively quenched in hydroxylic solvents, and to be completely extinguished, both of the 9,14-nitrogens on the extended (phenazine) part of the dppz ring are required to be H-bonded in the excited state.[11] However, when the phenazine nitrogens are shielded from forming H-bonds with the water molecules in a hydrophobic environment, such as in-between the DNA base pairs, their luminescence is turned on. Even more interesting, when bound to DNA, complexes of the general form $Ru(L)_2dppz^{2+}$ (L = ancillary polypyridyl ligand) exhibit almost invariably biexponential excited-state emission decays.[1, 12-14]

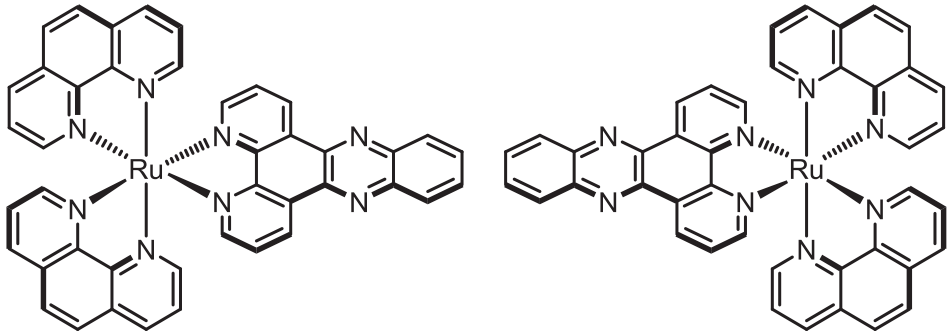

Figure 1 Structures of Λ- (left) and Δ-$Ru(phen)_2dppz^{2+}$ (right).

Octahedral tris-bidentate ruthenium complexes of the general form $Ru(L)_2dppz^{2+}$ are chiral and will adopt a structure much like a three-winged propeller, which can either have a right-handed (Δ) or a left-handed (Λ) configuration (Fig. 1). Being a right-handed helical structure in its common form, DNA is itself a chiral molecule. Not surprisingly, diastereomeric effects are observed when enantiopure Ru-bpy or Ru-phen are intercalated to DNA, where both

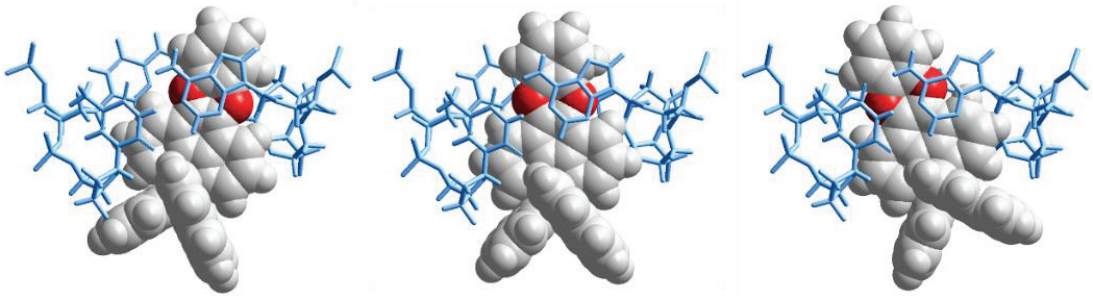

Figure 2 Schematic illustration of the proposed binding geometries of the *a* (left), the symmetric *c* (middle) and *b* (right) elementary units of Δ-Ru-phen viewed from above of the DNA helix axis. The 9,14-nitrogens on the extended part of the dppz moiety are colored red.

spectroscopic and calorimetric studies report a generally stronger binding affinity for the Δ-enantiomer than for the Λ-enantiomer.[14-20] The two emission lifetimes observed for both Ru-bpy and Ru-phen have previously been assigned to two distinct binding geometries, where the shorter life time is attributed to complexes centered in the intercalation pocket and the longer lifetime is from a more canted intercalation geometry (Fig. 2).[17, 21-22] This has further been supported by recent X-ray crystallography studies, reporting differently angled intercalation geometries for intercalation from the minor groove for Λ-Ru-phen.[23-24]

Both photophysical data and calorimetric data have previously revealed the DNA binding characteristics of the Λ-enantiomers of Ru-bpy and Ru-phen to be very similar to each other, with both the relative contributions from the two emitting species, their excited state lifetimes as well as very similar calorimetric titration isotherms.[17, 21] In contrast, the binding characteristics of the Δ-enantiomers are much more different in appearance, indicating a strong influence from the 1,10-phenanthroline B-ring, which is missing in 2,2'-bipyridine. The DNA molecule consists of long polymers of identical binding sites which overlap each other when occupied by bulky structures such as Ru-bpy and Ru-phen. Therefore, for any binding model to give a satisfactory global fit, cooperativity effects must be included, meaning that bound neighboring ligands may affect the binding geometry orientation of each other.[17, 20, 25] In our first global analysis of ITC and luminescence data for Ru-dppz complexes, the differences between the Δ-enantiomers was suggested to origin from a preference of forming doublets, canted away from each other, already at low binding densities of Δ-Ru-phen, whereas Δ-Ru-bpy was suggested to prefer a centered intercalation of single complexes at the same, low binding densities.[17]

In this study, we modeled the DNA strand as a homo-polymer of identical intercalation pockets using a generalized McGhee-von Hippel[26] binding isotherm algorithm.[17, 25] While this method[27] accounted for binding site interactions, it was still a complicated algorithm with limited efficiency that never gained any general popularity. Recently, we have developed a much simplified algorithm that is general enough to be utilized for modeling ligand binding to any type of linear biopolymer.[20] We demonstrated the practical usage of this algorithm by a series of competitive isothermal titration calorimetry (ITC) experiments using enantiopure Ru-bpy titrated to poly(dAdT)$_2$ (AT-DNA) already saturated by the opposite enantiomer.

While for Ru-bpy it is possible to fit calorimetric data to a simpler binding model with only one assumed binding geometry, the enthalpic changes for Ru-phen interacting with DNA are more prominent and might require a complicated binding model. While the earlier model with two distinct binding geometries accounts for the two emission lifetimes, it does not satisfactory explain why the fractions of short and long lifetimes appear to be temperature and salt concentration dependent in more recent results.[22] In this study, we seek to evaluate the earlier binding model for Ru-phen in a competitive setting as we did previously for Ru-bpy. If needed, our aim is to find an improved binding model that also accounts for the more recent extensive photophysical research performed on the ligand-DNA characterization of Ru-phen, using our newly developed simplified general algorithm.

Experimental

Materials and sample preparation

All experiments were performed in an aqueous buffer solution (pH = 7.0) containing 150 mM NaCl and 1 mM cacodylate (dimethylarsinic acid sodium salt). A stock solution of poly(dAdT)$_2$ (AT-DNA) (~5 mM nucleotides) was prepared by dissolving the sodium salt (Sigma-Aldrich) in buffer. Stock solutions of the complexes (~1 mM) were prepared by dissolving the chloride salts in buffer. Concentrations were determined spectrophotometrically using extinction coefficients: ε_{260} = 6600 $M^{-1}cm^{-1}$ per nucleotide for AT-DNA, and ε_{440} = 20000 $M^{-1}cm^{-1}$ for Ru(phen)$_2$dppz^{2+}. For ITC measurements the DNA solution was dialyzed against pure buffer for at least 48 hours at 8°C. Ruthenium complex solutions of appropriate concentrations were prepared by dilution of the stock solutions in the dialysate. The dialysis membrane used had a molecular weight cut-off of 3.5-5 kDa (Spectra-Por® Float-A-Lyzer® G2, Sigma-Aldrich).

Enantiopure Δ- and Λ-[Ru(phen)$_2$dppz]Cl$_2$ used in this study were prepared as previously reported.[14]

Other chemicals were purchased from Sigma-Aldrich and used without purification.

Absorption spectra were measured on a Varian Cary 4000 UV/vis spectrophotometer (Agilent Technologies) (path length = 1 cm).

Isothermal titration calorimetry

Isothermal titration calorimetry has many advantages when studying the binding interactions between biomolecules, and is often referred to as the "gold standard" for quantitative measurements of ligand-macromolecule associations. It is also the only method capable of direct thermodynamic measurement of all the energetics associated with the binding interaction process, enabling a full thermodynamic characterization (stoichiometry, association constant, enthalpy and entropy of binding).[28-30] It is a high-precision tool where the heat produced or absorbed upon addition of the complex to a DNA solution enables direct assessment of the binding free energy by integrating the power required to maintain the reference and sample cells at the same temperature. The experimental raw data consists of a series of heat flow peaks, and each peak corresponds to one injection of complex. These heat flow spikes are integrated with respect to time, which gives the total heat exchanged per mole injectant plotted against the ratio [Ru] / [base pairs].

Calorimetric data was obtained using a MicroCal iTC200 isothermal titration calorimeter (Malvern Instruments) controlled by Origin 7.0 software. The ITC profiles of the Δ and Λ enantiomers of Ru-phen were obtained by a single injection of 1 μL followed by 19 sequential titrations in 2 μL aliquots injections of complex from a syringe stock solution (~550 μM) into the sample cell (206 μL) loaded with AT-DNA in 150 mM NaCl aqueous solution (~408 μM nucleotides). We chose to use AT-DNA for the ligand-DNA interaction in order to avoid any effects from DNA heterogeneity.

This was subsequently followed by an additional 20 sequential injections (single injection of 1 μL followed by 19 injections of 2 μL aliquots) of the opposite enantiomer into the sample cell now loaded with AT-DNA saturated by the first complex. The injection spacing was 180 s, the syringe rotation was 1000 rpm, and there was an initial delay of 120 s prior the first injection. The primary ITC data was corrected the heat of complex dilution by subtracting the average heat per injection of complex titrated into buffer. There was negligible heat arising from DNA dilution. The raw ITC data peaks were automatically integrated using the Origin 7.0 software. For improved accuracy of the integration, the integration range for the spacing between each heat peak was narrowed, thus reducing the background noise from the baseline.

Binding models

A ligand bound to a homogenous one-dimensional lattice of binding sites can be in three distinct environments: either isolated, i.e. without any ligand neighbors, or with one ligand neighbor on one side and one empty binding site on the other (end binding), or with neighbors on both sides (interior binding). In the present study we have used two models: Model A, in which the ligand-ligand interaction energy is assumed to be additive and independent of the environment, and Model B, in which the ligand-ligand interaction energies may be taken to be different for ligands at ends and in the interior of a sequence of consecutively bound ligands.

In Model B, this is modelled by 4 different elementary units (two unsymmetrical units *a* and *b*, occurring only to the left and to the right, respectively, of a ligand neighbor; and two symmetrical units: *c*, occurring only in the interior of ligand sequences, and *d*, which only occur isolated. In the earlier model (denoted Model C) proposed by Andersson et al. there is only one symmetrical elementary unit *c* which can occur both isolated and in the interior of ligand sequences.[17] In addition, *c* may also be an end unit when bound next to either *a* or *b*. In Model B, this arrangement is not allowed but the end unit must be an unsymmetrical unit. Model C and Model B are illustrated in Fig. 3. For the simultaneous binding to a lattice of two different ligands 1 and 2, the cooperative factor matrix **Y** then becomes:

$$\begin{bmatrix} 1 & 1 & 0 & 0 & 1 & 1 & 0 & 0 & 1 \\ 0 & 0 & Ya1b1 & Ya1c1 & 0 & 0 & Ya1b2 & Ya1c2 & 0 \\ 1 & 0 & 0 & 0 & 0 & 0 & 0 & 0 & 0 \\ 0 & 0 & Yc1b1 & Yc1c1 & 0 & 0 & Yc1b2 & Yc1c2 & 0 \\ 1 & 0 & 0 & 0 & 0 & 0 & 0 & 0 & 0 \\ 0 & 0 & Ya2b1 & Ya2c1 & 0 & 0 & Ya2b2 & Ya2c2 & 0 \\ 1 & 0 & 0 & 0 & 0 & 0 & 0 & 0 & 0 \\ 0 & 0 & Yc2b1 & Yc2c1 & 0 & 0 & Yc2b2 & Yc2c2 & 0 \\ 1 & 0 & 0 & 0 & 0 & 0 & 0 & 0 & 0 \end{bmatrix} \quad (1)$$

The lattice with bound ligands is symmetrical, thus $Ya1c1 = Yc1b1$, $Ya2c2 = Yc2b2$, $Ya1b2=Ya2b1$, $Ya1c2=Yc2b1$, $Ya2c1=Yc1b2$ and $Yc1c2=Yc2c1$, but in general, $Ya1c2 \neq Ya2c1$.

If all cooperativity factors involving a particular pair of ligands 1 and 2 are equal ($Ya1b1 = Ya1c1 = Yc1c1 = Y_{11}$; $Ya2b2= Ya2c2= Yc2c2 = Y_{22}$; and $Ya1b2 = Ya1c2= Ya2c1 = Yc1c2 = Y_{12}= Y_{21}$) Model B is reduced to Model A, with **Y**:

$$\begin{bmatrix} 1 & 1 & 1 \\ 1 & Y_{11} & Y_{12} \\ 1 & Y_{21} & Y_{22} \end{bmatrix} \quad (2)$$

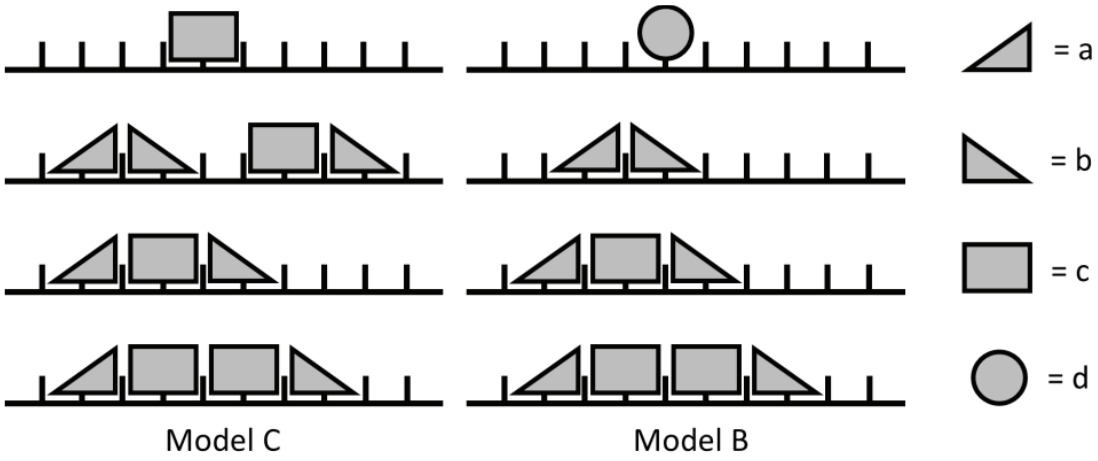

Figure 3 Schematic illustration comparing the old lattice Model C (left) with the proposed lattice Model B (right) showing the 4 different element units and their possible ligand-DNA interactions.

For both models, at a given total concentration of binding sites and ligands, the bound ligands are partitioned into the 3 categories (isolated, end or interior) by calculating the probability that a bound ligand has a certain neighbors using the conditional probabilities in the Markov chain transition matrix **P**. When two different ligands are present, the concentrations of all end ligands with a different type of ligand as neighbor are summed up, as are the concentrations of all interior ligands with at least one neighbor of a different type.

Fitting models to data

Photophysical data. The experimental pre-exponential factors (α-values), from the data of titrations of AT-DNA with Δ- and Λ-Ru-phen in 5 mM phosphate buffer given by McKinley et al.[21], were projected on the space spanned by the calculated probabilities *P* that a bound ligand belongs to one of the 3 categories (calculated as in Table 1) to obtain the least square fit.

$$\alpha_{\text{short,calculated}} = c_{\text{isol}}P_{\text{isol}} + c_{\text{end}}P_{\text{end}} + c_{\text{int}}P_{\text{int}} \quad (3)$$

Table 1 Calculation of category probability

Probability for	*isolated*	*end*	*interior*
Model A	P_{01}^2	$2P_{01}P_{11}$	P_{11}^2
Model B	$\theta_d(\theta_d + 2\theta_a + \theta_c)^{-1}$	$2\theta_a(\theta_d + 2\theta_a + \theta_c)^{-1}$	$\theta_c(\theta_d + 2\theta_a + \theta_c)^{-1}$

ITC data. The change in concentration upon addition of ligand was calculated for the categories (3 for Δ, 3 for Λ and 2 for Δ-Λ pairs), as well as the change in concentration of ligand dimers and of externally bound ligand.[20, 31] Ligand dimerization in solution was assumed not to be dependent on stereochemistry, whereas the external binding was assumed to be dependent on the chirality of the externally bound ligand, but not on the chirality of the intercalated ligand. The entire ITC-data set of one blank (buffer) and 5 ligand titrations (114 data points) was projected on the space of these concentration changes as 11 columns.

Global fit. The sum of the residual norm of the ITC fit and of the fit to the α-values was minimized by varying the binding constants K, the binding site coverage number n, the cooperativity factors y and the dimerization constant K_m using the *fminsearch* function of MATLAB.

Results

Isothermal titration calorimetry and model fitting

The raw ITC data with the enantiomers of Ru-phen and also racemic Ru-phen titrated into AT-DNA is shown in Fig. 4. The ITC profiles in the left column show the ligand titrated into AT-DNA only. At the end of the titration, further injections with the same enantiomer (not shown) only gave very small constant heat values, indicating full saturation of the DNA. This is attributed to heat of dilution of the free ligands and is in accordance to our previous results.[17, 20, 31] Proceeding the titration by switching to the opposite enantiomer, significant enthalpy changes are observed (Fig. 4, right), strongly indicating that both enantiomers are capable of displace each other on the DNA also in the Ru-phen series.[17, 31]

We recently showed that the 2 categories intrinsic binding and neighbor interaction, as calculated by Model A, could give a good fit to the ITC curves for the pure enantiomers of Ru-phen.[31] In the Ru-bpy series, augmenting these categories with a single Δ-Λ neighbor

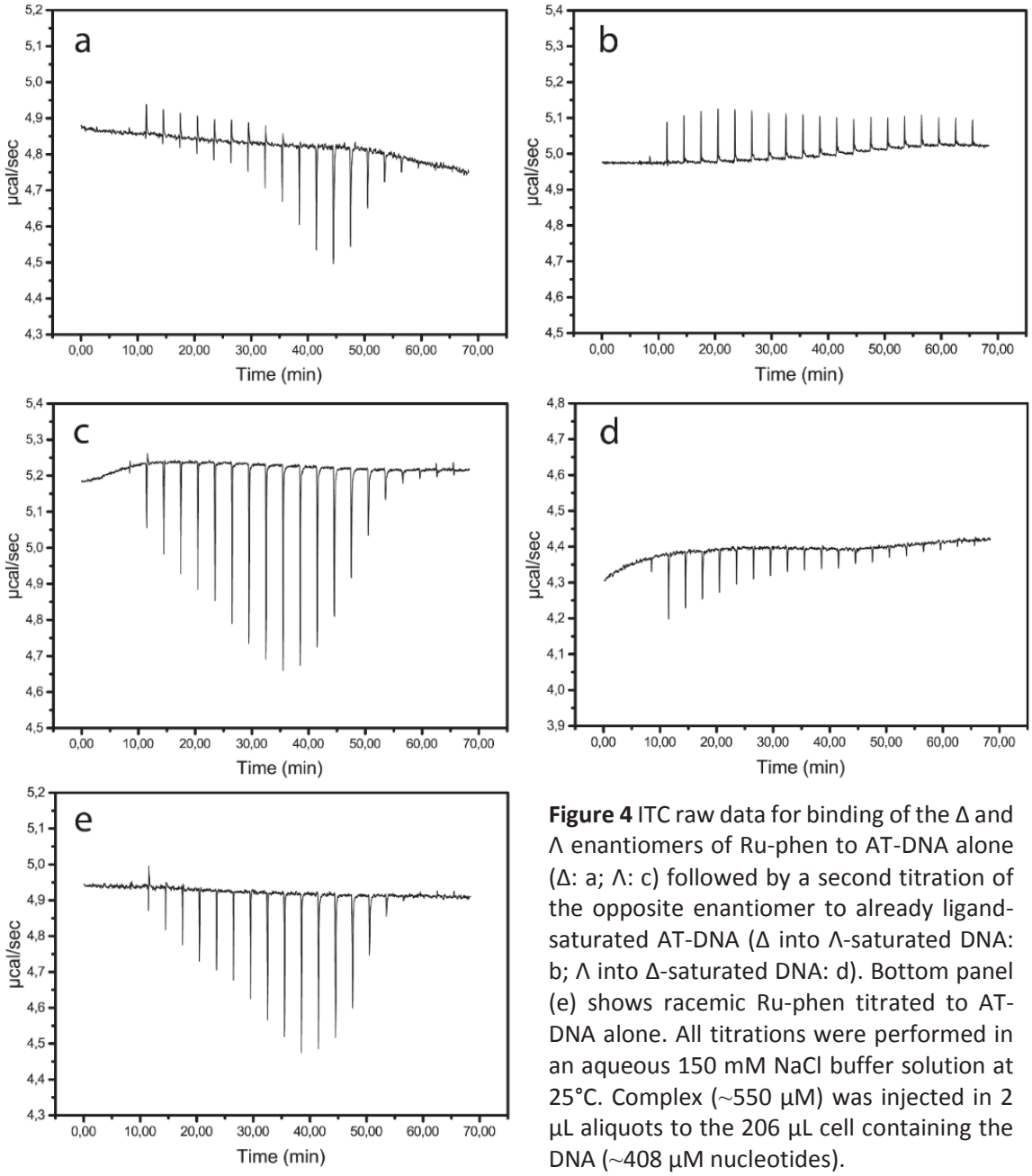

Figure 4 ITC raw data for binding of the Δ and Λ enantiomers of Ru-phen to AT-DNA alone (Δ: a; Λ: c) followed by a second titration of the opposite enantiomer to already ligand-saturated AT-DNA (Δ into Λ-saturated DNA: b; Λ into Δ-saturated DNA: d). Bottom panel (e) shows racemic Ru-phen titrated to AT-DNA alone. All titrations were performed in an aqueous 150 mM NaCl buffer solution at 25°C. Complex (~550 µM) was injected in 2 µL aliquots to the 206 µL cell containing the DNA (~408 µM nucleotides).

interaction was found to produce a very good fit of Model A to the competition ITC curves.[20] For the present ITC data set, the fit of Model A with 2 intrinsic binding (Δ and Λ) and 3 neighbor interaction (ΔΔ, ΛΛ and ΔΛ) categories was not as good. A better fit to the ITC data was obtained when the neighbor interaction category was differentiated into an end and an interior contribution, as described above under Methods. Nether the less, when calculating α-values by assigning the long lifetime exclusively to the end category, Model A failed

completely to simultaneously fit the ITC and the photophysical data. Similarly, Model C, used in our previous global analysis of ITC and photophysical data for Ru-phen enantiomers, which assigned the long lifetime exclusively to the end category,[17] failed to produce an acceptable global fit.

The strict assignment of excited state lifetimes to specific species defined by a binding model could be relaxed if it is assumed that every intercalated Ru complex could be in equilibrium with a long-lived and a short-lived species, and that it is the corresponding equilibrium constant that is affected by the neighbors. Thus assuming that the α-values could be calculated according to Eq. 3 gave much better global fits.

For Model A, the best fit was obtained by assuming equal binding to the alternating AT/AT and TA/TA steps. By contrast, for Model B, the best fit was obtained when binding was assumed to occur exclusively at one of these steps, moreover, the binding site coverage parameter *n* could be set to be exactly 1 for both enantiomers without significantly increasing the residual norm. Fig. 5 shows the best global fit to the integrated peaks of the raw data (Fig. 4) using Model B, which gave nRMSD = 11.1% (Table 2) (nRMSD: normalized root-mean-square-deviation, the Euclidian norm of the residual divided by the Euclidian norm of the data). The best global fit obtained for Model A is shown in Supplementary Information Fig. S1 which gave nRMSD = 14.3% (Table 2).

Table 2 nRMSD values for the best global fit of ITC and photophysical data with Model A or Model B.

	ITC	alpha
Model A	14.3%	4.4%
Model B	11.1%	2.5%

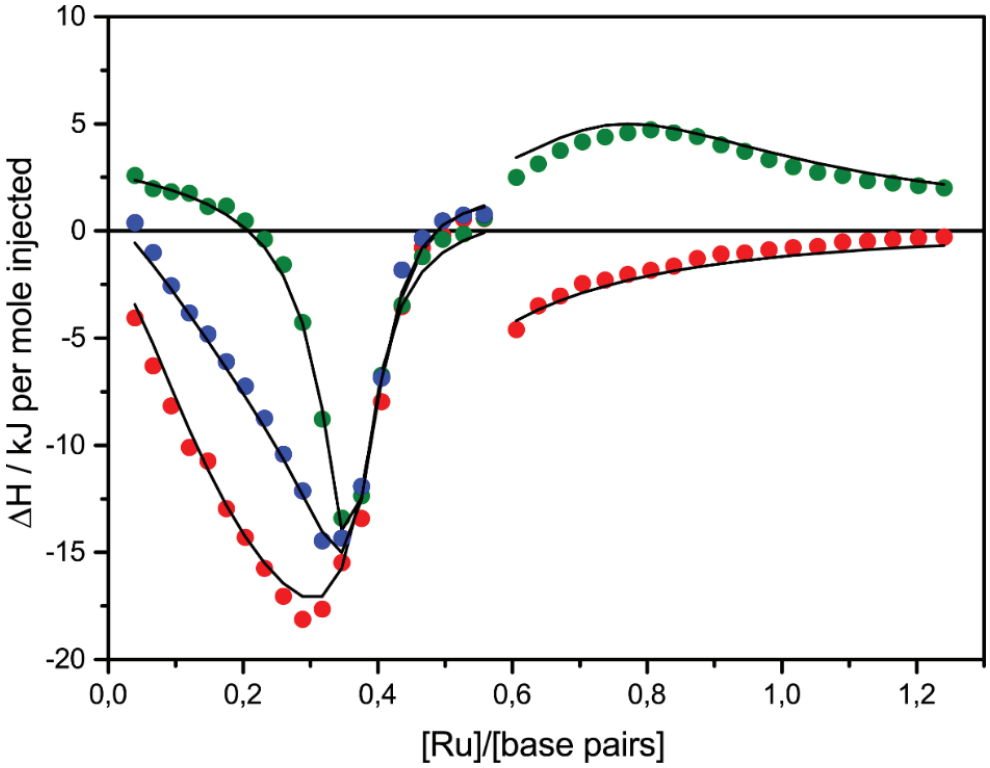

Figure 5 ITC profiles with fitted traces of Model B for the titrations of Δ and ΛRu-phen to AT-DNA alone (left) followed by a second titration of opposite enantiomer to already ligand-saturated AT-DNA (right). Also shown is the ITC profile for rac-Ru-phen titrated to AT-DNA alone. Symbols (Δ: green; Λ: red; rac: blue) indicate the normalized integrated heat absorbed or evolved upon 19 sequential 2 µL injections of the complex (~550 µM) into the 206 µL cell containing the DNA (~408 µM nucleotides). All titrations were performed in 150 mM NaCl aqueous solution at 25°C.

Table 3 compares the best global fit parameter values for Model A and Model B. Model A, with only one type of elementary unit has only one cooperativity factor *y*, which showed a slight cooperativity in the nearest-neighbor interactions of both Δ-Δ and Λ-Λ while Δ-Λ interactions were anti-cooperative. In Model B, Δ showed a modest cooperative interactions when bound to the DNA lattice as *a*-*b* (i.e. as an isolated dimer) but is essentially non-cooperative as the isolated trimer *a*-*c*-*b*, the latter which very reluctantly expands to tetramers *a*-*c*-*c*-*b* etc. due to the strong anti-cooperativity of the *c*-*c*-interaction. In contrast, while the isolated trimer *a*-*c*-*b* is also non-cooperative for Λ, the isolated dimer *a*-*b* is modestly anti-cooperative as is the *c*-*c*-interaction. Interestingly, the values for the heterochiral interactions are closer to Λ than to Δ.

Table 3 Binding parameter values from global fitting of Model A and Model B to ITC data. Included is also the parameters from the old Model C (data taken from Andersson et al.[17]).

	$K/10^6$	n	y	y_{ab}	y_{ac}	y_{cc}
Model A						
Δ	7.06	2.57	1.46			
Λ	2.09	2.31	1.08			
Δ-Λ			0.78			
dimer	2.0E-4					
Model B						
Δ	13.7			2.70	1.12	0.07
Λ	3.71			0.45	0.93	0.25
Δ-Λ				0.70	1.26	0.19
dimer	2.9E-4					
Model C		n_a/n_c				
Δ	1.1	2/1.8		56	6	0.01
Λ	0.2	2/1.8		9	9	0.05

The enthalpy ΔH° parameter values for the binding of the different categories from the global fitting of Model A and Model B are presented in Table 4, together with the enthalpy values for the outer binding mode to saturated DNA and the formation of dimer in solution. Derived standard thermodynamic values for the equilibrium parameters K and y_{ij} from the fit of model B are given in Table 5, in which the cooperativity factor enthalpies were calculated by linear combination of the categories enthalpies.

Table 4 Enthalpy parameter values[a] from global fitting of Model A and Model B to ITC data.

	outer[b]	isolated	end	interior	end, mix	interior, mix	dimer
Model A							
Δ	-1.0	-1.2	+1.4	-7.9	-11.0	-16.1	-14.2
Λ	+1.5	-5.0	-18.3	-14.9			
Model B							
Δ	+0.4	-0.7	-0.6	-24.5	-7.4	-21.3	-24.1
Λ	+0.8	-4.4	-17.3	-14.3			

[a](ΔH°/kJ mol^{-1}) [b]Assuming K_{outer} = 100

Table 5 Standard thermodynamic quantities at 25°C derived from the fit of Model B.

	Δ				**Λ**			
	K	y_{ab}	y_{ac}	y_{cc}	*K*	y_{ab}	y_{ac}	y_{cc}
Value	$13.7 \cdot 10^6$	2.70	1.12	0.07	$3.7 \cdot 10^6$	0.45	0.93	0.25
ΔG°/kJ mol^{-1}	-40.7	-2.5	-0.3	+6.6	-37.5	+2.0	+0.2	+3.4
ΔH°/kJ mol^{-1}	-0.7	+0.2	-11.8	-23.8	-4.4	-25.8	-17.8	-9.9
ΔS°/J mol^{-1} K^{-1}	+134	+8.9	-39	-102	+111	-93	-60	-45

Fig. 6 shows the best global fit for the experimental pre-exponential factors for the shorter lifetime α_s of Δ- and Λ-Ru-phen titrated to AT-DNA (data obtained from McKinley et al.[21]) using Model B, which gave nRMSD = 2.5% (Table 2). The best global fit obtained for Model A is shown in Supplementary Information Fig. S3 which gave nRMSD = 4.4% (Table 2). As the titration progresses, more and more binding sites on the DNA polymer become occupied by ligands, i.e. the DNA becomes saturated. Hence the fraction short excited state lifetime, which is more associated with the isolated elementary unit *d* decreases. For the Δ-enantiomer, the ratio α_s is subsequently lower than for the Λ-enantiomer, most likely caused by a higher number of a-b dimer conformations preferred by Δ. In addition, the slightly increased ratio α_s observed at the highest [Ru]/[base pairs] ratio for Δ is predicted to be caused by the reluctant formation of longer consecutive sequences like *a-c-c-b* units in the sterically crowded DNA lattice.

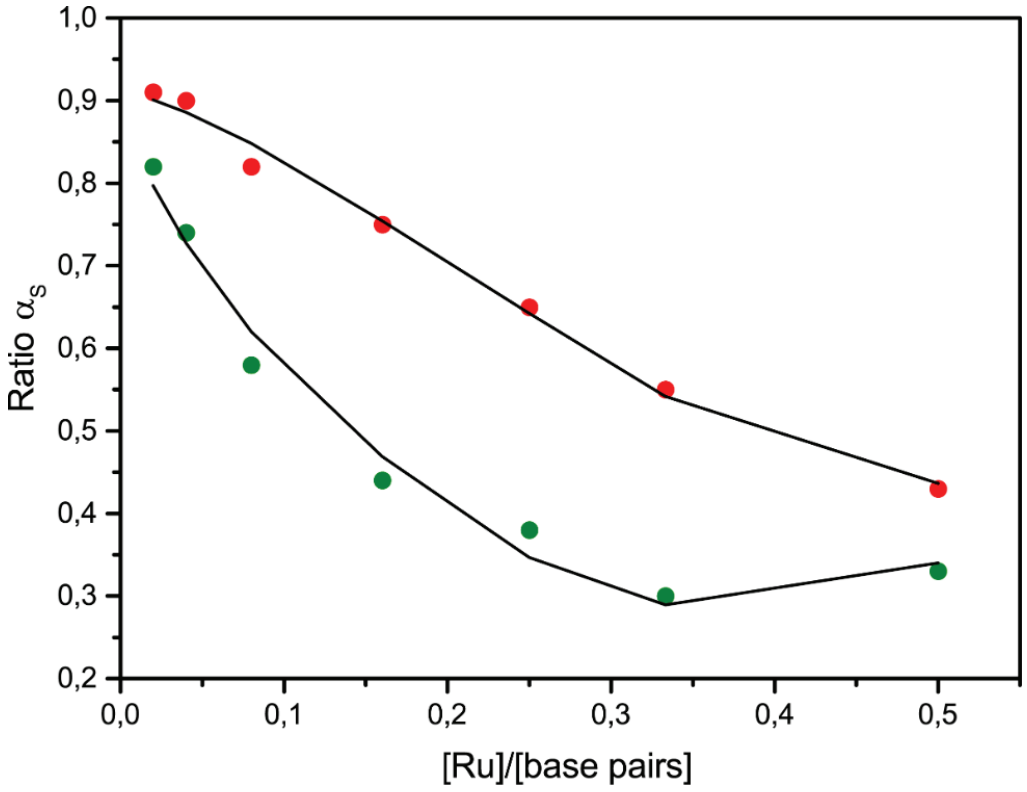

Figure 6 Fitted traces of Model B to the α-values for the short lifetime, data taken from the titrations of AT-DNA with enantiopure Ru-phen (Δ: green; Λ: red) by McKinley et al.[21] All titrations were performed in 5 mM phosphate buffer at 25°C.

Model A and B gave qualitatively similar results when fitted to the photophysical data, as shown in Table 6. It should be noted, however, that these data were obtained at a much lower salt concentration (5 mM sodium phosphate buffer) than used in the ITC experiments, and that it has been shown that the proportion of the long lifetime increases with ionic strength,[22] thus the results have to be interpreted with some caution. For Δ, the fit of Model B assigns the short lifetime almost exclusively to isolated and interior and the long lifetime to end ligands (see Table 5), in close parallel to our previous analysis, that used a smaller set of α-values obtained at the same high salt concentration as in the ITC.[17] In contrast, for Λ, the interior ligand is the dominating contributor to the long lifetime, with some end ligand contribution as well.

Table 6 Coefficients *c* for the best fit to experimental α_{short} data.

	Model A			Model B		
	isolated	end	interior	isolated	end	interior
Δ	0.82	0	0.45	0.89	0.07	1.00
Λ	0.92	0.51	0.30	0.91	0.65	0.11

Discussion

Our previous global analysis of ITC and excited state populations suggested that the two distinct lifetimes observed for each of the Ru-phen enantiomers bound to AT-DNA were directly corresponding to two distinct binding geometries, which were assigned to those observed by X-ray crystallography for the Λ-enantiomer.[17] The present results shows that this immediate correspondence needs to be modified, if a binding model of the type here investigated should be able to make a satisfactory global fit to competitive ITC titration and excited state population data. We suggest that instead of identifying each excited state lifetime with a specific geometric arrangement in the intercalation pocket, each intercalated complex could be regarded as being in equilibrium with a short and a long lifetime state, and that it is this equilibrium that might be altered by the neighbor ligands. This suggestion further provides a plausible explanation for the observation that the short lifetime α-value is found to decrease dramatically with temperature.[22] Since this value also decreases upon saturation of the DNA (see Fig. 6), i.e. as the number of complex interactions increases, a large decrease of α_{short} at a fixed Ru/base pair ratio upon an small increase in temperature must in the previous model then be due to a corresponding increase in a cooperativity factor, and hence such an equilibrium must be endothermic. But complex interaction equilibria appear exothermic when monitored by ITC. We propose that a more likely endothermic process that could explain the endothermic decrease in the short lifetime population is the release of a slowly exchangeable water molecule in the vicinity of a phenazine nitrogen of the intercalated dppz chelate.

Even if we ignore the not-so-good fit of Model A to the competitive ITC titrations (see Fig. S1 in Supplementary Information), Model B presents two advantages to Model A in the physical interpreting the model parameters:

1) The TA-step specificity, inferred for the Λ enantiomer from X-ray crystal structures, is inherent in the model.[23]
2) The binding site coverage number *n* can be set to unity for all bound ligands regardless of their environment, instead of being a freely adjustable non-integer parameter with different values for Δ and Λ. Thus, in Model B, all diastereomeric variation in binding affinity parameters is contained in the values of *K* and the y_{ij}.

Although Model C, employed in our previous global analysis, gave the same *n* values for Δ- and Λ-Ru-phen (2.0 for elementary units *a* and *b*, and 1.8 for *c*), it gave a large span (0.01 – 56) in the value of the cooperativity parameter *y*, and it was not able to fit the completion ITC data. With Model B, the span is much smaller (0.07 – 2.7), which facilitates a rationalization of the diastereomeric differences in structural terms. Our data supports the conjecture, originally made by Barton *et al.* for $Ru(phen)_3^{2+}$ more than 30 years ago[18], that a higher intrinsic binding constant *K* for Δ-enantiomers of trigonal metallo-intercalators is to be expected due to their better fit to the groove(s) of a right-handed double helix. Furthermore, the values of the cooperativity parameters suggest that a general steric crowding resists full lattice saturation ($y_{cc} < 1$ for all combinations), but that this crowding is modulated by diastereomeric differences in the attractive and repulsive intermolecular contacts.

As seen from the molecular models in Fig. 7, the phenanthroline B-ring can make a close contact with a neighboring complex only for the homochiral ΔΔ-pairs, which is consistent with the heterochiral *y*-values being more similar to ΛΛ than to ΔΔ. As suggested earlier, this arrangement further offers an explanation for the similarity in the ITC and luminescence data for the Λ-enantiomers of Ru-phen and Ru-bpy (in 2,2'-bipyridine, the CH=CH part of the phenanthroline B-ring is missing) and the dissimilarity in the data for the Δ-enantiomers.[17]

The values of the *y*-parameters can be expected to be a product of both attractive and repulsive factors, of which we expect the 4 most important to be:

1) A repulsive factor from the electrostatic repulsion of neighboring positive cations.
2) A repulsive factor due to inter-complex steric clashes.
3) An attractive factor due to hydrophobic/stacking interactions, primarily for Δ.
4) An attractive factor from binding to a groove already widened by the first bound complex, primarily for Λ.

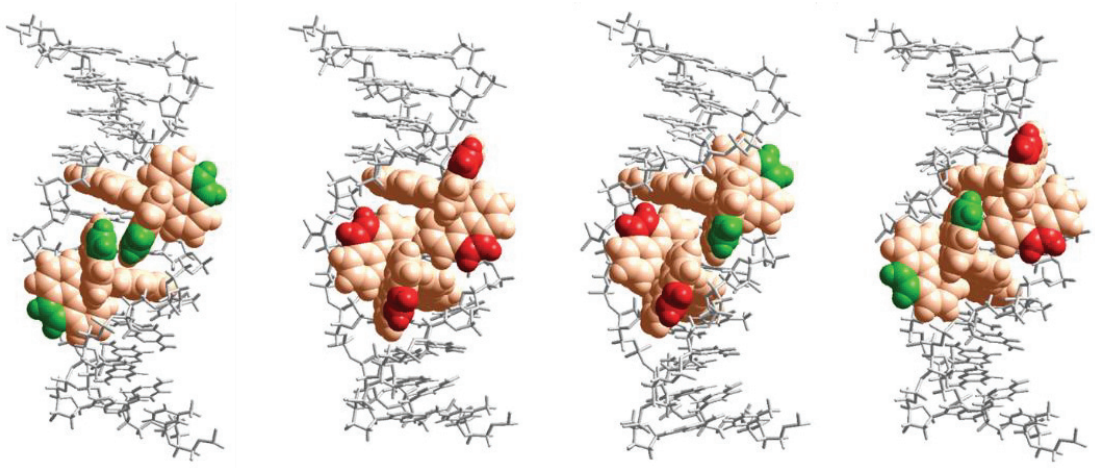

Figure 7 Schematic illustration of the proposed nearest-neighbor interaction geometries for the Δ- and Λ-enantiomers of $Ru(phen)_2dppz^{2+}$ when intercalated to DNA via the minor groove. The 5,6-carbons on the phen moieties are highlighted (green: Δ; red: Λ). The models were constructed by manual docking and subsequent energy minimization in a vacuum, using the Amber 2 force field in the HyperChem 8.0 software package (HyperCube, Inc.).

Since the y_{ac} parameter is close to unity for both homo- and heterochiral combinations, it appears that in all triplets *a-c-b*, the repulsive and the attractive contributions seem to balance. The Δ-enantiomer forms slightly cooperative *a-b* pairs, but very un-cooperative *a-c-c-b* quartets, suggesting that a weak hydrophobic attractive factor type 3 is gradually overcome by a steric repulsive factor type 2. By contrast, for the Λ-enantiomer, the steric repulsive factor 2 seem less prominent, and is balanced by an attractive factor type 4, slightly favoring isolated complexes *d* over *a-c-b* triplets. The pronounced diastereomeric differences in the binding enthalpy and entropy values in Table 5 for the binding equilibria are very likely to reflect the differences in the contributing factors discussed above, however, we believe that it would be too speculative to here attempt to resolve the contribution of each factor.

Conclusion

Even though our previous model for the ligand-DNA interactions of $Ru(phen)_2dppz^{2+}$ gave a satisfactory global fit for both calorimetric and photophysical experimental data by directly connecting the two distinct excited-state emission decays characteristic of this complex with

two distinct binding geometries, it could not fit the competitive calorimetric titrations, and would not properly explain the observed salt concentration and temperature dependence of the lifetime fractions without an extreme salt or temperature dependence of the equilibrium parameters. Here we propose a different interpretation, where all intercalated complexes are instead regarded to be in equilibrium with a short and a long lifetime state; and that this equilibrium is affected by interactions from neighboring bound ligands. The decrease in the cooperativity parameter value for complexes interior to consecutive sequences suggest steric crowding of the bulky ancillary ligands causing a general resistance of forming longer sequential chains of bound complexes upon DNA saturation, which is further consistent with the diastereomeric differences in intermolecular contacts suggested by molecular models.

Acknowledgements

We gratefully acknowledge the Swedish Research Council (Vetenskapsrådet) and Chalmers Area of Advance Nano for funding this project. We also thank COST Action CM1105 for providing a forum for stimulating discussions.

References

1. Friedman, A. E., Chambron, J. C., Sauvage, J. P., Turro, N. J. and Barton, J. K., Molecular light switch for DNA – $Ru(bpy)_2dppz^{2+}$. *J. Am. Chem. Soc.* **1990,** *112* (12), 4960-4962.
2. Jenkins, Y., Friedman, A. E., Turro, N. J. and Barton, J. K., Characterization of dipyridophenazine complexes of ruthenium(II): The light switch effect as a function of nucleic acid sequence and conformation. *Biochem.* **1992,** *31* (44), 10809-10816.
3. Hartshorn, R. M. and Barton, J. K., Noven dipyridophenazine complexes of ruthenium(II) – exploring luminescent reporters of DNA. *J. Am. Chem. Soc.* **1992,** *114* (15), 5919-5925.
4. Gill, M. R. and Thomas, J. A., Ruthenium(II) polypyridyl complexes and DNA – from structural probes to cellular imaging and therapeutics. *Chem. Soc. Rev.* **2012,** *41* (8), 3179-3192.
5. Erkkila, K. E., Odom, D. T. and Barton, J. K., Recognition and reaction of metallointercalators with DNA. *Chem. Rev.* **1999,** *99* (9), 2777-2795.
6. Coates, C. G., Olofsson, J., Coletti, M., McGarvey, J. J., Önfelt, B., Lincoln, P., Nordén, B., Tuite, E., Matousek, P. and Parker, A. W., Picosecond time-resolved resonance Raman probing of the light-switch states of $Ru(phen)_2dppz^{2+}$. *J. Phys. Chem. B* **2001,** *105* (50), 12653-12664.

7. Olson, E. J. C., Hu, D., Hormann, A., Jonkman, A. M., Arkin, M. R., Stemp, E. D. A., Barton, J. K. and Barbara, P. F., First observation of the key intermediate in the "light-switch" mechanism of $Ru(phen)_2dppz^{2+}$. *J. Am. Chem. Soc.* **1997,** *119* (47), 11458-11467.

8. Önfelt, B., Lincoln, P., Nordén, B., Baskin, J. S. and Zewail, A. H., Femtosecond linear dichroism of DNA-intercalating chromophores: Solvation and charge separation dynamics of $Ru(phen)_2dppz^{2+}$ systems. *Proc. Natl. Acad. Sci. USA.* **2000,** *97* (11), 5708-5713.

9. Olofsson, J., Önfelt, B., Lincoln, P., Nordén, B., Matousek, P., Parker, A. W. and Tuite, E., Picosecond Kerr-gated time-resolved resonance Raman spectroscopy of the $Ru(phen)_2dppz^{2+}$ interaction with DNA. *J. Inorg. Biochem.* **2002,** *91* (1), 286-297.

10. McKinley, A. W., Lincoln, P. and Tuite, E. M., Environmental effects on the photophysics of transition metal complexes with dipyrido 2,3-a:3',2'-c phenazine (dppz) and related ligands. *Coord. Chem. Rev.* **2011,** *255* (21-22), 2676-2692.

11. Olofsson, J., Önfelt, B. and Lincoln, P., Three-state light switch of $Ru(phen)_2dppz^{2+}$: Distinct excited-state species with two, one, or no hydrogen bonds from solvent. *J. Phys. Chem. A* **2004,** *108* (20), 4391-4398.

12. Westerlund, F., Pierard, F., Eng, M. P., Nordén, B. and Lincoln, P., Enantioselective luminescence quenching of DNA light-switch $Ru(phen)_2dppz^{2+}$ by electron transfer to structural homologue $Ru(phendione)_2dppz^{2+}$. *J. Phys. Chem. B* **2005,** *109* (36), 17327-17332.

13. Olofsson, J., Wilhelmsson, L. M. and Lincoln, P., Effects of methyl substitution on radiative and solvent quenching rate constants of $Ru(phen)_2dppz^{2+}$ in polyol solvents and bound to DNA. *J. Am. Chem. Soc.* **2004,** *126* (47), 15458-15465.

14. Hiort, C., Lincoln, P. and Nordén, B., DNA binding of Δ- and Λ-$[Ru(phen)_2DPPZ]^{2+}$. *J. Am. Chem. Soc.* **1993,** *115* (9), 3448-3454.

15. Haq, I., Lincoln, P., Suh, D. C., Nordén, B., Chowdhry, B. Z. and Chaires, J. B., Interaction of Δ- and Λ-$[Ru(phen)_2DPPZ]^{2+}$ with DNA – a calorimetric and equilibrium binding study. *J. Am. Chem. Soc.* **1995,** *117* (17), 4788-4796.

16. Lincoln, P., Broo, A., Nordén, B., Diastereomeric DNA-binding geometries of intercalated ruthenium(II) trischelates probed by linear dichroism: $[Ru(phen)_2DPPZ]^{2+}$ and $[Ru(phen)_2BDPPZ]^{2+}$. *J. Am. Chem. Soc.* **1996,** *118* (11), 2644-2653.

17. Andersson, J., Fornander, L. H., Abrahamsson, M., Tuite, E., Nordell, P. and Lincoln, P., Lifetime heterogeneity of DNA-bound dppz complexes originates from distinct intercalation geometries determined by complex-complex interactions. *Inorg. Chem.* **2013,** *52* (2), 1151-1159.

18. Barton, J. K., Danishefsky, A. T. and Goldberg, J. M., Tris(phenanthroline)ruthenium(II) – stereoselectivity in binding to DNA. *J. Am. Chem. Soc.* **1984,** *106* (7), 2172-2176.

19. Lincoln, P. and Nordén, B., Binuclear ruthenium(II) phenanthroline compounds with extreme binding affinity for DNA. *Chem. Commun.* **1996,** (18), 2145-2146.

20. Mårtensson, A. K. F. and Lincoln, P., Competitive DNA binding of $Ru(bpy)_2dppz^{2+}$ enantiomers studied with isothermal titration calorimetry (ITC) using a direct and general binding isotherm algorithm. *Phys. Chem. Chem. Phys.* **2018,** *20* (12), 7920-7930.

21. McKinley, A. W., Andersson, J., Lincoln, P. and Tuite, E. M., DNA sequence and ancillary ligand modulate the biexponential emission decay of intercalated $Ru(L)_2dppz^{2+}$ enantiomers. *Chem. Eur. J.* **2012,** *18* (47), 15142-15150.

22. McKinley, A. W., Lincoln, P. and Tuite, E. M., Sensitivity of $Ru(phen)_2dppz^{2+}$ light switch emission to ionic strength, temperature, and DNA sequence and conformation. *Dalton Trans.* **2013,** *42* (11), 4081-4090.

23. Niyazi, H., Hall, J. P., O'Sullivan, K., Winter, G., Sorensen, T., Kelly, J. M. and Cardin, C. J., Crystal structures of λ-$[Ru(phen)_2dppz]^{2+}$ with oligonucleotides containing TA/TA and AT/AT steps show two intercalation modes. *Nat. Chem.* **2012,** *4* (8), 621-628.

24. Hall, J. P., Cook, D., Morte, S. R., McIntyre, P., Buchner, K., Beer, H., Cardin, D. J., Brazier, J. A., Winter, G., Kelly, J. M. and Cardin, C. J., X-ray crystal structure of rac-$[Ru(phen)_2dppz]^{2+}$ with $d(ATGCAT)_2$ shows enantiomer orientations and water ordering. *J. Am. Chem. Soc.* **2013,** *135* (34), 12652-12659.

25. Mårtensson, A. K. F. and Lincoln, P., Binding of Ru(terpyridine)(pyridine)dipyridophenazine to DNA studied with polarized spectroscopy and calorimetry. *Dalton Trans.* **2015,** *44* (8), 3604-3613.

26. McGhee, J. D. and Hippel, P. H. V., Theoretical aspects of DNA-protein interactions – cooperative and non-cooperative binding of large ligands to a one-dimensional homogenous lattice. *J. Mol. Biol.* **1974,** *86* (2), 469-489.

27. Lincoln, P., A generalized McGhee-von Hippel method for the cooperative binding of different competing ligands to an infinite one-dimensional lattice. *Chem. Phys. Lett.* **1998,** *288* (5-6), 647-656.

28. Jelesarov, I. and Bosshard, H. R., Isothermal titration calorimetry and differential scanning calorimetry as complementary tools to investigate the energetics of biomolecular recognition. *J. Mol. Recognit.* **1999,** *12* (1), 3-18.

29. Ladbury, J. E. and Chowdhry, B. Z., Sensing the heat: The application of isothermal titration calorimetry to thermodynamic studies of biomolecular interactions. *Chem. Biol.* **1996,** *3* (10), 791-801.

30. Wiseman, T., Williston, S., Brandts, J. F. and Lin, L. N., Rapid measurement of binding constants and heats of binding using a new titration calorimeter. *Anal. Biochem.* **1989,** *179* (1), 131-137.

31. Mårtensson, A. K. F. and Lincoln, P., Effects of methyl substitution on DNA binding enthalpies of enantiopure $Ru(phenanthroline)_2dipyridophenazine^{2+}$ complexes. *Phys. Chem. Chem. Phys.* **2018,** *Advance article*, DOI: 10.1039/C8CP01151F.

Diastereomeric crowding effects in the competitive DNA intercalation of Ru(phenanthroline)$_2$dipyridophenazine^{2+} enantiomers.

Anna K. F. Mårtensson and Per Lincoln*

Supplementary information

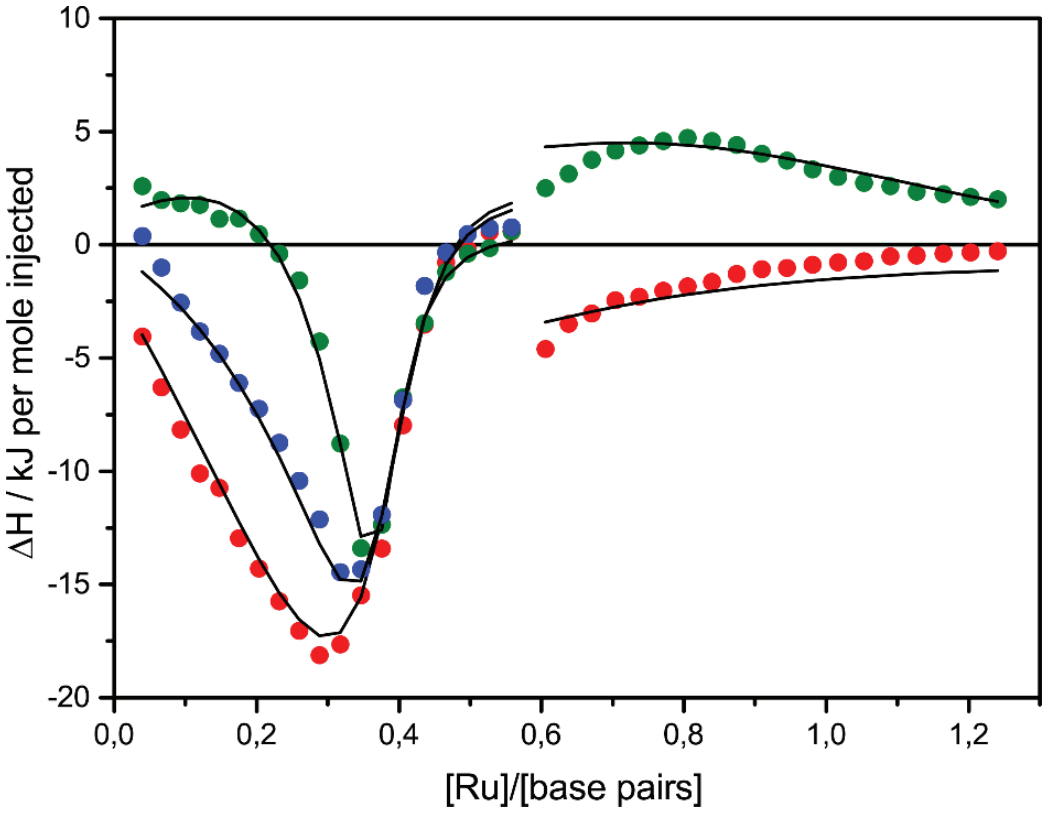

Figure S1 ITC profiles with fitted traces of Model A for the titrations of Δ and ΛRu-phen to AT-DNA alone (left) followed by a second titration of opposite enantiomer to already ligand-saturated AT-DNA (right). Also shown is the ITC profile for rac-Ru-phen titrated to AT-DNA alone. Symbols (Δ: green; Λ: red; rac: blue) indicate the normalized integrated heat absorbed or evolved upon 19 sequential 2 µL injections of the complex (~550 µM) into the 206 µL cell containing the DNA (~408 µM nucleotides). All titrations were performed in 150 mM NaCl aqueous solution at 25°C.

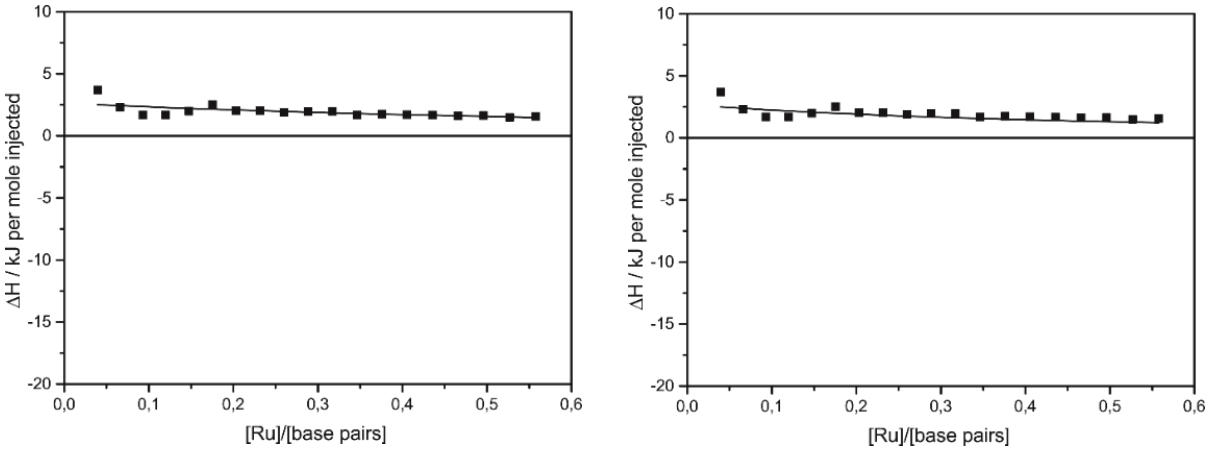

Figure S1 ITC profiles with fitted traces of Model A (left) and Model B (right) for the averaged titrations of Δ and ΛRu-phen to pure buffer. Black squares indicate the averaged normalized integrated heat absorbed or evolved upon 19 sequential 2 µL injections of the complex (~550 µM) into the 206 µL cell containing 150 mM NaCl aqueous solution. The titrations were performed at 25°C.

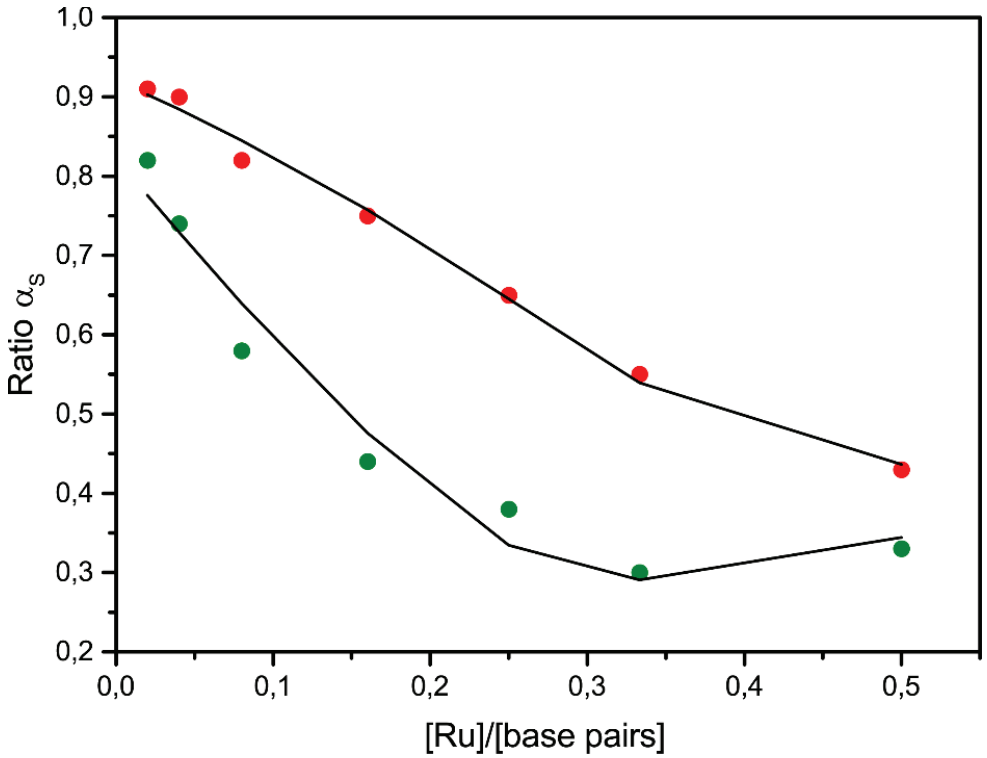

Figure S3 Fitted traces of Model A to the α-values for the short lifetime, data taken from the titrations of AT-DNA with enantiopure Ru-phen (Δ: green; Λ: red) by McKinley et al.[21] All titrations were performed in 5 mM phosphate buffer at 25°C.

Paper V

View this journal online at wileyonlinelibrary.com

Chirality

ISSN 0899-0042

Volume 28
Issue 11
2016

Included in this online edition:

Number 11 (November)

WILEY

Received: 10 March 2016 | Revised: 5 June 2016 | Accepted: 21 September 2016

DOI 10.1002/chir.22656

WILEY

SHORT COMMUNICATION

Diastereomeric bactericidal effect of Ru(phenanthroline)$_2$ dipyridophenazine

Anna K. F. Mårtensson[1] | Mattias Bergentall[2] | Valentina Tremaroli[2] | Per Lincoln[1]

[1] Department of Chemistry and Chemical Engineering, Chalmers University of Technology, Gothenburg, Sweden

[2] Wallenberg Laboratory and Sahlgrenska Center for Cardiovascular and Metabolic Research, Department of Molecular and Clinical Medicine, Institute of Medicine, University of Gothenburg, Gothenburg, Sweden

Correspondence
Anna K. F. Mårtensson, Department of Chemistry and Chemical Engineering, Chalmers University of Technology, SE-41296 Gothenburg, Sweden.
Email: marann@chalmers.se

Funding Information
Vetenskapsrådet, VR 2012–1661.

ABSTRACT

Metal susceptibility assays and spot plating were used to investigate the antimicrobial activity of enantiopure $[Ru(phen)_2dppz]^{2+}$ (phen =1,10-phenanthroline and dppz = dipyrido[3,2-*a*:2′,3′-c]phenazine) and $[\mu\text{-bidppz}(phen)_4Ru_2]^{4+}$ (bidppz =11,11′-bis(dipyrido[3,2-*a*:2′,3′-c]phenazinyl)), on Gram-negative *Escherichia coli* and Gram-positive *Bacillus subtilis* as bacterial models. The minimum inhibitory concentrations (MIC) and minimum bactericidal concentrations (MBC) were determined for both complexes: while $[\mu\text{-bidppz}(phen)_4Ru_2]^{4+}$ only showed a bactericidal effect at the highest concentrations tested, the antimicrobial activity of $[Ru(phen)_2dppz]^{2+}$ against *B. subtilis* was comparable to that of tetracyline. In addition, the Δ-enantiomer of $[Ru(phen)_2dppz]^{2+}$ showed a 2-fold higher bacteriostatic and bactericidal effect compared to the Λ-enantiomer. This was in accordance with the enantiomers relative binding affinity for DNA, thus strongly indicating DNA binding as the mode of action.

KEYWORDS

antimicrobial activity, chirality, confocal microscopy, emission, metal susceptibility assay, minimum bactericidal concentration, minimum inhibitory concentration, ruthenium complex

1 | INTRODUCTION

The treatment of bacterial infections has become more and more problematic due to the emergence of multidrug-resistant pathogens.[1,2] With few exceptions, the antibiotics that are currently available for clinical use all target the same limited set of bacterial components (the cell wall, the cell membrane, and a few enzymes essential for bacterial growth), thus increasing the risk for multiresistance.[3] Another problem is that new antibiotics that are coming onto the market are mostly variants of existing drugs, with the risk that resistance mechanisms have already developed.[4] A noteworthy exception is the recent discovery of teixobactin, the first member of a novel class of antibiotics that targets lipid II and lipid III, both membrane-anchored cell wall precursors essential for bacterial cell wall synthesis.[5]

There are several components in bacteria that have not been fully explored as potential antimicrobial targets. Bacterial DNA is an attractive antimicrobial target, provided that specificity to bacterial cells can be established, as DNA targeting compounds have the potential risk of also damaging eukaryotic cells. Actinomycin D, doxorubicin, and daunorubicin are a few examples of DNA binding antimicrobials that were deemed too cytotoxic for the host[6] and were therefore developed as anticancer treatments.[7–9]

While a number of reports have analyzed the combination of transition metals with antibiotics as a way to increase compounds' potency against infections

("metalloantibiotics"),[10–12] much fewer studies have tested the antimicrobial activity of metal complexes alone. Platinum-containing complexes such as cisplatin were shown to have antimicrobial activity, but were too damaging to eukaryotic cells, thus only suitable for anticancer treatment.[13,14] Ruthenium complexes show less general toxicity than platinum compounds,[15,16] and in particular ruthenium(II) polypyridyl complexes have several properties that would make them suitable for antimicrobial treatments (e.g., water soluble, coordinately saturated, and inert to substitution). While the DNA intercalating ability of chiral ruthenium(II) polypyridyl complexes have been extensively studied and debated for more than 30 years,[17–21] there has been comparably little interest in testing their antimicrobial activity despite the pioneering work of Dwyer et al. more than 60 years ago.[22,23] This is somewhat surprising, as they are very stable, readily synthesized, and have strong DNA binding ability.[24] In addition, their properties are readily modulated by the peripheral ligands, making it possible to influence DNA binding and enantioselectivity.[20] While the antimicrobial activity of mononuclear ruthenium(II) polypyridyl complexes has previously been demonstrated,[25,26] to the best of our knowledge no reported study resolved the complexes in their pure enantiomeric forms. Even fewer studies have been published on antimicrobial activity in binuclear ruthenium(II) polypyridyl complexes, with the exception of the work by Li and Keene et al. [27–33] By coordinating bidentate ligands to the ruthenium ion two conformations are possible: either a right- (Δ) or left-handed (Λ) helical structure. The resulting diastereomeric interactions when bound to a chiral macromolecule, such as DNA, would assumingly not be identical for both enantiomers.

In this study we analyzed the antimicrobial activity of enantiomeric pure $[Ru(phen)_2dppz]^{2+}$ (Ru-phen) (phen =1,10-phenanthroline and dppz = dipyrido[3,2-*a*:2′,3′-c]phenazine) and $[\mu\text{-bidppz}(phen)_4Ru_2]^{4+}$ (biRu-phen) (bidppz =11,11′-bis(dipyrido[3,2-*a*:2′,3′-c]phenazinyl)) (see Scheme 1). Both complexes are well-established DNA intercalators and Ru-phen has already been shown to not be cytotoxic against HeLa cells.[34] As bacterial models, we used Gram-negative *E. coli* and Gram-positive *B. subtilis.* As a reference for antimicrobial activity, we used tetracycline, a broad-spectrum antibiotic that is active against both Gram-positive and Gram-negative bacteria.

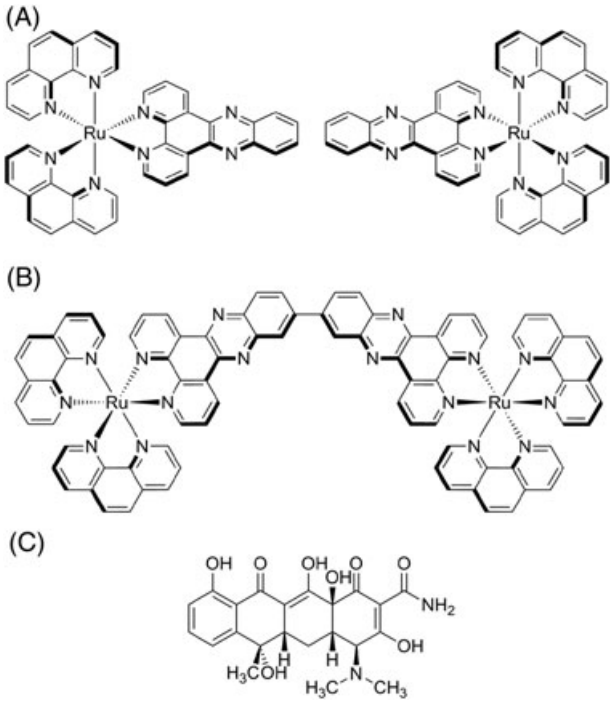

SCHEME 1 Structures of (**a**) Λ- (left) and ΔRu-phen (right), (**b**) ΛΛbiRu-phen, and (**c**) tetracycline

2 | MATERIALS AND METHODS

2.1 | Materials

Enantiopure $[Ru(phen)_2dppz]Cl_2$ and $[\mu\text{-bidppz}(phen)_4Ru_2]Cl_4$ used in this study were synthesized as described elsewhere.[35,36] Concentrations were determined spectrophotometrically using extinction coefficients: ε_{440} = 20 000 M^{-1} cm^{-1} for Ru-phen and ε_{262} = 200 000 M^{-1} cm^{-1} for biRu-phen. Tetracycline hydrochloride (Sigma-Aldrich, St Louis, MO), the DNA stain Hoechst 33342 (bis-benzimidine, Thermofisher, Waltham, MA), PFA (para-formaldehyde, Sarstedt, Sweden), SDS (sodium dodecyl sulfate, Sigma-Aldrich) and other chemicals were used without purification. Luria-Bertani (LB) medium (10 g/l tryptone, 5 g/l yeast extract, 10 g/l NaCl), 0.9% saline solution, 10 mM $NaPO_4$ + 1% LB medium (pH 7), LB agar plates and phosphate-buffered saline (PBS) were prepared at the department of Clinical Microbiology at the Sahlgrenska University Hospital.

2.2 | Bacterial Strains and Culture Conditions

The bacterial strains used in this study were *Escherichia coli* DSM 1103 and *Bacillus subtilis* 168. The strains were purchased from the American Type Culture Collection (ATCC, Manassas, VA) (ATCC 25922, ATCC 23857) and activated from freeze-dried conditions in accordance with the protocol provided upon delivery. Strains were grown on LB medium aerobically at 37°C. Stock solutions of the bacterial strains were prepared from freshly grown bacterial cultures and stored in 20% glycerol at −70°C.

2.3 | Stock Solutions of Tetracycline and Metals

A stock solution of 5 mg/ml tetracycline was prepared in 70% ethanol and stored protected from light at 8°C. Stock solutions of the complexes were prepared at 5 times the highest concentration used in the challenge plate (~2000 μM) by dissolving the chloride salts in autoclaved MilliQ water (Billerica, MA).

2.4 | Metal Susceptibility Assays

Metal susceptibility assays were performed using a method similar to the MBEC high-throughput assay as previously described.[37] Frozen stocks of the bacterial strains were streaked out on agar LB plates to obtain subcultures. After 24 h incubation, a single colony from each strain was collected from the subcultures and suspended in LB medium. After 24 h incubation, this suspension was diluted 100-fold in LB medium and left to grow an additional 4 h. To ensure that the bacterial growth was in the exponential phase, optical density (OD) at 650 nm was measured and the bacterial solutions were spot plated for colony count (OD = 0.3, CFU/ml = 10^8, diluted 1:3, used 20 μl so that CFU/well = 2×10^6). Serial dilutions of the ruthenium complexes were made in LB medium along the length of a sterile 96-well microtiter plate (the challenge plate), allowing the first column to serve as a sterility control and the last column to serve as a growth control. Each ruthenium complex and tetracycline were tested in triplicate and repeated once to ensure reproducibility. The challenge plates where incubated for 24 h. To ensure aerobic conditions, a shaking table was used for incubation of the plates and cultures. A schematic illustration summarizing the assay protocol can be found in the Supporting Information (Figure S1).

2.5 | Minimum Inhibitory Concentration and Minimum Bactericidal Concentration

The MIC is defined as the lowest concentration of a compound that inhibits the visual growth of an organism. We determined the MIC values by reading the optical density of the challenge plate at 650 nm (OD_{650}) on a SpektraMax Plus 384 Microplate Reader (Molecular Devices, MSD Analytical Technologies, UK). The cellular suspensions in each row of the challenge plate were then transferred to new sterile 96-well microtiter plates and diluted 10^1–10^8-fold with 10 mM $NaPO_4$ + 1% LB medium. Twenty-μl aliquots of each dilution of each bacterial culture were spot plated in duplicate onto LB agar plates and incubated for 24 and 48 h. The MBC is defined as the lowest concentration of an antibiotic required to kill a particular bacterial strain. The MBC values were determined by qualitatively scoring the spot plates for bacterial growth (this was done after 24 and 48 h to ensure complete eradication of the bacterial cells). The number of viable bacteria was expressed in CFU (colony-forming units) per ml:

$$\frac{CFU}{ml} = \frac{Average\ colony\ count}{Volume} \times dilution \qquad (1)$$

2.6 | DNA Binding Emission

Emission spectra were recorded on a Varian Cary Eclipse Fluorescence spectrophotometer (Agilent Technologies, Santa Clara, CA). Inoculums of *B. subtilis* and *E. coli* in the exponential phase were incubated overnight (37°C, 120 rpm), either with the enantiomers of Ru-phen and biRu-phen (40 μM) in LB medium or in the medium alone. After incubation, 1 ml of each bacterial suspension was centrifuged at 6000 *g* at room temperature. The pellet was washed twice in 1× PBS and then resuspended in 1 ml of 1× PBS solution. The samples were excited at 440 nm and emissions were recorded at 500–800 nm.

2.7 | Confocal Microscopy

Confocal microscopy images were obtained with a Leica TCS SP5 confocal scanning laser microscope (Leica Microsystems, Germany) controlled by Leica Application Suite Advanced Fluorescence (LAS AF) 2.6.0.7266 software. Inoculums of *B. subtilis* and *E. coli* in the exponential phase were incubated with Δ- and ΛRu-phen (40 μM) in LB medium overnight (37°C, 120 rpm) together with nonexposed bacterial suspensions as controls. After incubation, 1 ml of each bacterial suspension was centrifuged at 6000 *g* at room temperature. The pellet was washed twice in 1× PBS and then resuspended in 1 ml of 1× PBS solution. Droplets (40 μl) of each suspension were placed on microscopy glass slides (Superfrost, VWR), allowed to adhere for 10 min, and then fixed with 2% PFA in PBS for 10 min. The slides were washed using PBS solution and the bacteria were stained with Hoechst 33342 (1:10,000 dilution) for 15 min. The slides were washed one final time with PBS before mounting using fluorescence mounting medium (Invitrogen, La Jolla, CA). Samples were viewed using a 63× objective (total magnification 630×) and Ru-phen (λ_{ex} ~ 440 nm, λ_{em} ~ 610 nm) was excited using a 458 nm blue argon laser at 40% intensity. Emission fluorescence of Ru-phen was collected at 600–670 nm. Hoechst 33342 (λ_{ex} ~ 354 nm, λ_{em} ~ 486 nm) was excited with an ultraviolet diode laser and detected using a blue/cyan filter.

2.8 | Nucleotide Leakage

Measurements were performed in accordance with a previous method described by Henie et al., with minor modifications.[38] Solutions containing bacterial inoculum in the exponential phase treated with biRu-phen (~300 μM) were filtered through a 0.22-μm pore size Millipore Express Millex GP sterile syringe filter with PES membrane (Merck Millipore, Germany) at 0, 10, 20, 30, 40, 50, and 60 min; 3% SDS solution was used as a comparison. Absorption at 260 nm for bacterial nucleic acids were measured using a Varian Cary 4000 UV/vis spectrophotometer (Agilent Technologies). All measurements were performed in triplicate and repeated once to ensure reproducibility.

3 | RESULTS AND DISCUSSION

In this study we investigated whether there was an enantiomeric difference in antimicrobial activity of both

mononuclear and binuclear dppz-ruthenium(II)-centered complexes with phen as the peripheral ligands, and the plausible mode of action for their antimicrobial effect.

Neither ΔΔ- nor ΛΛbiRu-phen showed any significant antimicrobial activity against either bacterial strain, and no enantiomeric difference could be observed. The sudden drop in bacterial growth at the highest complex concentrations could be caused by lysis of the cellular membrane, and not by interaction with DNA. To verify this hypothesis, we exposed microbial cells to the highest concentration of binuclear complexes and quantified the release of nucleic acids. During 60 min of biRu-phen exposure the optical density at 260 nm of cell-free filtrates increased for both *B. subtilis* and *E. coli*, indicating nucleotide leakage (see Fig. S2 in the Supporting Information). Notably, the leakage of nucleic acid material was similar for the binuclear complexes and a 3% SDS solution, indicating a similar effect of the metal complexes and the detergent. The more gradual OD_{260} increase in *E. coli* compared to *B. subtilis* was most likely caused by the less-permeable outer membrane characteristic of Gram-negative bacteria.[39] No enantiomeric difference was observed. As bacterial membranes have a higher proportion of negatively charged phospholipids compared with eukaryotic cells, as well as negatively charged teichoic acid and lipopolysaccharides,[40–42] it is not surprising that the large binuclear ruthenium complex with a 4+ cationic charge would preferentially bind to the outer membrane of the bacterial cell.

TABLE 1 MIC and MBC values[a]

Compound	*B. subtilis*		*E. coli*	
	MIC	MBC	MIC	MBC
Δ	8	16	32	> 400
Λ	16	32	128	> 400
Δ Δ	ND[b]	150	ND[b]	300
Λ Λ	ND[b]	150	ND[b]	300
Tetracycline	8	16	< 1	< 1

[a]MIC and MBC values indicated as μM. (Ru-phen: 1 μM = 0.82 μg/ml; biRu-phen: 1 μM = 1.63 μg/ml; Tetracycline hydrochloride: 1 μM = 0.48 μg/ml).

[b]Not determined due to the ruthenium complex precipitating in the LB medium.

Table 1 shows a summary of determined MIC and MBC values. The lowest MIC value was observed with ΔRu-phen against *B. subtilis*, with an inhibitory effect comparable to that of tetracycline against the same bacteria. In contrast, ΛRu-phen was less effective, with a 2-fold increase in its MIC value. The enantiomeric difference in Ru-phen was even higher when tested against *E. coli*, with Λ requiring an 4-fold higher concentration for the same bacteriostatic effect as Δ, but with an overall weaker inhibitory effect compared with *B. subtilis.*

In order to determine the MBC values for both ruthenium complexes a series of spot plating was performed (Figure 1

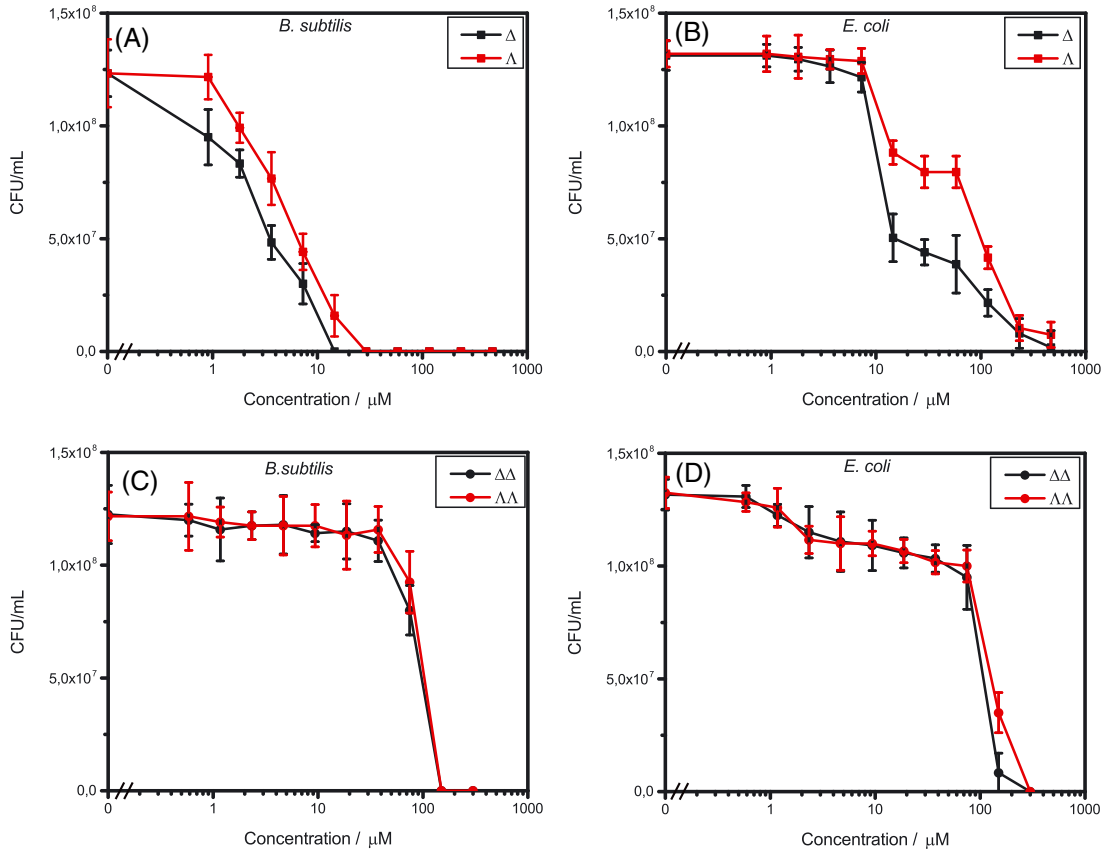

FIGURE 1 Surviving bacterial counts (CFU/mL) of *B. subtilis* (left column) and *E. coli* (right column) after 24-h exposure to Ru-phen (top row, **a,b**) and biRu-phen (bottom row, **c,d**) at 37°C. Each point is the mean of six replicate cultures. Error bars show standard deviations (SD: 3σ); when not visible, these bars are as small as or smaller than the symbols plotted

[SD: 3σ] and Table 1). *E. coli* was never fully eradicated even with the highest concentrations tested. However, both Δ- and ΛRu-phen showed a high bactericidal effect in *B. subtilis,* with a 2-fold higher efficiency in Δ compared to Λ. We also observed a plateau for the viability of *E. coli* at increasing concentrations of the mononuclear complexes (Figure 1b) before a sudden drop to almost zero bacterial growth. A similar yet much less pronounced effect can be seen for the binuclear complexes (Figure 1d). This response is likely the effect the emergence of a small subpopulation bacteria (so called "persisters") that is able to survive antimicrobial exposure, and is part of a survival strategy already well established in *E. coli*.[43–45] The slow-growing persister cells emerge as a response to environmental triggers such as antibiotics and acts as an insurance for the general bacterial population to survive in a stressful environment.

It is conceivable that DNA, being chiral due to its right-handed helical structure, would interact differently with the disymmeric nonintercalating peripheral pair of phen ligands on the ruthenium complex depending on chirality. Being either right- or left-handed, the Δ- and Λ-forms should fit differently into the grooves of the DNA. This could be observed in the early experiments with $[Ru(phen)_3]^{2+}$ where the Δ- and Λ-forms differed in their individual binding modes with DNA[17,46,47] and was further supported in studies with the intercalating analog Ru-phen, where ΔRu-phen was determined to have a stronger binding affinity (2–5 times) for DNA compared to the Λ-form.[48,49] The same chiral discrimination was observed in this study, with ΔRu-phen showing both stronger bacteriostatic effect against both *B. subtilis* and *E. coli* compared to the Λ-form, indicating DNA binding as the primary antimicrobial mode of action. To test this hypothesis, emission of the bacterial cells was recorded after an overnight incubation with the ruthenium complexes. The bacterial cells were exposed to an excess of ruthenium complex, as indicated by the yellow color of the supernatants after washing. No emission of the supernatants was observed, thus suggesting that the cellular membranes of the bacteria had remained intact. Both Ru-phen and biRu-phen are known as "light-switch complexes," meaning that they are completely quenched when unbound in aqueous solution, but show intense fluorescence when intercalated to DNA. Therefore, any fluorescence observed would suggest DNA binding. In both strains, the intensity of emission from the bacterial cells after incubation with ΔRu-phen was significantly higher than that of the Λ-form (Figure 2). A slight redshift was observed for ΛRu-phen in both strains, a phenomenon associated with DNA-complex interactions.[35,50] The largest difference was observed in *E. coli*, consistent with the results from the metal susceptibility assays. The smaller difference in emission for cells of *B. subtilis* exposed to ΔRu-phen or ΛRu-phen could depend on the base composition of the genome. The genome of *B. subtilis* has a higher content of the A and T nucleic acids (56.5%)[51] compared to the genome of *E. coli* (49.2%),[52] and

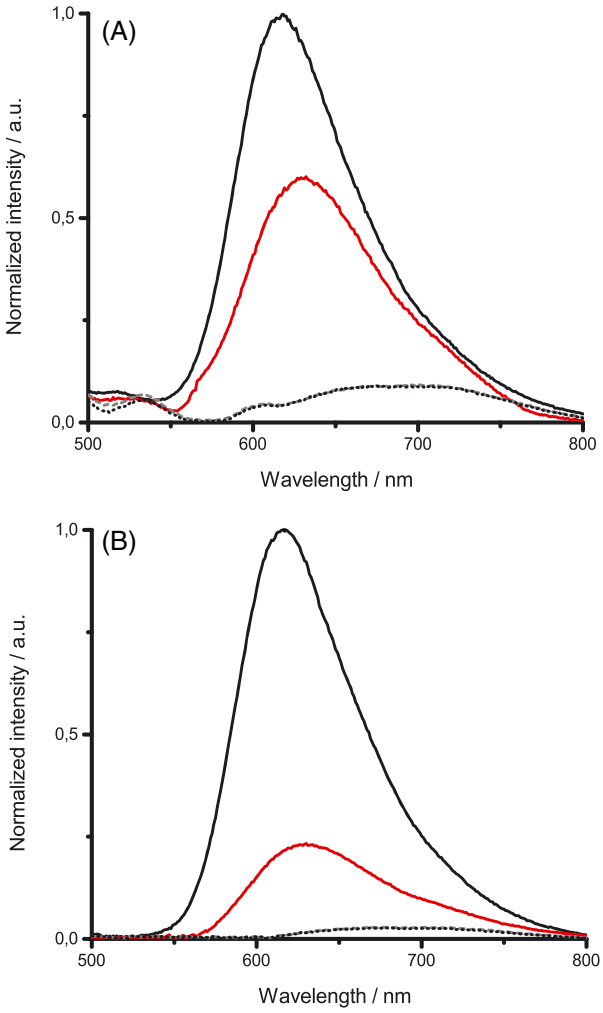

FIGURE 2 Normalized emission spectra of bacterial cells. (**a**) *B. subtilis*; (**b**) *E. coli* after overnight exposure to ruthenium complex (40 μM) at 37°C. The cells were washed twice and resuspended in 1× PBS solution. Emission from bacterial cells without exposure has been deducted. Black: ΔRu-phen; red: ΛRu-phen; black dot: ΔΔbiRu-phen; gray dash: ΛΛbiRu-phen

therefore could explain the less profound difference in intensities, in accordance with the early work by Hiort et al., where the same relative intensities were observed to differ less between Δ- and Λ-$[Ru(phen)_2dppz]^{2+}$ when bound to AT-sequences compared to calf thymus DNA.[35] No emission in the binuclear complex was observed, indicating no interaction with DNA.

Figure 3 shows a confocal microscopic picture of Hoechst-stained *E. coli* that had been previously treated with either enantiomer of Ru-phen. The figure clearly shows emission from both enantiomers, but with much higher intensity from the Δ-form. In addition, the relation between the intensity of the Hoechst stain and the intensity of the complex appears to be inverse; the cells with the highest intensity of ruthenium complex appears to have very weak if any fluorescence from the Hoechst staining, and vice versa. This relation is apparent for both enantiomers. The ruthenium complex and the DNA-stain compete for binding in the minor groove of DNA, thus explaining why bacterial cells with high signal

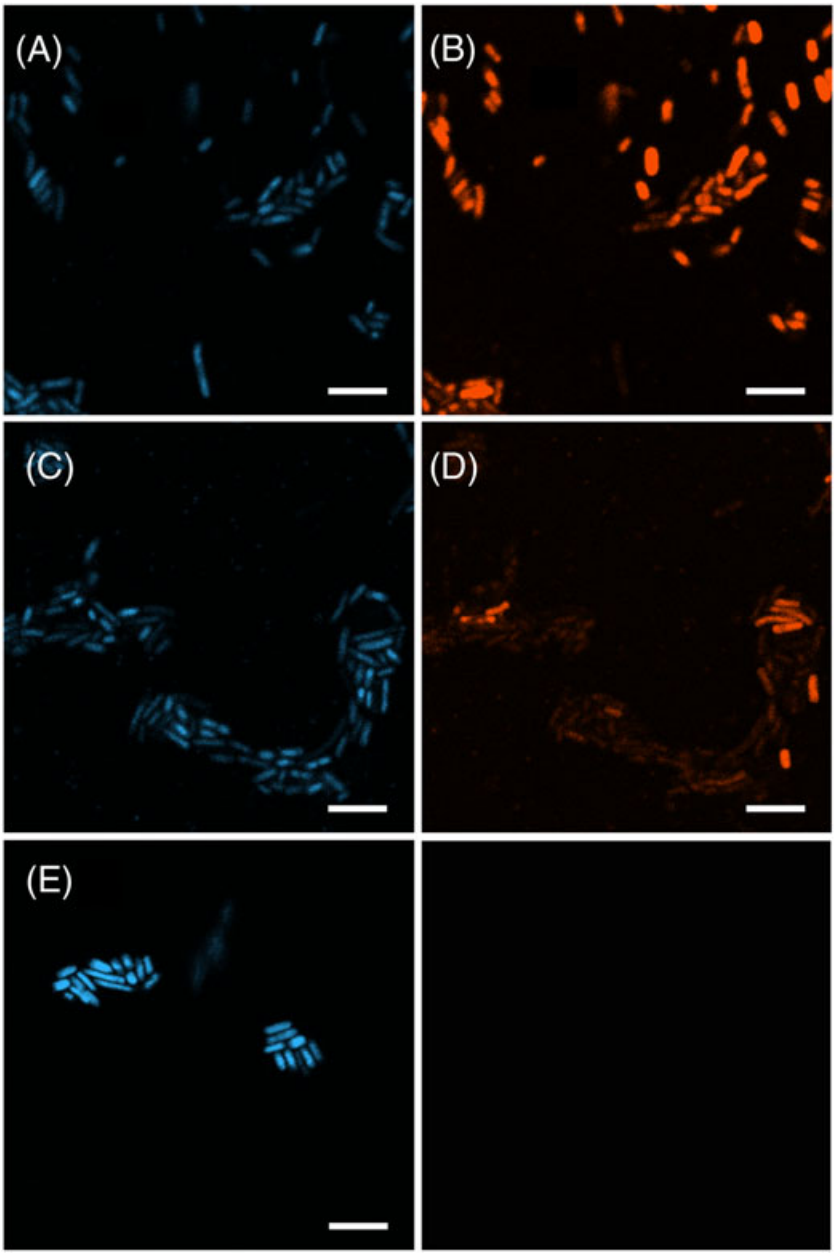

FIGURE 3 Confocal microscopy images of formaldehyde fixed *E. coli* samples incubated with Δ- (top row) and ΛRu-phen (middle row) overnight and then stained with Hoechst 33342. (**a**) fluorescence, Hoechst 33342 (Δ-sample); (**b**) fluorescence, ΔRu-phen; (**c**) fluorescence, Hoechst 33342 (Λ-sample); (**d**) fluorescence, ΛRu-phen; (**e**) fluorescence, control sample *E. coli* stained with Hoechst 33342 (Bottom right: a black square for visual aid). Scale bar =5 μm

for Ru-phen have poor emission from the DNA-stain due to saturation on binding sites on the DNA. The same effect could be observed in *B. subtilis,* while the enantiomeric difference in emission was not as distinct (shown in Figure S3 in the Supporting Information). Furthermore, unexposed bacterial cells used as controls showed significantly stronger emission from the Hoechst dye compared to bacteria exposed to ruthenium complex, again indicating that ruthenium complex and the DNA binding dye competes for the same binding sites.

In conclusion, this is the first reported work of the potential usage of enantiopure $[Ru(phen)_2dppz]^{2+}$ and $[\mu\text{-bidppz}(phen)_4Ru_2]^{4+}$ as antimicrobial compounds. While the binuclear complex had no major toxic effect on bacterial cells, the mononuclear complex showed a high antimicrobial activity, especially in *B. subtilis*, where the effect was comparable to that of tetracycline (as given in Table 1). Importantly, we observed the Δ-enantiomer of $[Ru(phen)_2dppz]^{2+}$ to be 2-fold more effective in both inhibiting and killing *B. subtilis* in comparison to the Λ-enantiomer. Our initial results suggest diastereomeric DNA interactions as the antimicrobial mode of action, which was further supported by stronger emission from Δ compared with Λ in bacterial cells exposed to the compounds. This study clearly demonstrates the potential of enantioselectivity in the bactericidal action of substitution inert transition metal complexes, and emphasizes the importance of studying enantiopure compounds.

4 | CONCLUSION

Two ruthenium(II) polypyridyl complexes were tested for their antimicrobial activity: $[Ru(phen)_2dppz]^{2+}$ and $[\mu\text{-bidppz}(phen)_4Ru_2]^{4+}$, both resolved into their pure

enantiomeric forms (Δ and Λ). Both enantiomers of [Ru(phen)$_2$dppz]$^{2+}$ displayed high bactericidal effect against Gram-positive *B. subtilis*, comparable to the antimicrobial activity of tetracycline, while having a more bacteriostatic effect on Gram-negative *E. coli*. In contrast, [μ-bidppz(phen)$_4$Ru$_2$]$^{4+}$ showed significantly lower antimicrobial activity against both bacterial strains with a bactericidal effect only at the highest concentrations tested.

ACKNOWLEDGMENTS

The authors thank Fredrik Bäckhed at the Wallenberg Laboratory (Sahlgrenska Academy) for funding the materials and equipment used in this study. Also, we thank Vetenskapsrådet (grant VR 2012–1661) and Chalmers Area of Advance Nano for funding and COST action CM1105 for providing a forum for stimulating discussions.

LITERATURE CITED

1. Nikaido H. Multidrug resistance in bacteria. *Annu Rev Biochem*. 2009;119–146.
2. Gootz TD. The global problem of antibiotic resistance. *Crit Rev Immunol*. 2010;30(1):79–93.
3. Projan SJ. New (and not so new) antibacterial targets — from where and when will the novel drugs come? *Curr Opin Pharmacol*. 2002;2(5):513–522.
4. Projan SJ. Why is big Pharma getting out of antibacterial drug discovery? *Curr Opin Microbiol*. 2003;6(5):427–430.
5. Ling LL, Schneider T, Peoples AJ, et al. A new antibiotic kills pathogens without detectable resistance. *Nature*. 2015;517(7535):455–459.
6. Demain AL, Sanchez S. Microbial drug discovery: 80 years of progress. *J Antibiot*. 2009;62(1):5–16.
7. Marchal JA, Prados J, Melguizo C, et al. Actinomycin D treatment leads to differentiation and inhibits proliferation in rhabdomyosarcoma cells. *J Lab Clin Med*. 1997;130(1):42–50.
8. Frei Iii E. The clinical use of actinomycin. *Cancer ChemotherRep*. 1974;58(1):49–54.
9. Braña MF, Cacho M, Gradillas A, De Pascual-Teresa B, Ramos A. Intercalators as anticancer drugs. *Curr Pharm Des*. 2001;7(17):1745–1780.
10. Ming LJ. Structure and function of "metalloantibiotics.". *Med Res Rev*. 2003;23(6):697–762.
11. Sabale PM, Kaur P, Patel Y, Patel J, Patel R. Metalloantibiotics in therapy: An overview. *J Chem Pharm Res*. 2012;4(11):4921–4936.
12. Uivarosi V. Metal complexes of quinolone antibiotics and their applications: An update. *Molecules*. 2013;18(9):11153–11197.
13. Cohen SM, Lippard SJ. Cisplatin: From DNA damage to cancer chemotherapy. 2001;93–130.
14. Kelland L. The resurgence of platinum-based cancer chemotherapy. *Nat Rev Cancer*. 2007;7(8):573–584.
15. Wee HA, Dyson PJ. Classical and non-classical ruthenium-based anticancer drugs: Towards targeted chemotherapy. *Eur J Inorgan Chem*. 2006;20:4003–4018.
16. Brabec V, Novakova O. DNA binding mode of ruthenium complexes and relationship to tumor cell toxicity. *Drug Resist Updates*. 2006;9(3):111–122.
17. Barton JK, Goldberg JM, Kumar CV, Turro NJ. Binding modes and base specificity of tris(phenanthroline)ruthenium(II) enantiomers with nucleic acids: Tuning the stereoselectivity. *J Am Chem Soc*. 1986;108(8):2081–2088.
18. Barton JK, Danishefsky AT, Goldberg JM. Tris(phenanthroline)ruthenium(II): stereoselectivity in binding to DNA. *J Am Chem Soc*. 1984;106(7):2172–2176.
19. Lincoln P, Nordén B. DNA binding geometries of ruthenium(II) complexes with 1,10-phenanthroline and 2,2 ‘-bipyridine ligands studied with linear dichroism spectroscopy. Borderline cases of intercalation. *J Phys Chem B*. 1998;102(47):9583–9594.
20. Erkkila KE, Odom DT, Barton JK. Recognition and reaction of metallointercalators with DNA. *Chem. Rev*. 1999;99(9):2777–2795.
21. Pages BJ, Ang DL, Wright EP, Aldrich-Wright JR. Metal complex interactions with DNA. *Dalton Trans*. 2015;44(8):3505–3526.
22. Dwyer FP, Reid IK, Shulman A, Laycock GM, Dixson S. The biological actions of 1,10-phenanthroline and 2,2′-bipyridine hydrochlorides, quaternary salts and metal chelates and related compounds. 1. Bacteriostatic action on selected gram-positive, gram-negative and acid-fast bacteria. *Austr J Exp Biol Med Sci*. 1969;47(2):203–218.
23. Dwyer FP, Reid IK, Shulman A, Laycock GM, Dixson S. Biological activity of complex ions. *Nature*. 1952;170(4318):190–191.
24. Gill MR, Thomas JA. Ruthenium(II) polypyridyl complexes and DNA-from structural probes to cellular imaging and therapeutics. *Chem Soc Rev*. 2012;41(8):3179–3192.
25. Bolhuis A, Hand L, Marshall JE, Richards AD, Rodger A, Aldrich-Wright J. Antimicrobial activity of ruthenium-based intercalators. *Eur J Pharm Scie*. 2011;42(4):313–317.
26. Lei W, Zhou Q, Jiang G, Zhang B, Wang X. Photodynamic inactivation of *Escherichia coli* by Ru(ii) complexes. *Photochem Photobiol Sci*. 2011;10(6):887–890.
27. Li F, Mulyana Y, Feterl M, Warner JM, Collins JG, Keene FR. The antimicrobial activity of inert oligonuclear polypyridylruthenium(ii) complexes against pathogenic bacteria, including MRSA. *Dalton Trans*. 2011;40(18):5032–5038.
28. Li F, Feterl M, Warner JM, Keene FR, Grant CJ. Dinuclear polypyridylruthenium(II) complexes: Flow cytometry studies of their accumulation in bacteria and the effect on the bacterial membrane. *J Antimicrob Chemother*. 2013;68(12):2825–2833.
29. Li F, Harry EJ, Bottomley AL, et al. Dinuclear ruthenium(ii) antimicrobial agents that selectively target polysomes in vivo. *Chem Sci*. 2014;5(2):685–693.
30. Li F, Harry EJ, Bottomley AL, et al. In vitro susceptibility and cellular uptake for a new class of antimicrobial agents: Dinuclear ruthenium(II) complexes. *J Antimicrob Chemother*. 2012;67(11):2686–2695.
31. Li F, Feterl M, Warner JM, Day AI, Keene FR, Collins JG. Protein binding by dinuclear polypyridyl ruthenium(ii) complexes and the effect of cucurbit[10]uril encapsulation. *Dalton Trans*. 2013;42(24):8868–8877.
32. Li X, Heimann K, Li F, Warner JM, Keene RF, Collins JG. Dinuclear ruthenium(II) complexes containing one inert metal centre and one coordinatively-labile metal centre: Synthesis and biological activities. *Dalton Trans*. 2016;45(9):4017–4029.
33. Li F, Collins JG, Keene FR. Ruthenium complexes as antimicrobial agents. *Chem Soc Rev*. 2015;44(8):2529–2542.
34. Tan CP, Lai SS, Wu SH, et al. Nuclear permeable ruthenium(II)beta-carboline complexes induce autophagy to antagonize mitochondrial-mediated apoptosis. *J Med Chem*. 2010;53(21):7613–7624.
35. Hiort C, Lincoln P, Nordén B. DNA binding of Δ- and Λ-[Ru(phen) 2DPPZ] 2+. *J Am Chem Soc*. 1993;115(9):3448–3454.
36. Wilhelmsson LM, Esbjörner EK, Westerlund F, Nordén B. LincolnMeso stereoisomer as a probe of enantioselective threading intercalation of semirigid ruthenium complex [μ-(11,11′-bidppz)(phen)4Ru2]4+. *J Phys Chem B*. 2003;107(42):11784–11793.
37. Harrison JJ, Tremaroli V, Stan MA, et al. Chromosomal antioxidant genes have metal ion-specific roles as determinants of bacterial metal tolerance. *Environ Microbiol*. 2009;11(10):2491–2509.
38. Henie EFP, Zaiton H, Suhaila M. Bacterial membrane disruption in food pathogens by *psidium guajava* leaf extracts. *Int Food Res J*. 2009;16(3):297–311.
39. Silhavy TJ, Kahne D, Walker S. The bacterial cell envelope. *Cold Spring Harbor Perspect Biol*. 2010;2:a000414.
40. Jenssen H, Hamill P, Hancock REW. Peptide antimicrobial agents. *Clin Microbiol Rev*. 2006;19(3):491–511.

41. Wu M, Hancock REW. Improved derivatives of bactenecin, a cyclic dodecameric antimicrobial cationic peptide. *Antimicrob Agents Chemother*. 1999;43(5):1274–1276.

42. Vooturi SK, Cheung CM, Rybak MJ, Firestine SM. Design, synthesis, and structure — Activity relationships of benzophenone-based tetraamides as novel antibacterial agents. *J Med Chem*. 2009;52(16):5020–5031.

43. Poole K. Stress responses as determinants of antimicrobial resistance in Gram-negative bacteria. *Trends Microbiol*. 2012;20(5):227–234.

44. Gefen O, Balaban NQ. The importance of being persistent: Heterogeneity of bacterial populations under antibiotic stress: Review article. *FEMS Microbiol Rev*. 2009;33(4):704–717.

45. Lewis K. Persister cells. *Annu Rev Microbiol*. 2010;64:357–372.

46. Chaires JB. Tris(phenanthroline)ruthenium(II) enantiomer interactions with DNA: Mode and specificity of binding. *Biochemistry*. 1993;32(10): 2573–2584.

47. Eriksson M, Leijon M, Hiort C, Nordén B, Gräslund A. Binding of Δ- and Λ-[Ru(phen)3]2+ to [d(CGCGATCGCG)]2 studied by NMR. *Biochemistry*. 1994;33(17):5031–5040.

48. Haq I, Lincoln P, Suh D, Nordén B, Chowdhry BZ, Chaires JB. Interaction of Δ- and Λ-[Ru(phen)2DPPZ]2+ with DNA: A calorimetric and equilibrium binding study. *J Am Chem Soc*. 1995;117(17):4788–4796.

49. Andersson J, Fornander LH, Abrahamsson M, Tuite E, Nordell P. LincolnLifetime heterogeneity of DNA-bound dppz complexes originates from distinct intercalation geometries determined by complex-complex interactions. *Inorgan Chem*. 2013;52(2):1151–115.

50. McKinley AW, Lincoln P, Tuite EM. Environmental effects on the photophysics of transition metal complexes with dipyrido 2,3-a:3′,2′-c phenazine (dppz) and related ligands. *Coord Chem Rev*. 2011;255(21–22):2676–2692.

51. Kunst F et al. The complete genome sequence of the gram-positive bacterium Bacillus subtilis. *Nature*. 1997;390(6657):249–256.

52. Blattner FR, Plunkett G III, Bloch CA, et al. The complete genome sequence of Escerichia coli K-12. *Science*. 1997;277(5331):1453–1462.

SUPPORTING INFORMATION

Additional Supporting Information may be found online in the supporting information tab for this article.

How to cite this article: Mårtensson A. K. F., Bergentall M., Tremaroli V. and Lincoln P. Diastereomeric bactericidal effect of Ru(phenanthroline) 2dipyridophenazine, *Chirality*, 2016; 28, DOI: 10.1002/chir.22656 713-720

Diastereomeric bactericidal effect of Ru(phenanthroline)$_2$dipyridophenazine

Anna K. F. Mårtensson*, Mattias Bergentall, Valentina Tremaroli and Per Lincoln

Supporting Information

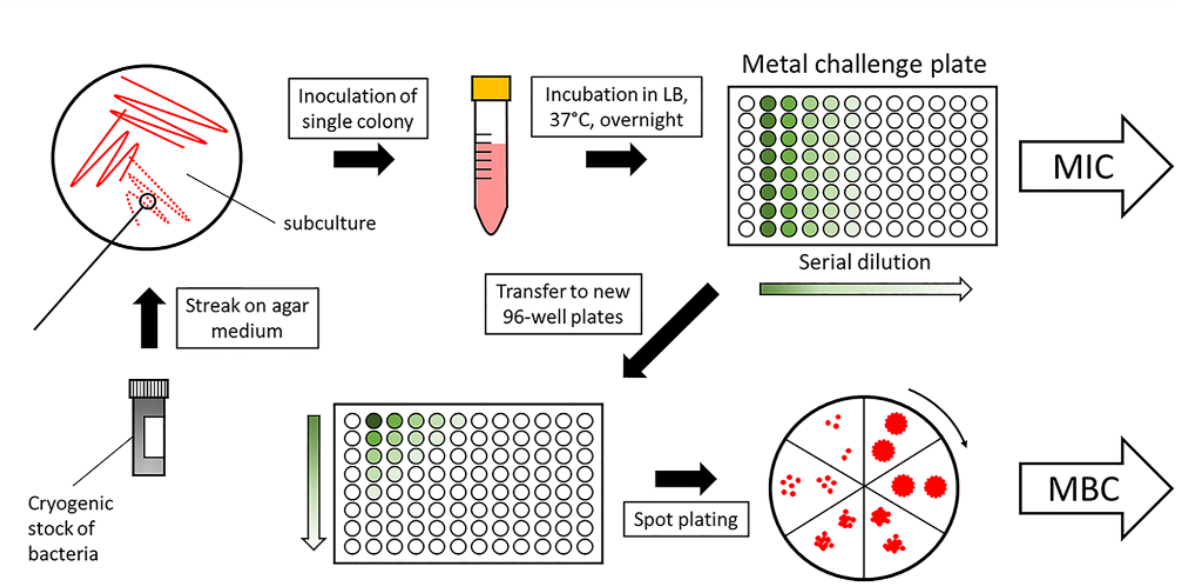

Figure S1 *Experimental setup of the metal susceptibility assay for antibiotic susceptibility testing.*

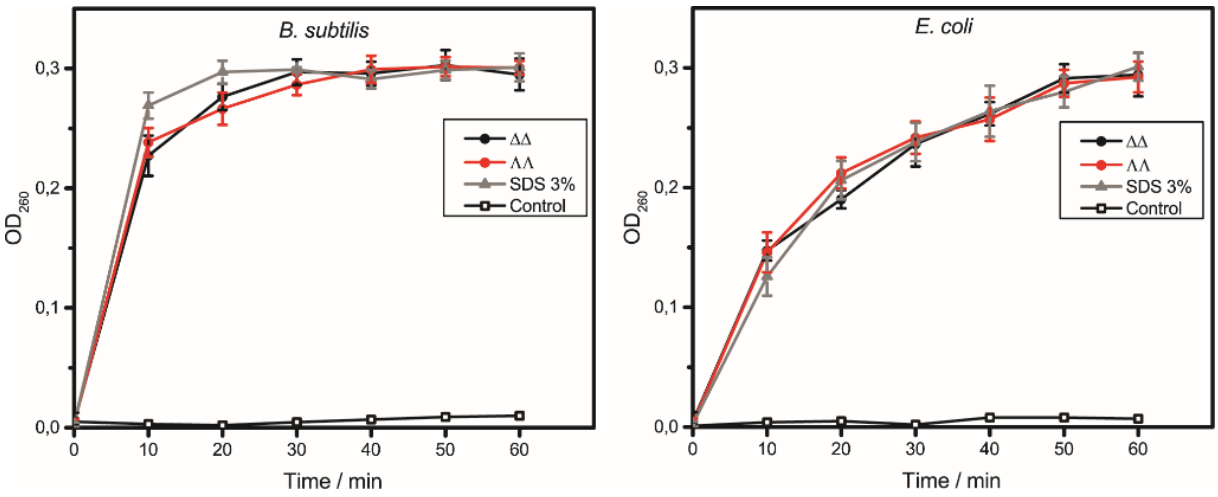

Figure S2 *Total nucleotide leakage measured by UV absorption at 260 nm from B. subtilis (left) and E. coli (right) treated with ΔΔ- (black dots) and ΛΛbiRu-phen (red dots) (~300 μM). 3% SDS solution was used as comparison (gray triangles). Each point is the mean of six replicate cultures. Error bars show standard deviations (SD: 3σ); when not visible, these bars are as small as or smaller than the symbols plotted.*

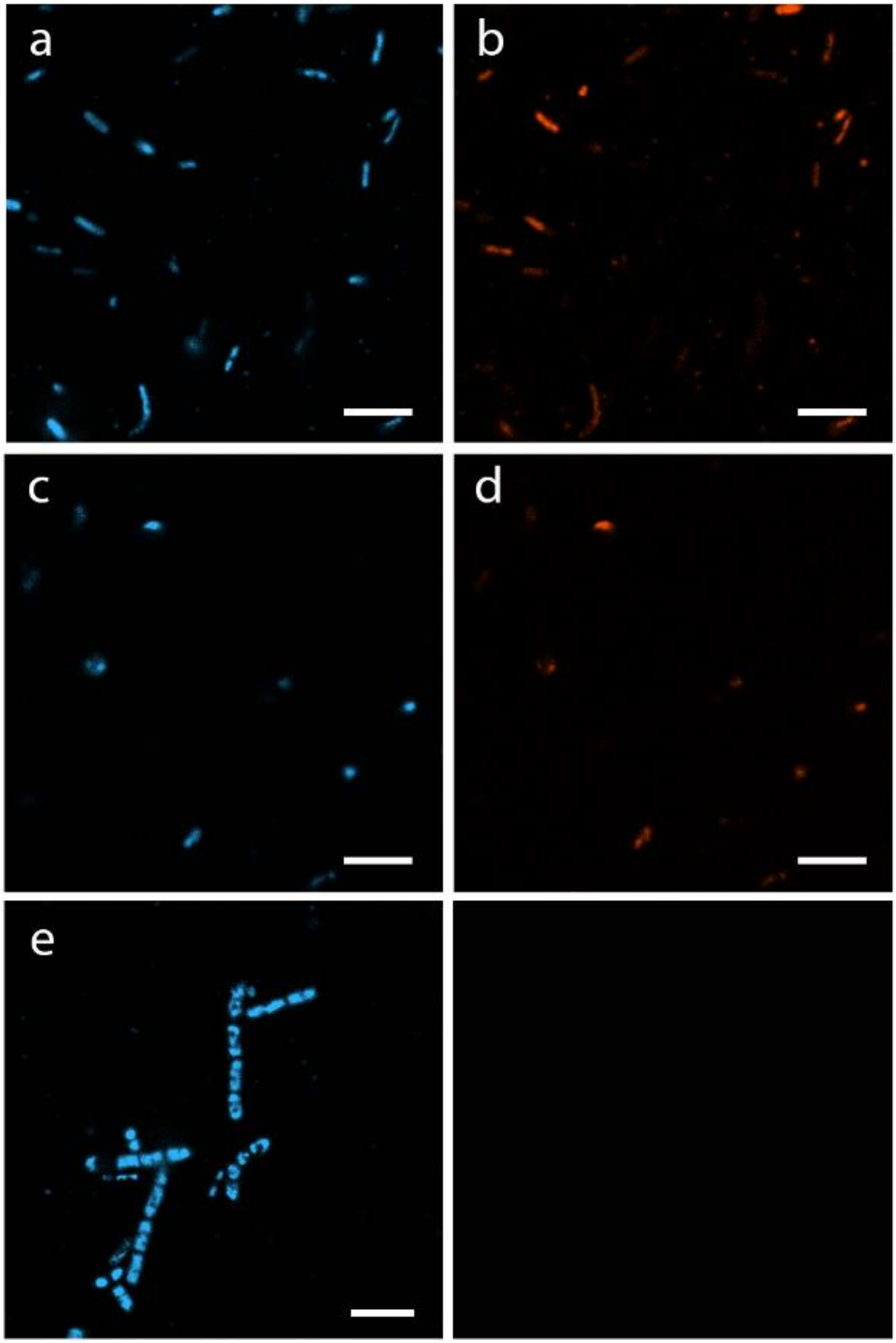

Figure S3 *Confocal microscopy images of formaldehyde fixed B. subtilis cells incubated with Δ- (top row) and ΛRu-phen (middle row) overnight and then stained with Hoechst 33342. (a) fluorescence - Hoechst 33342 (Δ-sample); (b) fluorescence - ΔRu-phen; (c) fluorescence - Hoechst 33342 (Λ-sample); (d) fluorescence - ΛRu-phen; (e) fluorescence - control sample B. subtilis stained with Hoechst 33342 (Bottom right: a black square for visual aid). Scale bar = 5 μm.*